

**2010 SUMMER RESEARCH PROGRAM FOR HIGH SCHOOL JUNIORS**  
**AT THE**  
**UNIVERSITY OF ROCHESTER'S**  
**LABORATORY FOR LASER ENERGETICS**

**STUDENT RESEARCH REPORTS**

**PROGRAM COORDINATOR**

**Dr. R. Stephen Craxton**

**April 2011**

**Laboratory Report 365**

**2010 SUMMER RESEARCH PROGRAM FOR HIGH SCHOOL JUNIORS**

**AT THE**

**UNIVERSITY OF ROCHESTER'S**

**LABORATORY FOR LASER ENERGETICS**

**STUDENT RESEARCH REPORTS**

**PROGRAM COORDINATOR**

**Dr. R. Stephen Craxton**

LABORATORY FOR LASER ENERGETICS

University of Rochester

250 East River Road

Rochester, NY 14623-1299

During the summer of 2010, 16 students from Rochester-area high schools participated in the Laboratory for Laser Energetics' Summer High School Research Program. The goal of this program is to excite a group of high school students about careers in the areas of science and technology by exposing them to research in a state-of-the-art environment. Too often, students are exposed to "research" only through classroom laboratories, which have prescribed procedures and predictable results. In LLE's summer program, the students experience many of the trials, tribulations, and

rewards of scientific research. By participating in research in a real environment, the students often become more excited about careers in science and technology. In addition, LLE gains from the contributions of the many highly talented students who are attracted to the program.

The students spent most of their time working on their individual research projects with members of LLE's scientific staff. The projects were related to current research activities at LLE and covered a broad range of areas of interest including experimental diagnostic development, computational modeling of implosion physics, opacity data for hydrodynamic simulations, laser physics, experimental and theoretical chemistry, materials science, cryogenic target characterization, target positioning and viewing systems, and database development. The students, their high schools, their LLE supervisors, and their project titles are listed in the table. Their written reports are collected in this volume.

The students attended weekly seminars on technical topics associated with LLE's research. Topics this year included laser physics, fusion, holography, nonlinear optics, atomic force microscopy, electrostatics, and electronic paper. The students also received safety training, learned how to give scientific presentations, and were introduced to LLE's resources, especially the computational facilities.

The program culminated on 25 August with the "High School Student Summer Research Symposium," at which the students presented the results of their research to an audience including parents, teachers, and LLE staff. Each student spoke for approximately ten minutes and answered questions. At the symposium the 14th annual William D. Ryan Inspirational Teacher Award was presented to Mr. Brad Allen, a

physics teacher at Brighton High School. This award honors a teacher, nominated by alumni of the LLE program, who has inspired outstanding students in the areas of science, mathematics, and technology. Mr. Allen was nominated by Leela Chockalingam, Aaron Van Dyne, and Harvest Zhang, participants in the 2009 Summer Program.

A total of 265 high school students have participated in the program since it began in 1989. The students this year were selected from over 60 applicants. Each applicant submitted an essay describing their interests in science and technology, a copy of their transcript, and a letter of recommendation from a science or math teacher.

In the past, several participants of this program have gone on to become semifinalists and finalists in the prestigious, nationwide Intel Science Talent Search. This tradition of success continued this year with the selection of Barry Xu as one of the 300 semifinalists nationwide in this competition.

LLE plans to continue this program in future years. The program is strictly for students from Rochester-area high schools who have just completed their junior year. Application information is mailed to schools and placed on the LLE website in early February with an application deadline near the end of March. For more information about the program, please contact Dr. R. Stephen Craxton at LLE.

This program was supported by the U.S. Department of Energy Office of Inertial Confinement Fusion under Cooperative Agreement No. DE-FC52-08NA28302.

<b>High School Students and Projects (Summer 2010)</b>			
<b>Name</b>	<b>High School</b>	<b>Supervisor</b>	<b>Project Title</b>
James Baase	Victor	G. Brent, D. J. Lonobile	Optimizing the Movement of a Precision Piezoelectric Target Positioner
Andrew Chun	Brighton	F. J. Marshall	X-Ray Imaging with Compact Kirkpatrick-Baez Microscopes
Robert Cooper	Allendale-Columbia	R. W. Kidder	Designing and Implementing an Ontology for LLE Experimental Diagnostics
Luke Coy	Greece Arcadia	R. S. Craxton, R. Rombaut	A Graphical User Interface for User Generated Opacity Files
Kyra Horne	Fairport	M. J. Guardalben	Reducing UV Near-Field Beam Modulation on OMEGA EP by Angularly Detuning the Frequency Conversion Crystals
Karin Hsieh	Webster Schroeder	W. T. Shmayda	Modeling Tritiated Water Desorption from Stainless Steel
Connie Jiang	Brighton	D. W. Jacobs-Perkins, R. Huff	Testing and Installation of the Reticule Projector on OMEGA's Target Viewing System
George Liu	Pittsford Sutherland	R. Epstein	Imploded Shell Parameter Estimation Based on Radiograph Analysis
Thomas Mo	Webster Schroeder	R. S. Craxton	X-Ray Backlighting of Shock Ignition Experiments on the National Ignition Facility
Eric Pan	Webster Thomas	T. B. Jones	Using Surface Evolver to Model the Behavior of Liquid Deuterium
Ryan Shea	Fairport	W. T. Shmayda	Tritium Desorption from Stainless Steel Surfaces at Variable Temperatures
Laura Tucker	Brighton	R. S. Craxton	A Design for a Shock Ignition Experiment on the NIF Including 3-D Effects
Katherine Wegman	Pittsford Mendon	K. L. Marshall	Liquid Crystal Beam Shaping Devices Incorporating Coumarin-Based Photoalignment Layers
Francis White	McQuaid	D. H. Edgell, M. D. Wittman	Determination and Correction of Optical Distortion in Cryogenic Target Characterization
Barry Xu	Brighton	S. X. Hu	Electron-Ion Temperature Relaxation Models for Inertial Confinement Fusion
Andrew Yu	Pittsford Sutherland	K. L. Marshall	Modeling Absorption Spectra of Optically Switchable Azobenzenes

# **Optimizing the Movement of a Precision Piezoelectric Target Positioner**

James Baase

Victor Senior High School  
Rochester, NY

Advisors: Gregory Brent, David Lonobile

Laboratory for Laser Energetics  
University of Rochester  
Rochester, NY  
Summer 2010

## I. Abstract

For any successful laser fusion experiment on the OMEGA or OMEGA EP laser systems, a target must be accurately positioned and stabilized at the location of beam convergence. New technology in the form of piezoelectric motors greatly improves upon the drawbacks inherent to existing DC motors and gearboxes. Unlike those conventional systems, piezoelectric motors can operate at cryogenic temperatures inside the target chamber. This eliminates the need for a long stalk conducive to vibration and a warm operating environment. Eventually, these motors might also provide a means of actively stabilizing the target by compensating for tremors in real time. In order to gain a better understanding of these miniature motors, an experiment was carried out to determine the force a piezoelectric motor could produce with various frequencies, voltages, and materials. At cryogenic temperatures, it is essential to optimize the functionality of the motor so that it moves efficiently and does not bind. It was discovered that the piezoelectric motor exerted the most force while containing slides made of polyether ether ketone (PEEK), at a frequency of 894 Hz and a voltage of 126 V.

## II. Introduction

At the Laboratory for Laser Energetics, cryogenic targets are currently positioned in the vacuum chamber with DC motors and high-ratio gearboxes (the motor output must be geared down to provide very small increments of motion). In order to use these components, which must remain warm and thermally isolated to operate, targets are placed on the end of long, insulating stalks. This approach suffers from several disadvantages that include larger size and mass, susceptibility to vibration, heat loading of cryogenic pumps, limited position

resolution, and gear backlash. Piezoelectric motors, when employed in the target chamber on all three axes (x, y, and theta), can solve these problems due to their characteristics and manner of operation. The motors can work at cryogenic temperatures, directly coupled to a shorter target stalk. For this reason, targets move more precisely with less induced vibration or oscillation. Furthermore, piezoelectric motors are compact and yet still provide significant levels of force (up to approximately 1 kg) and a step size of microns (the sending of a single electrical pulse). The design of the motor also involves a high degree of static friction that can impede motion when the piezoelectric element is not in use, thereby dampening instabilities from the external environment.

A piezoelectric motor is a small device that relies on an applied electric voltage to move. Its operation is unique: it utilizes the “slip-stick” effect that takes advantage of the difference between static and kinetic friction. As outlined by D. W. Pohl<sup>1</sup>, a waveform is applied to a static piezoelectric element, which applies force to a set of rails. The carriage rides on these rails as they are pushed in one direction until the force of static friction is exceeded by the force imparted by the element. At that moment, the carriage breaks free and enters kinetic friction. The waveform drops off (and as a result the element contracts and the rails return to their previous state), but the carriage continues sliding due to its momentum and inertia. Finally, kinetic friction brings it to a halt, at which point some net displacement has occurred on the axis of the piezoelectric element’s expansion. The carriage, having undergone one step, is again in static friction. For target positioning, this constitutes the smallest amount of distance the target can be moved – and due to the miniscule nature of the “slip-stick” effect, this is on the order of microns. If further movement is desired, the waveform can be repeated many times a second to generate a significant linear displacement.



### III. Initial Preparation

First, it was necessary to establish what it meant to “optimize” a piezoelectric motor. It was decided that the piezoelectric motor would be quantified in terms of maximum force exerted. To measure this, the motor would be attached to either a force gauge or load cell that could provide an accurate measurement of the motor’s performance. Since a load cell was on hand (Figure 1), it was tested for reliability and accuracy prior to connecting the piezoelectric motor and its associated equipment. The cell was connected to a computer with an analog to digital converter; it was subsequently calibrated and zeroed. Two separate experiments, one with beakers of water (of known volumes) and one with standardized masses, were performed to determine if the load cell was consistent and whether it could predict the amount of mass or the mass of the beaker placed on it. Figure 2 shows a plot of voltage versus mass, the data resulting from the standardized mass experiment. Different masses failed to yield linear and predictable changes in voltage. The load cell was 13% off in predicting the mass of the beaker and 15.6% off from a 500 g mass. Evidenced in Table 1, the load cell lacked consistency across different usage periods. In the three different tests noted, the cell’s voltage was recorded with nothing present to serve as a reference value and point of comparison. The resulting zero mass voltages fluctuated on each of the three separate occasions – a predicted mass difference (based on the first day’s zero value and a constant, best-fit slope generated from multiple mass tests) showed a variation of approximately 80 grams. As a result, a more stable force gauge was necessary.

To be used in the experiment, the new gauge would require high accuracy and sensitivity to measure slight differences in force output from the piezoelectric motor.

Mechanical force gauges, which allow for a manual reading of force at various integer values, were insufficient. In order to create an optimal experimental set-up, a digital force gauge was obtained that could interface with a computer for automated data acquisition. Additionally, the waveform generator's major components were assembled to create a device that could run up to five channels at once with whatever waveform, frequency, or voltage that was desired (Figure 3). This machine is crucial to the operation of the piezoelectric motor, as it externally applies voltage to the piezoelectric element.

In this experiment, the waveform and motor utilized are shown in Figures 4 and 5, respectively. The exponential waveform was determined<sup>2</sup> to be optimal at maximizing the “slip-stick” effect and, therefore, efficient translation of the carriage. The motor itself was designed at the Laboratory for Laser Energetics for use in the target chamber, as existing options worked sporadically or lacked the robustness needed for cryogenic laser targeting. The motor consists of two major parts, the stationary base and the moving carriage. Figure 6 shows the base with the carriage removed; it is mounted to a large platform of aluminum (for the experiment) with a mounting plate (visible at the corners), and in the center lies the piezoelectric element that supplies the force. Figure 7 shows the carriage that moves on the rails of the base; it interfaces with the base via slides that can be made of different materials. This particular experiment made use of four materials, as shown in Figure 8: stainless steel, PEEK, polyethylene, and Vespel.

#### IV. Experiment

Initially, despite the understanding that analog gauges wouldn't be feasible for the later part of the experiment, they were used to generate values of range and maximum force

to roughly characterize the piezoelectric motor. In addition, the tension placed on the motor via a spring and set screw, the screws holding the slides, and the placement of kapton tape were varied to create the best possible motor functionality. It was discovered that when the slides can flex minutely, the motor operates much more effectively – as a result, Bellevue washers were placed on the slide screws to allow for small amounts of compression. The kapton tape, when placed between the slide and carriage (on the side with the tension spring), ensured that the carriage always maintained optimum contact with the rails.

Subsequently, an experiment was performed to identify what frequency, voltage, and material resulted in the maximum force from the motor. Early testing had revealed that the motor needed to be interfaced with a force gauge in a way that dampened vibration; as a result, the set-up involved the motor pushing against a rubber stopper on the end of a rod connected to the digital force gauge (Figure 9). The motor and gauge were mounted to an aluminum plate placed on a level surface (Figure 10). The motor was screwed to the plate, while the gauge was mounted on sliders so that it could be adjusted. The waveform generator powered the piezoelectric motor, while the gauge was hooked up to the main computer. On that computer, custom LabVIEW software was created to both control the waveform generator and monitor the force gauge. In its final form, it was able to test the piezoelectric motor at a certain frequency or voltage setting (holding the other constant), increment that setting, reset the motor to its home position, read the gauge's maximum reported force value and write it to a file, reset the gauge, and repeat at the new setting. After completing the software and set-up, updating the waveform generator's firmware, and performing basic tests, the following was discovered: the motor would not run below 60 Hz or 50 V, and

frequency intervals of 10 Hz were too large for the final test (considerable fluctuation in force output could occur inside of 10 Hz increments).

The final experiment was carried out as follows. A given pair of slides, composed of one of the four materials, was mounted to the carriage. The motor was run from 60-2000 Hz, in increments of 2 Hz, at a constant 120 V. At each setting, the force output was measured by the gauge and recorded. This was then repeated two additional times, for a total of three data sets, which were then averaged. From this averaged data, the three strongest frequencies were identified. For each of these frequencies, three tests were run that varied the voltage from 50-140 V, in increments of 2 V, while holding frequency constant at the value determined in phase one of the experiment; each frequency's three trials were then averaged separately. The highest frequency-voltage pair was then recorded for that material, along with the actual force output, for later comparison with the other three materials. This procedure was repeated for all four materials. Finally, it was determined which material, at what frequency and voltage setting, yielded the most force.

## V. Results

Figure 11 demonstrates the results of the frequency modulation, for each of the four materials over the entire range of scanned frequencies. It is interesting to note that, regardless of material, the data has relative maxima and minima around the same frequencies (specifically, all surge around 700-900 Hz and 1300-1500 Hz and drop from 1000-1200 Hz) and PEEK appears stronger than the other materials over the majority of the frequency range. Figures 12-15 display the results of the voltage modulation for each of the four materials at their best three frequencies, as labeled. Clearly all four materials have a preference for a

voltage near 120 V. Figure 16 contains the optimal frequency-voltage pairs for each of the four materials, and those values constitute the settings at which data was generated for Figure 17; that last figure plots the absolute maximum amount of force output by each material, and is thus the culmination of the experiment. It is easy to conclude that the piezoelectric motor is strongest with slides made of PEEK, putting out almost 800 g at 894 Hz and 126 V. Stainless steel comes in second with a little over 700 g at 732 Hz and 116 V, while the other two materials produce much lower values as shown.

## VI. Conclusion

An experiment was performed in order to optimize and characterize the new piezoelectric motor system. These motors have many advantages that encourage the facility to replace DC motors for target positioning, and the only impediment is a lack of finalized design or refined operation of the piezoelectric system. The experiment involved the creation of software which can be used in the future to test the motors, possibly in cryogenic conditions similar to those of the target chamber. Additionally, a comprehensive set of data was obtained that represents motor performance with different materials and settings. It was found that PEEK produced the most force from the motor, followed closely by stainless steel and more distantly by the other two materials, polyethylene and Vespel. It was also found that kapton tape in collaboration with the tension spring, and slight compression on the slide screws, greatly aids motor performance. It is hoped that this experiment increases understanding of the piezoelectric system and will accelerate its adoption at the Laboratory for Laser Energetics.

## VII. Acknowledgments

I would like to thank Gregory Brent for his knowledge, insights, time, and patience. He taught me a tremendous amount of information, and even went above and beyond to ensure that I understood topics in electrical engineering beyond those involved in the experiment. His assistance with LabVIEW and numerous suggestions throughout the process will not be forgotten. I would also like to thank David Lonobile, for helping me perfect my presentation and establish an experimental procedure, and Eryk Druszkiewicz, for assisting with load cell validation and project set-up. Lastly, I would like to acknowledge Stephen Craxton for his time and effort in the high school program. If it weren't for his management of the program's organizational aspects, such a wonderful opportunity at the University of Rochester simply wouldn't exist; furthermore, I appreciate his careful review of each intern's materials.

## VIII. References

1. D. W. Pohl, "Dynamic piezoelectric translation devices," Rev. Sci. Instrum. 58, 54 (1987)
2. G. Brent, private communication (2010)

## IX. Table and Figures

**Table 1 The load cell voltages with zero applied mass at three separate times, and resulting mass predictions**

The load cell could clearly fluctuate without influence. As shown, this could upset any data taken by up to approximately 80 g.

Test	Zero Mass Voltage (V)	Predicted Mass Difference (g)
July 12	1.2438999	(reference)
July 13, Test 1	1.2452463	+ 79.2
July 13, Test 2	1.2440528	+ 9.0



**Fig. 1 The load cell**

This is the load cell that was tested for accuracy and reliability. Initial plans consisted of using this device to measure force from the motor, but experimentation proved that this was not feasible.

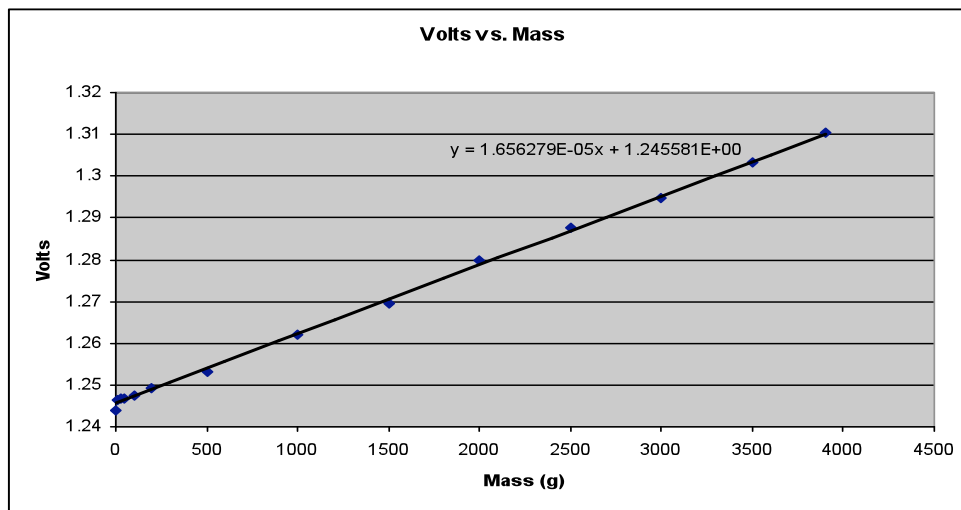


**Fig. 2 Graph of volts vs. mass resulting from initial load cell testing**

This data helped prove the load cell's inadequacy by demonstrating a slight curvature. Additionally, the slope was unable to yield accurate mass predictions.



**Fig. 3 The waveform generator**

Constructed for this experiment, the waveform generator was used to send any desired waveform, frequency, or voltage to the piezoelectric element.

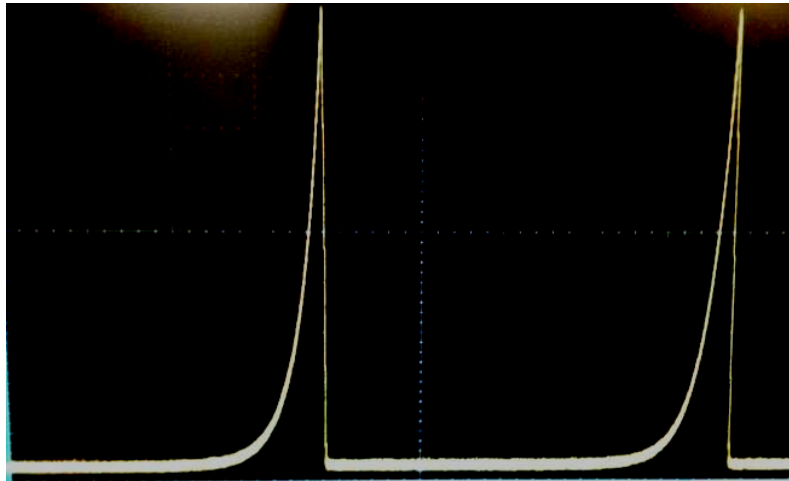


**Fig. 4** The exponential voltage waveform used to drive the piezoelectric motor

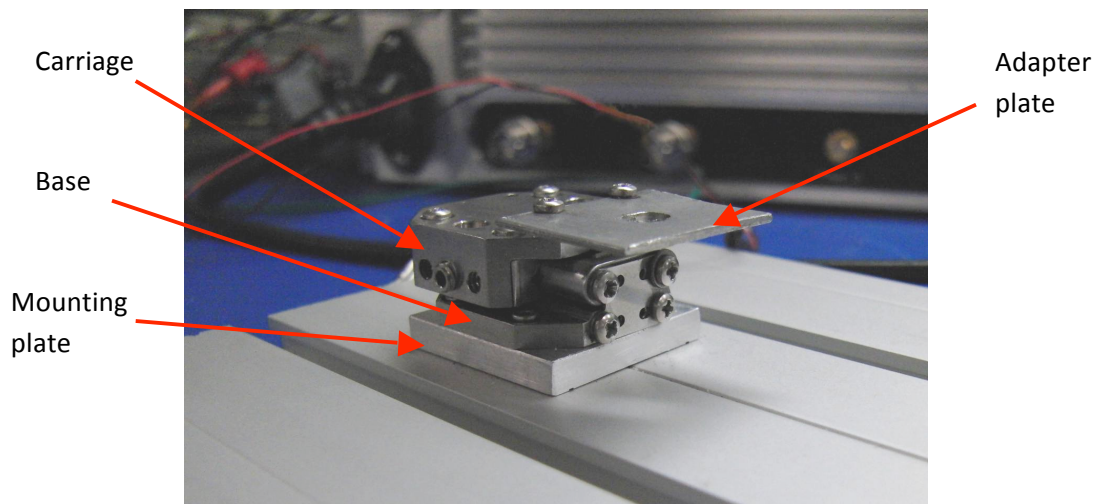


**Fig. 5** The piezoelectric motor, as configured for this experiment

Here the motor is fully assembled, and the base, carriage, adapter plate, and mounting plate are all visible.

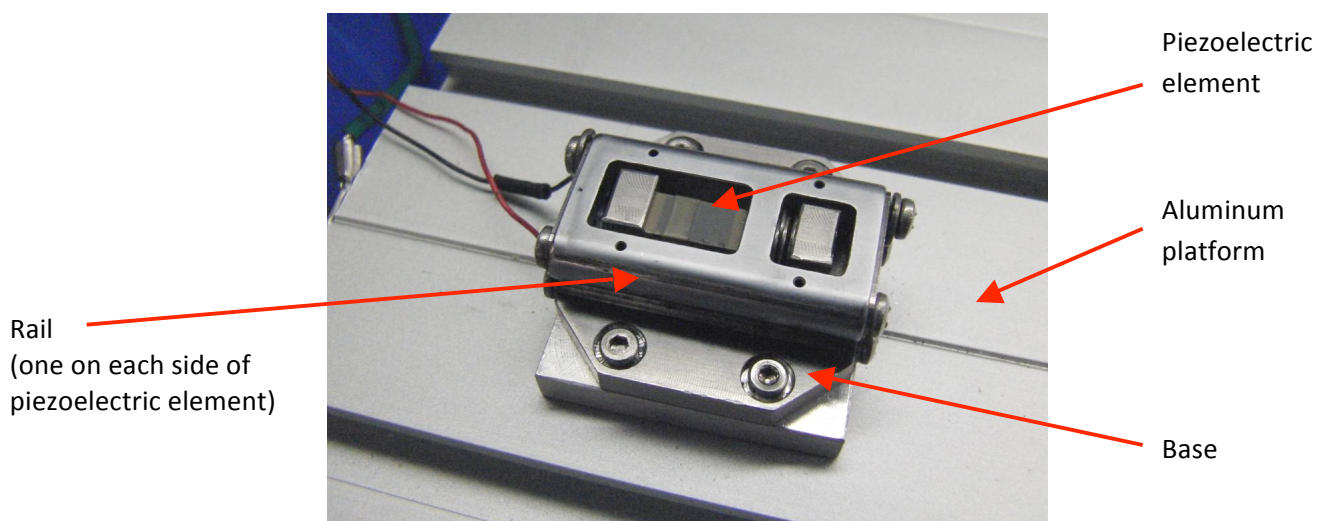


**Fig. 6** The base of the piezoelectric motor

In the center of the base (in gray and brown) is the piezoelectric element, which provides the vibrations that drive the motor.



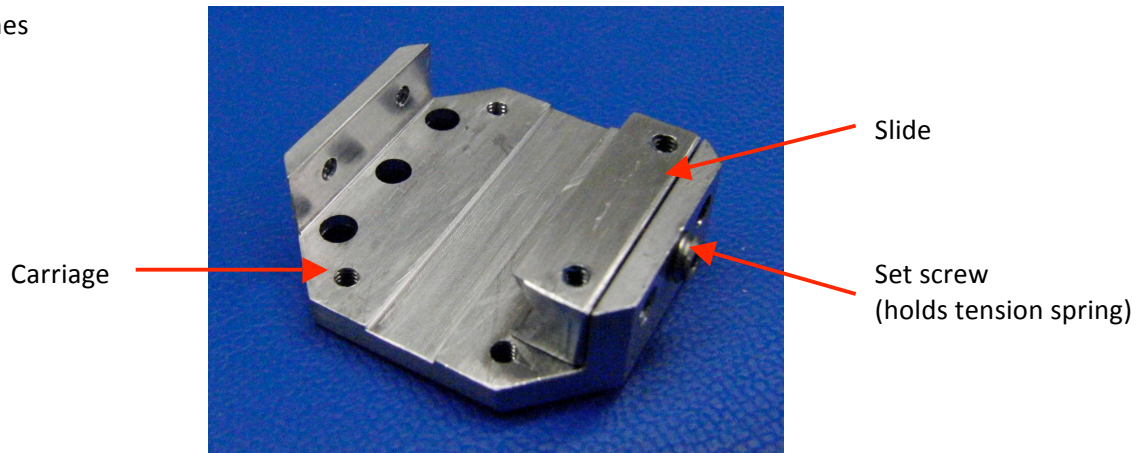


**Fig. 7 The carriage of the piezoelectric motor**

The carriage of the motor is what actually moves and positions the target. In this photo, the carriage has one of its two stainless steel slides installed on the right.

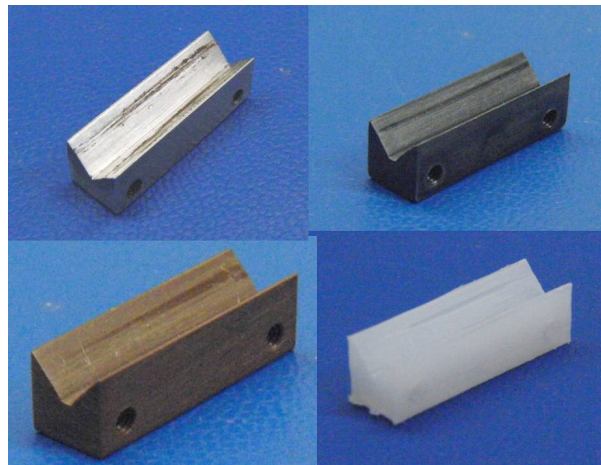


**Fig. 8 The four slide materials tested in the final experiment**

These four materials were tested extensively to determine force characteristics. The materials are, clockwise from top left, stainless steel, PEEK, polyethylene, and Vespel.

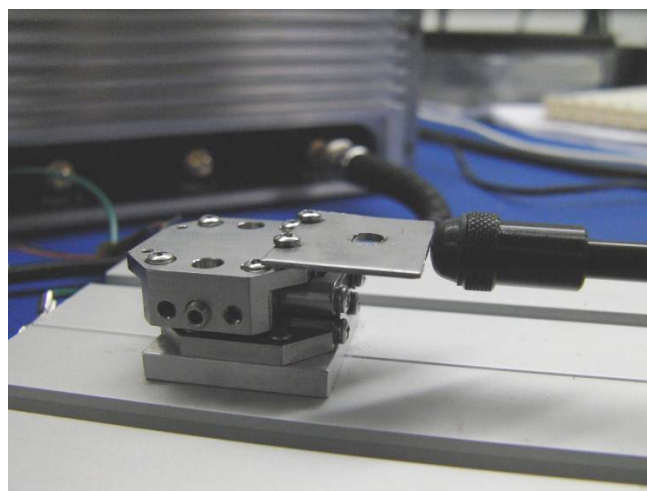


**Fig. 9 Piezoelectric motor interfacing with force gauge**

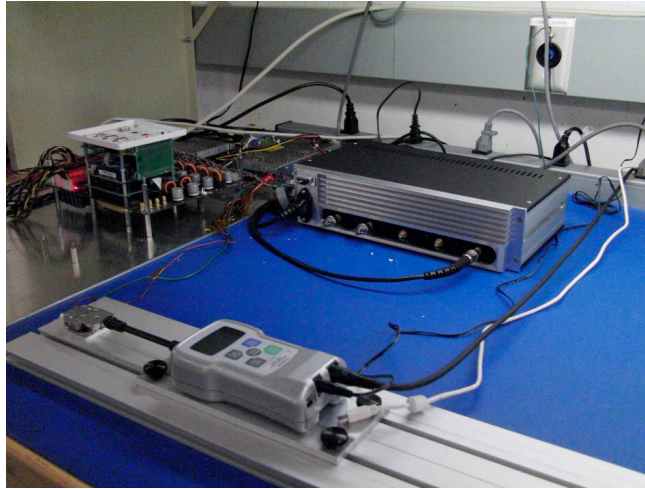


**Fig. 10 The final experimental set-up**

Here the piezoelectric motor, force gauge, waveform generator, and experimental platform are clearly visible.

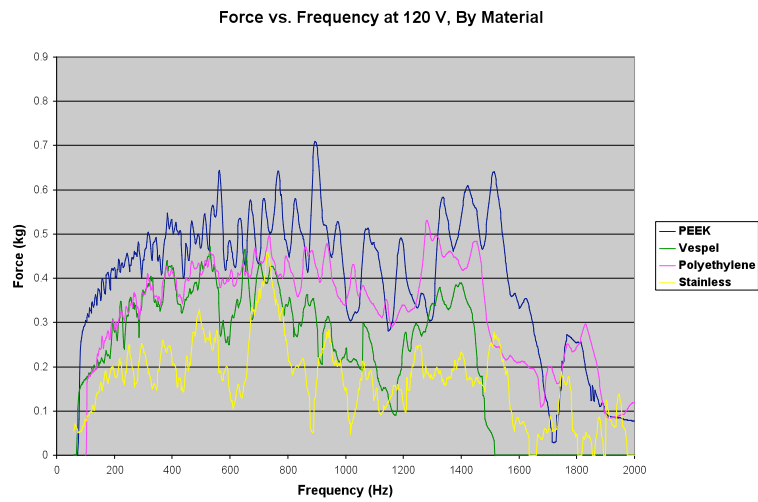


**Fig. 11 Forces output by the various materials over the scanned range of frequencies at 120 V**

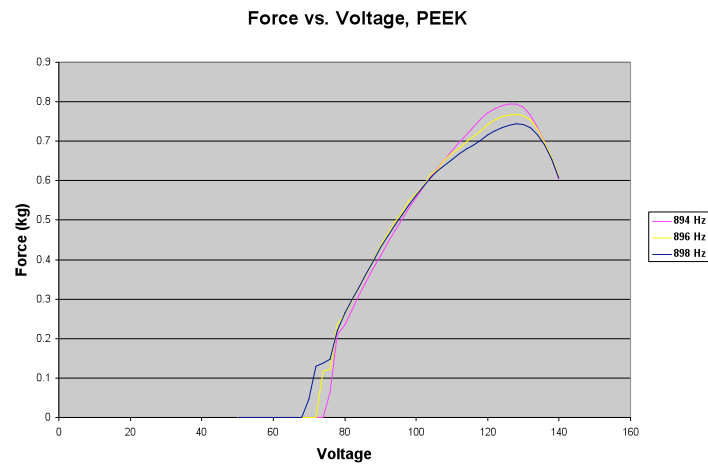


**Fig. 12 Force vs. voltage for PEEK slides, at given frequencies**

Each frequency line represents the average of three trials.

Force vs. Voltage, Vespel

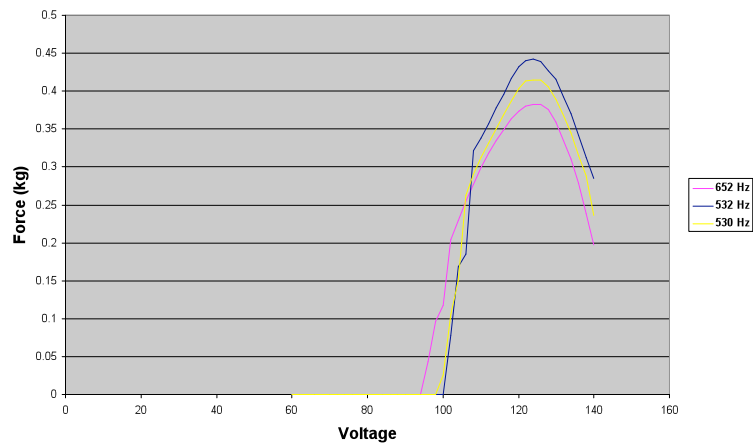


Fig. 13 Force vs. voltage for Vespel slides, at given frequencies

Each frequency line represents the average of three trials.

Force vs. Voltage, Polyethylene

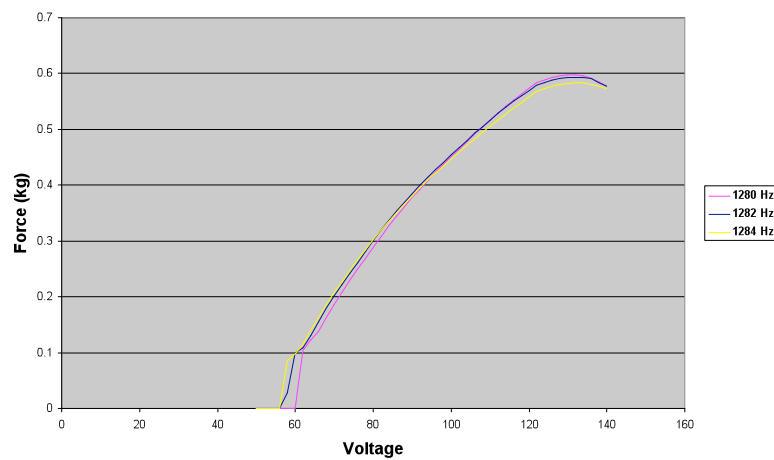


Fig. 14 Force vs. voltage for polyethylene slides, at given frequencies

Each frequency line represents the average of three trials.

Force vs. Voltage, Stainless

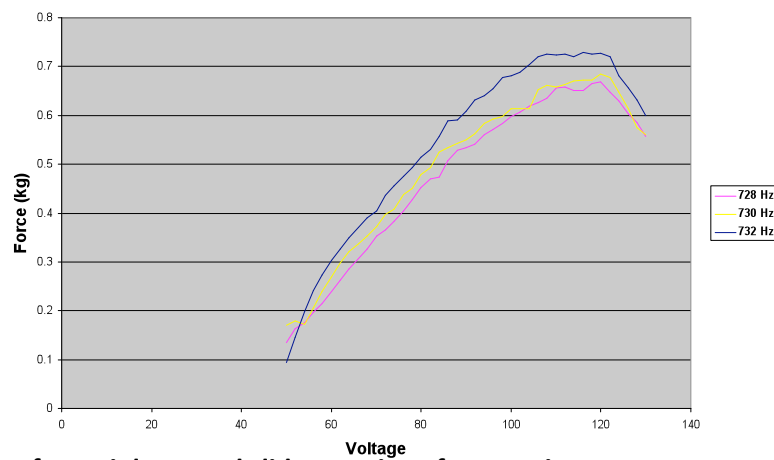


Fig. 15 Force vs. voltage for stainless steel slides, at given frequencies

Each frequency line represents the average of three trials.

### Optimum Electrical Settings

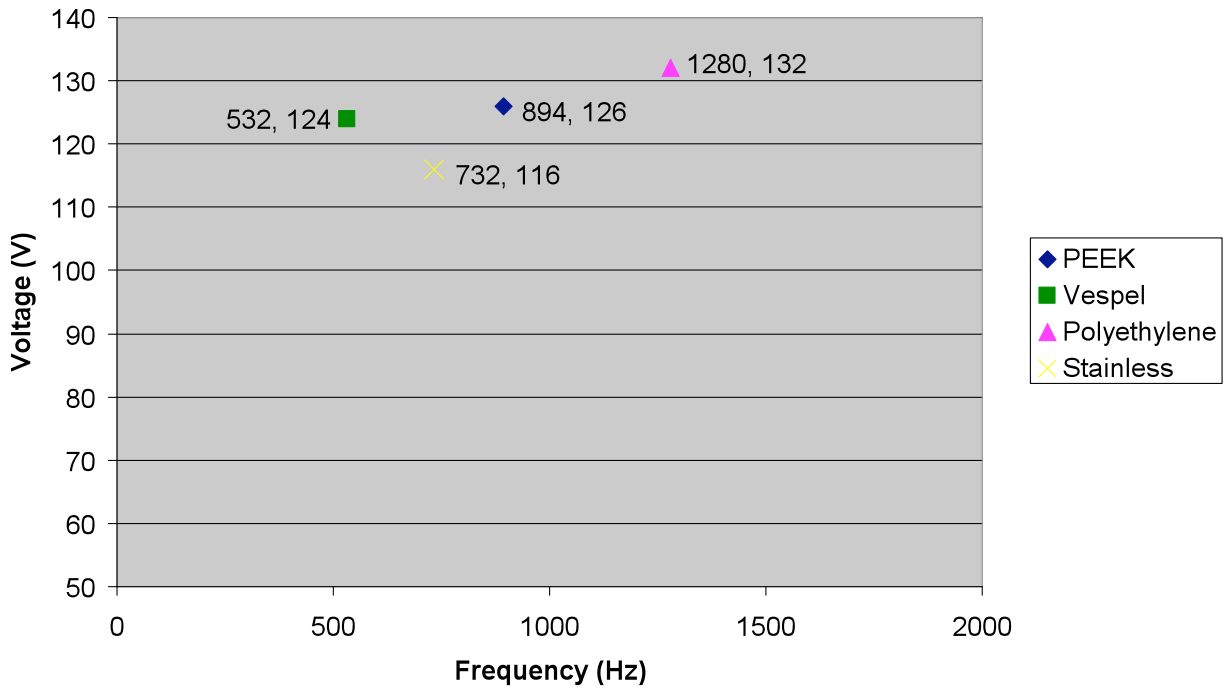


Fig. 16 Electrical settings used to generate maximum force, by material

### Maximum Force Exerted By Each Material

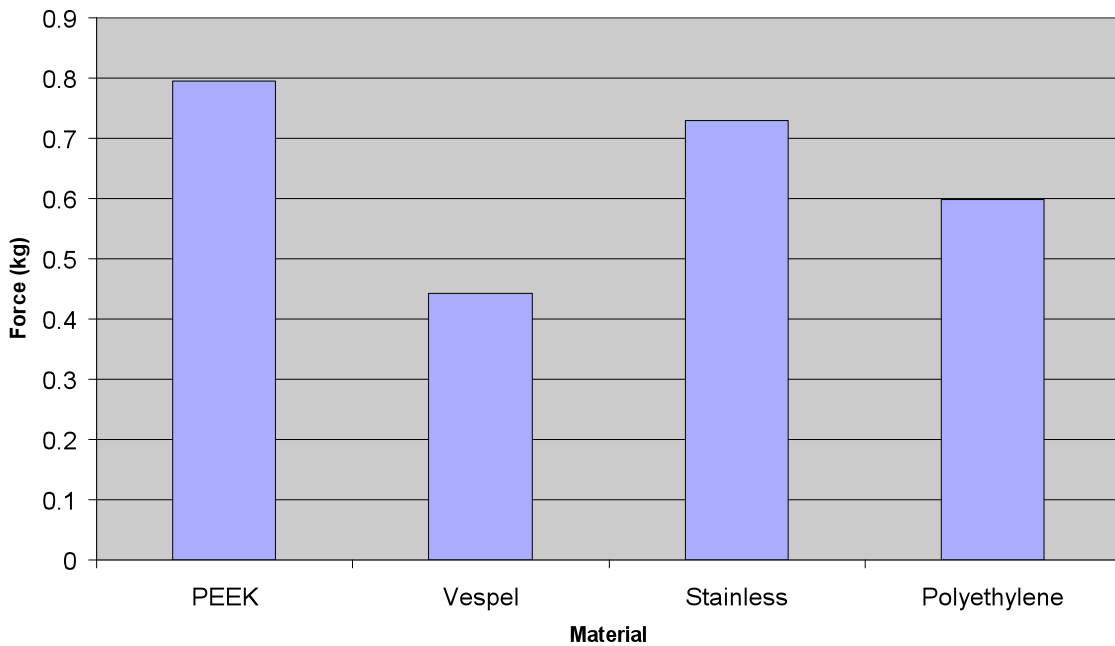


Fig. 17 Maximum forces exerted by each material

## *X-Ray Imaging with Compact Kirkpatrick-Baez Microscopes*

Andrew Chun  
University of Rochester Laboratory of Laser Energetics  
2010 Summer High School Program

### **Abstract**

X-ray imaging is needed to diagnose inertial confinement fusion (ICF) implosions. For example, radiography using an x-ray backlighter target allows the size, symmetry, and density of both the compressed core and surrounding shell to be determined. One means of imaging ICF target x-ray emission is a compact Kirkpatrick-Baez (KB) microscope. Before a KB microscope is used, the KB optic must have its best focus location and resolution determined. Test exposures were taken with an electron-beam-generated x-ray source. The test target was a copper grid with 25.4  $\mu\text{m}$  diameter wires and a reference hole to align different exposures. A PV-Wave program was written to efficiently take lineouts across the image. These lineouts graph the film density of the shadows created by the mesh grid. Measurements of the edge response of the shadows were subsequently used to determine the best focus positions in the images, as well as the point spread function near best focus. The calibrated mirror pairs will assist the continued development of a 16-image KB microscope.

### **Introduction**

Inertial confinement fusion (ICF) may one day provide mankind a nearly unlimited source of energy. In the ICF process, high-intensity laser beams are used to uniformly compress thermonuclear-fuel-bearing targets, filled with deuterium and tritium fuel.<sup>1</sup> The subsequent ablation of the target leads to an implosion confined by inertia, allowing the fuel to be driven to

extremely high temperatures (in excess of  $1.5 \times 10^7$  K) and extremely high densities ( $\sim 100$  g/cm<sup>3</sup>), comparable to conditions found at the center of the sun.

The fusion of a deuteron and a triton results in the creation of an energetic alpha particle and a neutron. The alpha particles can deposit their energy in the compressed fuel, resulting in additional fusion reactions. This process can produce a propagating thermonuclear burning region that gives off an enormous amount of energy. The ultimate goal of inertial confinement fusion research is to achieve ignition, a condition where the energy given off by the reactions is greater than the amount of energy required to initiate the fusion process. The National Ignition Facility (NIF) in Livermore, California hopes to become the first fusion facility to attain ignition in the laboratory.<sup>2</sup>

To support the NIF, the Laboratory for Laser Energetics at the University of Rochester carries out fusion-related experiments on its OMEGA<sup>3</sup> and OMEGA EP<sup>4</sup> lasers. OMEGA is a 60-beam ultraviolet laser system with an output of 30 kJ of energy in 1 nanosecond, corresponding to a power of 30 TW ( $30 \times 10^{12}$  W), typically used to irradiate a 1 mm diameter target. The laboratory's second laser system, OMEGA EP, is capable of picosecond ( $10^{-12}$  s) laser pulses with an on-target energy of approximately 1 kJ for two of its four beams, thereby operating at a power output of  $\sim 1$  PW ( $10^{15}$  W).

When the laser beams compress the target, an assemblage of charged particles, called a plasma, is formed. When the plasma is sufficiently heated ( $\sim 10^7$  K), it emits x rays. An imploding ICF target emits x rays during illumination by the laser beams and at stagnation when the kinetic energy of the plasma is transformed into thermal energy. The inner core of the fusion reaction gives off high-energy x rays, which are able to penetrate the plasma with their extremely

short wavelengths of 1 to 10 Å. The x rays emitted by the target are subsequently studied to obtain information about conditions in the target.

To study the fusion process, x-ray imaging is used to obtain critical information on the absorption of radiation, transfer of energy, and hydrodynamic behavior. In addition, with the ability to obtain the spectra of x rays emitted from the fusion plasma, x-ray imaging allows the approximation of core temperatures and the estimation of the size, symmetry, and density of both the fusion center and the surrounding imploding shell. These are all crucial diagnostics in assessing the performance of the target implosion and the process of laser fusion.

X-ray radiography uses an x-ray source and either photographic film or image plates to capture the penetrating radiation. To create images of inertial confinement fusion phenomena and study the conditions in the compressed cores, good spatial resolution and high energy sensitivity are needed. Instruments used for imaging nuclear fusion often include pinhole cameras and KB microscopes.<sup>5</sup>

A KB mirror pair and a pinhole camera assembly are shown in Fig. 1. The mirror pair is 17 mm long, 4.5 mm thick, and has a radius of curvature of approximately 26 m. The pinhole cameras used to image the OMEGA fusion target consist of a 10 μm hole. The delicate pinhole is placed on top of two collimators made of tungsten, an element noted for its high density. Then, the pinhole is covered with a beryllium shield that blocks unwanted soft x rays and only allows the desired x rays through. Finally, a third collimator is placed onto the beryllium shield. This collimator filters the x rays that go through to the pinhole and ensures that these rays are traveling parallel to the hole's entrance. A cover is then put onto the pinhole apparatus to protect the camera from any debris or damage from the laser plasma.

At LLE, in addition to the reliable and relatively inexpensive pinhole camera, the KB microscope often provides better resolution and better images of the ICF reaction. First developed in 1948, KB microscopes can image high-energy x-ray sources with the necessary resolution and sensitivity.<sup>6</sup> The KB microscope (Fig. 2) is a reflection system that makes two-dimensional images by using a pair of spherical, concave mirrors whose centers of curvatures are perpendicular to each other. Each mirror focuses in one plane, so two mirrors positioned perpendicularly will focus in two planes, thus forming a two-dimensional image.

As shown in Fig. 2, a baffle is often used in conjunction with a KB mirror pair to act as a field stop. Rays that reflect off both KB mirrors are the ones that form the desired two-dimensional image; those rays are the ones desired on the film. Rays that reflect off only one mirror will image in one dimension but are stopped by the baffle.

Each mirror has a high radius of curvature and follows the focus equation<sup>6</sup>

$$\frac{1}{p} + \frac{1}{q} = \frac{2}{R \sin i} \quad (1)$$

where  $p$  is the distance of the mirror to the object,  $q$  is the distance of the mirror to the image,  $R$  is the radius of curvature of the mirrors, and  $i$  is the grazing angle of the rays. Due to the high radius of curvature of the mirrors, the KB microscope reflects rays at small grazing angles. These small grazing angles are necessary for x-ray reflection, because the rays will only form images when the angle of incidence is less than one degree.

Rays reflected off the KB microscopes form images with high resolution, about 3  $\mu\text{m}$ , and high sensitivity, up to 9 keV. These properties, along with its small size and strong reflectivity, make the KB microscope suitable for inertial confinement fusion experiments. The



pinhole camera often has limited resolution due to the diffraction caused by the pinhole and is susceptible to damage because it must be in close proximity to the target.<sup>5</sup>

On the OMEGA laser, the KB microscopes have two perpendicular pairs that form four mirror pairs.<sup>7</sup> The compact microscope design allows the instruments to take four images of the target for each exposure. In addition, the KB microscopes can be modified to better accommodate the type of experiment being run. Often, multilayer coatings are used to increase reflectivity and increase the distance the microscope can be away from the object being imaged, meaning the microscope can be placed where it will not be damaged.<sup>8</sup> Another modification frequently used is the framing camera, which, when attached to the microscope, allows it to take multiple, time-gated images. The framing camera creates time resolution differences between the images, allowing images to be taken in time intervals of approximately 100 picoseconds.<sup>9</sup>

Currently, a 16-image KB microscope, shown in Fig. 3, is being developed at the University of Rochester's Laboratory for Laser Energetics.<sup>10</sup> The innovative design will allow 16 images to be taken during one exposure, as opposed to the traditional 4. For the continued development of this design, mirror pairs needed to be characterized and tested. To calibrate and test the KB microscopes to be used on OMEGA and OMEGA EP, the Laboratory for Laser Energetics has an x-ray diagnostics laboratory.

## **Experiments**

To take the x-ray exposures, the apparatus must be positioned with precision. To do so, a height gauge was used, as shown in Fig. 4. The KB optic must be the same distance from the mesh grid, positioned at the tip of the pointer, and the baffle. For this experiment, the distance from the grid to the optic and distance from the optic to the baffle were set to be 180.00 mm. To ensure this exact distance, a pointer was placed onto the optic that had a tip that was 180.00 mm

from the optic. Thus, when this pointer tip touched the mesh grid, this would indicate that the grid was 180.00 mm from the optic. For the optic to baffle distance, adjustable machine parts were used in combination with the height gauge to place the baffle onto the KB chassis 180.00 mm from the optic.

For test exposures in the diagnostics laboratory, a mesh grid made of copper is used, shown in Fig. 5. The grid consists of 25.4  $\mu\text{m}$  (0.001 in) diameter wires spaced 50.8  $\mu\text{m}$  (0.002 in) apart. The mesh also has a reference hole that allows the images taken to be aligned with each other. Consequently, the reference hole allows for the determination of the position in the image relative to the same point in space.

Images were obtained using an electron-beam generated x-ray source housed in a vacuum chamber (Fig. 6). An electron-beam current, generated using a high voltage supply, is directed onto a metal target with an adjustable magnetic field, causing x rays to be emitted. Soft x rays less than 3 keV cannot transmit through air, and so the chamber is sealed and pumped down to low pressure conditions ( $\sim 10^{-6}$  Torr), allowing x rays to travel through the apparatus unattenuated. After the x rays pass through the mesh grid and vacuum, the rays will travel through the KB microscope chassis. The chassis holds the KB optic and focuses the x rays formed by reflections off the KB mirror pairs onto Biomax-MS film, which records an image of the mesh grid. The film is exposed for a sufficient amount of time ( $\sim 30$  mins) to obtain an image upon development of the film. The film is subsequently digitized using a photomicrodensitometer, and the exposure allows for analysis of the optical characteristics of the KB mirror pair, including the best focus location, reflectivity, and resolution.

To generate the electron beam, current is passed through a thick tungsten filament, which, when heated, will subsequently go through thermionic emission and emit a stream of electrons.

The electrons are accelerated by a negative voltage (typically 10 to 20 keV) through the anode hole and directed by a pair of dipoles onto the desired metal target. A current through a coil at the magnets creates a magnetic field that focuses the beam. A target wheel on the x-ray generator apparatus rotates different metal targets into position, and each metal target results in different x-ray characteristics for the exposures because each metal has a unique x-ray emission.

The system parameters of the x-ray generator are variable and can be changed by a controller box with software controls. For this experiment, the bending current and the focus coil current of the magnets were 21 mA and 100 mA respectively. The electron beam current was set to 21 mA, while the filament current to create the beam was 19 A. The accelerating voltage was 14 kV. The pressure inside the target chamber was  $6 \times 10^{-7}$  Torr. The electron beam position was monitored with a digital camera.

For the experiment, a half-hour exposure was taken on Kodak Biomax-MS x-ray sensitive film with a 2 mm baffle behind the KB mirror pair. The film was developed with standard chemical processing, and the subsequent image was digitized with a Perkin-Elmer microdensitometer.<sup>11</sup>

A program, FWHMlineout (see Appendix), was written in PV-Wave<sup>12</sup> and used to analyze the image. In PV-Wave, a lineout of the image is taken that shows the film density of the image along a row or column of the mesh grid. This lineout is averaged over the space between the wires and median filtered to reduce noise. The resulting values are used to measure the width of the shadows of the wires. Measurements are taken across the lineout at each wire shadow. The resulting values are a measure of the KB-mirror-pair resolution as a function of position.

An exposure (Fig. 5) was taken using a single compact Kirkpatrick-Baez microscope. Both vertical and horizontal lineouts were taken from the image and used to find the best focus location and resolution of the image.

First, the image was rotated to follow the grid lines. This rotation was optimized by using perpendicular vertical lineouts along a horizontal line to ensure that the shadows lined up correctly, as depicted in Fig. 7. Since the shadows correctly line up with each other, this means that the vertical perpendicular lineouts match each other, meaning that the grid lines are straight and perpendicular. This graph is also used to set the lower and upper bounds of the following lineout, which is the number of pixels the lineout will be averaged over.

To perform additional calculations on the image, the magnification of the exposure must be determined. First, the known dimensions of the grid are used to find the actual length across 10 of the wires, which is 0.508 mm. Then, the length across 10 wires on the image is measured with PV-Wave, shown in Fig. 8, which is 6.62 mm. The magnification  $M$  is given by

$$M = \frac{q'}{p'} \quad (2)$$

where  $q'$  is the image size and  $p'$  is the object size. The magnification is calculated to be 13.03 horizontally. The same process is done in the  $y$ -direction. The vertical length across 10 wires of the image is measured to be 6.45 mm, meaning the magnification vertically is 12.70.

The shadows of the wires seen in Fig. 8 are also used to determine the resolution. The lineout's edges are measured as a function of position, and this edge response serves as a measure of resolution along the lineout. One edge response measurement is shown in Fig. 9. Narrower edges indicate better resolution, while wider edges indicate poorer resolution. The

graph of the edge width as a function of position is shown in Fig. 10, with edge width on the y-axis. The best focus position is where the width is smallest, shown in Fig. 10 to be approximately 8  $\mu\text{m}$ . Ideally, as shown by ray tracing, the edge width at best focus would be 0  $\mu\text{m}$ ; however, due to imperfections on the mirrors and diffraction, it cannot be achieved.

At the best focus position, the derivative of the edge response curve (an example is given in Fig. 9) is taken to determine the point spread function<sup>13</sup> (PSF), which serves as a measure of resolution. The better the resolution, the narrower the edge width will be at best focus, meaning the edge width will have a steeper slope. With such a steeper curve, the derivative will have a higher peak, in turn causing the PSF to be narrower and have a smaller full-width-at-half-maximum (FWHM). The PSF at best focus is shown in Fig. 11. This is seen to have a FWHM of  $\sim 6 \mu\text{m}$ . This is a measure of the best resolution of this compact KB mirror pair.

## Conclusions

Kirkpatrick-Baez (KB) mirror pairs are used at the University of Rochester's Laboratory for Laser Energetics to image x rays emitted by laser plasmas. To image the phenomena more efficiently, a 16-image KB optic is being developed. Mirrors must first be characterized and calibrated prior to constructing the 16-image optic. An electron-beam generated x-ray source was used to take exposures on Biomax MS film, and a digitizer was used to format the image for analysis in PV-Wave. The mirror pair apparatus was determined to have a magnification of approximately 13. In addition, the KB mirrors had their best focus position determined by measuring the edge widths of the image shadows, and the resolution at this best focus position was calculated to be  $\sim 6$  microns as the FWHM of its point-spread function.

**Acknowledgements**

I would like to thank Dr. Stephen Craxton for accepting me into the high school summer program and giving me a unique opportunity to research at the Laboratory for Laser Energetics. He always kept his door open for any questions that I may have had and made the facility a friendlier, more comfortable environment to work in. I would also like to express my gratitude for Dr. Frederic J. Marshall, my supervisor. Dr. Marshall's patience, understanding, and knowledge were critical in helping me complete this project. I would like to thank Brian Eichman and Dev Ashish Khaitan for helping me run the x-ray generator and program in PV-Wave. Furthermore, I would like to express my appreciation for the LLE film-developing and digitizing staff for their support.

## References

1. J.J. Duderstadt, G. A. Moses, *Inertial Confinement Fusion* (John Wiley & Sons, New York, 1982).
2. J. D. Lindl, *Inertial Confinement Fusion: The Quest for Ignition and Energy Gain Using Indirect Drive* (Springer-Verlag, New York, 1998).
3. T. R. Boehly *et al.*, Opt. Commun. **133**, 495 (1997).
4. L. J. Waxer, D. N. Maywar, J. H. Kelly, T. J. Kessler, B. E. Kruschwitz, S. J. Loucks, R. L. McCrory, D. D. Meyerhofer, S. F. B. Morse, C. Stoeckl, and J. D. Zuegel, Opt. Photonics News **16**, 30 (2005).
5. J. F. McGee and J. W. Burrows, *X-Ray Imaging* (SPIE, Bellingham, WA, 1977), Vol. 106, pp. 107-112.
6. P. Kirkpatrick and A. V. Baez, J. Opt. Soc. Am. **38**, 766 (1948).
7. F. J. Marshall, Q. Su, Rev. Sci. Instrum. **66**, 725-727 (1995).
8. F. J. Marshall, G. R. Bennett, Rev. Sci. Instrum. **70**, 617-619 (1999).
9. F. J. Marshall, J. A. Oertel, Rev. Sci. Instrum. **68**, 735-739 (1997).
10. F. J. Marshall, J. A. Oertel, and P. J. Walsh, Rev. Sci. Instrum. **75** (10), 4045-4047 (2004).
11. Perkin Elmer Microdensitometer (PDS), Perkin Elmer, Inc., (1998).
12. PV-Wave, Version 7.00, Visual Numerics, Inc., (1999).
13. F. J. Marshall, M. M. Allen, J. P. Knauer, J. A. Oertel, and T. Archuleta, Phys. Plasmas. **5** (4), 1118-1124 (1998).

## Appendix. FWHMlineout.

```

;Title: FWHMlineout.pro
;Author: Andrew Chun
;Date: 2010 August 6
;Description: FWHMlineout creates a plot of edge response as a function of position.
This data can subsequently be used to determine the resolution of a Kirkpatrick-Baez
mirror pair, in addition to finding where the mirror is in the best focus. The program
also creates a point spread function to determine the full-width at half-maximum and
resolution at best focus.
;Usage:
;   FWHMlineout, img, rimg, rdeg, pixsize, mag, width, splorange, fxvals, fwhm,
ofile
;
;       where
;
;           img           =   input array
;           rimg          =   rotated array
;           rdeg          =   returned rotation angle
;           pixsize       =   size of pixels in microns
;           mag           =   magnification of mirrors
;           width        =   width of mesh grid wires in microns
;           splorange     =   number of pixels subplot of absolute value of
derivative graph will show (recommend 60 for 20 micron pixels, 120 for 10 micron
pixels)
;           fxvals       =   position of middle of edge shadows
;           fwhm         =   value of edge shadow widths
;           ofile        =   path to desired output file for results
PRO FWHMlineout, img, rimg, rdeg, pixsize, mag, width, splorange, fxvals, fwhm, ofile

;Adjusting for different pixel sizes
adj= 20/pixsize

;Rotating image
s= size(img)
window, 0, xsize= s(1)/2, ysize= s(2)/2
loadct, 16
tvsc1, congrid(img, s(1)/2, s(2)/2, /interp)
print, "click mouse on left and right portion of a line"
cursor, ax1, ay1, /device, /up
cursor, ax2, ay2, /device, /up
rdeg= atan(ay2-ay1, ax2-ax1)*!rdeg
print, "rdeg", rdeg
rimg= rot_int(img, rdeg)
tvsc1, congrid(rimg, s(1)/2, s(2)/2, /interp)

;Establishing subimage to work with
print, "click mouse on bottom left and upper right corner of desired subimage"
cursor, sx1, sy1, /device, /up
cursor, sx2, sy2, /device, /up
simg= rimg(sx1*2:sx2*2, sy1*2:sy2*2)
window, 0, xsize= (sx2-sx1), ysize= (sy2-sy1)
tvsc1, congrid(simg, sx2-sx1, sy2-sy1, /interp)

;Plotting horizontal lineout
print, "click mouse on center of left box, best focus box, and right box"
cursor, bx1, by1, /device, /up
cursor, bx2, by2, /device, /up
cursor, bx3, by3, /device, /up
window, 1
plot, findgen(61*adj)+(by2*2-(30*adj)), avg(simg(bx2*2-(5*adj):bx2*2+(5*adj)),
by2*2-(30*adj):by2*2+(30*adj)), 0, xstyle= 1, xrange= [by2*2-(30*adj),
by2*2+(30*adj)], linestyle= 0, title= "Lineout", xtitle= "Pixel Number", ytitle= "Film
Density * 800"
oplot, findgen(61*adj)+(by2*2-(30*adj)), avg(simg(bx1*2-(5*adj):bx1*2+(5*adj)),
by1*2-(30*adj):by1*2+(30*adj)), 0, xstyle= 1, xrange= [by2*2-(30*adj),
by2*2+(30*adj)], linestyle= 1
oplot, findgen(61*adj)+(by2*2-(30*adj)), avg(simg(bx3*2-(5*adj):bx3*2+(5*adj)),
by3*2-(30*adj):by3*2+(30*adj)), 0, xstyle= 1, xrange= [by2*2-(30*adj),
by2*2+(30*adj)], linestyle= 3

```



```

;Rotation checking loop
ans= "string"
WHILE ans NE 'y' DO BEGIN
    print, "is this rotation angle satisfactory? (y/n)"
    read, 'answer = ', ans
    IF ans EQ 'n' THEN BEGIN
adjusted?"
        read, 'answer = ', r
        rdeg= rdeg + r
        print, rdeg
        ring= rot_int(img, rdeg)
        simg= ring(sx1*2:sx2*2, sy1*2:sy2*2)
        wset, 0
        tvscl, congrid(simg, sx2-sx1, sy2-sy1, /interp)
        print, "click mouse on center of left box, best focus box,
and right box"
        cursor, bx1, by1, /device, /up
        cursor, bx2, by2, /device, /up
        cursor, bx3, by3, /device, /up
        window, 1
        plot, findgen(61*adj)+(by2*2-(30*adj)), avg(simg(bx2*2-
(5*adj):bx2*2+(5*adj), by2*2-(30*adj):by2*2+(30*adj)), 0), xstyle= 1, xrange= [by2*2-
(30*adj), by2*2+(30*adj)], linestyle= 0, title= "Lineout", xtitle= "Pixel Number",
ytitle= "Film Density * 800"
        oplot, findgen(61*adj)+(by2*2-(30*adj)), avg(simg(bx1*2-
(5*adj):bx1*2+(5*adj), by1*2-(30*adj):by1*2+(30*adj)), 0), xstyle= 1, xrange= [by2*2-
(30*adj), by2*2+(30*adj)], linestyle= 1
        oplot, findgen(61*adj)+(by2*2-(30*adj)), avg(simg(bx3*2-
(5*adj):bx3*2+(5*adj), by3*2-(30*adj):by3*2+(30*adj)), 0), xstyle= 1, xrange= [by2*2-
(30*adj), by2*2+(30*adj)], linestyle= 3
        ENDIF
    ENDWHILE

;Setting upper and lower bounds to average over
print, "click mouse on lower and upper bounds in that order"
cursor, cx1, cy1, /data, /up
cursor, cx2, cy2, /data, /up

;Plotting lineout
xvals= (bx3*2)-(bx1*2)
yvals= median(avg(simg((bx1*2):(bx3*2), (cx1):(cx2)), 1), 3)
window, 2
plot, findgen(xvals)+(bx1*2), yvals, xstyle= 1, xrange= [bx1*2, bx3*2], title=
"Lineout", xtitle= "Pixel Number", ytitle= "Film Density * 800"

;Adjusting plot with energy cutoff
print, "what is the desired energy cutoff for this lineout?"
read, "answer = ", ecut
eyvals= yvals-ecut
plot, findgen(xvals)+(bx1*2), eyvals, xstyle= 1, xrange= [bx1*2, bx3*2],
ytitle= "Film Density * 800"

;Energy cutoff checking loop
ans= "string"
WHILE ans NE 'y' DO BEGIN
    print, "is this energy cutoff satisfactory? (y/n)"
    read, 'answer = ', ans
    IF ans EQ 'n' THEN BEGIN
        print, "by how much should the energy cutoff be adjusted?"
        read, 'answer = ', e
        ecut= ecut + e
        print, ecut
        eyvals= yvals-ecut
        wset, 2
        plot, findgen(xvals)+(bx1*2), eyvals, xstyle= 1, xrange=
[bx1*2, bx3*2], ytitle= "Film Density * 800"
        ENDIF
    ENDWHILE

```

```

;Initializing and using loop to find full-width at half-maximum points with respective
to position
  i= 0
  fxvals= fltarr(1000)
  fwhm= fltarr(1000)
  ix= 0
  s2= size(eyvals)
  index= findgen(2000)
  x= fix(width*mag/pixsize)
  WHILE ((ix+splotrange) lt s2(1)) DO BEGIN
    window, 3
    plot, index(ix:ix+splotrange), eyvals(ix:ix+splotrange), xstyle= 1,
xrange= [ix, ix+splotrange], ystyle= 1, yrange= [0,1500], title= "Lineout", xtitle=
"Pixel Number", ytitle= "Film Density * 800"
    print, "click mouse on top of the edge of the lineout peak. Use left
click to record data. Use right click to skip data"
    cursor, ex1, ymax, /data, /down
    print, "click mouse on bottom of the edge of the lineout peak. Use left
click to record data. Use right click to skip data"
    cursor, ex2, ymin, /data, /down
    IF (!mouse.button EQ 1) THEN BEGIN
      fxvals(i)= (((ex1+ex2)/2)*pixsize)/mag)/1000
      fwhm(i)= (ex2-ex1)*pixsize/mag
      i= i+1
    ENDIF
    ix= ex1+x-(10*adj)
  ENDWHILE
  fxvals= fxvals(0:(i-1))
  fwhm= fwhm(0:(i-1))

;Plotting full-width at half-maximum as a function of position
  window, 4
  plot, fxvals, fwhm, psym= 4, title= "Resolution", xtitle= "Position (mm)",
ytitle= "Edge Response (Microns)", xstyle= 1, xrange= [0, 1.5], ystyle= 1, yrange= [0,
20]

;Plotting error bars with averaged x values and fwhm values
  n= i/2
  n= fix(n)
  n= n*2
  i= 0
  xavg= fltarr(1000)
  yavg= fltarr(1000)
  err= fltarr(1000)
  REPEAT BEGIN
    xavg(i)= (fxvals(i)+fxvals(i+1))/2
    yavg(i)= (fwhm(i)+fwhm(i+1))/2
    err(i)= yavg(i)-fwhm(i)
    i= i+1
  ENDREP UNTIL i EQ (n-1)
  xavg= xavg(0:i)
  yavg= yavg(0:i)
  err= err(0:i)
  window, 5
  plot, xavg, yavg, psym= 4, title= "Resolution", xtitle= "Position (mm)",
ytitle= "Edge Response(Microns)", xstyle= 1, xrange= [0, 1.5], ystyle= 1, yrange= [0,
20]
  oploterr, xavg, yavg, err, 4

;Saving results to an output file
  openw, 1, ofile
  FOR j= 0, i DO BEGIN
    printf, 1, xavg(j), yavg(j), format= "(F8.2, F8.2)"
  ENDFOR
  close,1

```

```

;Plotting the point spread function
print, "where is the best focus location? (mm)"
read, 'answer = ', bf
bf= bx1*2+((bf*1000)*mag)/pixsize
window, 6
plot, median(avg(simg(bf-(30*adj):bf+(30*adj), cx1:cx2), 1), 3), title=
"Lineout", xtitle= "Pixel Number", ytitle= "Film Density * 800"
print, "click mouse on one edge of the lineout peak"
cursor, fx1, fy1, /data, /up
print, "click mouse on other edge of the lineout peak"
cursor, fx2, fy2, /data, /up
a= median(avg(simg(fx1-(30*adj):fx2+(30*adj), cx1:cx2), 1), 15)
b= median(avg(simg(fx1-(30*adj)+1:fx2+(30*adj)+1, cx1:cx2), 1), 15)
window, 7
plot, findgen((fx2+(30*adj))-(fx1-(30*adj))*pixsize/mag), smooth(abs(a(fx1-
(30*adj):fx2+(30*adj))-b(fx1-(30*adj):fx2+(30*adj))), 5), title= "Point Spread
Function", xtitle= "Pixel Number", ytitle= "Film Density * 800 / Pixel Number"
print, "click mouse on desired peak"
cursor, hx, hy, /data, /up
plot, findgen((hx+20)-(hx-20)*pixsize/mag), smooth(abs(a(hx-20:hx+20)-b(hx-
20:hx+20)), 5), title= "Point Spread Function", xtitle= "Position (microns)", ytitle=
"Film Density * 800 / Pixel Number", xrange= [(hx-20)*pixsize/mag,
(hx+20)*pixsize/mag], xstyle= 1

;Calculating the full-width at half-maximum
print, "click mouse on peak of subimage"
cursor, xmid, ymax, / data, /up
plots, [hx-20, hx+20], [ymax*0.5, ymax*0.5]
print, "click mouse on full-width at half-maximum points"
cursor, gx1, gy1, /data, /up
cursor, gx2, gy2, /data, /up
fwhm= (gx2-gx1)*pixsize/mag
print, "fwhm (microns)", fwhm

```

END

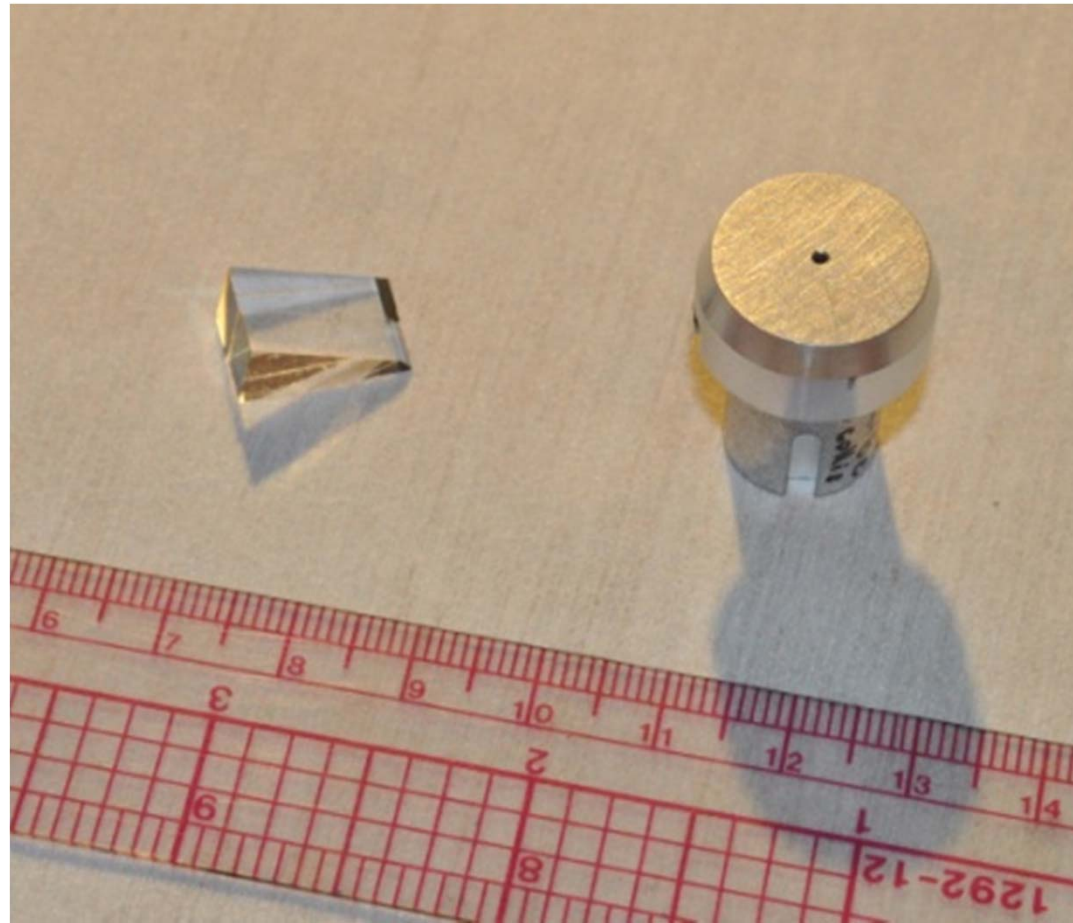


**Figure 1.** Kirkpatrick-Baez mirror pair (left) and pinhole camera (right).

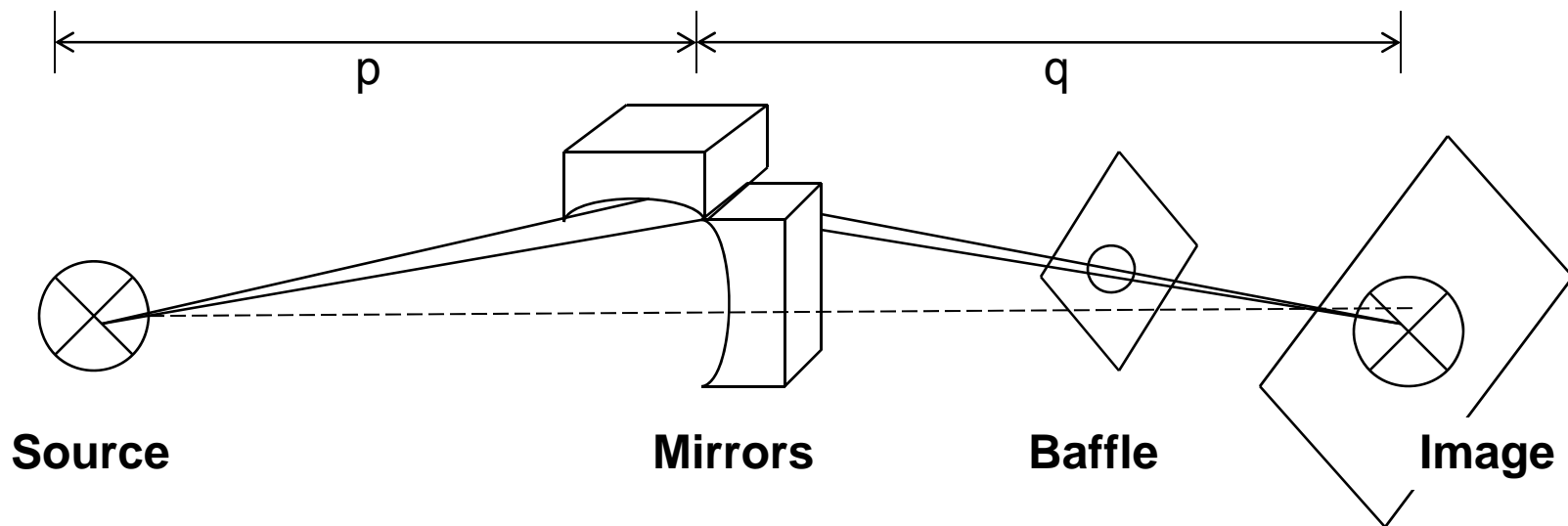


**Figure 2.** Kirkpatrick-Baez mirror pair perpendicularly crossed. Each mirror will focus in a different dimension, so rays that reflect off both mirrors will form two-dimensional images. A baffle is also used to filter out the 1-dimensional images and straight-through x rays.

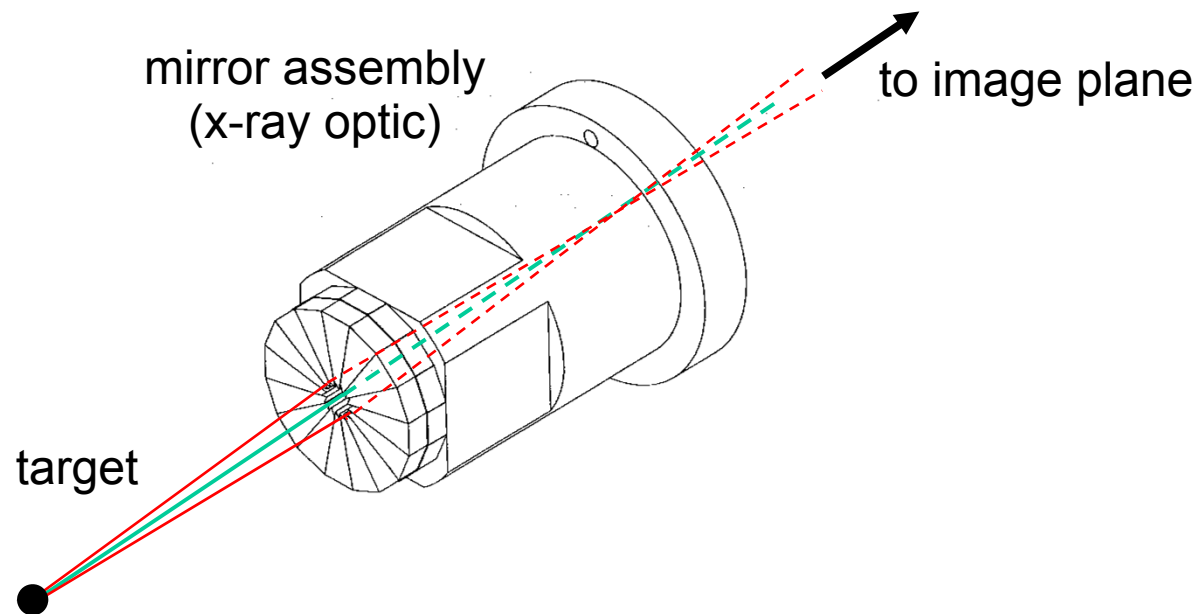


**Figure 3.** Design of the 16-image Kirkpatrick-Baez microscope. The microscope uses 16 mirror pairs to take 16 images for each exposure.

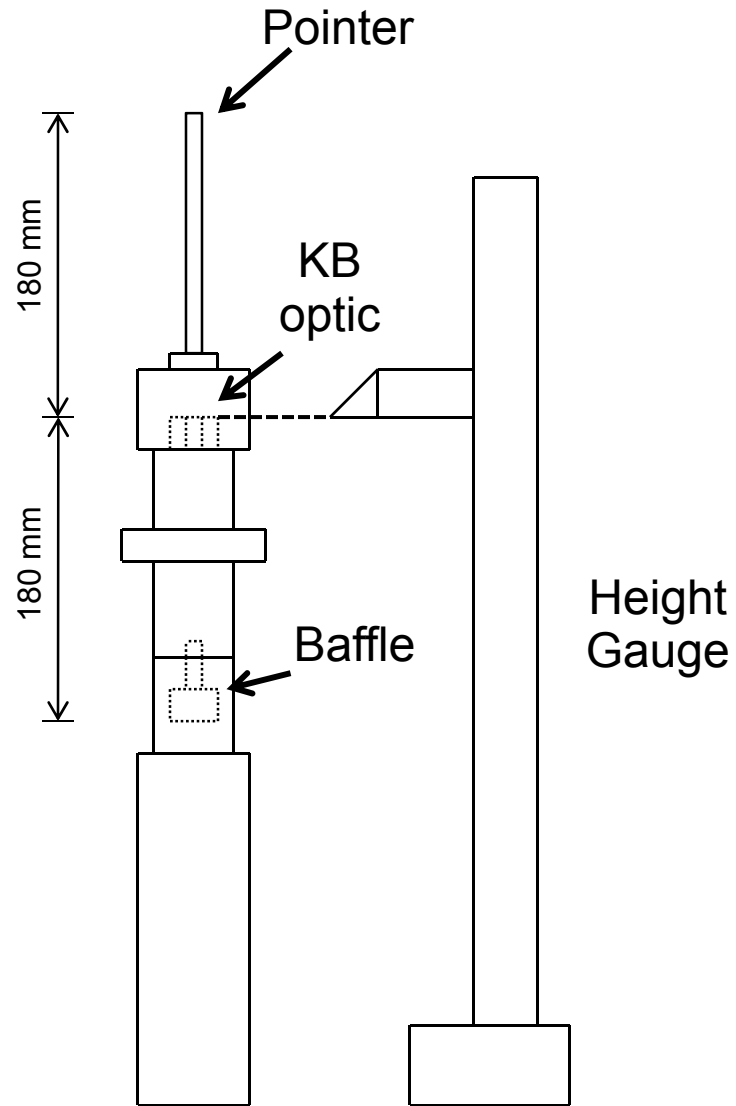


**Figure 4.** Kirkpatrick-Baez microscope precisely positioned with a height gauge. The pointer and the baffle are set 180 mm away from the Kirkpatrick-Baez optic.

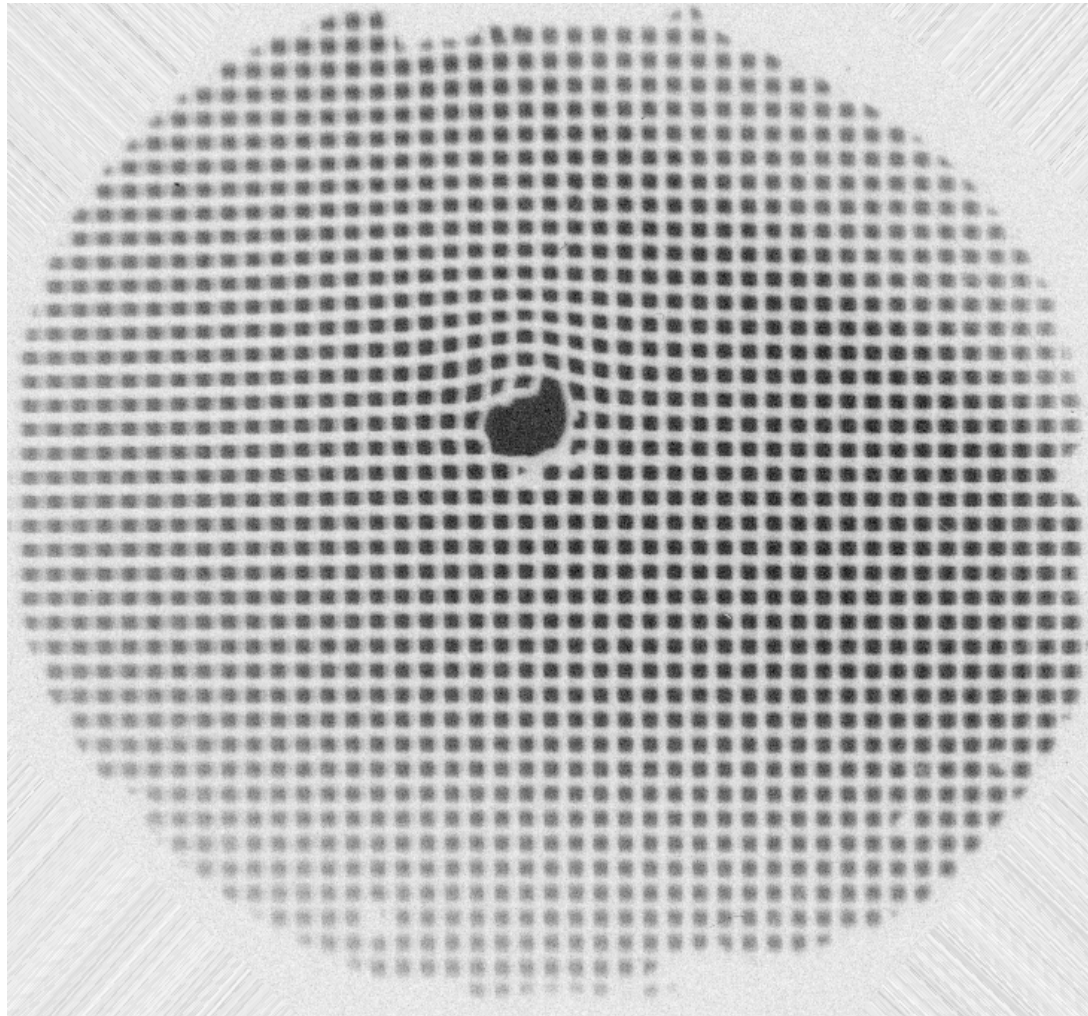


**Figure 5.** KB microscope image of a copper mesh grid target. The target has  $25.4\ \mu\text{m}$  diameter wires spaced  $50.8\ \mu\text{m}$  apart. A reference hole is made for alignment purposes.



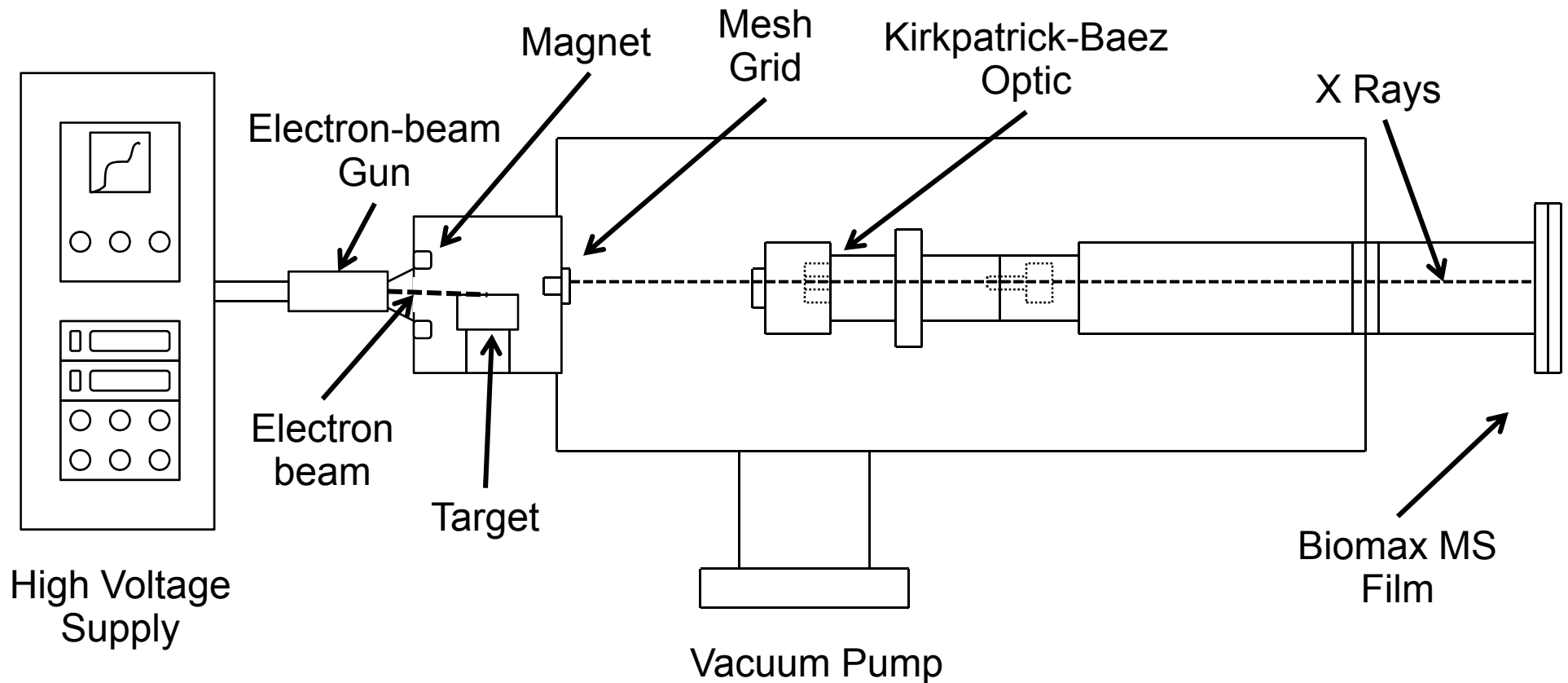


**Figure 6.** Apparatus for testing the KB microscope. An electron beam is deflected onto a metal target, which when heated emits x rays. The x rays go through the Kirkpatrick-Baez microscope chassis to expose film at the end of the apparatus.

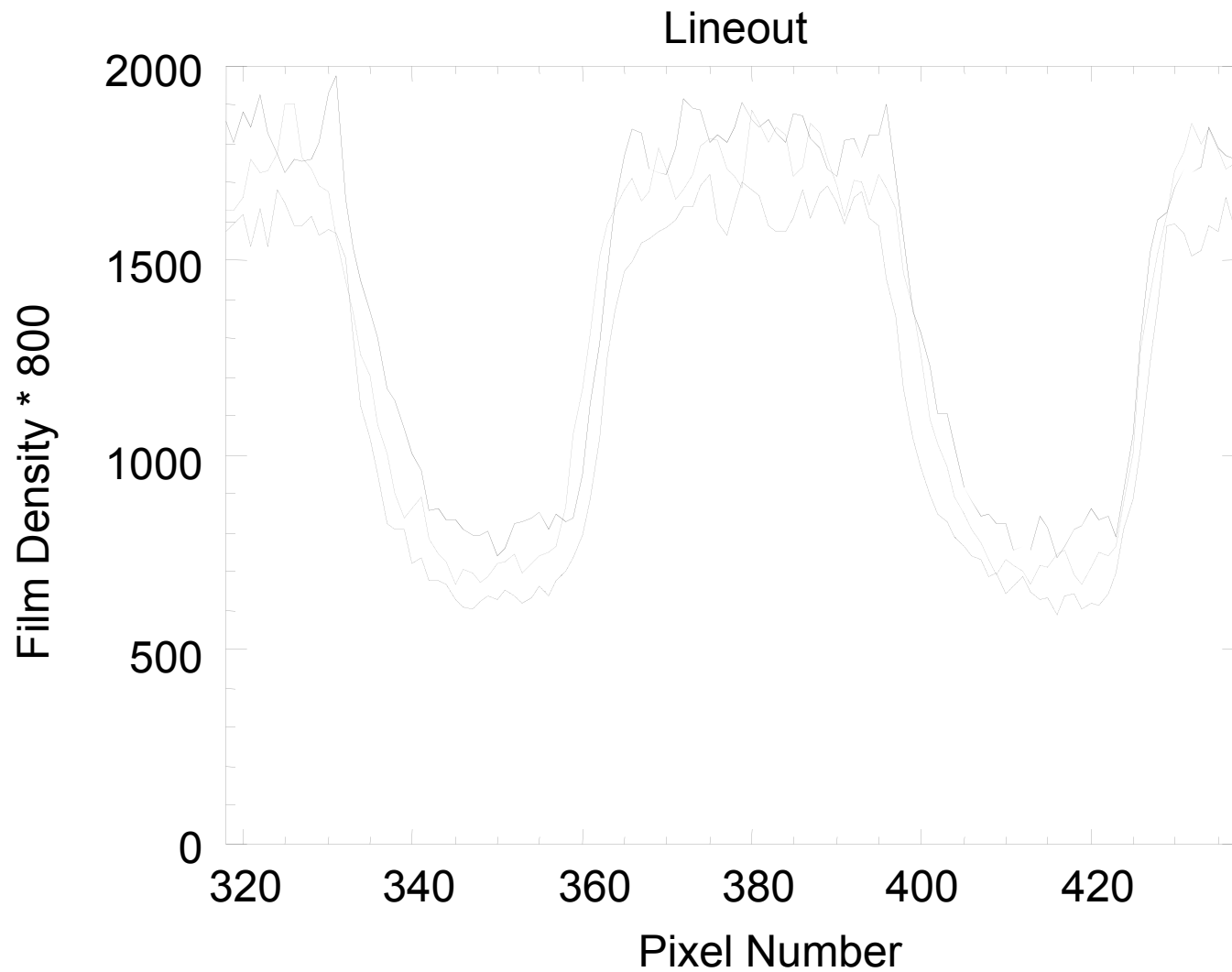


**Figure 7.** *Optimized rotated image is achieved by comparing vertical lineouts at different horizontal positions. The best rotation angle occurs when the shadows of the wires are aligned.*

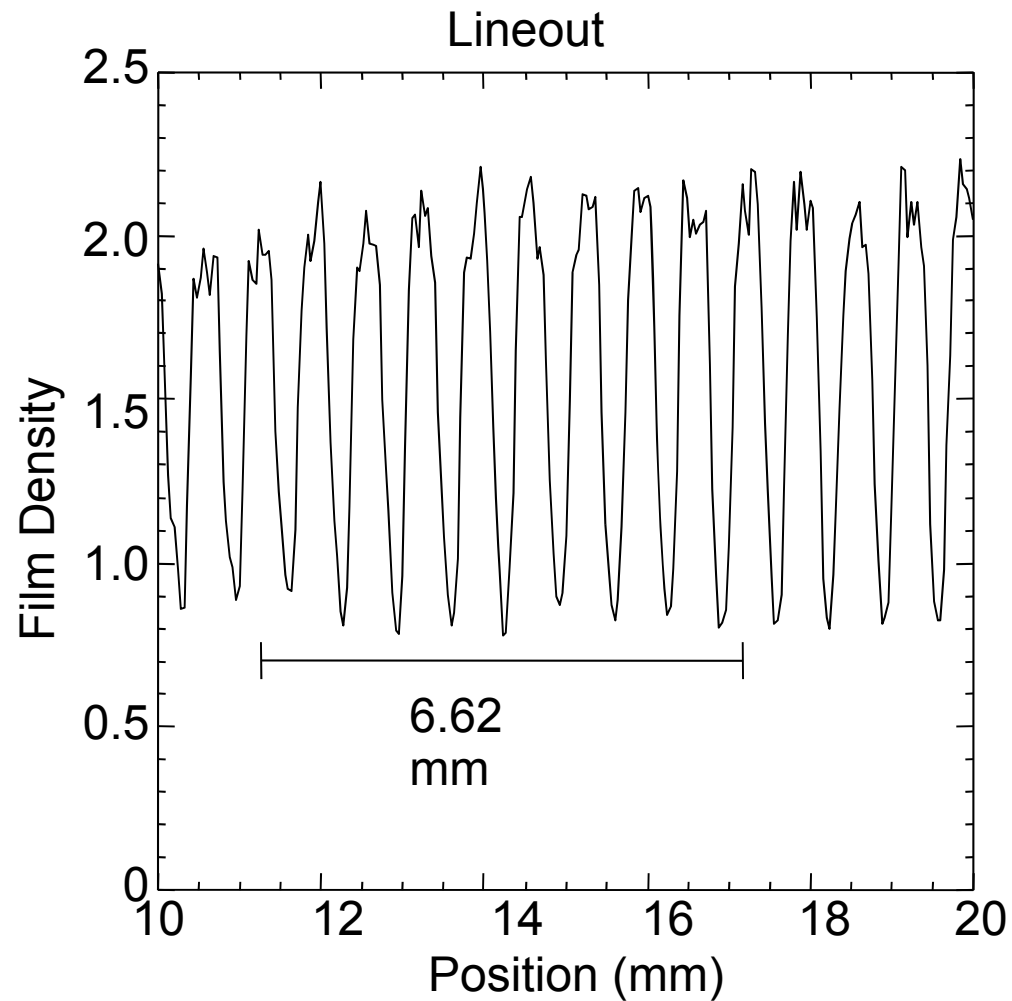


**Figure 8.** Measurement of 10 shadows of horizontal lineout. The image length of 10 wires is compared to the actual length to determine the magnification.

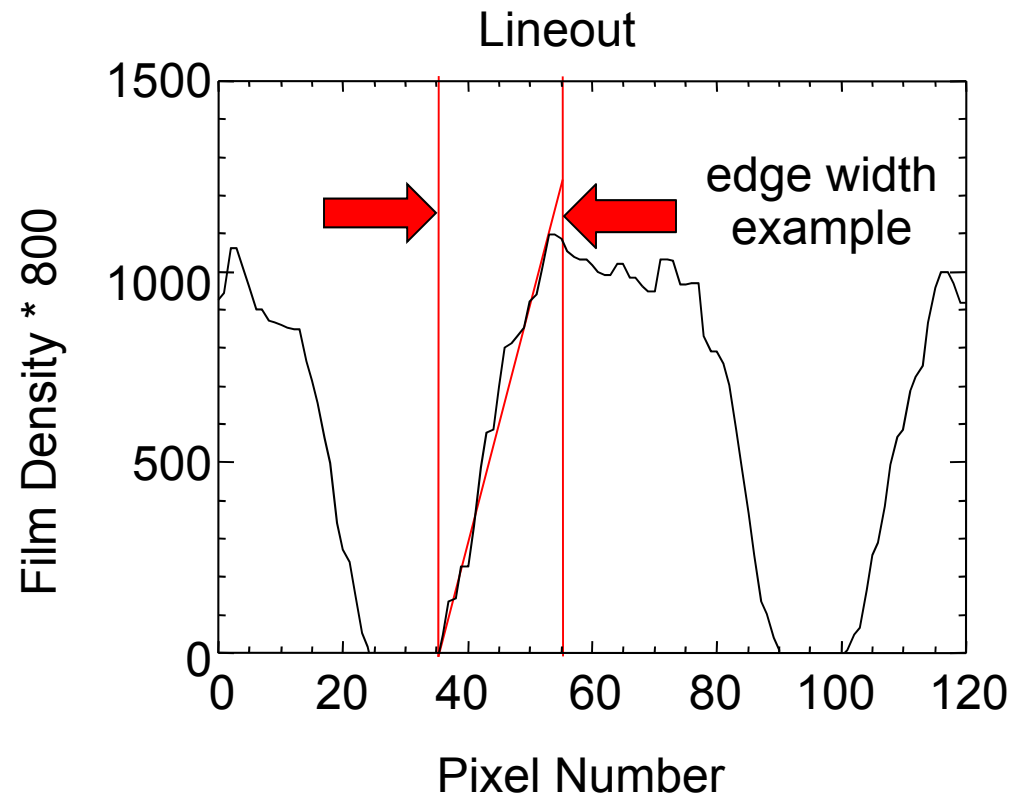


**Figure 9.** Example of edge width response. The edge widths are measured across the lineout to determine the best focus position and resolution.

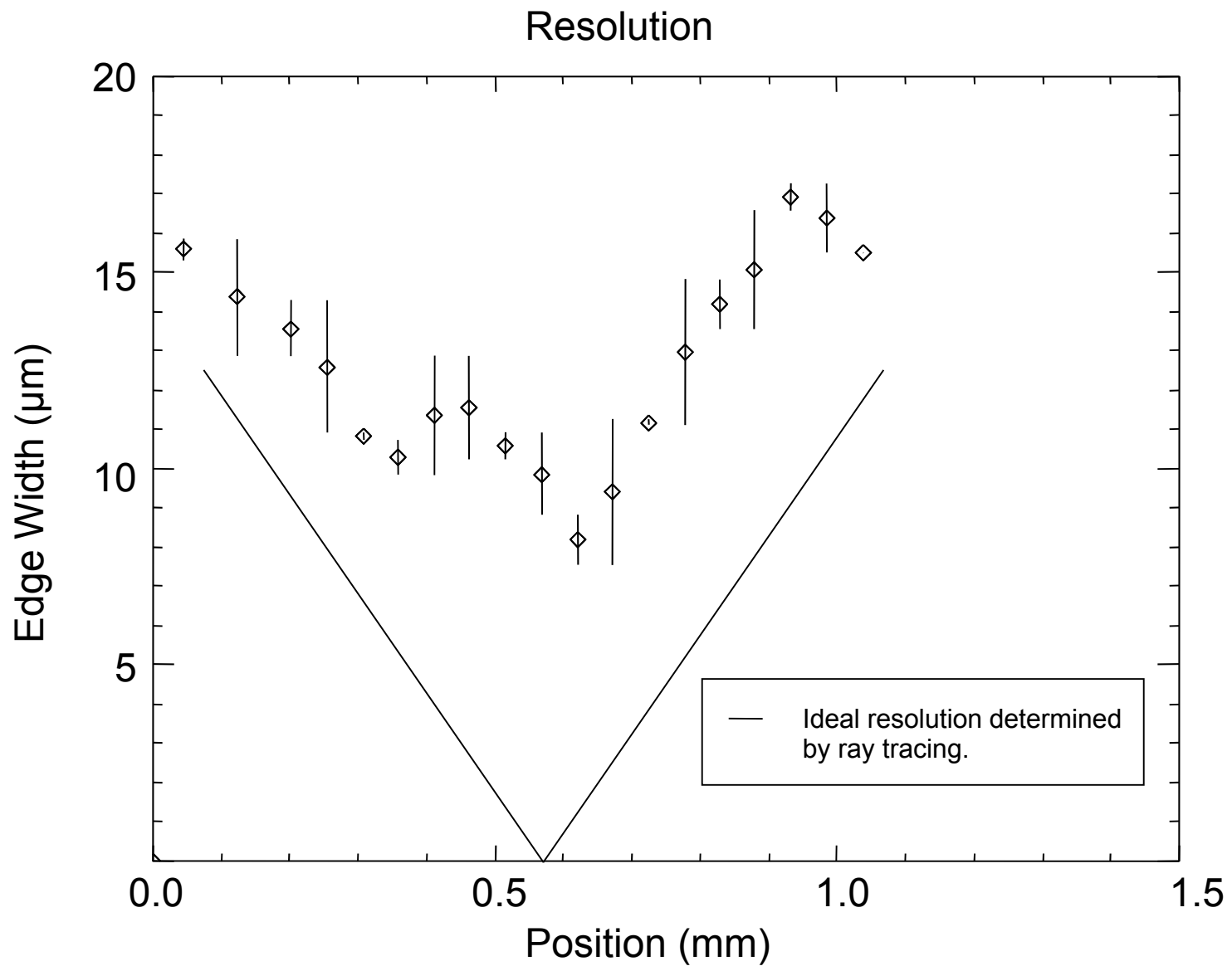


**Figure 10.** Measurements of the edge response across a lineout. Diffraction and imperfections of the mirrors prevent the ideal resolution from being obtained.

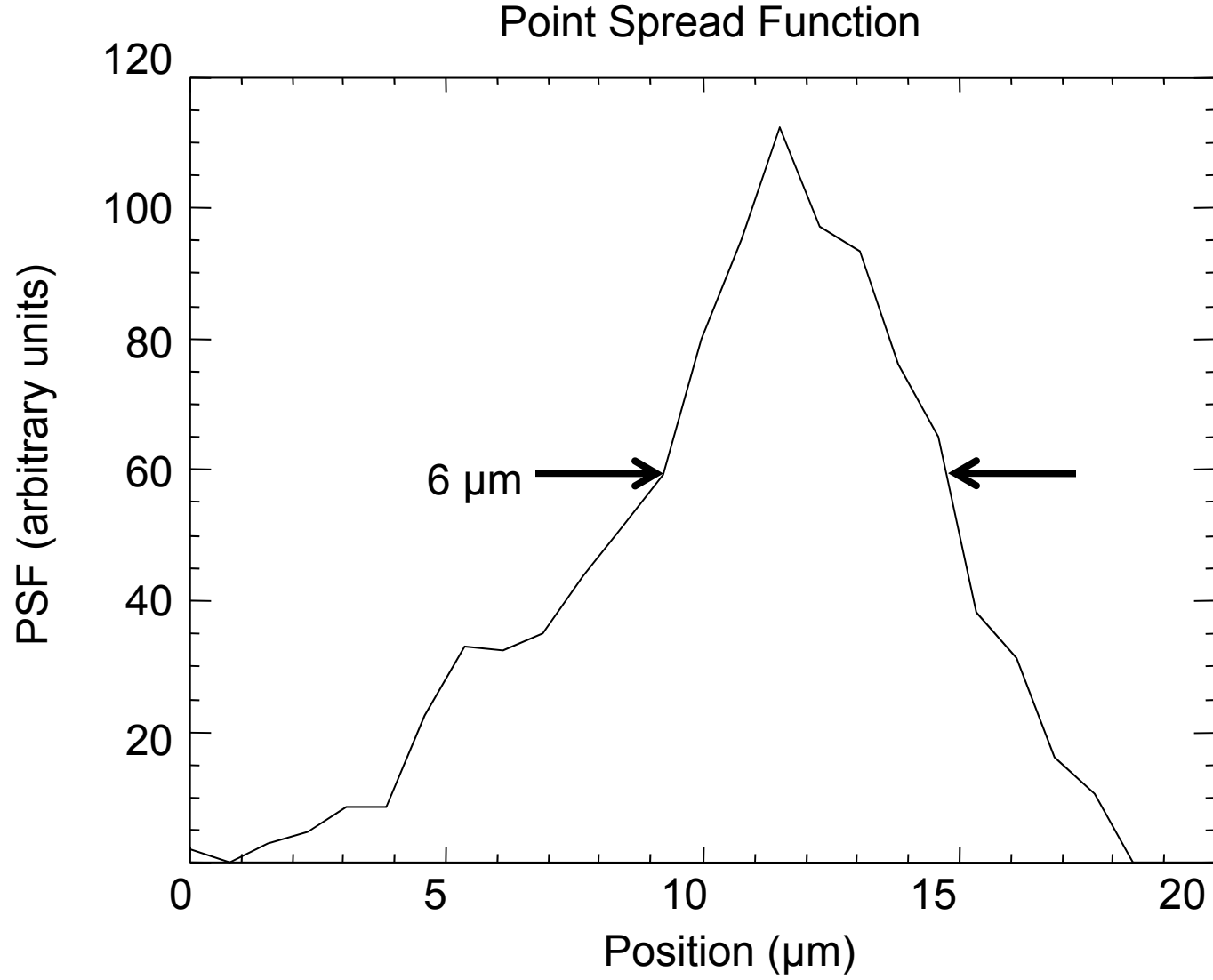


**Figure 11.** Point spread function determined from the best focus edge response.

# *Designing and Implementing an Ontology for LLE Experimental Diagnostics*

Robert W. Cooper, III  
Allendale Columbia School  
Advisor: Rick Kidder  
Summer 2010

## **Abstract:**

The OMEGA Laser experimental diagnostics operations were researched to discover how knowledge of the operation and set up of these systems is managed. The goal of the project was to see if a technology existed that provided mechanisms to capture this knowledge into an artificial intelligence environment, making it more accessible to the many users of the experimental lab. Semantic web technologies were investigated for this purpose and to determine what platform was best for designing an ontology (a computerized representation of knowledge based on relationships between data) for LLE experimental diagnostics. The research determined that open source editors like ProtégéOWL were available that simplified designing the ontology, and Web Ontology Language Descriptive Language (OWL DL), a semantic web standard, was the most useful syntax for the project. Once the basic design was complete, the ontology was developed into a prototype application using Java NetBeans Integrated Development Environment (IDE). The combination of this work provided a centralized repository for the extraction of useful information about the modeled diagnostics. The wide range of complex relationships were mapped out in the ontology allowing users to search for extremely specific result sets, eliminating the need to manually parse documents. The application also provided results windows, which were programmed to provide the user with links to other, potentially useful information. The application has also been equipped with data entry windows to allow users to increase the ontology's scope. The simplicity of the NetBeans interface was

demonstrated and makes enhancements of the code relatively easy. As a result, the ontology can be further developed to capture virtually every aspect of LLE's laser systems.

## **Introduction:**

### The current systems

LLE has accumulated an enormous amount of useful knowledge about its laser controls, imaging and diagnostic systems over the course of its existence. Unfortunately, LLE's knowledge repositories are dispersed over several disjointed systems with no common thread in between. This type of structure requires a variety of inefficient methods to access the wealth of information, which wastes users' time and often prevents the most useful information from being discovered and utilized. LLE has several repositories of information: the Product Data Management (PDM) system, the Oracle database, operation documents called Volumes and individuals who work at LLE. Individuals maintain knowledge on various networked and non-networked hard drives, notebooks and in their heads. Data retrieval is dependent on the source. Accessing data in the PDM system consists of a keyword search, in which any documents containing words or phrases that match the query are returned. The user is then required to manually parse the documents for the piece of desired information. The Oracle database contains all shot-related data from the OMEGA and OMEGA EP laser systems and must similarly be queried by keyword and parsed manually. Finally, the human-based resources are even more difficult to query, with data filed on personal computers, hidden among stacks of paperwork, and simply present in the minds of individual researchers. Accessing this information is difficult, as general users may not know the data even exist, may not understand methods to retrieve the data, and may not even know the many locations or types of data.



## An overview of the Semantic Web

A semantic web is a basic form of artificial intelligence in which a machine is able to interpret data as knowledge. This process is made possible by using machine-readable data called metadata (data about data) as tags. These metadata tags describe relationships between other data, and contain important information about the tagged data. As the computer interprets these

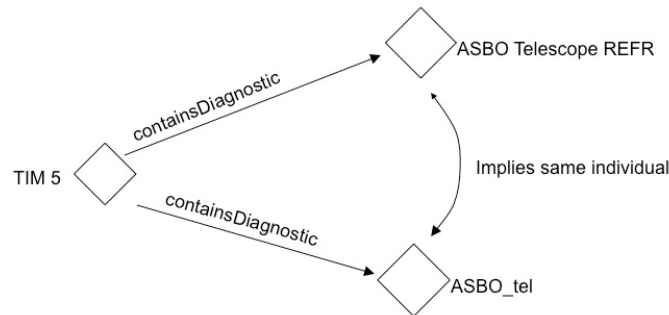


*Figure 1: Graphical representation of a functional property. Also known as a “single valued property,” a functional property for a given individual stipulates that only one other individual can be related via this property. In the above case, ASBO Telescope REFR and ASBO\_tel must be the same individual because containsDiagnostic is functional.*

relationships, it is able to make inferences on the actual information represented by the data. The three main types of relationships, or “properties,” found in ontologies can be seen in Figures 1, 2, and 3. Functional properties, illustrated in Figure 1, require that an individual can be related to only one other individual. Therefore, functional properties enable machines to determine whether two or more entities with different identifiers are, in fact, the same individual. This ability would

greatly enhance the organization of a knowledge database, as confusion resulting from an individual with more than one name would be avoided.

Transitive properties (Figure 2) help to illustrate pathways. By linking a linear progression of individuals, these properties

enable machines to navigate through linear hierarchical relationships using “shortcuts,” as transitive properties allow reasoners to jump straight to the final point instead of parsing each

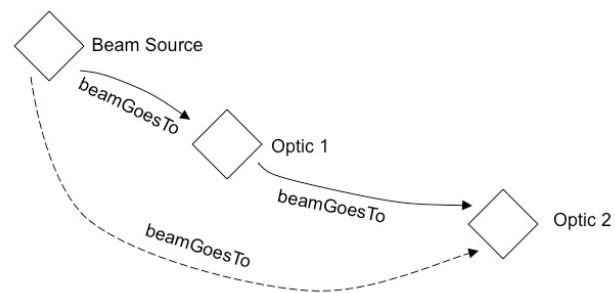


*Figure 2: A graphical representation of a transitive property. If a transitive property relates individual 1 to 2 and 2 to 3, then individual 1 is also related to individual 3 by the same property.*

intermediate step individually. Finally, symmetric properties (Figure 3) will make data entry a

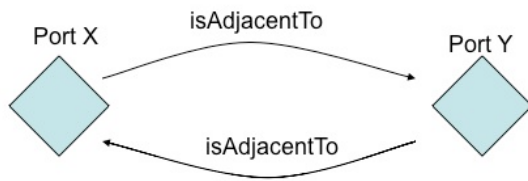


Figure 3: A graphical representation of a symmetric property. A symmetric property implies that if individual 1 is related to 2, then 2 is related to 1 by the same property.

much more efficient process. These properties will enable machines to automatically fill in information on one individual when a user makes changes to its symmetrically related partner.

A functioning, trusted semantic web is made up of several parts, illustrated in the “Semantic Web Stack” in Figure 4. The bottom, red layer makes up the semantic web’s basic essentials – a character set and identifier. Moving up

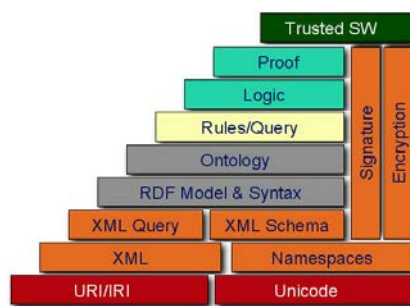


Figure 4: The “Semantic Stack.”

into the horizontal orange blocks are the machine-readable parts of the semantic web. These enable documents to be interpreted and interacted with by computers. The grey section, where this project was focused, is the framework of the ontology and the language and syntax used to create it. To the right and upwards of this grey area are more “optional” features of a semantic web, including the level of interaction by users, security measures, and logic reasoners.

### Ontologies at LLE

Implementing a semantic web at LLE would greatly increase the efficiency of the process of searching for information in the current database in several ways. First, the data would be concentrated in one location. Second, instead of performing a generic keyword search and parsing documents, specific information would be returned along with links to other, potentially useful items. This specificity would most likely be the greatest benefit of an ontology, as poring through hundreds of documents for a particular line or figure would no longer occur.

Consequently, over the past few years developing semantic web technologies have been researched at LLE [1-3]. As these technologies are still relatively new, much of the preliminary research revolved around exploring how a semantic web works and is constructed. An ontology editor, Protégé, was discovered [2], and a prototype model of a basic semantic web was constructed [3]. Although these projects were based more on researching a developing technology than creating and implementing an ontology itself, they made for a very solid foundation for this project.

### **Research and Development:**

#### Understand the Diagnostics

In order to virtually model an experimental diagnostic, one must fully understand the physical object first. As LLE possesses a wide range of complex systems, finding a method to categorize them is similarly complex. Due to the enormous quantity of diagnostics systems at LLE, fixed diagnostics for the OMEGA laser system were focused on. Nine characterizations were created to describe a sampling of 33 of the fixed OMEGA diagnostics. Each of these diagnostics could fall into any three of the nine characterizations. These categories were titled "optical," "x-rays," "neutrons," "charged particles," "electromagnetic radiation," "time integrated," "time resolved," "spectrally resolved," and "spatially resolved." Each of these characterizations describes an aspect of each diagnostic, and is intended to direct the user's attention to possible uses for the diagnostic. As such, each of these categories can be used to model metadata tags in an ontology. Further down the application's lifecycle, they will be refined into quicksearch categories and utilized to make the relationships between virtual models of diagnostics far more detailed.

### Pick a technology

Returning to Figure 4, this project resided mostly in the grey section of the chart: the Resource Description Framework (RDF) data model and the ontology itself. Protégé, the editor chosen to construct LLE's experimental diagnostics ontology, is compatible with a variety of syntaxes, schema, and metadata sets. Protégé allows the user to construct an ontology in "straight RDF," RDF Schema (RDFS), and the Web Ontology Language (OWL). Both RDFS and OWL use RDF as a base standard, and elements of RDFS are used in OWL. As a result, OWL has a less limited vocabulary than RDFS, which in turn is less limited than straight RDF. OWL was therefore determined to be the ideal language with which to construct the ontology.

OWL has three distinct sublanguages: OWL Lite, OWL DL (named after its correspondence with descriptive logic), and OWL Full. The main difference between these three sublanguages is the level of expressiveness available to the user. OWL Lite is the least expressive of the three, and only supports primitive constraints. OWL DL supports reasoning software, and is as expressive as possible while still allowing the software to properly function. OWL Full is the most expressive of the three, but it is based on a slightly different framework from the other two and is too expressive to support complete reasoning. OWL DL was consequently determined to be the most useful sublanguage to design the ontology, as its logic reasoner would enable quick and efficient sorting and searching and its expressiveness would support the relatively complex classes required for the experimental diagnostic database.

Finally, a metadata set was needed to tag the ontology's data. ProtégéOWL provided a relatively basic RDFS metadata vocabulary, but its scope was rather limited. Consequently, a variety of other metadata sets were explored, including Dublin Core, Friend of a Friend (FOAF), Semantically-Interlinked Online Communities (SIOC), and Simple Knowledge Organization

System (SKOS). After researching the structures of each vocabulary, it was determined that Dublin Core would be the most suitable metadata set. FOAF and SIOC are designed to describe relationships between people and social networking, respectively, and SKOS is generally used for dictionary or thesaurus-type structures. Dublin Core, on the other hand, is perfect for describing and annotating objects, which would enable the experimental diagnostic ontology to have an increased degree of specificity.

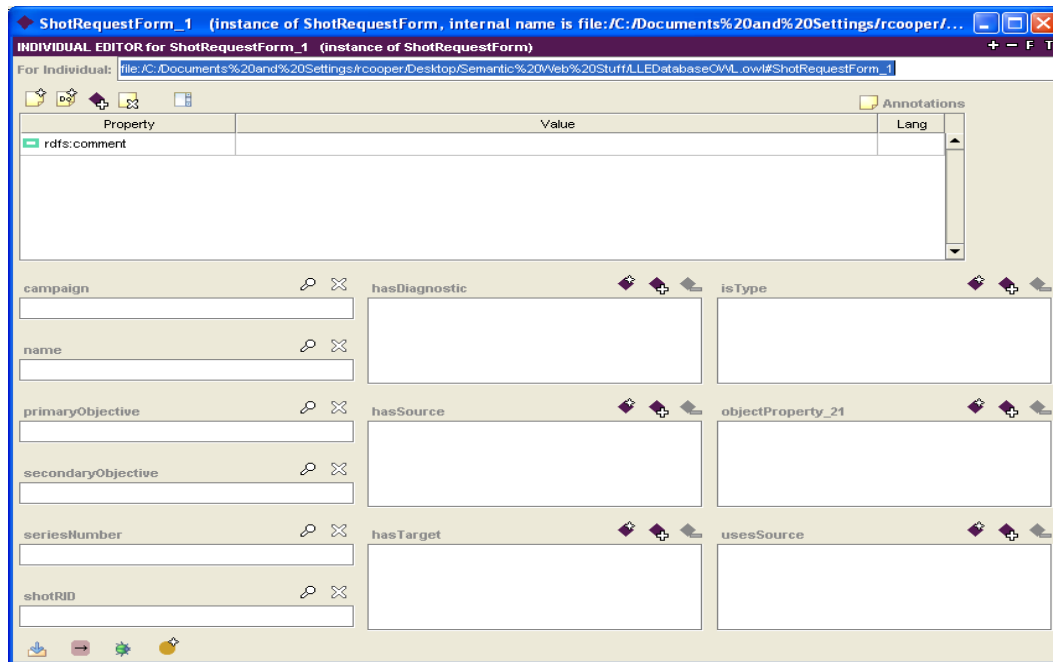
The ontology designed with ProtégéOWL would also have to be programmed into an application. There are two methods of creating such an application: exporting the ontology from ProtégéOWL directly to a Java format, or programming from scratch using the ontology as a model. Exporting directly from ProtégéOWL returns an interface for each object in the ontology, which was not desirable for the application's needs. Therefore, NetBeans Integrated Development Environment (IDE) was used to design and program several user interfaces to implement the ontology.

### Protégé Ontology

Classes for Shot Request Form (SRF), Diagnostic, Source, Target, and Experiment Type were created. Each class was given properties that corresponded with the data requested on each SRF in the PDM database. Properties such as hasTarget, hasDiagnostic, and hasSource in the SRF class were all made as symmetric properties with isTargetForShot, isDiagnosticForShot, and isSourceForShot, respectively. The editor window for an SRF individual is shown in Figure 5. The six text-entry boxes in the lower left portion of the screenshot each represent a functional property of the SRF, and serve as data labels for the individual. The six remaining boxes represent properties that link the SRF to other individuals. Individuals listed in these boxes are clickable links to similar windows for their respective classes. The Diagnostic class was given

symmetric properties for past experiments and experiments each diagnostic is designed for. Similar symmetric properties were given to the Source and Target classes, in order to link them

Figure 5: Screenshot of Individual Editor in ProtégéOWL.



to the other three. These specified relationships allowed ProtégéOWL's Pellet reasoner to automatically link individuals. Consequently, when a user adds an individual to the Protégé hierarchy, the reasoning software instantly places it in its correct place, and enables the user to quickly navigate between the individual and other related ones.

### NetBeans Application

Windows for Shot Request Forms (SRF), Diagnostic, and Experiment Type were designed with both user-input and readonly options. The user-input windows are designed to allow database managers to easily add to and edit the existing items in the database. Code was written to mimic the behavior of Protégé's Pellet reasoner, such that relationships between objects could be quickly determined and new individuals could be linked to existing ones in the database immediately upon entry. The readonly windows corresponded directly to the layouts of

the user-entry windows, without the ability to edit the contents. An example of a results window for the Diagnostic class is shown in

Figure 6. Elements in each window

that were based off any of the

symmetric properties outlined in

Protégé were made clickable to

enable the user to quickly navigate

between related elements.

### The Project's Future

The application is still in its

prototype form, so there are still some minor problems to be worked out. Once the final version

is completed, it can be exported and distributed to as many users as necessary. Developers

should be able to easily link the distributed applications to one, central database, so that the

ontology may be accessed from a variety of locations. Also, NetBeans and Protégé are user-

friendly applications, so editing the code and the model for the ontology itself can be easily done

by an administrator. Consequently, the ontology can be expanded to include any and all

documents pertaining to LLE. In fact, the future ontology could conceivably form a virtual

representation of all of LLE's experimental systems, making research and shot-planning a

considerably more efficient and useful process.

### **Acknowledgements:**

I would like to thank Rick Kidder and Stephen Craxton for giving me the opportunity to

spend my summer at LLE. I would especially like to thank Mr. Kidder for his advice, support,

and guidance throughout my project. I would like to thank Andrew Zeller for his frequent

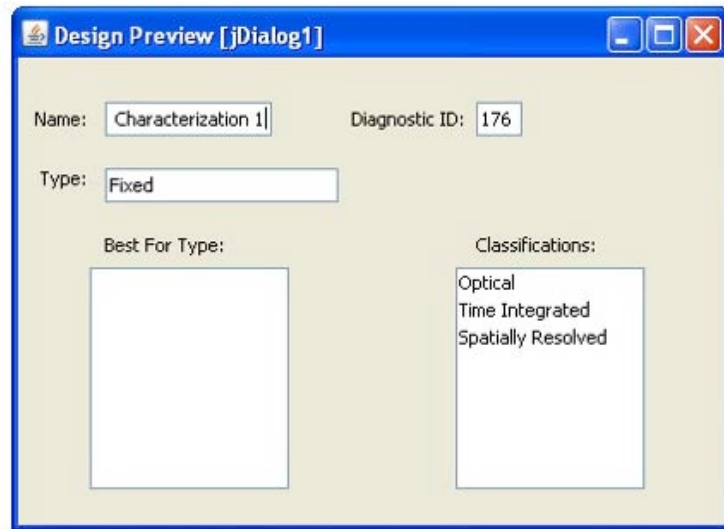


Figure 6: A search result window. In this case, the user either searched by diagnostic name or ID.

assistance and accessibility. I would also like to thank Eugene Kowaluk and Dino Mastrosimone for their suggestions on the structure and purpose of the ontology. Finally, I would like to thank Ricky Marron, Dan Gresh, and Chris Baldwin for the excellent foundation that they created in semantic web research.

**References:**

1. D. Gresh, "Implementing a Knowledge Database for Scientific Control Systems," 2006 Summer High School Research Program at the University of Rochester's Laboratory for Laser Energetics, LLE Report No. 348.
2. R. Marron, "Development of an Ontology for the OMEGA EP Laser System," 2007 Summer High School Research Program at the University of Rochester's Laboratory for Laser Energetics, LLE Report No. 353.
3. C. Baldwin, "Exploring Metadata for Laser Diagnostics and Control Systems on the OMEGA EP Laser System," 2008 Summer High School Research Program at the University of Rochester's Laboratory for Laser Energetics, LLE Report No. 357.



***A Graphical User Interface for User Generated Opacity Files***

Luke D. Coy

Advisors: Dr R.S. Craxton & Robert Rombaut

Laboratory for Laser Energetics

University of Rochester  
250 East River Road  
Rochester, NY 14623

## ***1. Abstract***

A Graphical User Interface (GUI), *Vermillion* was created that graphs opacity data produced by the *APLMIX* code for mixtures of elements. The GUI produces graphs that display the opacity on the vertical axis and the user's choice of density, temperature, or frequency on the horizontal axis. This provides the user with a convenient way to assess the adequacy of the density, temperature, and frequency grids chosen for use with *APLMIX*. Features of the GUI include linear or logarithmic horizontal axis, drag-and-click zooming, dynamic panning, and various customizations. If the user wants to resolve structure in the opacity as a function of frequency by adding multiple points to the frequency grid, he/she can rapidly display the spectrum at different (temperature, density) points and identify where more frequency points are required.

## ***2. Introduction***

Hydrodynamic simulations are a significant part of research for the University of Rochester's OMEGA laser - these simulations are vital for ignition experiments. The hydrodynamic targets used in these simulations require subsets of opacity data. Opacity is the measure of the ability of an object to obstruct the penetration of x rays. Opacity is measured in units of  $\text{cm}^{-1}$ , which is equivalent to the distance that a photon will travel before being absorbed by an electron in a material. The higher the value of opacity, the more obstructed x rays are when passing through a material. LLE uses a large database of opacities for 30 elements from hydrogen to zinc, obtained from Los Alamos.<sup>1</sup> Opacity is stored for every possible density, temperature, and frequency combination. The opacity database consists of 14,900 frequency data points per temperature – density point. There are roughly 20 density points and 50 temperature points in a typical opacity file. Hydrodynamic simulations conducted at LLE need to work with subsets of opacity data and need to be able to mix elements as well. Mixed opacity data files are created using a FORTRAN

program, *APLMIX*.<sup>2</sup> A Java program, *Opacity Viewer*,<sup>3</sup> allows the user to view the complete Los Alamos opacity data for individual elements. However, prior to this work, there was no simple user-accessible way to view the mixed opacity data files. The GUI (Vermillion) described in this report was designed to address this issue.

### 3. Vermillion

*APLMIX* compiles specified data from the opacity database and produces opacity data for the desired material. The User must identify the material, temperatures, densities, and boundaries for frequencies. *APLMIX* then calculates the average opacity for each of the frequency ranges, and inserts this data in FORTRAN output files known as FORT.20.

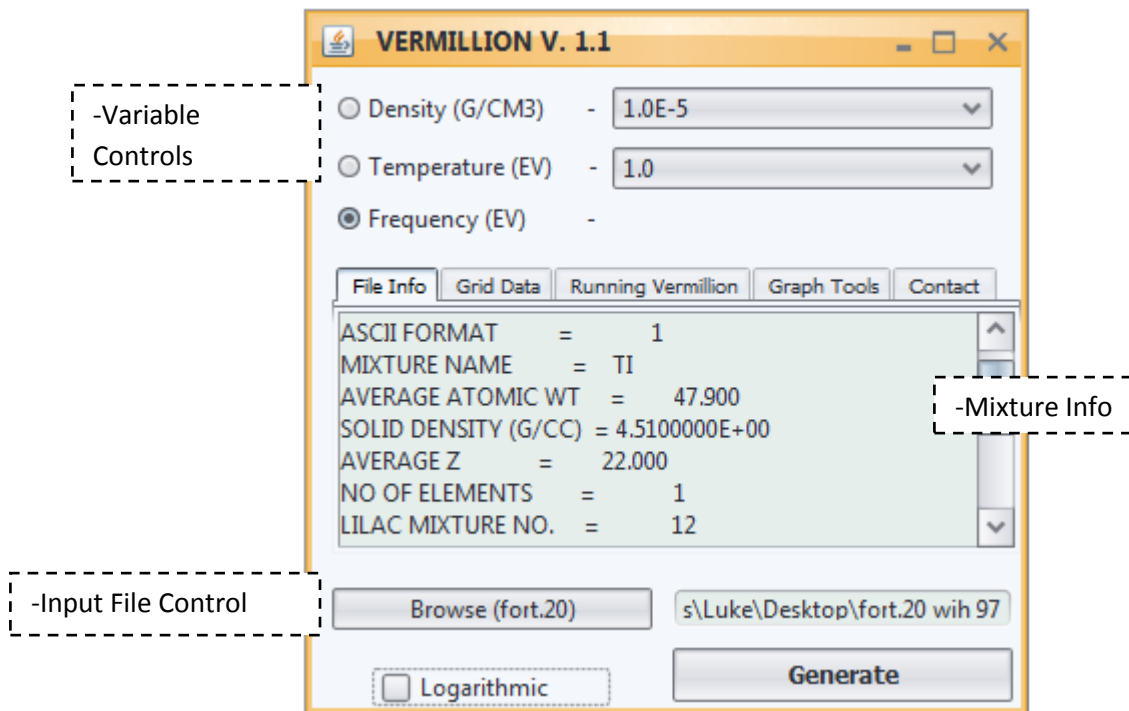


Figure 1 – Vermillion Menu 1.1 with configured graph controls and mixture information.

Figure 1 shows *Vermillion*'s three sections: the variable selection, the FORT.20 browser, and the file information. Before the graph of opacity can be created by *Vermillion*, the User must specify the directory of the FORT.20 file created by *APLMIX*. This is simply done by navigating the browse menu located at the bottom left corner of the GUI.

*Vermillion* will extract mixture information from the FORT.20 file such as the name of the mixture, the solid density, the atomic weight, etc. This information is displayed under the "File Info" tab of figure 1.

*Vermillion* will also extract the opacity data for every available density-temperature point. After this information is processed, the user has to select the two constant variables and the independent variable that will be used for the graph. In the example shown in figure 1, the density and temperature are selected as constants and frequency is chosen as the independent variable. This is the most common usage. The graph will then be generated. *Vermillion* displays opacity values logarithmically ( $\log_{10} [\text{Opacity}] \text{ cm}^{-1}$ ) as given by *APLMIX*.

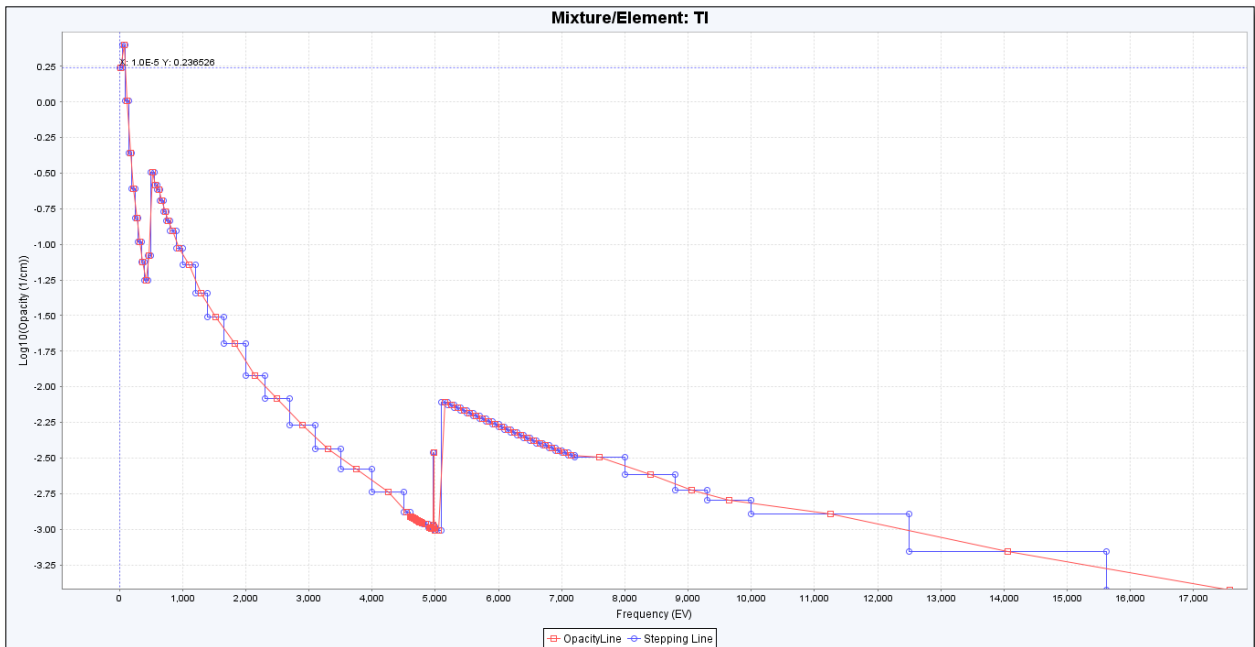


Figure 2 - Opacity as a function of frequency for Titanium, at a density of 1E-5 g/cc, and a temperature of 1.0 eV

A typical opacity graph is shown in figure 2. The range axis is always represented by logarithmic opacity, given in inverse centimeters. The domain is represented by the independent variable selected on the *Vermillion* menu. As figure 2 shows, two distinctly colored lines are given that connect two differently colored sets of points. Blue points represent the frequency grid boundaries selected by the user while red points represent the average opacity between boundaries. *Vermillion* has a number of graphing tools for ease of use. Dynamic zooming is implemented for simple one-click zooming. Dynamic panning allows the user to manipulate the window range of the graph. Other features include .PNG exporting, XY coordinate display, and direct printing.

#### 4 Frequency Grid Adjustment

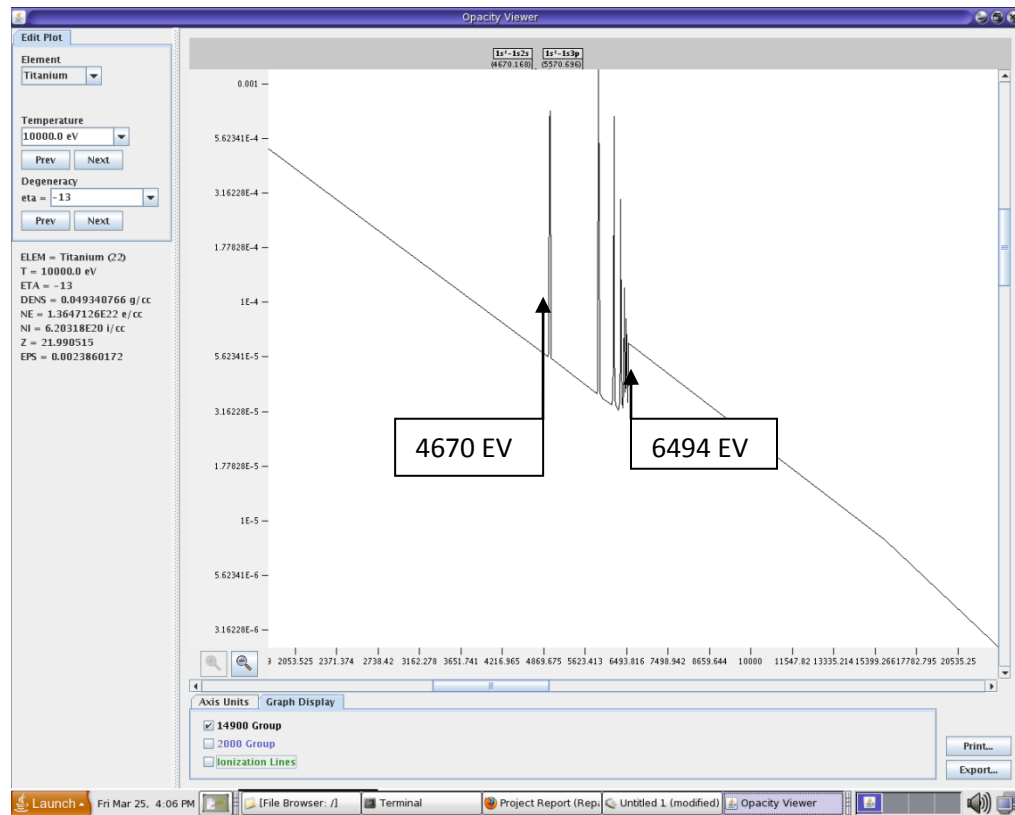


Figure 3 – Opacity vs Frequency as shown by Opacity Viewer for Ti at a density of 0.0315 g/cc and a temperature of 10000 eV

For many elements the opacity data is highly structured in the frequency domain. An example for titanium is shown in figure 3, produced by Opacity Viewer. The graph plots all 14,900 frequency points for the selected density and temperature. The result is a highly detailed graph of titanium opacity. A “standard” opacity file used in many hydrodynamic simulations uses just 48 frequency points, 18 density points, and 17 temperature points. This resolution, seen in figure 4, fails to resolve the structure of opacity for most elements and pales in comparison to its 14,900-point counterpart.

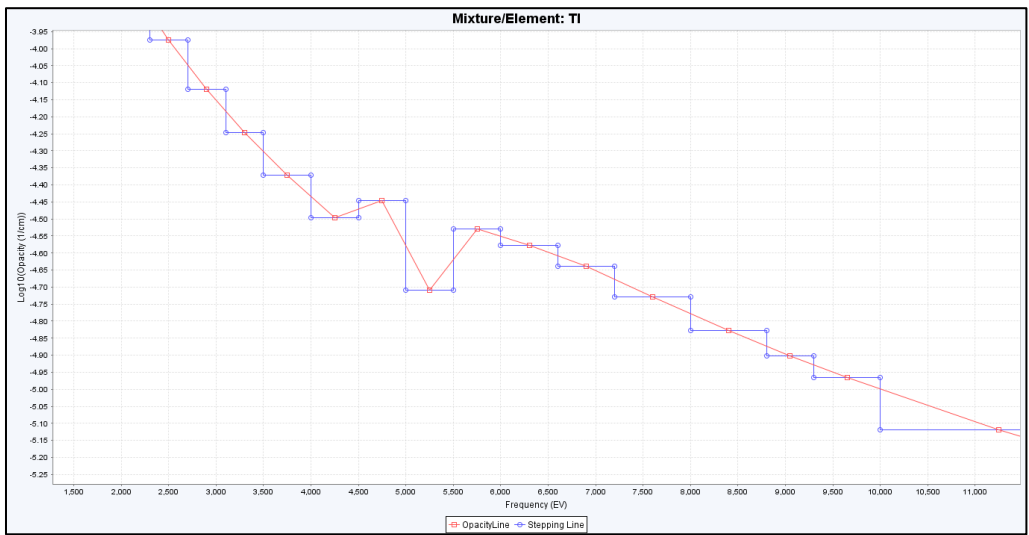


Figure 4 – Opacity of Ti as a function of frequency at a density of 0.0316 g/cc and a temperature of 10000 eV, for the “standard” 48 frequency groups.

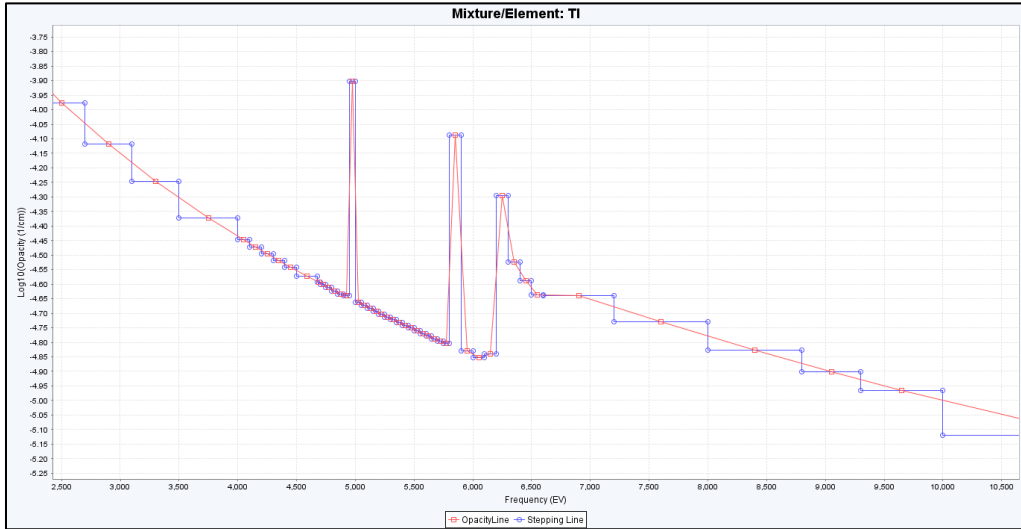


Figure 5 – Opacity of Ti as a function of frequency at a density of 0.0316 g/cc and a temperature of 10000 eV, for 80 frequency groups.

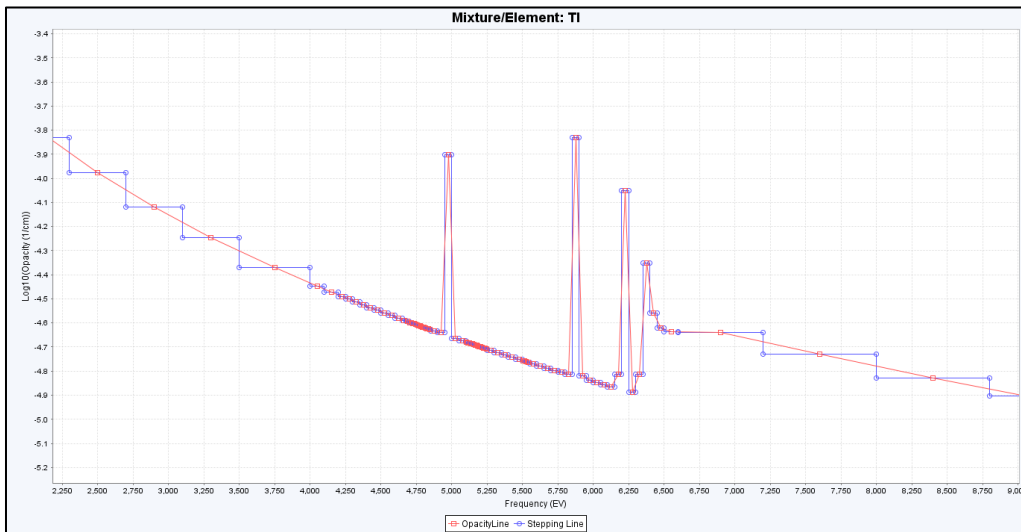


Figure 6 – Opacity of Ti as a function of frequency at a density of 0.0316 g/cc and a temperature of 10000 eV, for 120 frequency groups.

## **5 Conclusion**

A Graphical User Interface, *Vermillion*, has been programmed for the easy viewing of opacity files for mixtures of elements. Scientists will use *Vermillion* to view opacity data under various conditions. The resulting information garnered from this data will help scientists perform more accurate hydrodynamic simulations.

## **6 Acknowledgements**

I would like to thank Dr RS Craxton for helping me understand the science of opacity, as well as the numbers behind the opacity data itself. I would also like to thank Robert Raumbaut for his help and consultation with the programming and design of *Vermillion*.

## **7 References**

- [1] W.F. Huebner, A.L. Merts, N.H. Magee Jr., M.F. Argo, "Astrophysical Opacity Library," Los Alamos National Laboratory Report LA-6760-M (1977).
- [2] R.S. Craxton, "Generating Opacity Data for Mixtures," Theory Group Report #12 (1980).
- [3] P.W. Hopkins, "Comparing Opacity Data Groups with a Java-Based GUI Solution," Laboratory for Laser Energetics High School Research Program (1999).



# **Reducing UV Near-Field Beam Modulation on OMEGA EP by Angularly Detuning the Frequency Conversion Crystals**

Kyra Horne  
Fairport High School

LLE Advisor: Mark Guardalben

University of Rochester  
Laboratory for Laser Energetics  
Summer High School Research Program 2010

## **Abstract**

The frequency-conversion crystals (FCC's) mounted in the OMEGA EP laser system are used to convert an infrared beam to a third-harmonic ultraviolet beam. Currently, the FCC's are angularly tuned to maximize the conversion efficiency. When operated in this manner, the laser damage thresholds of the current UV optics require that the IR laser intensity be maintained at a relatively low level ( $\sim 1 \text{ GW/cm}^2$ ). In this regime, small IR intensity variations produce large UV intensity variations, causing the UV beam to be highly modulated. We show, both in simulations and experimentally, that by angularly detuning the doubler crystal, the UV beam intensity modulation can be significantly reduced. Measurements on OMEGA EP show a reduction in peak UV fluence of 13% for the detuned FCC. Standard deviations of UV beam fluence distributions were 21% and 14.7% for the tuned and detuned cases, respectively, indicating a significantly smoother beam for the detuned FCC for the same UV energy. This should allow more energy to be delivered to a target while maintaining peak intensities below the damage threshold limit.

## Introduction

Frequency-conversion crystals are used to decrease the wavelength (increase the frequency) of a beam. The frequency-conversion crystals in the OMEGA EP laser system convert an infrared beam to a third-harmonic ultraviolet beam in a two-step conversion process as shown in Fig. 1. The beam first passes through the doubler crystal and then through the tripler crystal.

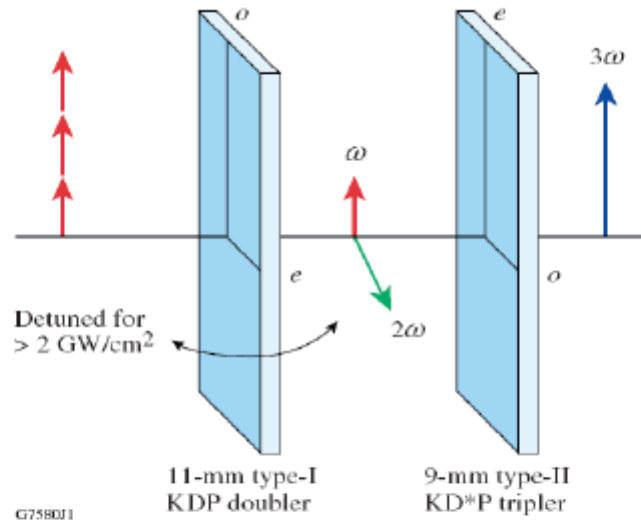
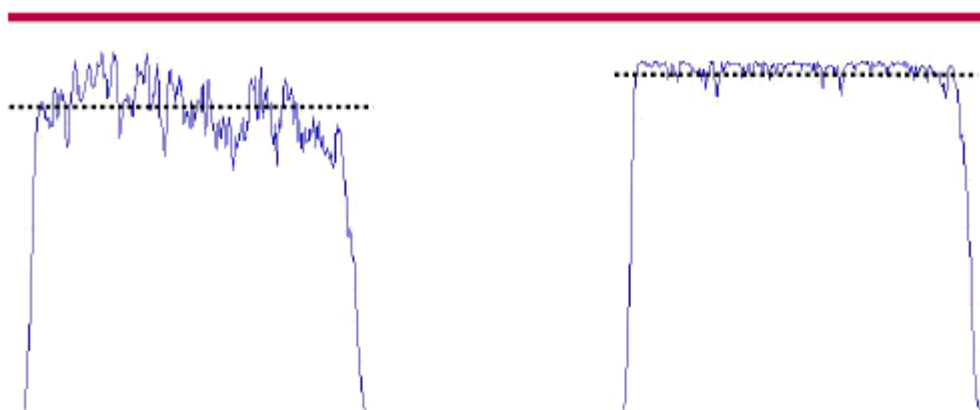


Figure 1: Schematic of the frequency conversion process using the doubler and tripler. Three infrared photons aligned with the o-axis pass through the doubler and two convert into a green light photon while the third remains infrared. The green and infrared photon then pass through the tripler and form an ultraviolet photon aligned with the e-axis.

The FCC's are angularly tuned to maximize conversion efficiency. However, they must currently be operated at a relatively low level of IR laser intensity, approximately  $1 \text{ GW/cm}^2$ , due to the low laser damage thresholds of the current UV optics. This results in a highly modulated UV beam. This large UV intensity variation lowers the laser energy because the peak intensities must be kept below the laser damage threshold (see Fig. 2).

## Laser Damage Threshold



*Figure 2. Beam intensity lineouts (left) with high modulation and (right) with reduced modulation. In both cases, the highest intensities must be beneath the laser damage threshold to avoid damage to the UV optics after the frequency conversion crystals. The beam with low modulation can be operated with a higher average energy.*

In this work it is proposed that within the current operating regime of the OMEGA EP laser system, a detuned doubler can produce a smaller range of UV intensities than a tuned doubler. This follows the observation in Ref. 1 that intensity modulations can be reduced by detuning the tripler, albeit with some loss of conversion efficiency.

### Simulation

Using predictions of the frequency conversion code *Mixette* (based on Ref. 1), graphs of UV output intensity versus IR input intensity were plotted at various combinations of doubler and tripler detuning. These plots were compared to determine the detuning angle that would produce the lowest UV beam modulation, while remaining within the OMEGA EP system's allowed IR input intensity level and beneath the UV laser damage threshold.

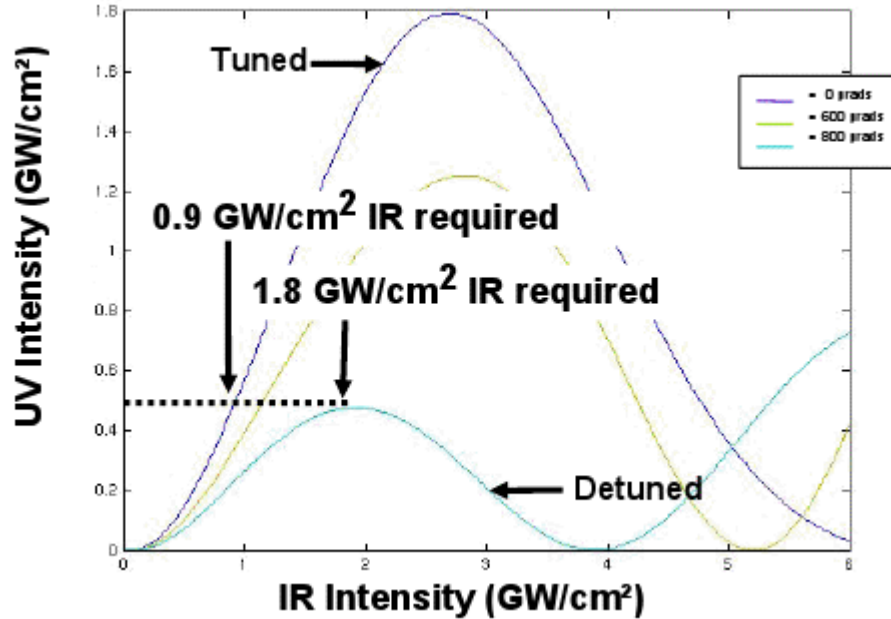


Figure 3: Graph of UV intensity vs. IR intensity. A tuned doubler requires less IR intensity input to achieve the same UV intensity as a detuned doubler.

Simulations (Fig. 3) confirm the proposal that a detuned doubler may produce less UV intensity variation. In Fig. 3, a UV intensity of 0.5 GW/cm<sup>2</sup> can be produced either using 0.9 GW/cm<sup>2</sup> of IR with a tuned doubler or 1.8 GW/cm<sup>2</sup> of IR with a doubler detuned by 800 μrad. In the first case IR intensity modulations produce large UV intensity modulations, while in the second case UV intensity modulations are minimized. It requires a greater amount of IR intensity input to achieve the lessened variation.

It was determined that the best system used a doubler detuned 800 μrad with a tuned tripler. This system also required a relatively low level of IR intensity to achieve significantly less UV beam modulation and had low angle sensitivity.

MATLAB simulations for the tuned and detuned cases were compared using the same measured IR beam and pulse shape and showed less modulation for the detuned case. In Fig. 4,

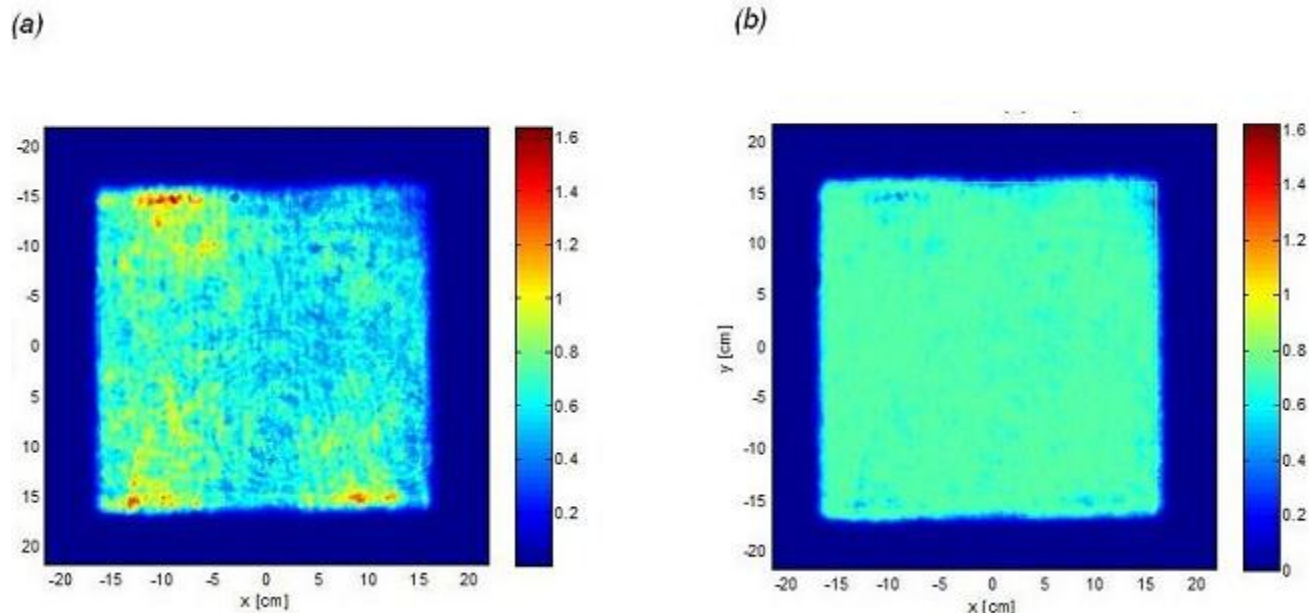


Figure 4: Simulations of the UV output beam intensity ( $\text{J}/\text{cm}^2$ ) for (a) a tuned doubler and (b) a detuned doubler at  $800 \mu\text{rad}$ . The tuned beam has higher modulation, a UV energy of 642 J, a contrast of 24.2%, and peak fluence of  $1.62 \text{J}/\text{cm}^2$ . The detuned beam has reduced modulation, a UV energy of 722 J, a contrast of 5.9%, and a peak fluence of  $0.73 \text{J}/\text{cm}^2$ .

the UV beam fluence maps ( $\text{J}/\text{cm}^2$ ) simulated with MATLAB show an increase in UV energy from the tuned to detuned, 642 J to 722 J, respectively. The simulations also show a decrease in standard deviation in fluence (averaged over the beam) from 24.2% to 5.9% and in peak fluence ( $1.62 \text{J}/\text{cm}^2$  to  $0.73 \text{J}/\text{cm}^2$ ).

## Experiment

The simulations were verified experimentally on OMEGA EP proving that detuning the crystals can produce a beam with reduced modulation. Shots were fired on the system and measurements were taken for the tuned and detuned-doubler cases (Figs. 5 and 6, respectively).

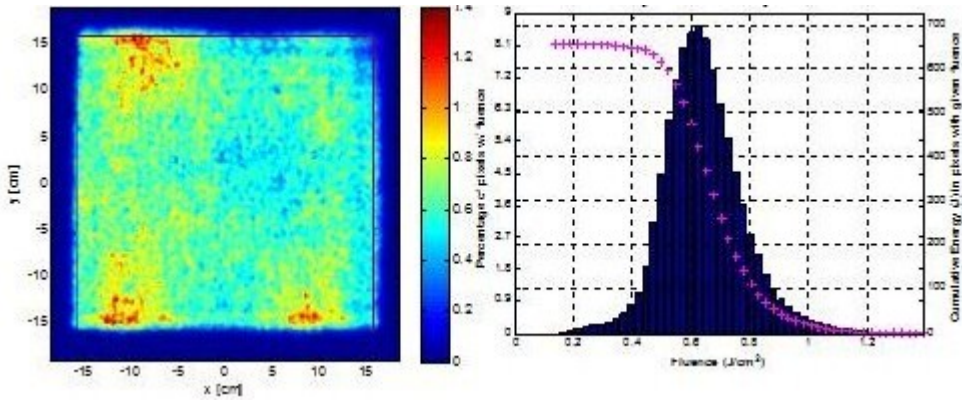


Figure 5: Experimental UV beam fluence map and histogram from a shot on OMEGA EP for a tuned doubler. The tuned beam has higher modulation, a UV energy of 683 J, a contrast of 21.2%, and a peak fluence of 1.39 J/cm<sup>2</sup>.

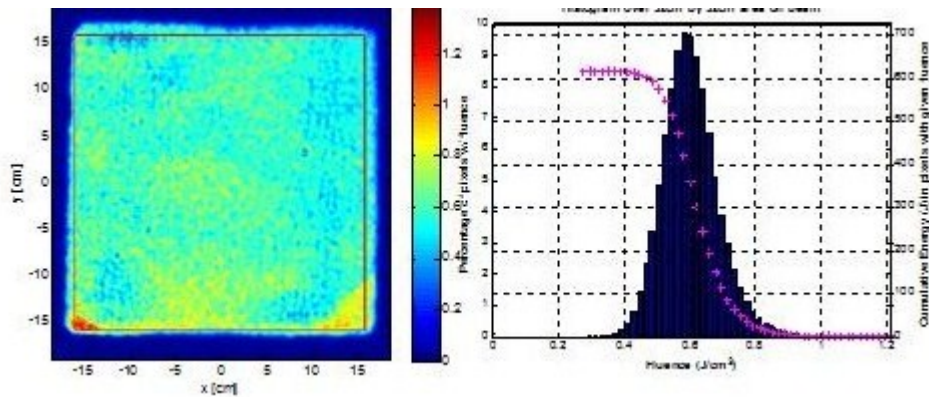


Figure 6: Experimental UV beam fluence map and histogram from a shot on OMEGA EP for a detuned doubler at 800  $\mu$ rad. The detuned beam has reduced modulation, a UV energy of 694 J, a contrast of 14.7%, and a peak fluence of 1.21 J/cm<sup>2</sup>.

The tuned doubler required 1680 J of IR input energy and produced a UV output energy of 683 J. The standard deviation was 21.2% and the peak fluence in the beam was 1.39 J/cm<sup>2</sup>. The detuned doubler required 3939 J of IR input energy and produced a UV output energy of 694 J. The standard deviation was 14.7% and the peak fluence in the beam was 1.21 J/cm<sup>2</sup>. The peak fluence was reduced by 13% and the standard deviation was reduced by nearly 7%. The reduction in peak fluence allows for a 13% increase in UV output energy for the beam.

## **Future Work**

The experiment done on the OMEGA EP laser system served as a proof-of-concept experiment and was carried out at relatively low energies to ensure safety of the laser system. The next step is to increase the IR energy to show that more UV energy can be safely delivered to a target with a detuned FCC than a tuned FCC. This will require determining the proper amount of detuning for each pulse shape and input energy, and additional shots on OMEGA EP to confirm the simulations.

## **Acknowledgements**

Thank you to Dr. R. Stephen Craxton for directing the LLE Summer Program and giving me the opportunity to do research at the LLE facility. I also thank my advisor Mark Guardalben for instructing and supervising me in this research.

## **References**

[1] R.S. Craxton, IEEE J. Quant. Electronics, QE-17, No. 9, pp. 1771-1782, Sept. 1981

# **Modeling Tritiated Water Desorption from Stainless Steel**

**Karin Hsieh**

**Webster Schroeder High School  
Rochester, NY**

**Advisor: Dr. W. T. Shmayda**

**Laboratory for Laser Energetics  
University of Rochester  
Rochester, NY  
September 2010**



## **Abstract**

A simple mathematical model has been developed to describe the outgassing rate of tritium from solids as a function of time. The model is based on the assumptions of a homogeneous material that can be characterized with a single diffusion coefficient. The model was used to fit the experimental tritium desorption rates from pre-tritiated, type 316, stainless steel over a temperature range of 20 to 400°C. The basic model did not fit the experimental data accurately at longer times, except for data obtained at 20 and 400°C. Including carrier gas flow rate and temperature ramping did not improve the fitting results at the longer times. It is likely that at 20°C, the desorption process is dominated by a single diffusion coefficient that describes tritium diffusion through and desorption from the surface oxide layer. At 400°C, the desorption process is dominated by atom transport through the bulk metal. At intermediate temperatures, atom transport is dependent on diffusivity through the oxide and the bulk, and thus resulted in a poor curve fit since the model assumes a unique diffusion coefficient within a single homogeneous layer. We conclude that the bulk diffusion model alone cannot describe the tritium desorption processes from stainless steel with an oxide top layer. A more accurate model that includes desorption from the surface oxide layer, diffusion through the oxide layer, and diffusion within the bulk has been proposed for future work.

## **Introduction**

Tritium (H-3) is a radioactive, naturally occurring isotope of hydrogen, with a half-life of 12.32 years. Tritium has commercial, research, and defense applications. The commercial and research uses of tritium, which accounts for only a fraction of tritium used worldwide, include tracers in biological diagnostics and environmental studies and safety signs in low-light applications where electrical power is not available. Additionally, tritium provides an extremely sensitive tool for studying the fundamentals of water desorption from metals. A significant amount of research has gone into understanding how water bonds to and desorbs from surfaces. In particular, industries that require ultra-pure streams for their chemical processes (such as the semiconductor industry) have identified adsorbed water as a contaminant and work hard to eliminate water from the inside of metal process lines. Tritium-labeled water is an excellent tool for better understanding the processes.

The interest in the behavior of tritium in stainless steel mainly stems from its widespread usage in tritium-handling equipment and components. In addition to having excellent mechanical properties, stainless steel has favorable properties concerning hydrogen permeation and dissolution, hydrogen-induced embrittlement, and tritium-decay accelerated corrosion [1, 2]. A particular challenge to a systematic investigation of the interaction of hydrogen isotopes with stainless steel is the multi-elemental composition of the bulk, a different multi-element makeup in the near surface and a complex oxide structure. There is significant evidence in the literature describing the influence of the chemical composition of the surface on the kinetics of hydrogen absorption and desorption from stainless steel [1, 2].

Hydrogen and its isotopes behave similarly in many regards. They are diatomic gases that dissociate on metal surfaces and dissolve in the metal lattice as atoms. These atoms readily recombine once they return to any air-surface interface. This high mobility implies that metals in general are not good barrier materials for tritium [1, 2]. By contrast, ceramics and oxides are typically very good barrier materials if they are not porous. In most cases, the low permeation is due to extremely low solubility for hydrogen isotopes in ceramic materials, especially metal oxide materials [3, 4].

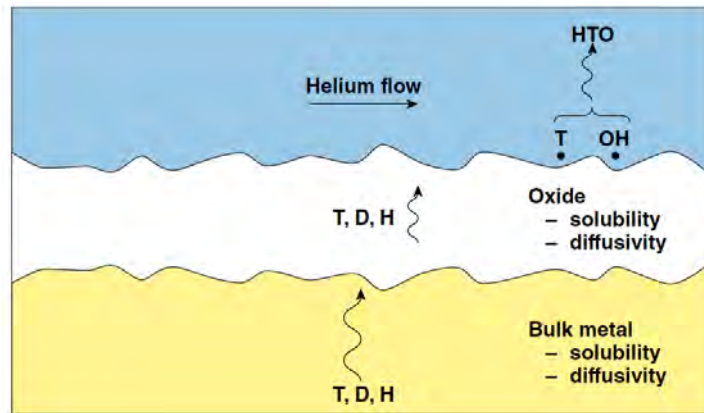


Fig. 1: Cross-section of a metal coupon in the vicinity of the metal-air interface

This paper describes the modeling of tritium transport from the bulk of 316, stainless steel to the surroundings in the presence of water vapor. The key aspects of the model are shown in Figure 1. Helium containing water vapor flows over the metal surface. Hydrogen isotopes diffuse from the bulk through the oxide layer and accumulate on the uppermost surface of the oxide. Water vapor collides with the surface and dissociates to form hydroxyl radicals and protons that remain bound to the surface. After residing on the surface for a short length of time that depends on the metal temperature among other factors, the protons and hydroxyl radicals recombine and desorb from the surface. Occasionally the hydroxyl radicals recombine with tritons instead of protons, which also reside on the surface to form tritiated water (HTO). In this case HTO desorbs from the surface. This desorption process depletes the concentration of tritons on the surface and establishes a concentration gradient between the surface and the bulk. Tritons migrate from the bulk to the surface as a result of the concentration gradient. A simple model based on diffusion from the bulk to the surface that uses a single diffusion constant is developed in a subsequent section and tested against experimental data. Understanding the factors that control tritium removal from metals is important if techniques to reduce chronic tritium emissions from metals are to be developed [4, 5].

## Experimental Setup

The experimental setup to measure the rate of tritium release from contaminated coupons is provided in Figure 2.

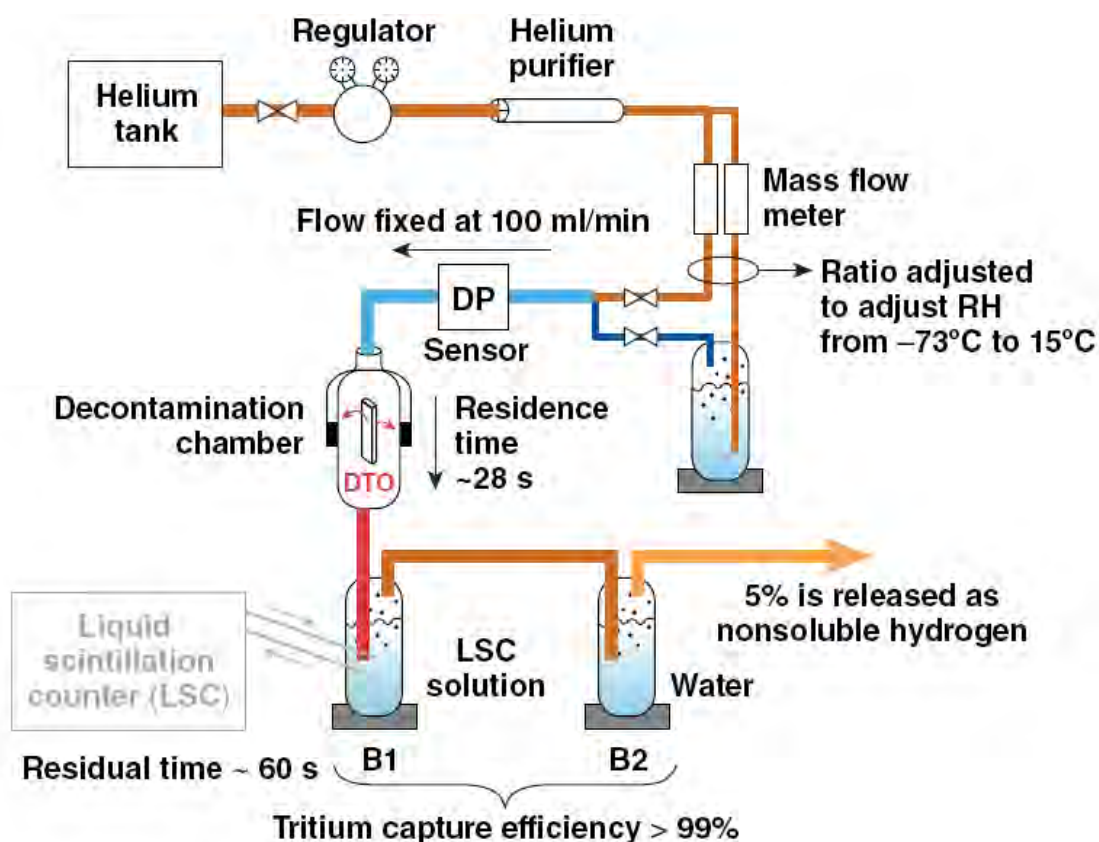


Fig. 2. Experimental setup to measure tritium desorption from contaminated coupons

Type 316, stainless steel coupons (5 x 1.8 x 0.3 cm) were contaminated by exposing them to 690 Torr of deuterium-tritium (DT) gas for 23 h at room temperature. Subsequently the coupons were stored in a dry helium environment and then transferred to the decontamination chamber under a helium blanket to ensure that air and humidity did not come in contact with the samples before the experiment. High purity helium was passed through a purifier to remove trace impurities and introduced into the decontamination chamber at 100 ml/min. The humidity of the helium carrier could be adjusted by diverting a fraction of the carrier through a wash bottle filled with water. The humidity was measured using a dew point sensor once the two streams were recombined before entering the decontamination chamber. In the current set of experiments the humidity of the carrier was held at  $-70^{\circ}\text{C}$  or lower. At a flow rate of 100 ml/min, the gas content of the exposure chamber would be replaced every 28 seconds. Previous work has shown that more than 95% of the tritium that is released from a metal surface will be released as tritiated water (HTO) and more than 99% of the

tritium will be captured by a set of two bubblers [3,4]. The same contaminated coupon was used to investigate desorption at 25, 100, 150, 200, 250, 300, and 400°C respectively in this study.

## Theory

Fick's second law of diffusion describes the concentration (  $c$  ) of hydrogen in a metal as a function of time (  $t$  ) and depth (  $x$  ) [6].

$$\frac{\partial c}{\partial t} = D \frac{\partial^2 c}{\partial x^2}$$

The following boundary equations apply to hydrogen transport from the bulk of a metal sample of finite size to the surface:

$$\begin{aligned} c &= c_1, \text{ at } x = 0 \text{ for all times,} \\ c &= c_2, \text{ at } x = l \text{ for all times, and} \\ c &= c_0, \text{ at } t = 0 \text{ for } 0 < x < l \end{aligned}$$

The method of separation of variables is used to solve the above second order differential equation by assuming that the concentration comprises two parts, one dependent on position, the other on time:

$$c(x, t) = X(x)T(t)$$

Substituting into and reorganizing the diffusion equation to separate the variables, the diffusion equation becomes:

$$\frac{1}{T} \frac{dT}{dt} = \frac{d^2X}{dx^2} \left( \frac{D}{X} \right)$$

Since each side of this equation is independent of each other, they must equal the same constant, which is taken to be  $-\lambda^2 D$ .

$$\frac{1}{T} \frac{dT}{dt} = \frac{d^2X}{dx^2} \left( \frac{D}{X} \right) = -\lambda^2 D$$

The solutions for  $T(t)$  and  $X(x)$  are:

$$T(t) = e^{-\lambda^2 D t}$$

$$X(x) = A \sin(\lambda x) + B \cos(\lambda x)$$

where A and B are constants of integration. The concentration dependence on position and time,  $c(x,t)$ , can be written as:

$$c(x, t) = [A \sin(\lambda x) + B \cos(\lambda x)]e^{-\lambda^2 D t}$$

The general form of the above solution is the sum of solutions of the same type.

$$c(x, t) = \sum_{m=1}^{\infty} [A_m \sin(\lambda_m x) + B_m \cos(\lambda_m x)]e^{-\lambda_m^2 D t}$$

where the values of  $A_m$ ,  $B_m$ , and  $\lambda_m$  are determined from the boundary and initial conditions listed above.

For  $c = c_1$ , at  $x = 0$  to hold for all times,  $B_m = 0$ , and to satisfy the condition  $c = c_2$  at  $x = l$  for all times requires:

$$\lambda_m = \frac{m\pi}{l}$$

The concentration  $c(x,t)$  reduces to:

$$c(x, t) = \sum_{m=1}^{\infty} \left[ A_m \sin\left(\frac{m\pi x}{l}\right) \right] e^{-\frac{m^2 \pi^2 D}{l^2} t}$$

To meet the initial condition  $c = c_0$ , at  $t = 0$  for  $0 < x < l$  requires:

$$c(x, 0) = C_0 = \sum_{m=1}^{\infty} A_m \sin\left(\frac{m\pi x}{l}\right)$$

$$\int_0^l C_0 \sin\left(\frac{p\pi x}{l}\right) dx = \int_0^l \sum_{m=1}^{\infty} A_m \sin\left(\frac{m\pi x}{l}\right) \sin\left(\frac{p\pi x}{l}\right) dx$$

where:  $p=0, 1, 2, 3 \dots$

$$-\frac{lC_0}{p\pi} \cos\left(\frac{p\pi x}{l}\right) \Big|_0^l = \left\{ (0 \text{ if } m \neq p); \left(\frac{A_m l}{2} \text{ if } m = p\right) \right\}$$

$\therefore$  for  $m = p = 1, 3, 5 \dots$

$$\frac{2lC_0}{m\pi} = \frac{A_m l}{2}$$

$$A_m = \frac{4C_0}{m\pi}$$

Finally, the solution to the diffusion equation for a solute of constant concentration diffusing into a slab becomes:

$$C(x, t) = \frac{4C_0}{\pi} \sum_{n=0}^{\infty} \frac{1}{2n+1} \sin\left(\frac{(2n+1)\pi x}{l}\right) \exp\left(-\frac{D(2n+1)^2\pi^2}{l^2} t\right)$$

where the slab is bounded by  $x = 0$  and  $x = l$ . In the present case, the solid is symmetric if the origin ( $x = 0$ ) is placed along the mid-plane in the sample and the diffusion length  $l$  is taken to be half the thickness of the coupon. The solution to the diffusion equation becomes:

$$C(x, t) = \frac{4C_0}{\pi} \sum_{n=0}^{\infty} \frac{1}{2n+1} \sin\left(\frac{(2n+1)\pi x}{2l}\right) \exp\left(-\frac{D(2n+1)^2\pi^2}{4l^2} t\right)$$

The flux of tritium ( $F(t)$ ) approaching and then leaving the surface of the coupon at  $x = l/2$  is:

$$F(t) = -D \frac{\partial c}{\partial x} \quad \text{evaluated at } x = l/2$$

$$= -D \left[ -\frac{4C_0}{\pi} * \frac{\pi}{2l} * \sum_{n=0}^{\infty} \cos\left(\frac{(2n+1)\pi x}{2l}\right) \exp\left(-\frac{D(2n+1)^2\pi^2}{4l^2} t\right) \right]$$

$$F(t) = \frac{2C_0D}{l} \sum_{n=0}^{\infty} \exp\left(-\frac{D(2n+1)^2\pi^2}{4l^2}t\right)$$

and the rate at which tritons leave the coupon of surface area (A) at  $x = l/2$ , will be

$$\dot{n}_s = A * F(t) = \alpha * e^{-t/\tau} \quad (1)$$

where:

$$\tau = \frac{4l^2}{D\pi^2} \quad (2)$$

and

$$\alpha = \frac{2c_0DA}{l} \quad (3)$$

In the limit of long times,  $n=0$ , the summation can be dropped.

Tritons released from the metal surface are swept from the decontamination chamber volume (V) at a flow rate (F). The rate at which tritium particles leave the chamber depends on the number of particles in the chamber, the carrier flow rate, and the chamber volume according to the relation:

$$\dot{n}_f = \frac{F}{V} * N(t) = \beta N(t) \quad (4)$$

where  $N(t)$  is the number of tritons in the chamber at time  $t$ .

The number of tritons in the chamber at any time,  $t$ , equals the number released from the metal surface minus those swept away by the carrier:

$$\frac{dN}{dt} = \dot{n}_s - \dot{n}_f$$

or using equations 1 and 4:

$$\frac{dN}{dt} = \alpha e^{-t/\tau} - \beta N \quad (5)$$



The method of using an Integrating Factor can be used to solve the mass balance equation (equation 5). Multiplying equation 5 by  $e^{\beta t}$  and separating the variables yields:

$$e^{\beta t} \frac{dN}{dt} + \beta N e^{\beta t} = \alpha e^{(\beta - \frac{1}{\tau})t}$$

Integration yields:

$$N e^{\beta t} = \alpha \left( \frac{1}{\beta - \frac{1}{\tau}} \right) e^{-\frac{t}{\tau}} * e^{\beta t} + C$$

or

$$N(t) = \gamma e^{-\frac{t}{\tau}} + C e^{-\beta t} \quad (6)$$

where:

$$\gamma = \frac{\alpha \tau}{\beta \tau - 1} \quad (7)$$

and C is a constant of integration.

At the start of the experiment ( $t = 0$ ), the number of tritons in the carrier  $N(0) = N_0$ , the background value. Applying this condition to equation 6 shows that the constant of integration is:

$$C = (N_0 - \gamma)$$

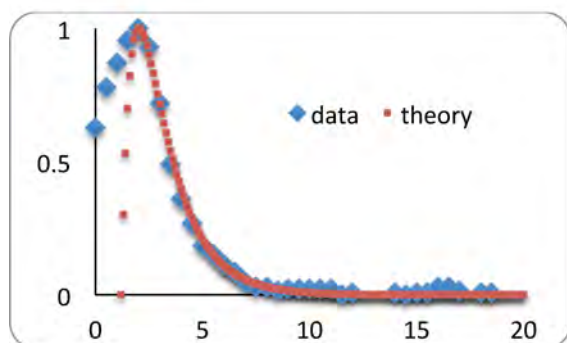
and equation 6, the number of tritons swept from the chamber at any time, t, becomes:

$$N(t) = \gamma e^{-\frac{t}{\tau}} + (N_0 - \gamma) e^{-\beta t} \quad (8)$$

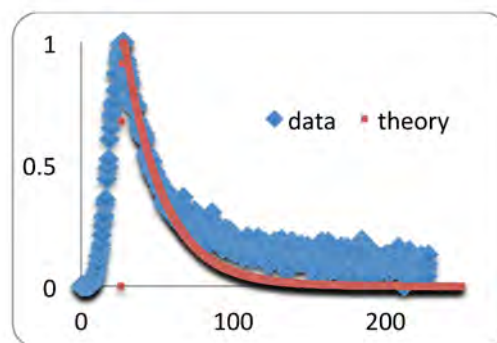
where all the parameters are known except for the diffusion coefficient. Since the source of the tritons is the metal surface, equation 8 multiplied by the carrier flow rate, divided by the chamber volume and the surface area of the coupon represents the rate at which tritons desorb from the metal surface per unit time and area, i.e. the outgassing rate.

## Results and Discussion

Equation 8 was fit to the data by varying the diffusion coefficient until the best fit to the experimental data was obtained. These fits are shown in Figure 3 for the different outgassing temperatures. The experimental data shown in these figures was obtained by differentiating the amount of activity collected in bubbler (B1) with respect to time and by dividing the result by the surface area of the coupons. Each data set shows the same basic structure of a quick rise in the outgassing rate followed by a slow decay in the outgassing rate. Seven cases are shown: in each of these cases, the furnace was brought to a specific temperature within 3 minutes and subsequently held at that temperature for the remainder of the experiment. The coupons could take up to 20 minutes to reach the target temperature. Both the data and the theoretical fits in these figures were normalized to their respective maximum values. The model has two major shortcomings: it does not fit the data very well at both short and long times except for the 20 and 400°C cases. This suggests that at these temperatures, the outgassing rate is dominated by a single diffusion coefficient. At 20°C, desorption may be restricted by tritium diffusion and desorption from the surface oxide layer. On the other hand, at 400°C, tritium diffusion through the metal may be the rate-limiting step. At the intermediate temperatures, at least two processes are involved in the transfer of tritium from the bulk to the carrier stream resulting in a poor curve fit when modeled by a single adjustable parameter.



20°C



100°C

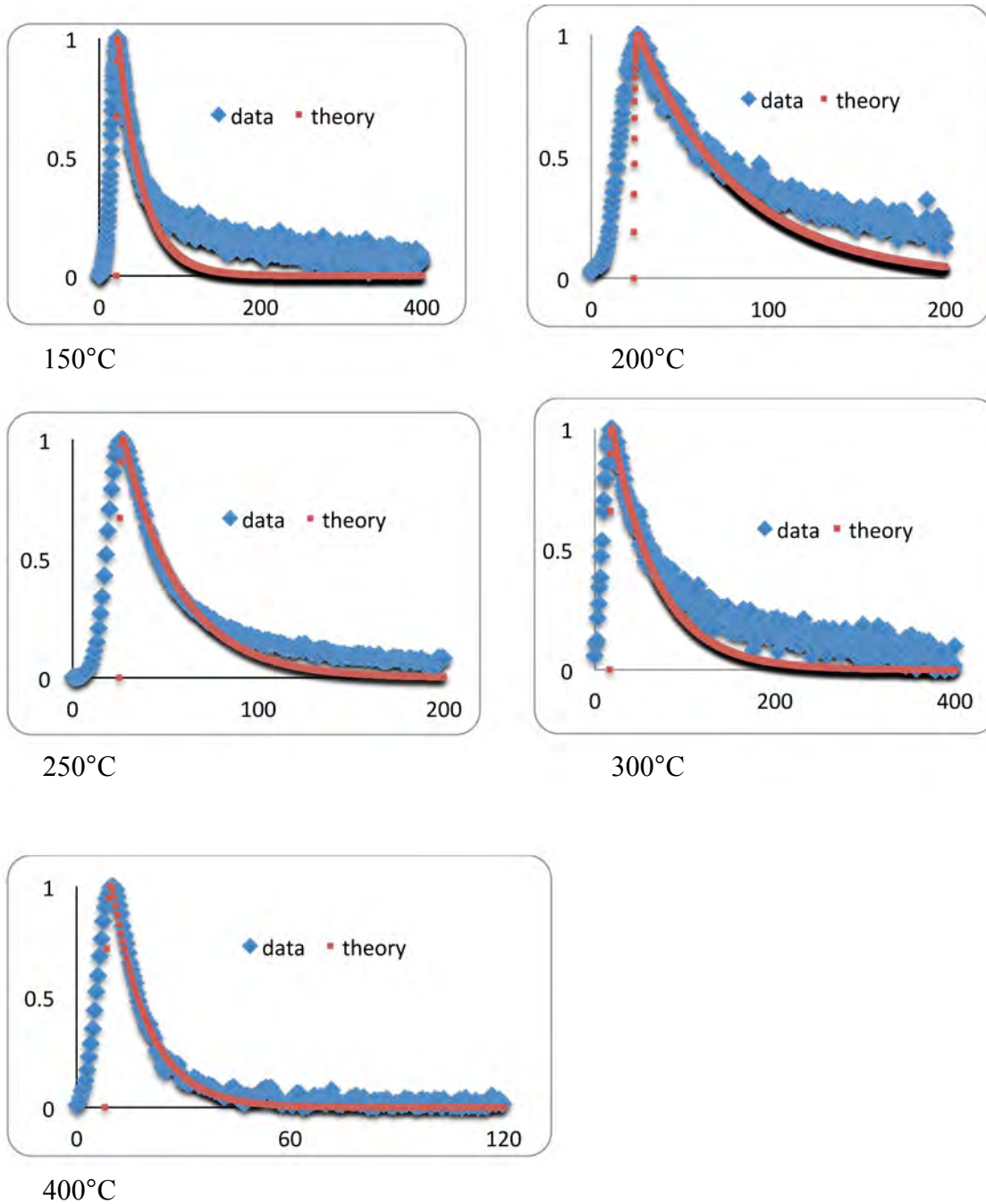


Figure 3 Comparison of normalized predicted outgassing rate with normalized experimental data against time in minutes for different coupon temperatures

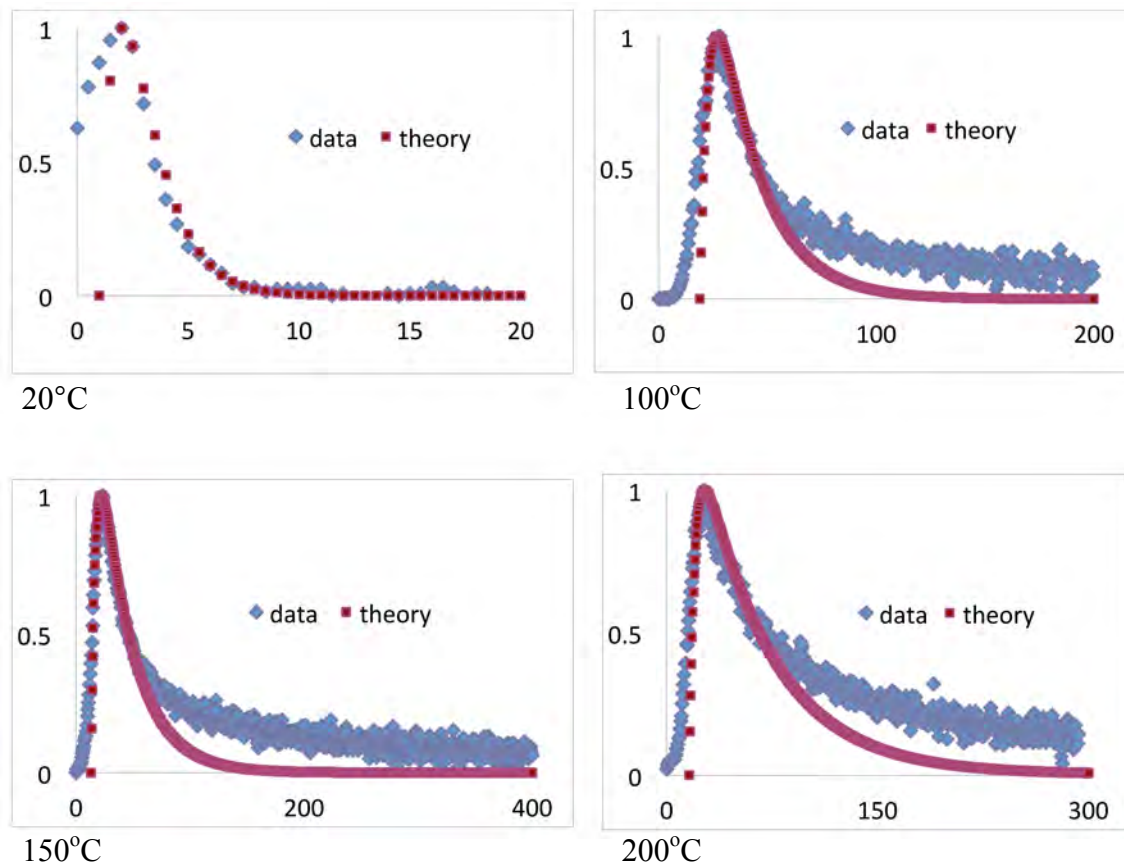
The model described above assumes the diffusion coefficient to be constant, fixed at the final desorption temperature for the duration of the experiment. In reality however,

tritium was released from the metal surface during the first 30 minutes of the experiment while the coupon was heating up to its final temperature. The diffusion coefficient, which has the following Arrhenius dependence on temperature:

$$D(T) = D_o \exp\left(-\frac{E_a}{RT}\right)$$

where  $D_o$  is the diffusion coefficient ( $\text{cm}^2/\text{s}$ ),  $E_a$  is the activation energy for diffusion ( $\text{kJ/mol}$ ), and  $R$  is the gas constant ( $8.314 \text{ J/mol}\cdot\text{K}$ ), increases as the sample is heated up to its final temperature. Consequently the time constant  $\tau$  specified in equation 2 and  $\gamma$  by equation 7 modify equation 8.

Figure 4 compares the normalized predicted outgassing rate with experimental data against time for the different coupon temperatures taking into account the changing diffusivity during the first 30 minutes.



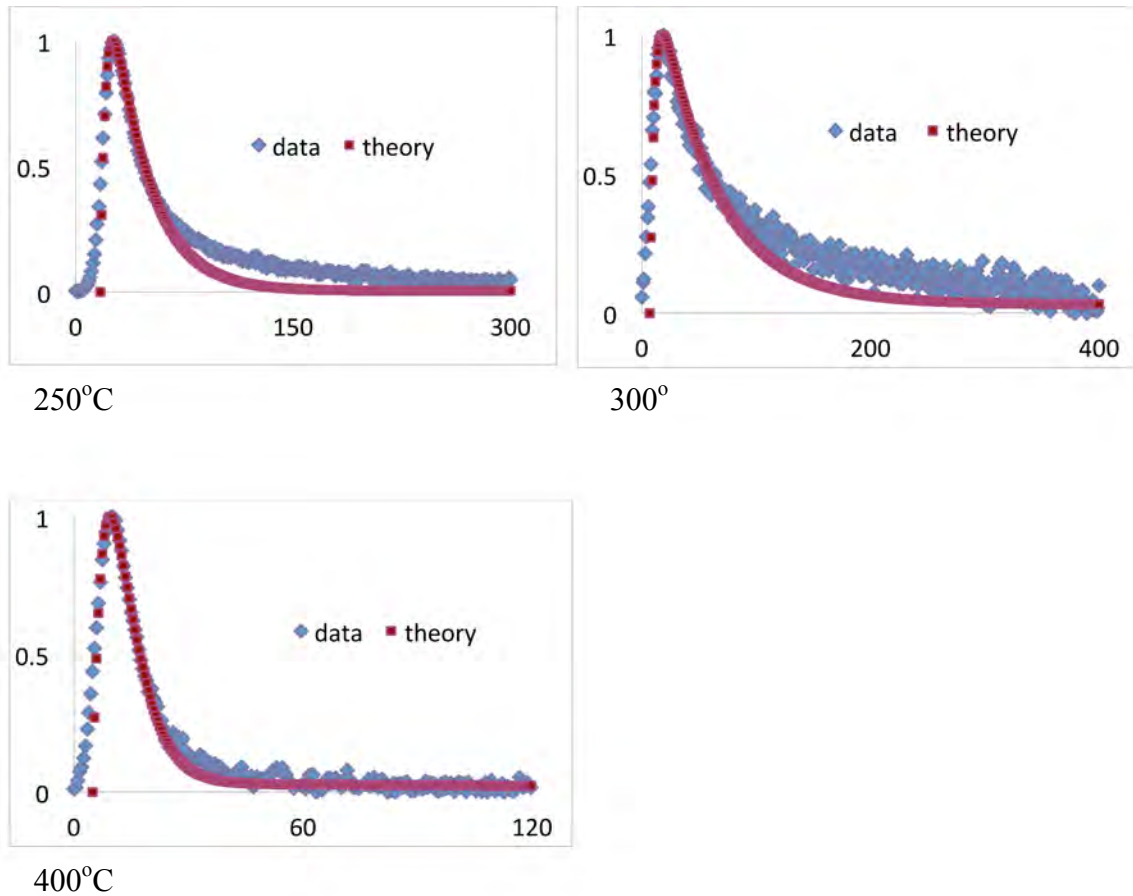


Figure 4: Comparison of normalized predicted outgassing rate with normalized experimental data against time in minutes for different coupon temperatures and accounting for the temperature dependence of the diffusivity.

As expected the fit between normalized prediction and experimental data improves noticeably during the first hour of each run in which the temperature is ramped above room temperature. The fit at longer times remains poor for the intermediate temperatures.

Figure 5 compares the diffusion coefficients calculated from the fits at each temperature to data published by Austin [8] and Tanabe [9, 10] for diffusion of tritium through bulk stainless steel (type 316). With the possible exception of the two data points at the highest temperatures investigated in this study, 300°C and 400°C, the magnitude and trend of the inferred diffusivities do not agree with literature values. The diffusivities

inferred from the tritium release at temperatures below 300°C do not follow the expected temperature behavior. The surface oxide must play an important role in restricting tritium mobility from the bulk to the air/metal interface. The decay time in equation 8 depends on both  $\tau$  and  $\beta$ , the former dependent on the  $l^2/D$  ratio and the latter on the purge rate through the decontamination chamber. If the purge rate remains fixed, the decay time in equation 8 will remain unchanged if the  $l^2/D$  ratio remains unchanged. If the diffusivity through the oxide layer dominates hydrogen transport and is assumed to be of the same order of magnitude as for stainless steel, then the oxide layer must be approximately 0.1  $\mu\text{m}$  at room temperature. Stainless steel typically has between 100 and 300 monolayers on its surface. Since each monolayer is approximately 0.3 nm thick, typical oxide thicknesses on stainless steel range from 0.03  $\mu\text{m}$  to 0.1  $\mu\text{m}$  in line with the estimate given above. The transport of hydrogen from the bulk through the oxide into the carrier must depend on the diffusivity through bulk metal and metal oxide in the temperature range 20°C and 300°C.

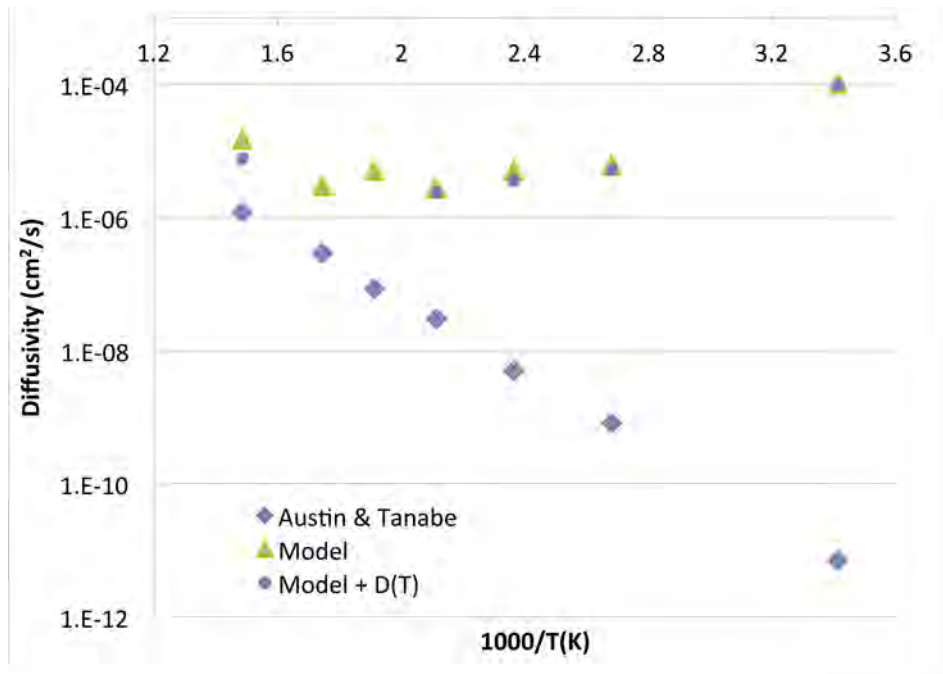


Figure 5. Plot of the tritium diffusion coefficient dependence on temperature of stainless steel

## Summary and Future Work

A simple model has been developed to describe the outgassing rate of tritium from a finite solid as a function of time. The model is based on the assumption that hydrogen transport through a homogeneous substrate can be characterized with a single diffusion coefficient. The model was used to fit experimental tritium desorption rates of tritiated type 316 stainless steel over a temperature range of 20 to 400°C. The model reproduces general features of the outgassing data. However, the diffusion coefficients inferred from the fitted curves do not agree with published data although the inferred values approach published values at the highest temperatures investigated. Additionally the model cannot accurately predict the experimental data over the entire desorption profile suggesting that the model using a single fit parameter cannot describe the processes of tritium desorption from stainless steel with an oxide layer.

A more comprehensive model is needed to describe tritium release accurately. This model should include three components:

- 1) desorption from the surface of the oxide layer,
- 2) diffusion through the oxide layer, and
- 3) diffusion through the bulk.

## References

1. San Marchi, C.; Somerday, B. P.; Robinson, S. L. Permeability, Solubility and Diffusivity of Hydrogen Isotopes in Stainless Steels at High Gas Pressure. *Inter. J. Hydrogen Energy*, 32, 100-116 (2007).
2. Causey, R. A., Karnesky, R. A., & San Marchi, C. (2011). "Tritium Barriers and Tritium Diffusion in Fusion Reactors". In R. J. M. Konings, & R. E. Stoller (Eds.), *Comprehensive Nuclear Materials* (Chapter 116). Elsevier. ISBN: 008056027X.
3. Antoniazzi, A.B., Shmayda, W.T., Surette, R.A., *Fusion Technol*, 21, 867, (1992)
4. Shmayda, W.T., Antoniazzi, A.B., Surette, R.A., Ontario Hydro Research Division, Report # 92-51-K, (1992)
5. Carslaw, H.S.; Jaeger, J.C.; *Conduction of Heat in Solids 2<sup>nd</sup> Ed.*, Clarendon Press: Oxford, England, 1959, p. 93
6. Penzhorn, R.-D.; Torikai, Y.; Naoe, S.; Akaishi, K.; Perevezentsev, A.; Watanabe, K.; Matsuyama, M., *Fusion Sci. Tech.* 57, 185 (2010).
7. Hollenberg, G.W.; Simonen, E.P.; Kalinin, G., *Fusion Eng. Design*, 28, 190 (1995).
8. Takeishi, T.; Nishikawa, M.; Katayama, K. *Fusion Eng. Design*, 61-62, 591 (2002).
9. Postolache, C.; Matei, L. *Fusion Sci. Tech.*, 48, 413 (2005).

10. Carslaw, H.S.; Jaeger, J.C. *Conduction of Heat in Solids*, 2<sup>nd</sup> Ed. Clarendon Press, Oxford, England. 1986. p. 93 – 96
11. Austin, J. H.; Elleman, T.S., *J. Nuc. Mater.*, 43, 119 (1972).
12. Tanabe, T.; Yamanishi, Y.; Sawasa, K.; Impto, S.; *J. Nuc. Mater.* 122 & 123, 1568 (1984).
13. Tanabe, T. *Fusion Eng. Design*, 10, 325 (1989).



**Testing and Installation of the Reticle Projector on OMEGA's Target Viewing System**

**Connie Jiang**

Brighton High School

LLE Advisors: Dr. Douglas Jacobs-Perkins, Mr. Raymond Huff

February 2011

**Abstract**

A reticle projector is an optical device that forms a calibration test pattern. This paper describes how a reticle projector was designed, built, and installed on the OMEGA Target Viewing System at the University of Rochester's Laboratory for Laser Energetics. In this design, a 780-nm infrared laser shines through a grid to a lens which forms the optical Fourier transform of a grid pattern (reticle) to create a periodic spot pattern. This pattern is re-imaged to a focal plane at the center of the target chamber so that it can be captured by each of five cameras in the Imager assembly on the opposite side of the target chamber. By projecting a common image onto all cameras simultaneously, one can measure relative magnification, image rotation, pattern registration, and distortion. The reticle projector was first tested in a laboratory setting where images were acquired, analyzed using MATLAB, and compared with synthesized images. Preliminary results suggest that this system meets the design objectives. This paper begins with an overview of the Target Viewing System, presents the design and analysis of the reticle projector and concludes with sample data and recommendations for future work.

## 1. Introduction – Overview of the Target Viewing System

The Target Viewing System (TVS) on the OMEGA laser is not only used for viewing the target; it also plays a large role in the feedback system ensuring correct placement of the target. In order to measure the position of objects in three dimensions, two viewing axes having an angular separation of approximately 90 degrees are required. Each view is composed of an Illuminator and an Imager. The Illuminator side consists of four dichroic mirrors that combine four LED colors and the reticle projector's infrared beam<sup>1</sup> (Fig. 1).

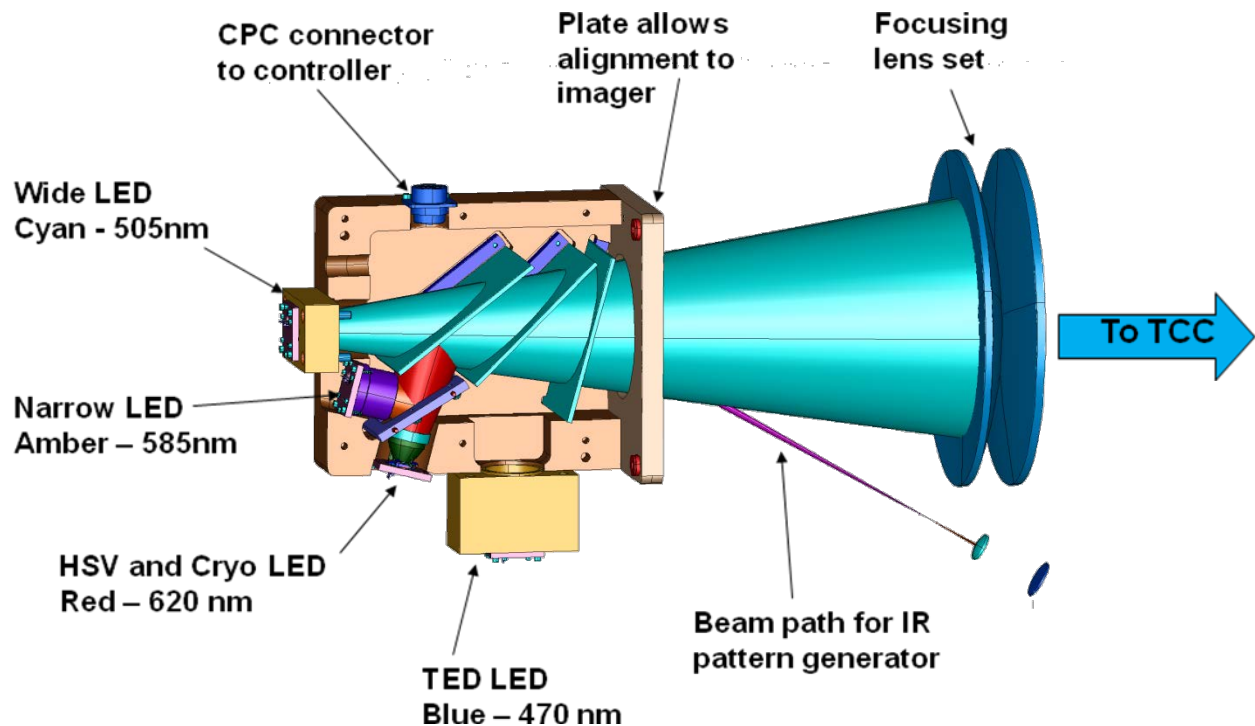


Figure 1: CAD (computer aided design) model of the Illuminator assembly. Four dichroic mirrors combine four LEDs and, with the addition of the reticle projector, a 780 nm infrared laser into a single beam heading towards the center of the target chamber. Each LED color corresponds to a camera on the Imager assembly.

The Imager side, on the other hand, consists of five cameras which each correspond to one of the LED colors in the Illuminator assembly (Fig. 2). The Narrow camera, used as the “master” camera, captures only amber light, for instance. Each camera has a different purpose.

<sup>1</sup> Source wavelengths: 470nm (blue), 505nm (cyan), 585nm (amber), 620nm (red), 780nm (infrared)

A problem can arise if these five cameras are not calibrated to each other. In the system before the reticle projector was installed, camera recalibration was very difficult.

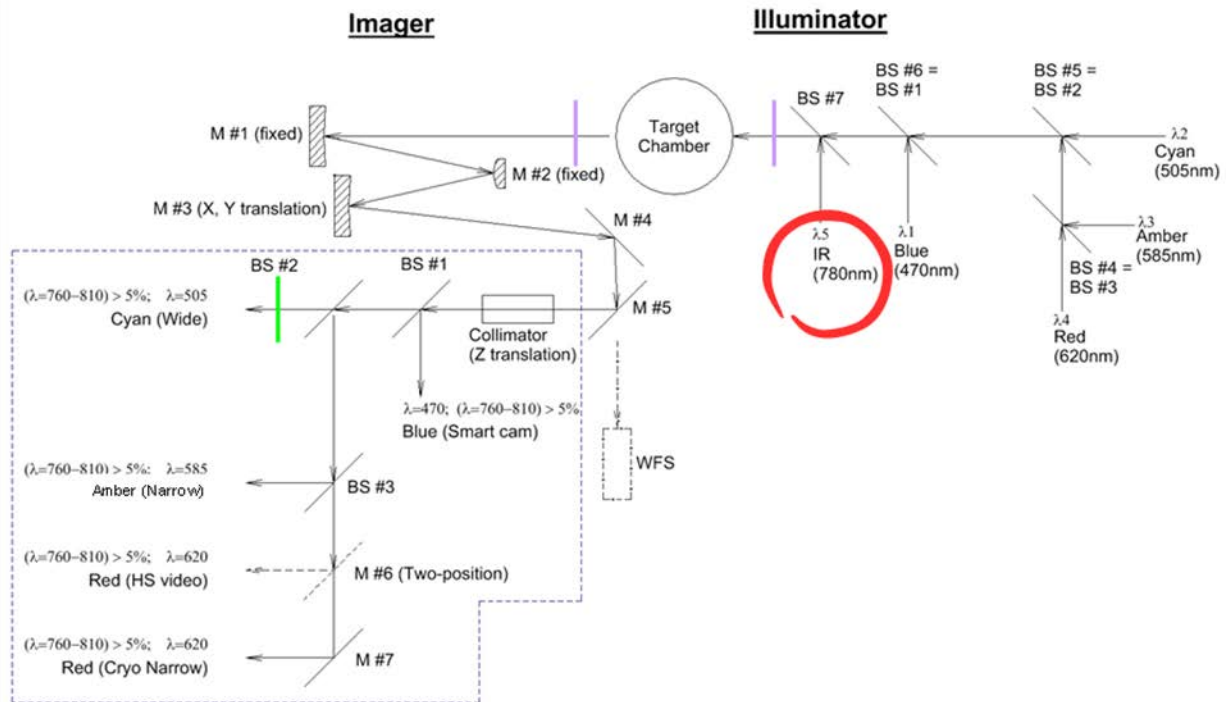
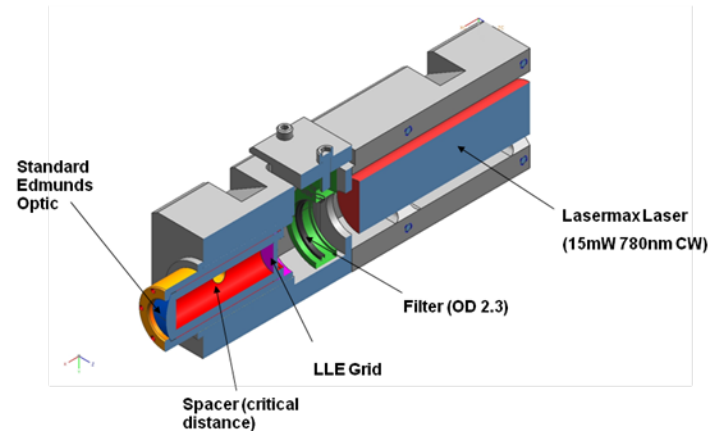


Figure 2: Schematic of the TVS. The circled IR source is the pattern generator, located in the Illuminator assembly. The combined beam propagates through TCC to the other side of the target chamber and the Imager assembly, where certain wavelengths of light are directed into each camera (the green line represents a Tiffen green filter that keeps the blue wavelength out of the wide-field camera). The purple lines are UV filters on either side of the target chamber.

## 2. Motivations and Design

The idea for the reticle projector was for it to simultaneously project a pattern onto all of the cameras in a single view. The resulting images could be matched to each other and would allow for cross-calibration relative to the Narrow-field camera. One way of accomplishing this would have been to put a grid in the center of the target chamber. This is possible; however, it is time consuming to load and insert the grid inside the vacuum chamber, and it requires special equipment and trained personnel. The reticle projector has the benefit of turning on/off with the flip of a switch (actually controlled by TVSII software), allowing calibration to be done at almost any time without special training.

In this design, a 15 mW, 780 nm continuous wave infrared laser is directed through an exchangeable filter and then through the grid, forming a grid pattern (Fig. 3). This grid pattern continues through a lens which takes the optical Fourier transform of the grid pattern to form a periodic spot pattern, which is re-imaged to a focal plane at the target chamber center (TCC), to be captured by each of the five cameras in the Imager assembly.



*Figure 3: Cross-section of the reticle projector. Key components include a 15 mW 780 nm continuous wave (CW) infrared laser, a filter, an LLE grid (the reticle), a lens barrel, and a plano-convex lens. The filter is used to reduce the optical output power to match camera sensitivity; currently both axes include filters of optical density 2.3.*

## 2.1 The Optical Fourier Transform

The Fourier transform, used in the formation of the pattern projected to target chamber center from the reticle projector, is a mathematical operation often used in digital image processing that breaks a signal up into its fundamental frequencies.

According to Fourier's theorem, any continuous function defined over some distance  $L$  can be synthesized by a sum of harmonic functions whose wavelengths are integral submultiples of  $L$ , (such as  $L/2$ ,  $L/3$ , ...); essentially, every curve can be exactly reproduced by superimposing simple harmonic curves on top of one another<sup>1</sup>.

Figure 4 is an example of a very basic optical Fourier transform setup. In this setup, parallel light is scattered into plane waves by a transparency in the front focal plane of a converging lens; these scattered waves are collected by the lens, and parallel bundles of rays converge at the back focal plane (the transform plane, marked by  $\Sigma_t$  in the schematic). If a

screen were to be placed there, the far-field diffraction pattern of the transparency would be imaged there<sup>2</sup>.

In the case of the reticle projector, a Fourier transform was taken of a reticle, or grid. Each individual grid section was 200  $\mu\text{m}$  (vertical) by 100  $\mu\text{m}$  (horizontal); the opaque section was 190  $\mu\text{m}$  by 90  $\mu\text{m}$ , leaving 10  $\mu\text{m}$  transparent on each side. The two sides were made unequal so that cross-calibration

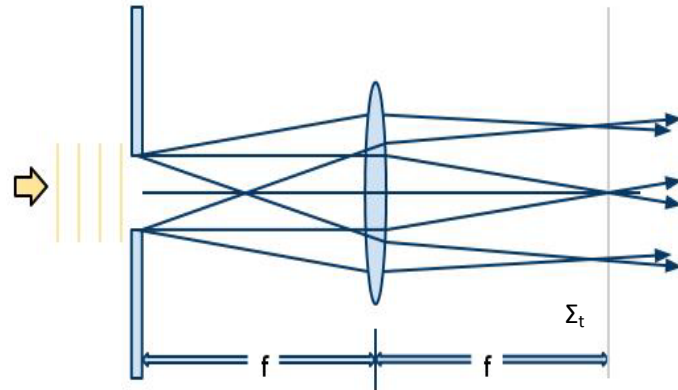


Figure 4: Schematic depicting a basic optical Fourier transform setup. Light diffracted by the transparency at the object focal point of a lens converges to form the far-field diffraction pattern at the image focal point of the lens.

later would be easier. MATLAB simulations were run and, using the repmat() function, were able to replicate the reticle. The Fourier transform was taken of this image in MATLAB to provide comparison for future experimental results (Fig. 5). The difference in side lengths manifest themselves in the Fourier transformation in that the higher spatial frequency of the 200  $\mu\text{m}$  sides lead to closer dot spacing in the transform plane than that of the 100  $\mu\text{m}$  sides.

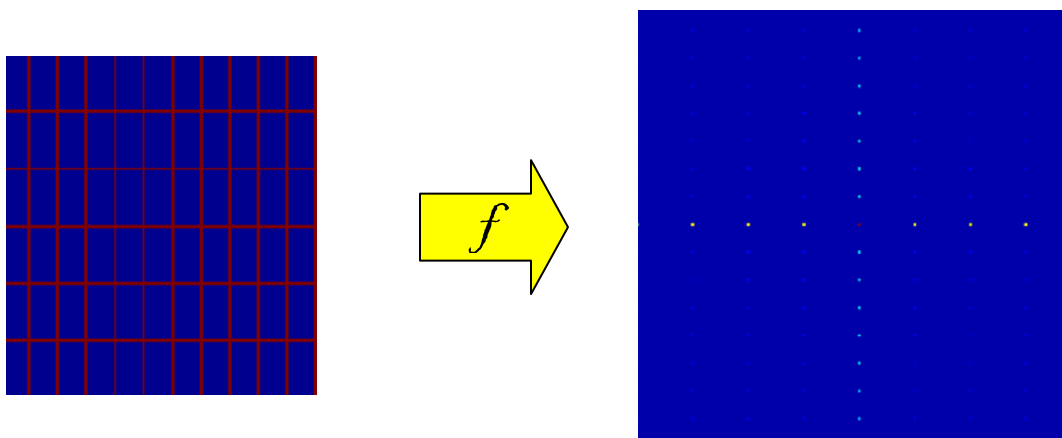


Figure 5: Simulation of reticle and Fourier transform of reticle taken in MATLAB. When the Fourier transform of the grid is taken, it forms a cross-shaped dot pattern; the spaces between dots are wider in the horizontal direction. The center dot is red because of its higher peak intensity; likewise, yellow is greater in intensity than blue.

Since the same pattern is to be projected onto each of the five cameras, images taken from each of them can be compared for magnification, image rotation, pattern registration, and possibly distortion. This comparison is made with respect to the Narrow-field camera because it has the finest optical resolution ( $5\ \mu\text{m}/\text{pixel}$ ) and no moving optics in the beam path (i.e. no focus adjustment). Calibration of the Narrow-field cameras must be done rigorously with certified calibration objects.

In this way the reticle projector will allow for individual calibration of the camera systems. Should a camera need to be replaced, it can be calibrated according to its own pattern of dots as well as the patterns displayed on the other cameras (particularly the narrow-field one, our designated control). The images can be compared and cross-calibrated and corrections can be made to camera placement so that all five images correspond to each other.

Also theoretically possible will be calibration of focus stage walk-off on future cameras. Because the optical axis has now been aligned to the current mechanical axis and the projection does not move, any further misalignment of the mechanical axis relative to the optical axis (perhaps due to the installation of a new camera) will be apparent and therefore adjustable.

There are a number of notable features in the design of both the projector and the pattern generator assembly in which it is housed. The lens barrel in the reticle projector adjusts independently within the lens assembly with relationship to the fixed laser and has a lock nut to keep it in place once the focus is found.

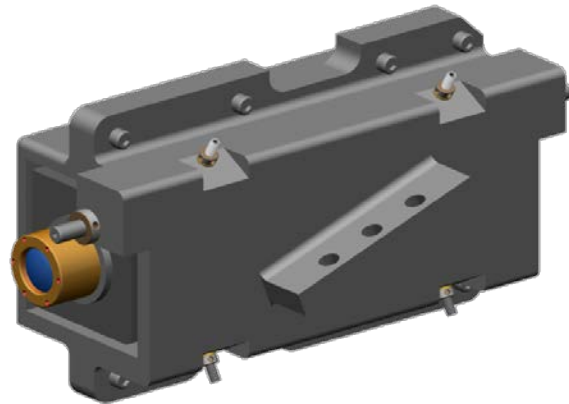


*Figure 6: Drawing of the pattern generator assembly. The reticle projector fits within the housing and is adjusted by the set screws located around the sides.*

The projector itself is also adjustable via 8 set screws in the pattern generator assembly: two sets of three fine-pitch set screws are set  $120^\circ$  apart, which can tip and tilt, and two

longitudinally mounted set screws help the system focus to TCC (Fig. 6). Altogether, this allows for  $\pm 1.6^\circ$  of travel.

There are additional ways to adjust the image projection once the pattern generator assembly is mounted. A mirror mount is adjustable for tip, tilt, and translation (and includes locking screws). This entire assembly mounts to the Extension Tube Weldment on the Illuminator assembly with spherical washers (Fig. 7).

Safety concerns in regards to the laser were addressed as well. The projector housing has no openings, so stray laser light cannot escape. An exchangeable filter in the reticle projector as well as a partially transmissive reticle

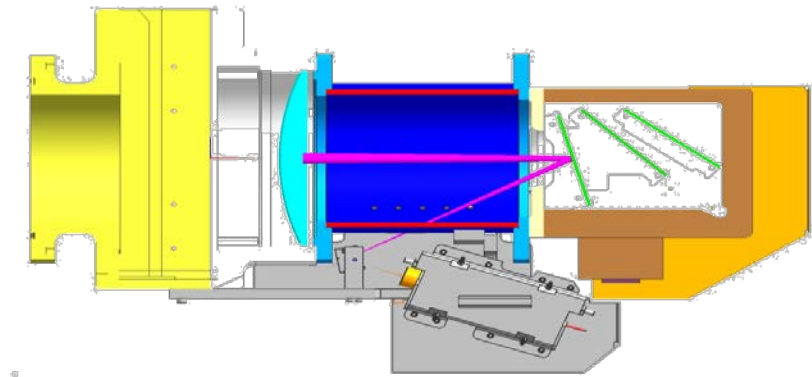


*Figure 7: Cross-section of the Illuminator assembly. The pattern generator assembly, in shades of grey, is mounted to the Illuminator. The beam emitted from the reticle projector is directed towards a dichroic beam splitter by a mirror mount.*

ensures that optical output power is set to the minimum practical level. Actual measurements show that the output of the laser with no filtration is 14.6 mW, the transmitted power through the reticle and lens is 2.65 mW (showing that the reticle is approximately 18% transmissive), and the output is 1.27  $\mu$ W with the additional filtration (of OD 2.3). While the laser may be turned on and off using a button control on the TVS Illumination dialog, a keyed power switch may be used to disable the laser when necessary to protect anyone working in the target chamber; a sheet metal cover was provided for this keyed on/off control for the laser to prevent accidental operation. Further safety measures include procedural measures (when the laser must be turned off, for instance) and the fact that all operators of the reticle projector must wear the proper laser safety eyewear.



The pattern generator is housed in the Illuminator assembly. The infrared light given off by the laser is directed towards a dichroic beam splitter that combines it with the LED beams (as shown in Figure 2). Unlike these colored beams, a fraction of the infrared (IR) laser beam reaches all five cameras. This is clearly shown when the beam splitter coatings are graphed in terms of what wavelengths they allow through. The same beam splitter coatings are used to combine the colors as to separate them (Fig. 8).

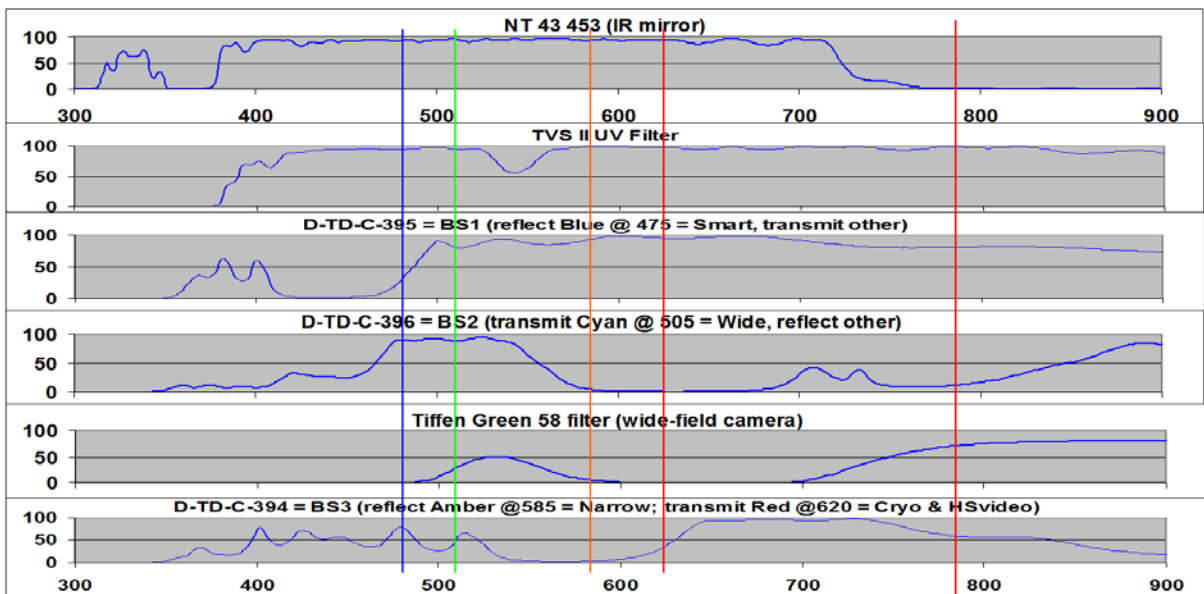


Figure 8: Transmission as a function of wavelength for the beam splitter coatings. The five vertical lines from left to right represent the four LEDs (blue, cyan, amber, and red) and the infrared source. The infrared source is completely reflected by the IR mirror and completely transmitted by the UV filter; once it reaches the beam splitters, however, some of it is transmitted and some is reflected each time.

We can use the graphs in Figure 8 and the schematic in Figure 2 to estimate the total amount of infrared light that reaches any of the cameras. For example, Figure 2 shows that to reach the Narrow-field camera, the infrared beam must be transmitted through the UV filter and BS1, reflected off BS2, and finally reflected off BS3 into the Narrow-field camera. Using Figure 8, then, we can estimate the actual percentage of light transmitted or reflected in each case; all of the infrared light is transmitted through the UV filter, but close to 20% is reflected off BS1, leaving 80% of the initial infrared beam. Then around 90% of the remaining light is reflected off BS2, leaving 72% of the initial beam. Finally, close to 45% of this light is reflected off BS3 into

the Narrow-field camera, meaning that approximately 32.4% of the original infrared beam is directed to the Narrow-field camera.

### 3. Testing and Image Analysis

After the reticle projector was built, it had to be tested in a laboratory setting before it could be installed onto the OMEGA laser system. Initial testing of the projector was conducted with a 632.8 nm Helium-Neon laser, though later on an actual 780 nm infrared laser was used. Sets of mirrors and extra lenses, as well as a SMART camera were used to take images in the laboratory.

Once images were taken, they had to be analyzed; in this way the lab testing generated a form of image analysis that was conducted using MATLAB functions and masking in order to evaluate individual spots. Figure 9 demonstrates how a mask was formed using binarization as well as erosion and dilation (noise-minimizing) techniques from the original image. This mask was then superimposed over the original image, allowing the analysis to focus solely on the brightest spots and the cross-shape, with

everything else set to zero: this is shown by the lineout taken of the masked image: the blue

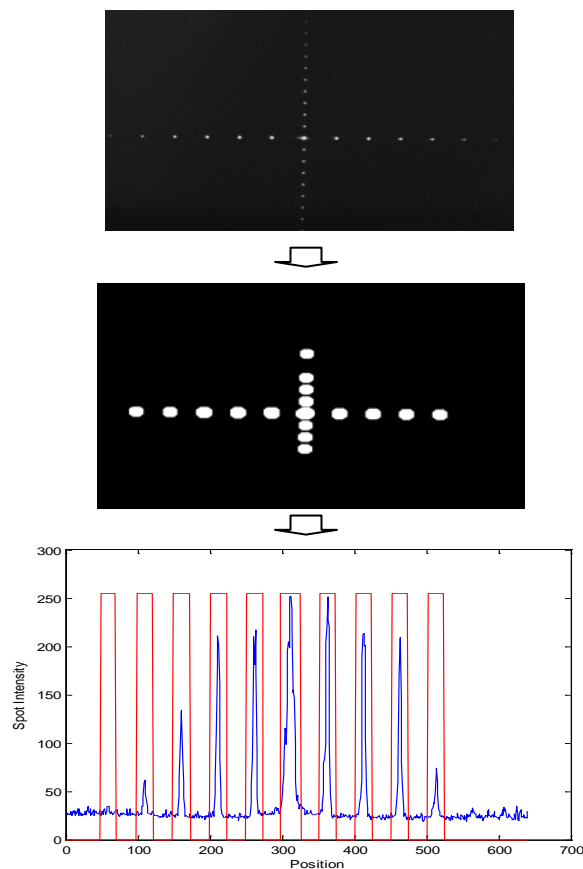


Figure 9: Diagram of the process of image analysis to extract peak intensities. The original image is used to form a mask which is then used to effectively cut out the noise from the original image so that only the brightest spots are analyzed. The graph at the bottom is a horizontal lineout going through the center dot; the blue is from the original image (intensities vary) while the red is from the mask.

represents the variation in intensity of the actual image, whereas the red is the mask; only the parts of the image that fall within the mask (the blue peaks within the red rectangles) are shown in the masked image.

Once the masked image is formed, comparison of radial distance, angular displacement, average distance between adjacent spots, spot area ratios, and peak intensity ratios allow for the examination of images and differences between images from different cameras.

Corresponding spots on images taken from different cameras are matched up with each other using spot area ratios and peak intensity ratios; in theory, the ratio of the central spot to any of the other spots will be the same on each camera. A ratio is used so that magnification does not matter. The center spot is determined by its high peak intensity and its centroid is set as the

center of the image, correcting for any shift in the image.

After corresponding spots are determined, radial distance from the center, angular displacement from normal, and the average distance between adjacent points are used to find any magnification or image rotation that might have taken place. These measurements can be used to graph the spot centroids onto a polar plot (Fig. 10).

This graphing of the spot pattern makes it easier to see angular as well as radial displacement from the center.

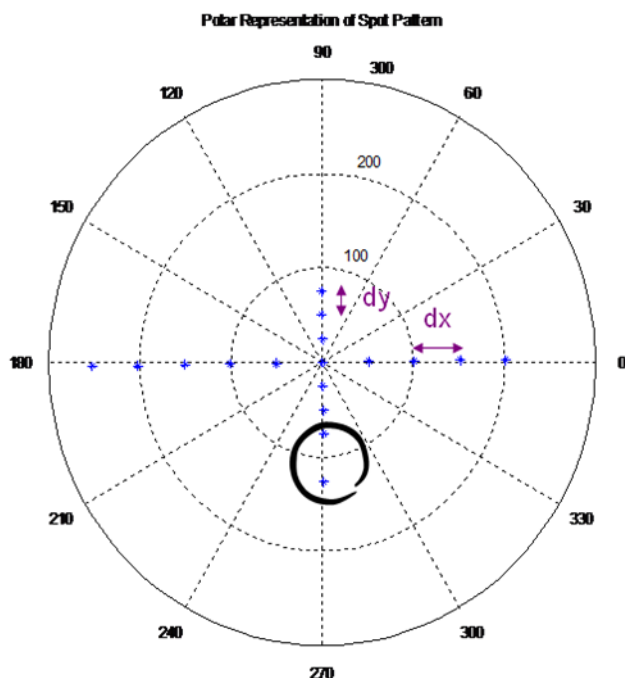


Figure 10: Polar representation of reticle projector spot pattern, as seen at TCC. Average distances are indicated by "dy" and "dx" and are taken because occasionally spots are not captured on the camera, as indicated by the black circle.

#### 4. Installation and Alignment of the projector on OMEGA

After the projectors (one for each axis) were assembled and tested in the lab and cleared for safety features, the next logical step was to mount them onto the OMEGA TVS. The Y-axis reticle projector was installed on August 9, 2010, and the X-axis one was installed a couple of weeks later, on August 20, 2010. Pointing and centering were used to align optics to the wide-field camera over the full travel of its focus stage by first moving it 20 mm towards TCC and aligning it, and then moving it back and aligning it and repeating, so that the end result was an image that does not shift when the camera moves along its focus stage.

Once the optic axis was aligned to the mechanical axis motion, the image itself had to be focused at TCC. This was accomplished using the set screws in the pattern generator as well as the mirror mount in the full assembly. Ultimately, the X-axis reticle projector was pretty much in focus at normal camera position, but the Y-axis reticle projector was focused at a +20 mm focus stage position on the wide-view camera (20 mm away from TCC). It has since been fixed.

Images were then taken of the aligned patterns (Fig. 11).

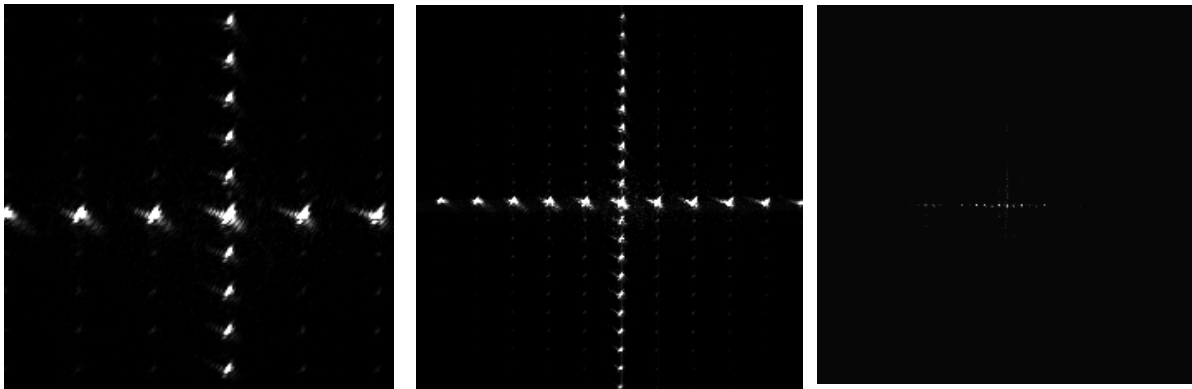


*Figure 11: Images taken from the X-axis reticle projector. From left to right, these images were taken from the Cryo Narrow camera, the Narrow-field camera, and the Wide-field camera. The field of view size increases from left to right (Cryo has a field of view of 5 mm x 5 mm, Narrow has 10 mm x 10 mm, and Wide has 50 mm x 50 mm); all are used for different purposes.*

These images, taken from the X-axis reticle projector, look much like the MATLAB-simulated one above in the dot pattern and spacing. The pattern seems to be almost perfectly

cross-shaped, and the vertical spacing is closer than the horizontal spacing (as it should be). A notable difference is in saturation and spot area; the simulated image is controlled so that each spot takes up one pixel. With the actual images, however, each spot takes up a different area depending on its proximity to the center, brightest spot.

Ghost reflections are seen in these images as well (some of what looks like blurring from afar are actually reflection spots). These occur because there is some internal reflection at each surface which causes superpositioning of the ghost reflection on top of the actual image.

At the same time, these images seem to be experiencing some saturation, evidenced by the blooming of the spots. Less blooming is seen across the vertical spots because they are less intense than the horizontal ones. This image is focused particularly well, as even the dim spots in the quadrants are visible; however, these spots may disappear under further filtration. In order to see these spots, the incident intensity must be quite high (part of what causes the blooming). In any case, they are not included in the current analysis process.

## **5. Future**

The reticle projector seems to be fine for its current purposes. It is able to project an image onto each of the five cameras, and these images are comparable. In Figure 11 above, it appears that the three cameras used (Cryo Narrow, Narrow, and Wide) are reasonably cross-calibrated; the pattern is imaged at roughly the same location on each of them.

More work needs to be done, however, to make sure this remains a useful tool. As of yet it can be difficult to tell, when something is out of focus, whether it is out of focus because the distance between the camera and image (at TCC) is too large or too small.

Preliminary images suggest that perhaps there is some distortion on the Y-axis cameras (Fig. 12). Each spot appears to be the superposition of multiple spots, possibly caused by surface reflections that were not included in our simulations. Both the MATLAB simulations as well as images taken from the X-axis cameras suggest that the axes should be orthogonal and

the spots relatively circular and clearly defined; neither is the case in these Y-axis images.

Information from these images is being used to help understand the source of this distortion and determine how to remove or compensate for it.

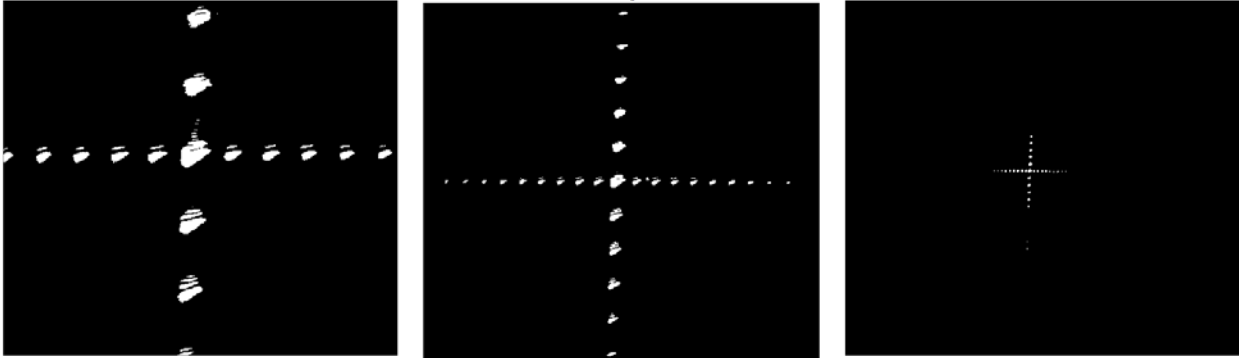


*Figure 12: Images taken from the Y-axis reticle projector.* These images are taken from the corresponding cameras on the Y-axis as the images of Figure 11 (Cryo Narrow, Narrow, and Wide). On these, however, it is apparent that the images have been rotated  $90^\circ$  relative to the images in Figure 11 (the axes are tilted so that the horizontal spots are closer together), and the axes themselves are not orthogonal. The fact that there are extra reflected spots suggests that something may be wrong with the cameras (and/or other optics in the beam path).

Though these images do not contain enough information to determine the source of the reflections, the overlapping suggests that perhaps they come from a thin plano optic, such as the cover glass used to protect a camera sensor; however, because the reflections are visible on all cameras, they are more likely to be caused by one or more of the beam splitters shared by the cameras. Because the reflections overlap, they most likely do not come from a lens or other curved surface because such reflections would diverge instead. At the same time, these ghosts should not interfere with the intended use of the cameras, as the distortion is displayed in all five of the cameras; they can still be cross-calibrated.

Although currently there are only plans to use the reticle projector as a calibration and diagnostic tool, useful for cross-calibration of the cameras, the projector may also be used to detect distortion. The image analysis conducted in this project focused only on the brightest cross of spots in the pattern; however, the spots within the quadrants may aid in detecting distortion.

## **Conclusion**

The reticle projector was designed, built, and installed onto the Illumination side of the target viewing system of the OMEGA laser system. In it, a 780 nm infrared laser shines through a reticle and then passes through a series of lenses, focusing a Fourier transform image at TCC. This image is then captured by the cameras located on the Imager assembly on the opposite side of the target chamber. Because the pattern will likely have some distortion or defining features, and the projector is not physically in the target chamber, this system is useful in identifying corresponding spot patterns on the different camera images as well as any differences in magnification, rotation, or pattern registration, as well as distortion. This will enable periodic recalibration of the cameras. The reticle projector was first tested in a laboratory setting where images were taken, compared, and analyzed using MATLAB. Preliminary results suggest that this system is capable of detecting discrepancies in camera rotation, magnification, distortion, and misalignment between cameras. Though it is meant to be primarily a calibration and diagnostic tool, other uses for it may be apparent in the future.

## **Acknowledgements:**

I would like to thank Dr. Craxton for inviting me to the summer program and my advisors Dr. Jacobs-Perkins and Mr. Huff for all the support they have given me throughout the project and beyond. I would also like to acknowledge all of the people who helped me complete this project including Ethan Burnham-Fay, Frank Ehrne, Nermina Mahmutovic, Marcia Barry, Tim Flannery, Diana Coppenbarger, Andrew Sorce, Lance Lund, Tim Duffy, and Richard Fellows.

**References:**

1. "Optical Processing." Football Physics. Web. 31 Jan. 2011.  
<<http://electron9.phys.utk.edu/optics421/modules/m6/opticalprocess.htm>>.
2. Hecht, Eugene, and Alfred Zajac. Optics. 2nd ed. Reading, MA: Addison-Wesley Pub., 1987. Print.



**Imploded Shell Parameter Estimation Based on Radiograph Analysis**

George Liu

Pittsford Sutherland High School

LLE Advisor: Reuben Epstein

**Laboratory for Laser Energetics**

University of Rochester

Summer High School Research Program

March 21, 2011

**Abstract**

High target density is an important condition for achieving ignition in direct-drive fusion experiments. High densities are momentarily created during a successful implosion. The OMEGA laser's 60 beams heat the target, causing the surface to ablate and compress the fusion fuel.<sup>1</sup> X-ray radiography is used to analyze the compressed target's optical thickness, which in turn describes the target's density. The higher the optical thickness, the darker the shadow cast. By recording the intensity of the backlighter x rays across the radiograph, the radiograph gives an attenuation profile. In a simple model of the shell, the changing attenuation across the radiograph depends on three parameters: inner radius, outer radius, and central radial optical thickness. A FORTRAN program was created to calculate the variances of the estimates of these three parameters in the presence of measurement error and a finite number of attenuation measurements limited by the finite resolution of the imaging device. Choosing the optimum optical thickness for the target by adjusting the backlighter photon energy minimizes the uncertainties of these estimates.

**Introduction**

The Laboratory for Laser Energetics uses two laser systems, OMEGA and OMEGA EP, to irradiate target capsules in inertial confinement fusion (ICF) experiments.<sup>1</sup> If the target reaches temperatures and densities high enough, it can achieve ignition, a condition during which fusion produces enough energy to sustain itself. The target does not always compress properly, however, due to imperfections in the spherical shell. To analyze and improve upon future direct-drive experiments, it is important to have diagnostics that can track the target capsule compression. X-ray radiography is one such diagnostic.

The density of the target can be measured indirectly by measuring the target's optical thickness  $\tau$ , a description of the target's ability to absorb x-ray radiation. When the target absorbs x rays, a shadow is formed on the radiograph. By analyzing the shadow it is possible to estimate the optical thickness of the target. Estimation however always possesses some uncertainty. Measurement precision is limited, the x-ray framing camera has finite resolution, and other uncertainties may exist in the source of the backlighter, such as nonuniformity. For free-free radiography, the target's optical thickness varies with the photon energy of the penetrating x rays. This allows one to select the backlighter photon energy that provides the optimum shell optimal thickness, which creates a radiograph with a contrast profile that will allow the most precise model parameter estimates to be obtained. The central radial optical thickness  $\tau_0$ , which is half the optical thickness of the imploded target viewed through its center, was chosen as the measure of the target's optical thickness. The value  $\tau_0 = 0.5$  provides a unit central optical thickness that is the optimal value for a uniformly thick slab. To find the optimal optical thickness of a spherical capsule, whose optical thickness varies over the radiograph plane, a FORTRAN program was designed to calculate the parameter estimate uncertainties of a simple spherical shell capsule using covariance analysis based on hypothetical data. The dependence of the parameter estimate uncertainties on the central optical thickness was found and is shown below.

### **Parameter Estimation Uncertainty**

The backlighter energy must be carefully selected to produce a useful radiograph. Information is lost if the backlighter produces too high or low an optical thickness. A high optical thickness (saturation) creates a dark shadow that allows only the outer edge of the shell to

be seen, while a low optical thickness (transparency) lets nearly all the x rays pass through, offering too low a contrast for the actual transmission contrast to be distinguished from the noise level  $\sigma_I$ . By modifying the target's optical thickness to produce shadows with distinct edges at both the inner and outer shell radii, it is possible to reduce the uncertainty in the parameter estimates.

### The Radiograph Model and Optical Thickness

The radiograph model is a simplified representation of an imploded target shell and the x-ray intensity attenuation profile seen in its radiograph. Figure 1 shows a simple schematic of the radiography setup for a target shell that is assumed to be perfectly spherical and homogenous. Parallel x rays of intensity  $I_0$  pass through the hollow target at various distances  $r$  from the capsule center and strike the radiograph plate with diminished intensity  $I$ . An actual radiography configuration of an experiment is more complicated because the target may not be uniform, homogenous, and spherical, and the backlighter rays selected by the imaging device may not be parallel. Nevertheless, this model provides a simple and relatively accurate representation that suffices for the purposes of this analysis.

The x-ray attenuation through the target is captured as the shadow on the radiograph and can be compared to the theoretical attenuation given by

$$I(r) = I_0 e^{-\tau(r)}, \quad (1.1)$$

where  $\tau(r)$  is the optical thickness,<sup>2</sup> defined as the integral of the opacity  $\kappa$ , a function of spherical radius  $\rho$ , along the path  $s$

$$\tau(r) = \int \kappa(\rho) ds. \quad (1.2)$$

Equation (1.1) ignores the effects of self-emission, the radiation emitted by the target, effectively assuming that the backlighter intensity  $I_0$  is large in comparison to the self-emission. When the initial x-ray intensity  $I_0$  and final intensity  $I$  are known, Eq. (1.1) can yield  $\tau(r)$ . The optical thickness can be calculated for every planar radial distance  $r$  to create an optical thickness profile  $\tau(r)$ . It is important to distinguish between the radii  $r$  and  $\rho$  in Eq. (1.2). The variable  $r$  is the radial coordinate in the plane of the radiograph, and  $\rho$  is the target-centered spherical radial coordinate at a point along the x-ray path. The variable  $r$  is planar while  $\rho$  is in 3-D space (see Fig. 1).

If the target's opacity is assumed to be uniform and if the x-ray path is assumed to be a straight line, Eq. (1.2) simplifies to the product of opacity and x-ray path length through the target:

$$\tau(r) = \kappa s(r), \quad (1.3)$$

where  $s$  is the straight-line x-ray path length as a function of radius  $r$  in the image plane. The path length function can be expressed as three separate path length functions for three sections of the radiograph: where the x-ray travels through the shell and hollow, travels through the shell only, and misses the capsule entirely (see Fig. 1). Substituting the appropriate expressions for each condition of  $s$  yields the piece-wise function

$$\tau(r) = \begin{cases} 2\kappa \left( \sqrt{R_2^2 - r^2} - \sqrt{R_1^2 - r^2} \right) & \text{if } 0 < r < R_1 \\ 2\kappa \left( \sqrt{R_2^2 - r^2} \right) & \text{if } R_1 < r < R_2 \\ 0 & \text{if } r > R_2 \end{cases}, \quad (1.4)$$

for a target capsule with inner radius  $R_1$  and outer radius  $R_2$ .

## Methodology

Parameter estimate uncertainties were found using the weighted least-squares method. In this method, measurement errors are assumed to fall in a normal distribution, and the model, Eq. (1.4), is assumed to predict the correct values of  $\tau(r)$  for the correct values of the parameters  $\kappa$ ,  $R_2$ , and  $R_1$ . The most likely values of these parameters, based on a set of  $N$  measurements  $I_{obs,i}$  at radius  $r_i$  with a random error  $\sigma_i$ , are those that minimize  $\chi^2$ , the weighted sum of the measurement errors, which is given by

$$\chi^2 = \sum_{i=1}^N \frac{(I_{obs,i} - I(r_i))^2}{\sigma_i^2}, \quad (1.5)$$

where  $i$  is one of  $N$  measurements with random measurement error known as “variance”  $\sigma_i^2$ . The observed measurements  $I_{obs,i}$  are readings from the experiment, and the predicted measurements  $I(r_i)$  are the corresponding theoretical values obtained from the model.<sup>3</sup> For a model with  $M$  unknown parameters, collectively described as  $\{x_j; j = 1, M\}$ , the minimization of Eq. (1.5) is obtained when the partial derivative equations with respect to each parameter  $x_j$  equal zero:

$$\frac{\partial \chi^2}{\partial x_j} = 0. \quad (1.6)$$

The intensity model from Eq. (1.1), with  $\tau$  replaced by its subcomponents given in Eq. (1.4), attempts to fit, using  $M = 3$  parameters,  $\kappa$ ,  $R_2$ , and  $R_1$ , an intensity model to a set of  $N$  intensity readings from a radiograph experiment with an uncertainty  $\sigma_i = \sigma_I$  for each intensity measurement. The model has three partial derivative equations that must be set to zero to minimize  $\chi^2$ :

$$\frac{\partial \chi^2}{\partial x_1} = \frac{\partial \chi^2}{\partial \kappa} = 0, \quad (1.7)$$

$$\frac{\partial \chi^2}{\partial x_2} = \frac{\partial \chi^2}{\partial R_2} = 0, \quad (1.8)$$

$$\frac{\partial \chi^2}{\partial x_3} = \frac{\partial \chi^2}{\partial R_1} = 0. \quad (1.9)$$

This set of equations can be written in matrix notation as

$$\sum_{i=1}^M \mathbf{J} \Delta \mathbf{x} = \mathbf{r}, \quad (1.10)$$

where the coefficient matrix  $\mathbf{J}$  is a square matrix of length and width  $M$ , and  $\Delta \mathbf{x}$  and  $\mathbf{r}$  are both vectors of length  $M$ . The coefficient matrix  $\mathbf{J}$  is given by

$$J_{jl} = \sum_{i=1}^N \frac{1}{\sigma_I^2} \frac{\partial I(r_i)}{\partial x_j} \frac{\partial I(r_i)}{\partial x_l}. \quad (1.11)$$

The residual vector  $\mathbf{r}$  is found in a similar manner by

$$r_j = \sum_{i=1}^N \frac{1}{\sigma_I^2} \frac{\partial I(r_i)}{\partial x_j} (I_{obs,i} - I(r_i)). \quad (1.12)$$

The residual vector  $\mathbf{r}$  is multiplied with the inverse of  $\mathbf{J}$  to produce the set of corrections  $\Delta x_j$  that, when added to the set of parameter estimates  $x_j$ , give a better set of parameter estimates. The improved parameter estimates are then used to calculate a new  $\chi^2$ , and the process is repeated to find a new set of corrections. The process is iterated until the corrections become negligible, at which point  $\chi^2$  may be considered to have been minimized.

In planning an experiment in the absence of actual experimental measurements, the weighted least-squares method still provides formal estimates of the uncertainties of the parameter estimates.<sup>3</sup> It can be shown that the variances of the parameter estimates,  $\sigma_K^2$ ,  $\sigma_{R_2}^2$ , and  $\sigma_{R_1}^2$ , defined as the expected value of the squared difference between the parameter estimates

and their true values, are given by the diagonal elements of the inverse of the coefficient matrix  $\mathbf{J}$ ,

$$\sigma_i^2 = J^{-1}_{ii}. \quad (1.13)$$

This new matrix is referred to as the covariance matrix  $\mathbf{J}^{-1}$ .<sup>3</sup>

The covariance matrix yields the uncertainty of the parameter estimates as the variances  $\sigma_\kappa^2$ ,  $\sigma_{R_2}^2$ , and  $\sigma_{R_1}^2$ , which describe the uniqueness of the model's fit to the data. The variances scale directly with the factor  $\sigma_I^2/N$  and roughly inversely with the square of the model's sensitivity to their respective parameters, as given by Eqs. (1.7) - (1.9) and suggested by Eq. (1.11).<sup>3</sup> Low uncertainty estimates indicated by small values of  $\sigma_{R_1}$ ,  $\sigma_{R_2}$ , and  $\sigma_\kappa$  suggest that the parameter estimates can be accepted with greater confidence, while high uncertainty estimates suggest that the fit of the model to the data does not have a unique solution and that different sets of values of the parameters may fit the data comparably well. When  $\sigma_{R_1}$ ,  $\sigma_{R_2}$ , and  $\sigma_\kappa$  are high, it is difficult to claim that the exact values of  $R_1$ ,  $R_2$ , and  $\kappa$  have been estimated correctly.

### **Difficulties in Partial Differentiation**

The weighted least-squares method relies extensively on partial derivatives of the intensity model to obtain  $\mathbf{J}$  from Eq. (1.11). Due to the circularly symmetric nature of the radiograph data, it is not necessary to sum the partial derivative of every individual data point in assembling the coefficient matrix. Instead, a radial line of points from  $r = 0$  to  $r = R_2$  can give a close approximation for the summation by weighting each point to account for all other points of similar radial distance from the center. If each point is thought of as an arc segment, the circular radiograph can be partitioned into thin rings of width  $\Delta r$  such that any given ring will consist of a number of congruent segments given by



$$N_r = \frac{2\pi r}{\Delta r}, \quad (1.14)$$

where  $r$  is the ring's radial distance from the center, and  $N_r$  is the number of slices that “weights” the partial derivative of a single slice in the ring. The total number of measurements,  $N$ , is the sum of  $N_r$  over all the rings.

The finite-segment approximation of each data point also helps resolve conflicts in differentiation that arise when the radiograph readings are assumed to occupy an infinitesimal area. Taking the partial derivative of Eq. (1.1) with respect to each parameter yields

$$\frac{\partial I}{\partial \kappa} = -2(L_2 - L_1)e^{-2\kappa(L_2-L_1)}I_0, \quad (1.15)$$

$$\frac{\partial I}{\partial R_2} = \frac{-2\kappa R_2}{L_2}e^{-2\kappa(L_2-L_1)}I_0, \quad (1.16)$$

$$\frac{\partial I}{\partial R_1} = \frac{-2\kappa R_1}{L_1}e^{-2\kappa(L_2-L_1)}I_0, \quad (1.17)$$

where

$$L_1 = \begin{cases} \sqrt{R_1^2 - r^2} & \text{if } 0 < r < R_1, \\ 0 & \text{if } r > R_1 \end{cases}, \quad (1.18)$$

$$L_2 = \begin{cases} \sqrt{R_2^2 - r^2} & \text{if } 0 < r < R_2. \\ 0 & \text{if } r > R_2 \end{cases}. \quad (1.19)$$

The partial derivatives given by Eq. (1.16) and Eq. (1.17) contain  $L_1$  and  $L_2$  in the denominator, which cause predicted partial derivative values near  $r = R_1$  and  $r = R_2$  to approach negative infinity. This is due to the piecewise nature of optical thickness in Eq. (1.4) which is embedded in the intensity model from Eq. (1.1) (see Figure 1). Trapezoidal approximations were used to estimate the partial derivatives at non-differentiable points.

The trapezoidal method assumes that the partial derivative of the intensity model changes at a constant rate across the width of a data point. The partial derivative can be approximated by averaging the partial derivatives of two neighboring points around the non-differentiable point. This method was used to calculate the partial derivative of Eq. (1.1) with respect to  $R_1$  at  $r = R_1$ , where the partial derivative encounters a vertical asymptote. The approximation works because the data points are discrete with finite differences in their intensity values. By measuring the average partial derivative, one obtains a reliable estimate that may be used in Eq. (1.11).

### **Parameter Estimation from Radiograph Model**

The FORTRAN program uses covariance analysis to calculate the uncertainty of the estimates of the three parameters  $R_1$ ,  $R_2$  and  $\kappa$  from the uncertainty of the hypothetical intensity measurements, which is equal to the intensity noise  $\sigma_I$ , and the spatial resolution, as expressed by the number of data points  $N$ . The variance calculation for each parameter was scaled to account for differences in resolutions and intensity variances of radiographs. The scaled variance multiplies the initial variance with the square root of  $N$  divided by the relative  $\sigma_I$  squared to divide out the effects of sample size and noise. The variance is also expressed as a ratio relative to the parameter estimate because the effects of uncertainty must be considered proportionally. Each is plotted against the central optical thickness  $\tau_0$ , which was defined as  $\tau_0 \equiv \frac{1}{2} \tau(0)$  to describe the path of travel along half the target diameter.

The graph of optical thickness variance in Fig. 2 shows a broad minimum near  $\tau_0 \approx 0.5$  where the scaled optical thickness variance is minimized. The rapid increase of the variance as  $\tau_0$  increases or decreases suggests that departures from  $\tau_0 \approx 0.5$  can result in significant degradation of the estimates. Even as the ratio of inner to outer radii changes, the minima of the

three plots remain approximately the same. The graph appears to support the initial proposed optimal central optical thickness of  $\tau_0 \approx 0.5$  that applies to a uniformly thick slab.

The graphs of the scaled inner and outer radius variances in Fig. 3 show the same minimum near  $\tau_0 \approx 0.5$  as seen in Fig. 2. The curves plotting the inner radius variance (“Radius 1 variance”) have minima at slightly below  $\tau_0 \approx 0.5$ , and the graph of outer radius variance (“Radius 2 variance”) continues to decrease past the minimum range, suggesting that departures above  $\tau_0 \approx 0.5$  are safe for estimating the outer radius. This is because as the central optical thickness  $\tau_0$  increases, the outer shadow edge gets sharper. The graph of scaled opacity variance behavior in Fig. 4 is similar to the inner radius variance behavior, and further supports the optimal optical thickness calculation.

The graph in Fig. 5 shows the same results as Fig. 2 but with a linear vertical axis and logarithmic horizontal axis, showing more clearly the degradation when  $\tau_0$  is small and allowing it to be compared with comparable degradation at higher  $\tau_0$  values, where degradation due to saturation comes on rapidly. These results suggest that the degradation at lower optical thicknesses,  $\tau_0 \lesssim 0.1$ , such as in Compton radiography, may still be feasible in spite of the  $\tau_0$  value being off the optimum value, and that even stronger degradation is obtained with only modestly high optical thickness,  $\tau_0 \gtrsim 1.0$ . Fig. 2 offers less comparison between small and large  $\tau_0$  uncertainty estimates because the  $\tau_0$  scale is compressed at small  $\tau_0$ .

## Conclusion

Covariance analysis of hypothetical data with a simple, idealized model confirmed the optimum central radial optical thickness  $\tau_0 \approx 0.5$  for the radiography of a perfectly spherical and homogenous imploded target in inertial confinement fusion experiments. The parameters

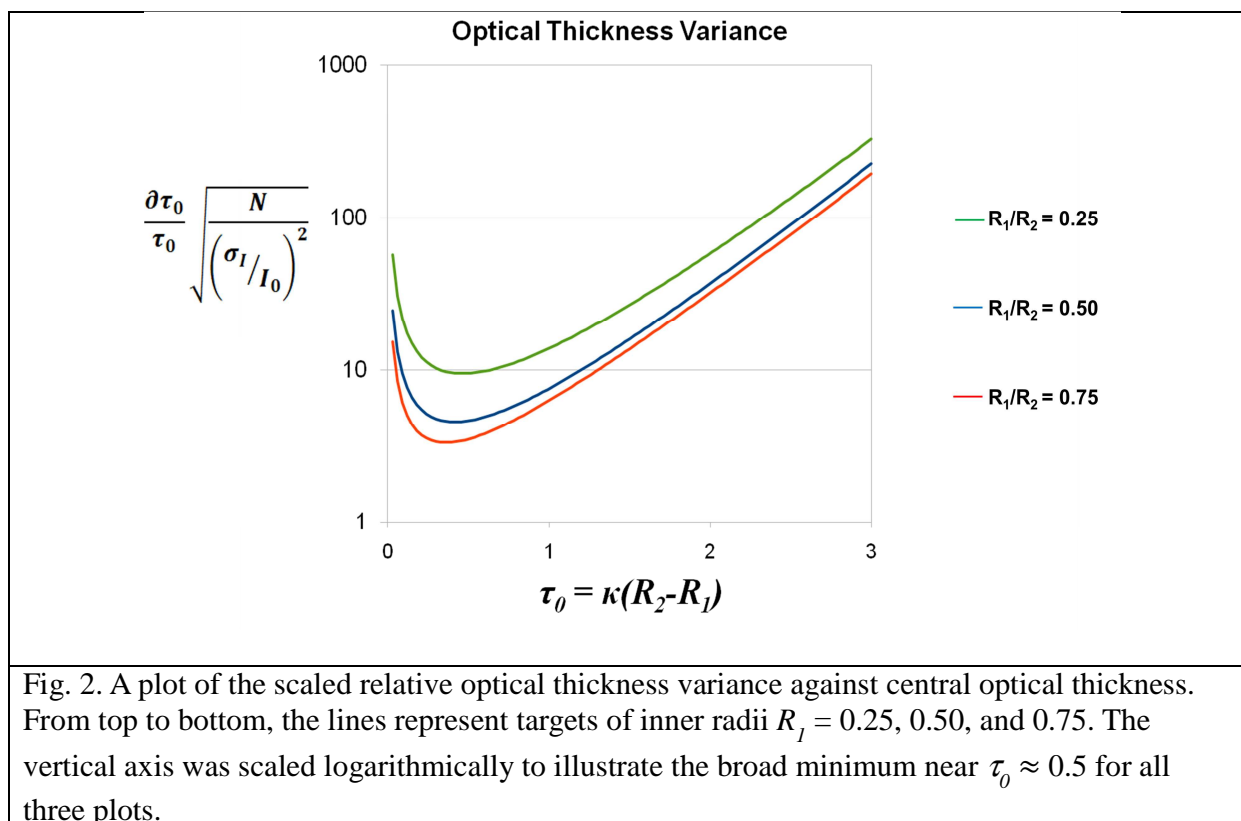
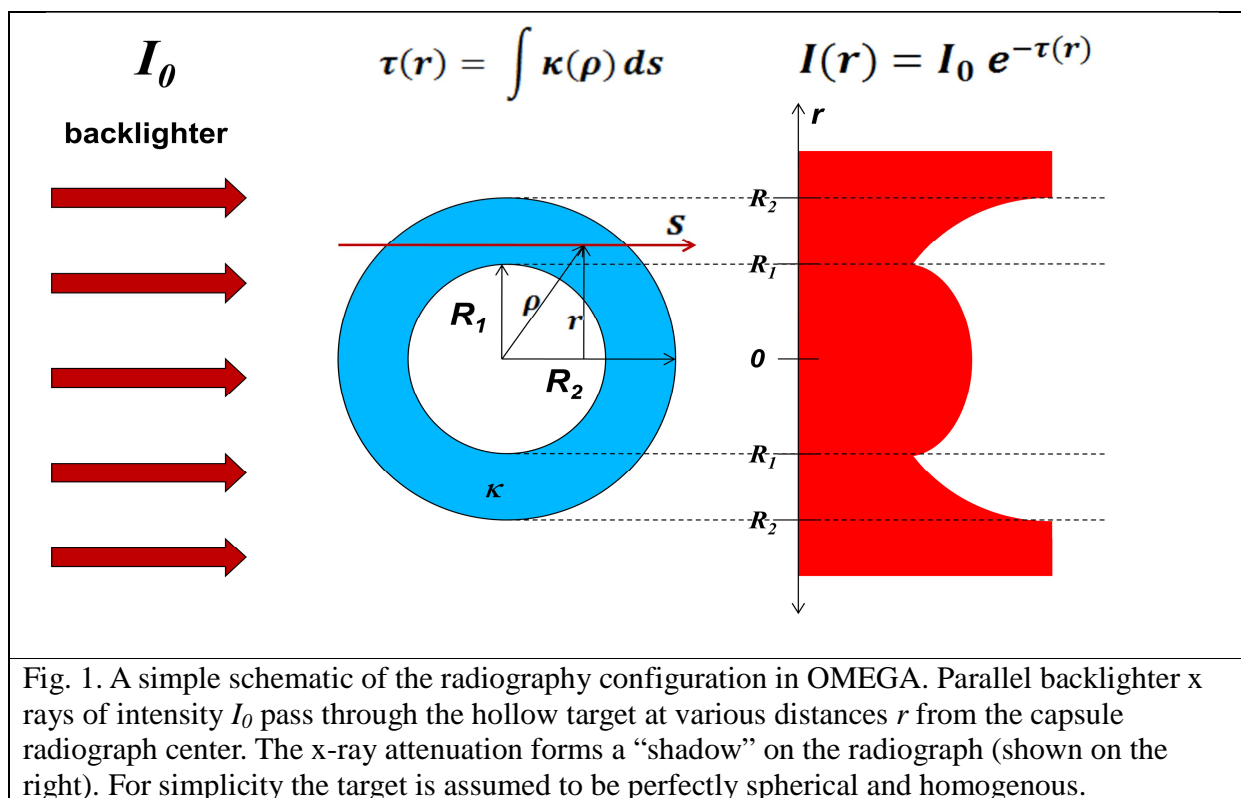
degrade rapidly as the target approaches saturation, with the exception of the outer radius  $R_2$ , and all of the parameters degrade as the target approaches transparency. The graphs obtained suggest the behavior of the parameter estimate degradation as  $\tau_0$  departs from the optimum. For example, estimation uncertainty is worse at  $\tau_0 = 2.0$  than it is at  $\tau_0 = 0.1$ , which is surprising because the degradation at  $\tau_0 = 2.0$ , a relatively low saturation, is comparable to the degradation at  $\tau_0 = 0.1$ , a very weak signal. These results provide a better understanding of how radiography experiments may be tuned to produce better radiographs for parameter estimation.

### Acknowledgments

I would like to thank Dr. Reuben Epstein for his time and support throughout the project. I would also like to thank Dr. Stephen Craxton for his encouragement and generosity for running the summer high school research program.

### References

1. Lois H. Gresh, Robert L. McCrory, and John M. Soures. *Inertial Confinement Fusion: An Introduction*. Laboratory for Laser Energetics: Rochester, NY. 2009.
2. S. Chandrasekhar, *Radiative Transfer*, Dover Publications, New York, 1960; Reuben Epstein, "The Equation of Transfer," personal manuscript - private communication, 2010.
3. S. L. Meyer, *Data Analysis for Scientists and Engineers*, John Wiley & Sons, Inc., New York, 1975; Reuben Epstein, "Weighted Least-Squares Maximum-Likelihood Parameter Estimation," personal manuscript - private communication, 2010.



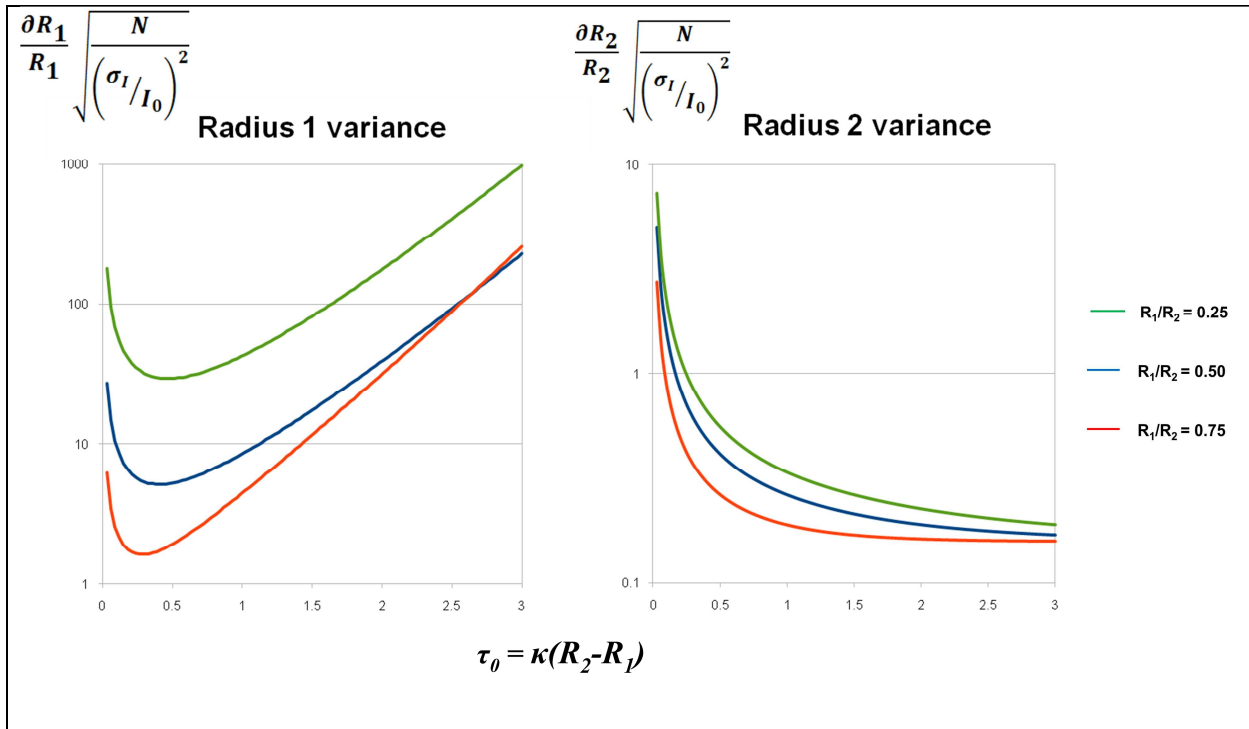


Fig. 3. Same conditions as in Figure 2. The scaled relative variances of  $R_1$  and  $R_2$  were plotted against the target's central optical thickness  $\tau_0$ .

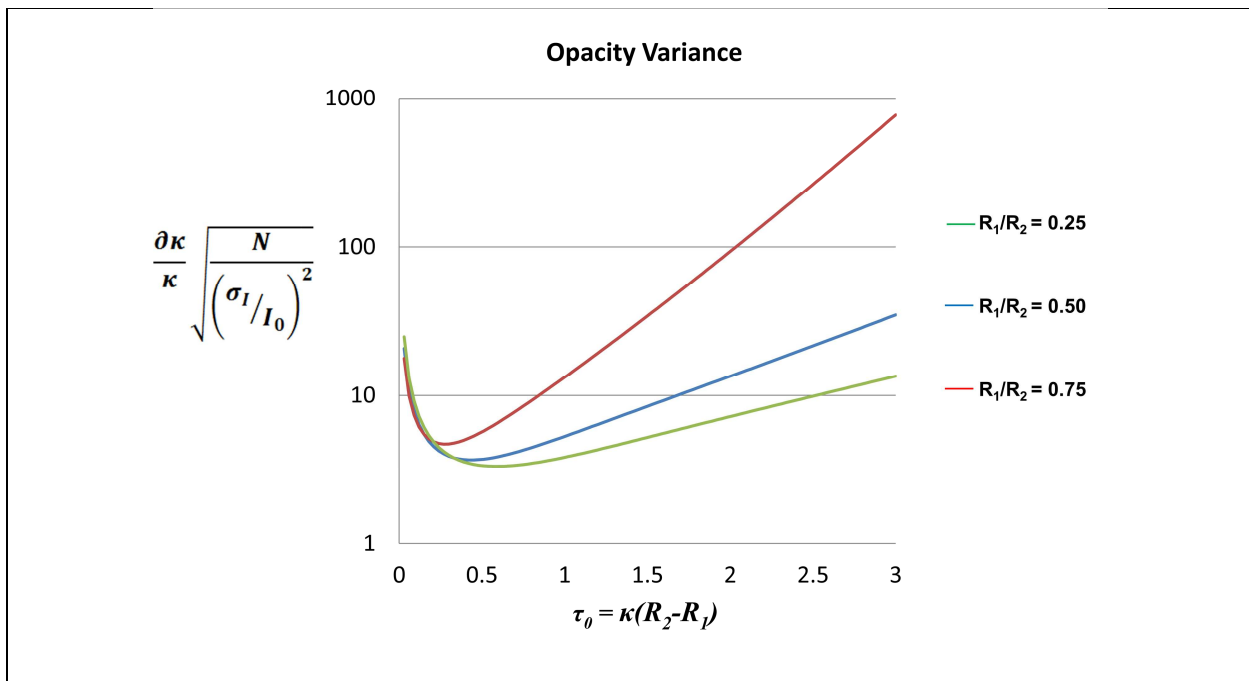
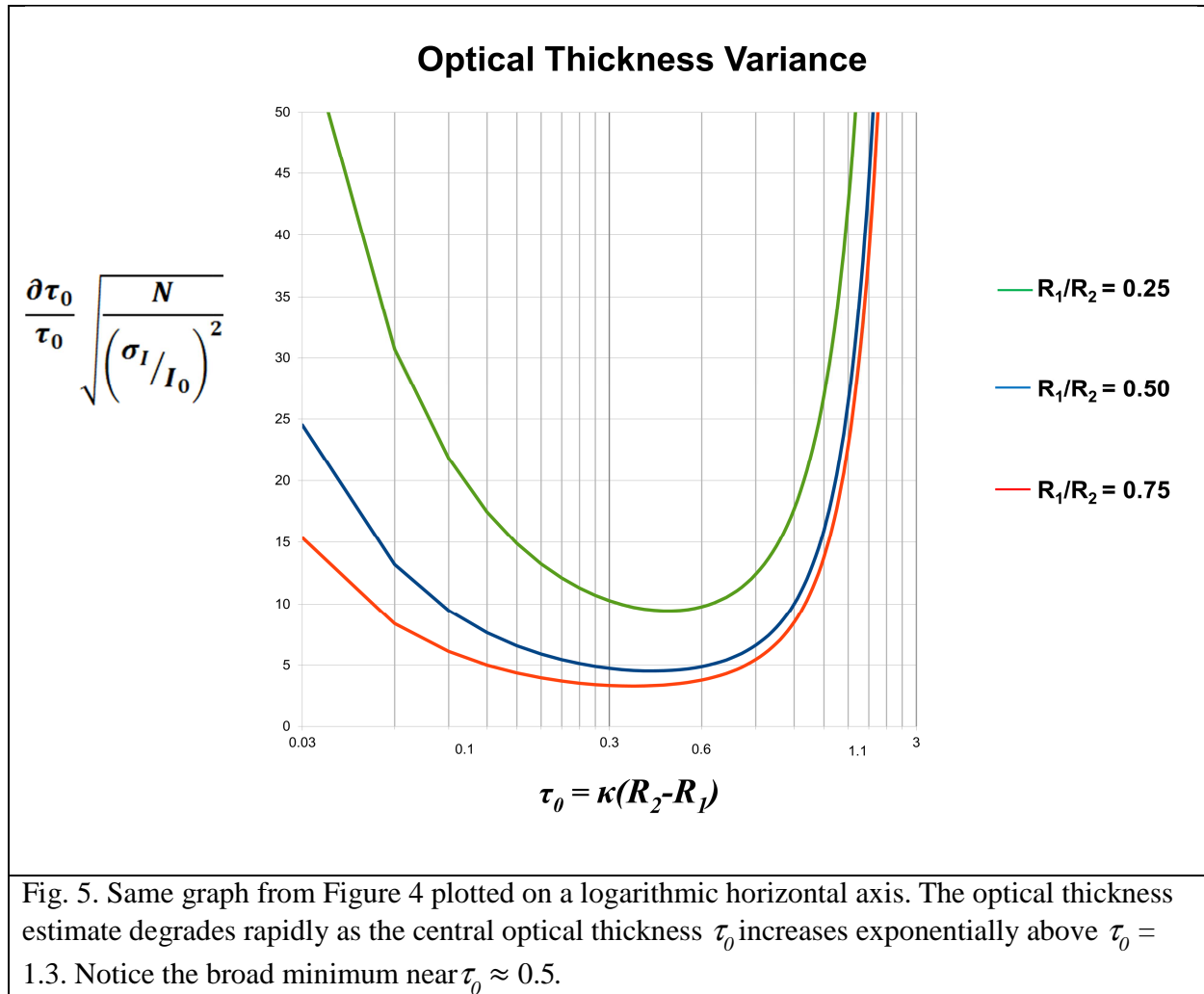


Fig. 4. Same conditions as in Figure 2. The scaled relative variance of opacity  $\kappa$  was plotted against the target's central optical thickness  $\tau_0$ .



## **X-Ray Backlighting of Shock Ignition Experiments on the National Ignition Facility**

**Thomas Mo**

Webster Schroeder High School

LLE Advisor: **Dr. R.S. Craxton**

Laboratory for Laser Energetics

University of Rochester

Rochester, New York

November, 2010



**Abstract:**

A computer code *Blackthorn* has been written to model the radiography of an imploding fusion target using an x-ray backlighter. *Blackthorn* traces x rays from the backlighter source through the target to a camera, which is at an arbitrary viewing angle. *Blackthorn* can model the target at any specified time and x-ray energy, drawing a contour plot that imitates an actual image produced by an x-ray backlighter, including self-emission, from the perspective of the viewing position. Input files from a computer code SAGE, which contains a 3D grid of center of mass radius, are combined with input files from another code, LILAC, which contains 1D profiles of mass density and electron temperature versus radius, to produce a 3D representation of the target density. The capabilities of *Blackthorn* are illustrated by application to a fusion target proposed for shock-ignition polar-drive experiments on the National Ignition Facility (NIF). A view from the polar position can be used to diagnose the azimuthal uniformity of the target, while a view from the equator can be used to diagnose the balance of compression between the polar and equatorial positions. *Blackthorn* is being used to help design and optimize x-ray backlighting diagnostics for the proposed experiments. Using 1D line-plots created by *Blackthorn*, 3500eV has been determined as an optimal frequency to view backlighting images.

## 1. Introduction:

Fusion is the process through which two or more nuclei fuse together to form a single heavier nucleus. Normally, fusion creates a more stable nucleus and results in the release of a large quantity of energy. To achieve fusion, the nuclei must be at a high density and temperature. These conditions will increase the number of collisions between the nuclei and

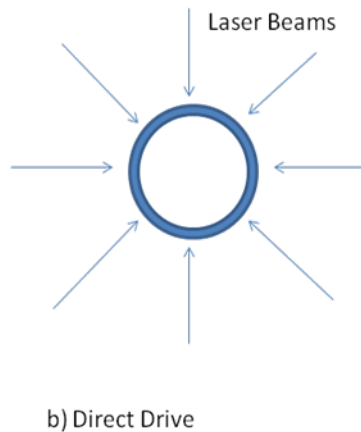
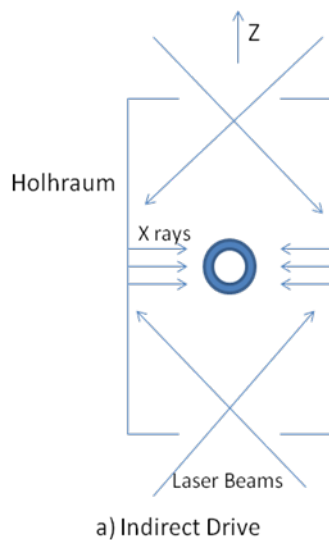


Figure 1: Two types of laser fusion. (a) In indirect drive fusion, laser beams strike the inside of a hohlraum, which then emits x-rays to irradiate a spherical fuel capsule. (b) In direct drive fusion, the laser beams directly and uniformly irradiate the capsule from all incident angles.

increase their kinetic energy, so that the nuclei will overcome their repulsive electrostatic forces in favor of their attractive nuclear forces and fuse together. In hydrogen fusion, a deuterium nucleus fuses with a tritium nucleus to create a helium nucleus and a neutron with a large amount of energy. Applying this concept to a spherical fuel capsule

consisting of a thin plastic shell filled with deuterium and tritium, fusion reactions can be carried out. These fusion reactions can provide a means of creating a future source of energy. The conditions for fusion can be met by using high-energy lasers to strike the capsule. The lasers deposit energy on the outside of the capsule so the outside ablates and the inside implodes. If the implosion is uniform and the conditions are met, fusion will occur.

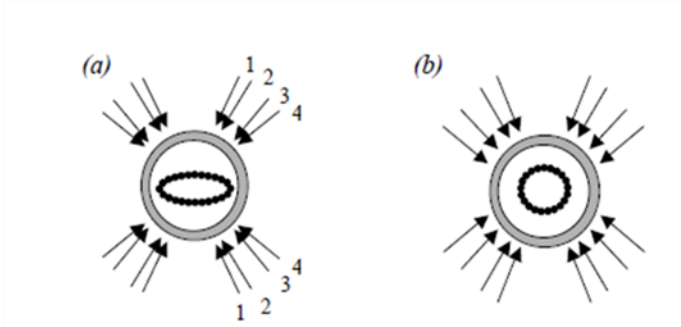


Figure 2: Two types of NIF beam pointings: direct drive and polar direct drive. (a) In direct drive, the target increases in non-uniformity as it implodes when the laser beams are initially pointed at the target center. (b) In polar direct drive, the beams are pointed away from the center, to improve the overall implosion uniformity. (from Ref. 5)

from the top and bottom, which then emits x-rays to irradiate the fuel capsule, located at the center of the cylinder. The National Ignition Facility (NIF) in Livermore, California is built for and currently specializes in indirect drive experiments. The NIF uses 192 beams of lasers organized into 48 quads (set of four lasers), in which all are designed to irradiate the inside of the hohlraum wall from the top and bottom. The quads are located at angles of 23.5, 30, 44.5, and 50 degrees to the z axis above and below the equator. On the other hand, in direct drive fusion, the laser beams directly and uniformly irradiate the target from all incident angles. Since the NIF facility has no equatorial beams, as it was constructed primarily for indirect drive experiments, polar direct drive<sup>3,4</sup> has been designed to enable direct drive experiments to be performed on the NIF. In polar direct drive, the beams maintain their indirect drive port configurations, but are re-pointed from the center of the target to achieve the best uniformity after compression (Fig. 2).

Currently, there are two main types of direct drive that may provide a path to attaining fusion energy in the future: hotspot ignition and shock ignition. Hotspot ignition<sup>6</sup> consists of the simultaneous heating and compression of the target center to start fusion in the center. Once fusion is present in the center, alpha particles (helium nuclei) will propagate outward and heat the fuel, creating a chain reaction. However, compressing a target full of "hot fuel" is very difficult, so an alternative technique, called shock ignition, has been proposed (Fig. 3). Shock

There are two ways to implode the target with lasers: indirect drive fusion<sup>1</sup> and direct drive fusion<sup>2</sup> (Fig. 1). Indirect drive fusion involves laser beams striking the inside of a hohlraum, a metallic cylinder through which the laser beams enter

ignition<sup>8,9</sup> contains two steps. In the first step, the “cold fuel” is compressed at low velocity, represented by the portion of the red curve with lower power ( $P_{main}$ ) in Fig. 3. In the second step, a powerful laser pulse, represented by the  $P_{shock}$  portion of the red curve, is used to launch a short, strong, spherically convergent shock on the outside of the target. The shock propagates inward, and the focused energy heats the center rapidly to generate fusion. Shock ignition can only be performed with direct drive because

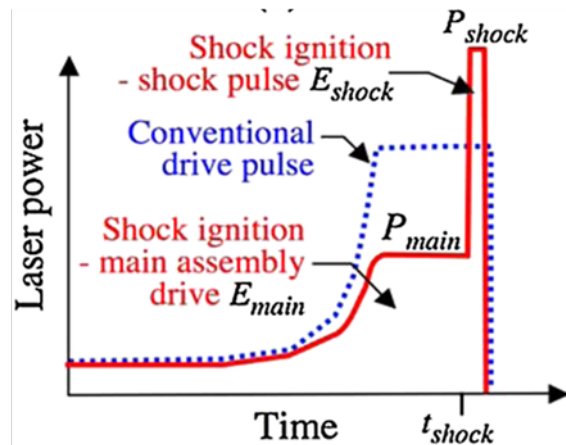
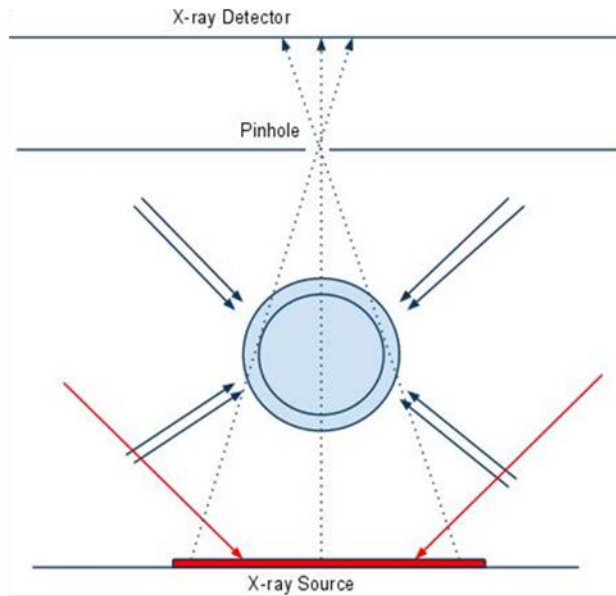


Figure 3: A graph comparing conventional hotspot ignition (blue) and shock ignition (red). The shock-ignition pulse has a drive pulse with power  $P_{main}$  followed by a shock pulse with power  $P_{shock}$ . (from Ref. 7)

the short laser pulse cannot heat the holhraum to a high enough temperature rapidly enough.

Perkins has proposed to test polar direct drive shock ignition on the NIF<sup>7</sup>. Half of NIF's beams, 96 main beams, are used to form the compression pulse and the other half, the 96 igniter beams, are used to form the shock pulse<sup>7</sup>. During the first part of the experiment, only the compression step is proposed to see if the fuel capsule, also referred to as the target, can be compressed sufficiently and uniformly using only half of the NIF beams. Tucker<sup>10</sup> has developed a design for this compression stage, but since this design and future designs may not produce perfect uniformity in compression, x-ray backlighting is needed to diagnose the uniformity, which is vital to achieving fusion. For x-ray backlighting, some laser beams not used to irradiate the target strike an x-ray source and create a layer of plasma (Fig. 4). The layer of plasma then emits x-rays which pass through the target, and those rays that pass through the pinhole and onto the x-ray detector create the backlighting image.



**Figure 4:** A diagram representing a proposed x-ray backlighting system for the NIF. The blue arrows represent laser beams used to compress the target in the center. The red arrows represent laser beams used to power the x-ray source. The red layer represents the plasma created from lasers striking the source. X-rays that pass through the pinhole create an image of the target on the detector. In reality, the target is much smaller than depicted, so the x-rays travel almost in parallel to each other.

Unfortunately, NIF shots are exceedingly limited; the system is capable of shooting up to three times per day, but presently the NIF only shoots once per day. Therefore, simulations of x-ray backlighting must be completed before the actual experiment is carried out. Tucker's design, obtained using the code SAGE<sup>11</sup>, can

provide predictions of the 3D target shell, but prior to this work the capability to simulate the x-ray backlighting image of the 3D object did not exist. This work describes a computer code *Blackthorn* that has been written to predict the image seen by an x-ray detector from any detector angle relative to the capsule.

## 2. X-ray Propagation in *Blackthorn*:

### 2.1: Theory

For an x ray of frequency  $\nu$  moving along a path whose position is measured by its distance of travel  $s$ , (Fig. 5(a)), its spectral intensity  $I_\nu$  is given by the equation of radiation transfer<sup>12</sup>:

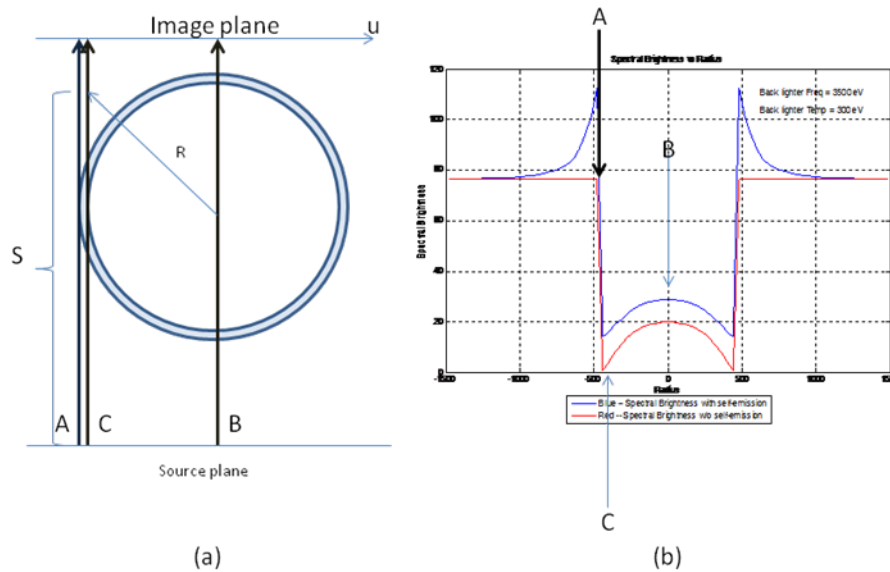


Figure 5: (a) A diagram indicating x-ray paths through a target and (b) graphs of spectral intensity vs. radius in the image plane produced by *Blackthorn* with self emission (blue) and without self-emission (red). The ring in (a) represents the target shell. For an x-ray of distance  $s$  along its path, it is at a radius  $R$  from the target center. The opacity is high in the ring and very low everywhere else. There is almost nonexistent attenuation for the path starting at A, intermediate at B, and high at C.

$$\frac{dI_\nu}{ds} = -k'_\nu I_\nu + k'_\nu B_\nu \tag{1}$$

where  $k'_\nu$  is the opacity and  $B_\nu$  is the blackbody spectral intensity evaluated at the local temperature. The first term on the right hand side depends on  $I_\nu$ , where  $I_\nu^* ds^* d\Omega^* dt^* dv$  equals the energy crossing a x-ray receiving area  $ds$ ,  $dv$  is the frequency interval of the x ray,  $d\Omega$  is the

solid angle, and  $dt$  is the time interval. The second term depends on  $B_\nu$ , the blackbody spectral intensity of the target given by Planck's law<sup>12</sup>:

$$B_\nu(T) = \frac{(2h\nu^3)}{c^2} * \left( \frac{1}{e^{\frac{h\nu}{kT}} - 1} \right) \quad (2)$$

where  $h$  is Planck's constant,  $\nu$  is the x-ray frequency,  $c$  is the speed of light,  $k$  is Boltzmann's constant, and  $T$  is the local temperature. Eq. 2 shows that  $B_\nu$  is only a function of the x-ray frequency and the local temperature at the x-ray position.

In Eq. (1), the first term represents absorption and the second term represents self-emission. Since  $B_\nu$  is a function of temperature, if it is assumed that  $T=0$  so that  $B_\nu$ , and consequently the self-emission term, becomes negligible, Eq. 1 becomes:

$$\frac{dI_\nu}{ds} = -k'_\nu I_\nu \quad (3)$$

Solving for  $I_\nu$ , Eq. 3 becomes:

$$I_\nu(s) = I_{\nu, start} e^{-\int k'_\nu ds} \quad (4)$$

the ideal case of backlighting. In this equation  $I_{\nu, start}$  is the spectral intensity emitted by the backlighter source, and the integral of  $k'_\nu ds$  is the optical depth. Since  $k'_\nu$  is consistently large inside the target shell and approximately zero outside, the optical depth depends mainly on the distance of x-ray travel through the shell. Therefore, the optical depth is almost 0 for rays starting at A, intermediate at B, and large at C (Fig. 5). Unfortunately, the local temperature on the x-ray path can reach up to several thousand electron volts, causing self-emission to become a significant factor.

To solve Eq. 1,  $I_{\nu, start}$  needs to be known. It can be parameterized as a function of the backlighter temperature  $T_{XR}$ :

$$I_{v,\text{start}} = B_v(T_{\text{XR}}). \quad (5)$$

Currently, 300 eV has been determined as a reasonable<sup>13</sup> backlighter temperature.

## 2.2: Numerical algorithm for integrating an x-ray path

The x-ray is integrated along its path taking small steps of interval  $ds$ . Assuming that the temperature and opacity are constant on the interval, Eq. 1 can be rewritten as:

$$\frac{d(I_v - B_v)}{ds} = -k'_v(I_v - B_v) \quad (6)$$

since  $dB_v/ds=0$ . Integrating each side,

$$I_v(s + ds) - B_v = (I_v(s) - B_v)e^{-\int k'_v ds} \quad (7)$$

is obtained. This gives the spectral intensity at the new position:

$$I_v(s + ds) = I_v(s) * e^{-k'_v ds} + B_v(s)(1 - e^{-k'_v ds}). \quad (8)$$

As in Eq. 1, the first term of Eq. 8 on the right hand side represents the absorption while the second term represents the self-emission. Eq. 8 maintains the assumption that the spectral emission occurring during an interval of x-ray travel  $ds$  is defined by Eq. 2 for the local temperature and opacity at the beginning of the interval. Since the temperature and opacity can change quickly, especially when the x-ray is near the shell of the target, a small  $ds$  needs to be used to accommodate this assumption. Convergence is achieved once the  $ds$  is small enough that an image created with a value  $ds$  and another image created with a value  $\frac{1}{2}ds$  are almost indistinguishable.

## 3. Solutions for 1-D hydrodynamic profiles:

### 3.1: Introduction of 1-D hydrodynamic profiles

In order to solve Eq. 8, the opacity and  $B_v$  need to be known. For the ideal case of a spherically symmetric shell, the temperature and density profiles can be obtained from a 1-D



hydrodynamic code such as LILAC. LILAC provides densities and temperatures as a function of radius R, the distance from the target center (Fig. 6). In Fig. 6, the target shell is between 400 and 500 microns in radius. On the right side of the high density spike, the outside of the shell is hot from the lasers striking the surface. Inside the shell (left), the DT has a low density, and is

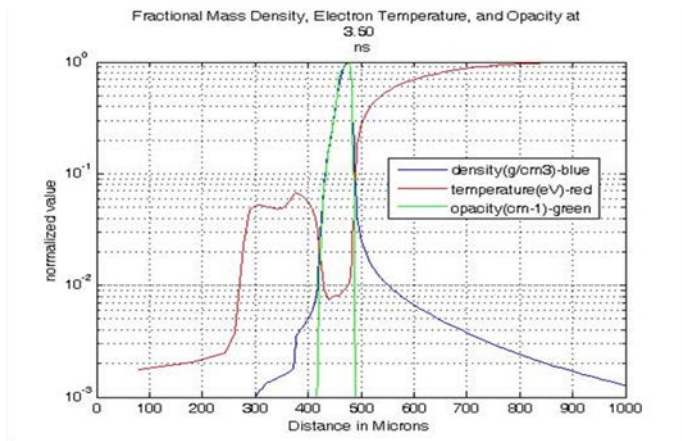


Figure 6: A LILAC plot showing the normalized density, temperature, and opacity versus radius at the end of the laser pulse. The blue line represents density, the red line represents temperature, and the green line represents opacity. The opacity is proportional to the density inside the shell because the temperature is low. The target shell is now between 400 and 500 um in radius, halfway from the initial radius of 865 um.

heated by energy from the shock propagating inwards. Since the curves of density and temperature versus radius are smooth, the density and temperature of any given radius can be found using linear

interpolation. One of the quantities needed to solve Eq. 8

is opacity,  $k'_\nu$ . This is provided by

data from the Los Alamos Astrophysical Opacity Library,<sup>14</sup> giving opacity as a function of density, temperature, and frequency. Therefore, for any given x-ray with a known frequency and radius R, the opacity can be found using interpolation with respect to the density,

temperature, and frequency. The

other quantity needed to solve Eq.

8,  $B_\nu$ , is a function of the

temperature and frequency.

A plot superimposing

opacity, temperature, and self-

emission, or  $k'_\nu B_\nu$ , versus radius

clearly illustrates the relationship

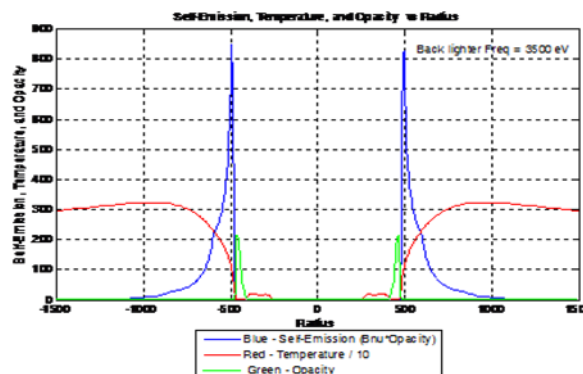


Figure 7: Self-emission (blue), temperature (eV/10, red), and opacity (1/cm, green) versus radius. The self-emission reaches a maximum just outside the shell. The opacity and self emission are used by *Blackthorn* to solve Eq. 8.

between the three values (Fig. 7). The opacity is high for the shell, where the temperature and self-emission are low. The self-emission reaches a maximum just outside the shell when the temperature is still moderately high. Self emission drops inside the target because the inside of the target is cool relative to the hot shell. As the radius increases, the self-emission also decreases due to a decrease in opacity.

### 3.2: Predicted backlighting for 1D target profiles

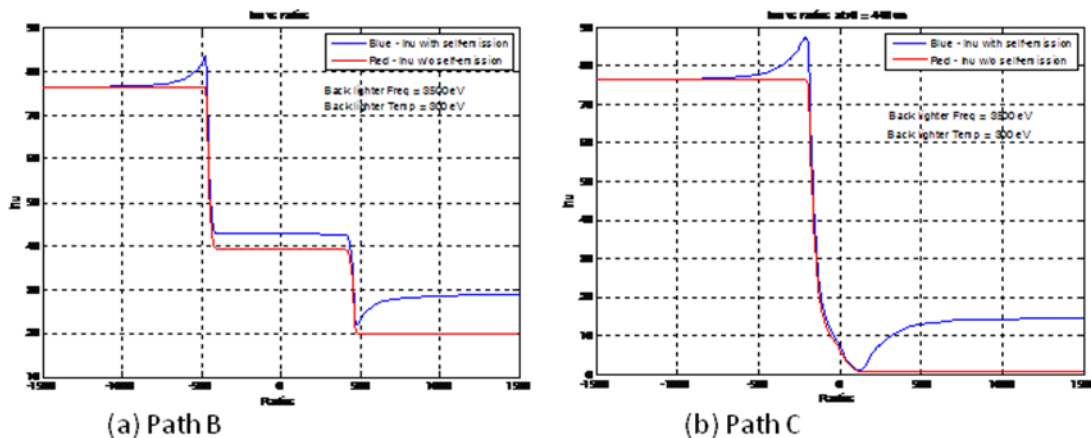


Figure 8: Spectral intensity versus the distance along the path of for an x-ray going through the center of the target (a) and starting at a distance  $u = -440 \mu\text{m}$  away from the center of the target, near the edge of the shell (b) with (blue) and without (red) self-emission. (a) corresponds to the x ray B and (b) corresponds to the x ray C in Fig. 5. Self emission increases the spectral intensity whenever the x ray is just outside the target shell.

Fig. 8 shows graphs of spectral intensity versus distance  $s$  along the x-ray paths B and C of Fig. 5a, containing superimposed curves of the spectral intensity with and without self-emission. Figure 8a displays rays passing through the center of the target and Fig. 8b rays closest to the edge of the target shell. In both cases, the self emission increases the spectral intensity directly outside the target shell and after it passes completely through the target. Since the x-ray in Fig. 8b has a longer portion of its path inside the shell, more absorption occurs, and less intensity emerges from the target.

To predict what experimentalists would see on the backlighting images, Fig. 5b shows graphs of spectral intensity versus radius in the image plane with and without self-emission. The

transmission begins to rapidly drop just inside the outer radius of the target shell and reaches a minimum at the edge of the inner radius of the shell. This allows the backlighting image to reveal the inside and outside edges of the target. Self-emission increases the spectral intensity shown on the backlighting image inside the target and creates an increase of the spectral intensity to values above  $I_{v,start}$  around the outside edge of the target. However, the self-emission in Fig. 5b does not affect the location of the inner or outer edges of the shell.

### 3.3: Frequency Optimization

To find an optimal frequency, superimposed plots of transmission versus radius in the image plane for different x-ray frequencies can be used (Fig. 9). Fig. 9 is similar to Fig. 5b, but

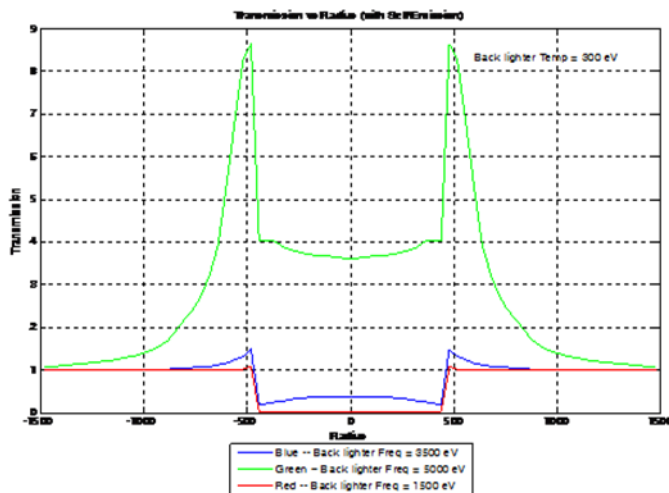


Figure 9: Transmission vs. radius in the image plane calculated at different frequencies. The green line represents a frequency of 5000 eV, the blue line 3500 eV, and the red line 1500 eV. An image using the 5000 eV frequency would become dominated by self-emission, and an image using the 1500 eV frequency would show almost no self-emission. However, neither frequency provides information about the inside of the target.

dramatically for the x-ray source than the plasma, so  $I_{v,start}$  is greatly reduced for higher x-ray frequencies. In this case, the target becomes dominated by self-emission, as shown by the curve representing an x-ray frequency of 5000 eV. The minimum transmission inside the target becomes 3.5, and the maximum transmission, caused by the x-rays that are skimming the

instead of spectral intensity ( $I_v$ ), the transmission,  $I_{v,final}/I_{v,start}$  is plotted. The transmission depends strongly on the x-ray frequency.

As the x-ray frequency increases, the value of the exponential in Eq. 2 also increases, and would result in a lower  $B_v$  in the plasma and a lower  $I_{v,start}$ . This exponential term changes much more

outside of the shell, is more than 8.5. At the other extreme, shown by the curve with an x-ray frequency of 1500 eV, the transmission inside the shell is consistently close to zero. The shape of this curve is similar to the transmission curve with no self-emission (red) shown in Fig. 5b.

Having too high or too low of an x-ray frequency is problematic because in both cases there is a lack of information about the inside of the shell. In the 5000 eV case, the image would be created primarily by the target's self emission. On the other hand, for the 1500 eV x-rays, the x-rays are so strongly attenuated that little energy reaches the inside of the target, so x rays don't fully penetrate the target and emerge with sufficient energy to provide details about the inside. The 3500 eV x-rays create a curve that comes closest to the ideal transmission curve; the transmission is 1 outside the target (except the regions directly outside the target slightly affected by self-emission), and the transmission curve reaches a minimum just inside the shell and increases towards the center, following the limb effect. Therefore, a frequency of 3500 eV has been temporarily chosen.

### 3.4: Images taken after the end of the laser pulse

The backlighting image can also be taken after the laser pulse has been turned off. This can be simulated by using a temperature factor, wherein all the temperatures obtained from the LILAC profile are multiplied by this factor in order to mimic the cooling of the target over

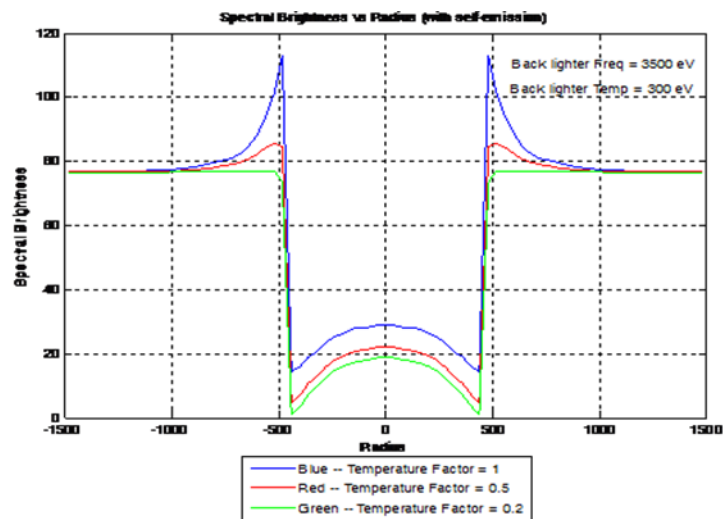


Figure 10: Spectral intensity versus radius in the image plane with the temperature multiplied by factors of 1 (blue), 0.5 (green), and 0.2 (red). As the temperature factor decreases, the effect of self emission, and also the spectral intensity, decreases. Therefore, images taken just after the laser turns off would show less self-emission.

time after the laser pulse has ended. A 1-D plot of spectral intensity versus radius in the image plane with superimposed plots with three different temperature factors can be used to analyze the effects of cooling (Fig. 10). The temperature factors used are 1, 0.5, and 0.2, simulating the target 0, 0.35, and 0.85 nanoseconds after the laser pulse has been shut off. As the temperature factor decreases, the transmission maxima decrease, signifying that the amount of self-emission also decreases. Once the temperature factor is as low as 0.2, almost no self-emission is shown, shown by the flat spectral intensity outside of the target. In addition, a much clearer minimum just inside the shell can be seen. Therefore, images taken after the laser pulse should be better than those taken during the pulse. To adjust for this advantage, the laser pulse could possibly be switched off slightly earlier to obtain self-emission-free images for more times.

#### 4. Modeling of 3D target profiles

Each target position can be represented by a spherical angle  $(\theta, \Phi)$  where  $\theta$  is the angle clockwise from the positive z-axis and  $\Phi$  is the angle clockwise from the x-axis in the x-y plane. As described by Tucker<sup>10</sup>, the computer code SAGE calculates the center of mass radii for positions all around the target as a function of  $(\theta, \Phi)$ . Typical plots of the center of mass radii are

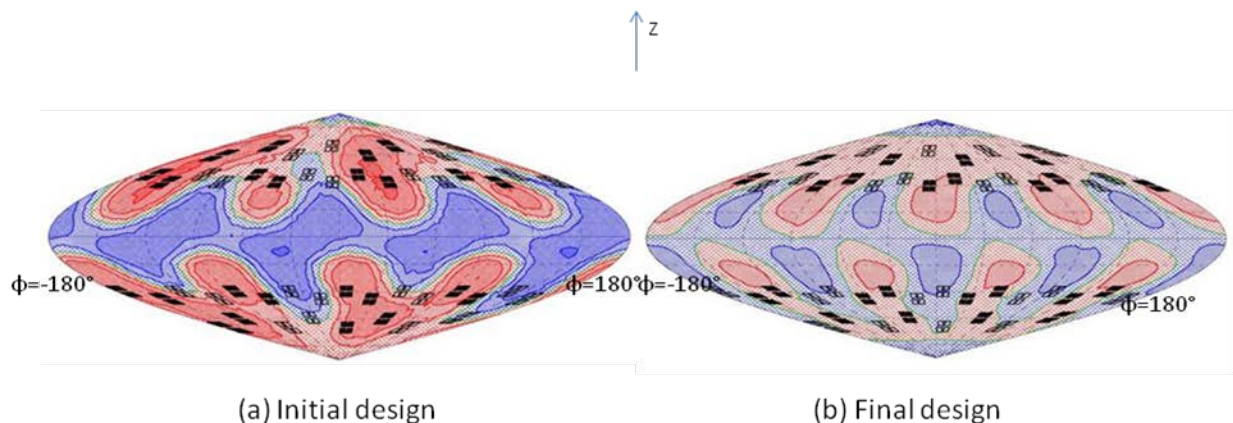


Figure 11: SAGE plots of Tucker's initial and final designs displaying the center of mass radius of the target. The black quads are those that are used to implode the target. The projection maps the whole sphere to the plane and displays radius as a function of the spherical angle  $(\theta, \Phi)$ . The rms variation of 22 $\mu$ m in the initial design was reduced to 8 $\mu$ m in the final design. (from Ref. 8)

shown in Fig. 11 for Tucker's initial and final designs. Red areas represent areas that are over-compressed, while blue areas represent ones that are under-compressed. The darker the color is, the more over/under compressed the area is. In both (a) and (b), the equatorial positions are compressed less than the polar positions. However, it is obvious that the initial design shows a much greater difference in the compression between the polar and equatorial positions.

SAGE produces profiles similar to the LILAC profiles of density and temperature versus radius, but with less resolution, since SAGE is a 2D code. To compensate for the lower resolution, a LILAC profile can be

combined with the SAGE center of mass calculations by shifting the LILAC profiles in each direction  $(\theta, \Phi)$  to match the center of mass provided by SAGE. In the solutions described above for 1D

hydrodynamic profiles, calculations were made purely based on LILAC, where the radius used for interpolation was the distance  $R$

from the current x-ray position to the center of the target (see Fig. 5a). For 3D targets, with an x ray at position  $(R, \theta, \Phi)$ , *Blackthorn* first finds the center of mass radius ( $r_{cm}$ ) in the direction  $(\theta, \Phi)$ , and then calculates a new radius  $r_{new}$  to correspond with the LILAC profile using the equation:

$$r_{new} = (R - r_{cm}) + r_{max\_density} \quad (9)$$

where  $r_{max\_density}$  is the radius in the LILAC profile corresponding to the maximum density.  $r_{new}$  is then used to interpolate for density, temperature, and opacity in LILAC. So, for example,

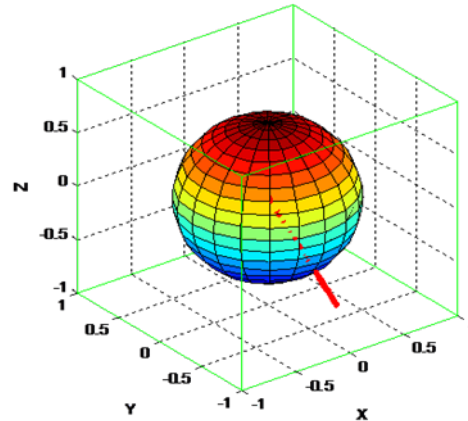


Figure 12: Grids on the six faces of a cube used to obtain  $r_{cm}$  as a function of direction  $(\theta, \Phi)$ .  $r_{cm}$  is stored at each grid point. For a direction given by the red line  $r_{cm}$  is found using bilinear interpolation at the point where the line intersects one of the grids.

whenever the x ray radius  $R$  is equal to  $r_{cm}$ , Eq. 9 will cause the LILAC values to be calculated at  $r_{new} = r_{max\_density}$ . SAGE records the radii  $r_{cm}$  by creating a three-dimensional cube that encloses the target with grids, usually 20x20 or 30x30, on each of the 6 faces (Figure 12). This method is described in Ref. 15. At the center of each square on each grid is a grid-point at which the center of mass radius  $r_{cm}$  is stored. When the x ray moves to a new position  $(x,y,z)$  for which  $(R, \theta, \Phi)$  are calculated, *Blackthorn* finds the coordinates where the red line in the direction  $(\theta, \Phi)$  intersects one of the grids. Then, *Blackthorn* calculates  $r_{cm}$  in that direction using bilinear interpolation.

#### 4.1: Selection of rays:

Given a viewing direction  $(\theta, \Phi)$ , a unit vector  $c=(\sin(\theta)\cos(\Phi), \sin(\theta)\sin(\Phi), \cos(\theta))$  can be used to represent the direction of the camera and of x-ray travel with respect to the  $x,y,z$  axes. Using the components of the direction vector, an imaginary  $(u,v)$  plane, which is perpendicular to the direction of x-ray travel, can be created. The  $(u,v)$  plane is placed 1500  $\mu\text{m}$  away from the target center and simulates the image plane (see Fig. 5a), where x-rays strike and form the image. The components of unit vectors in the  $u$  and  $v$  directions can be defined by  $u_1=(-\sin(\Phi), \cos(\Phi), 0)$  and  $v_1=(-\cos(\theta)\cos(\Phi), -\cos(\theta)\sin(\Phi), \sin(\theta))$ . Given the coordinates of the x-ray starting position in the  $(u,v)$  plane, the unit vectors are used to find the starting coordinates in the  $(x, y, z)$  plane.

*Blackthorn* shoots rays in a polar fashion from the center of the  $(u,v)$  plane. The x-rays are first shot along the radial direction at angle of 0 with respect to the positive  $u$ -axis. This is repeated for the other angles. Polar ray tracing allows the curves of the contour plot to be smoother than the jagged curves resulting from a rectangular grid of x-rays. Therefore, it allows a much smaller number of rays to be used in order to reach convergence.

### 5. Predicted images for 3D target profiles

Two different camera angles are available on the NIF for viewing backlighting images. A

view from the pole position ( $\theta=0, \Phi=0$ ) can be used to diagnose the azimuthal uniformity of the target

while a view from the equator

( $\theta=90, \Phi=79$ ) can be used to diagnose the balance of compression between the polar and equatorial positions.

Fig. 13 shows a polar-view backlighting image of Tucker's initial design. The x-ray energy used is 3500 eV and  $T_{XR}$  is 300 eV. The yellow portion shows the outside of the target, where the transmission is 1. The orange ring indicates that the transmission is greater than 1, and is caused by self-emission from just

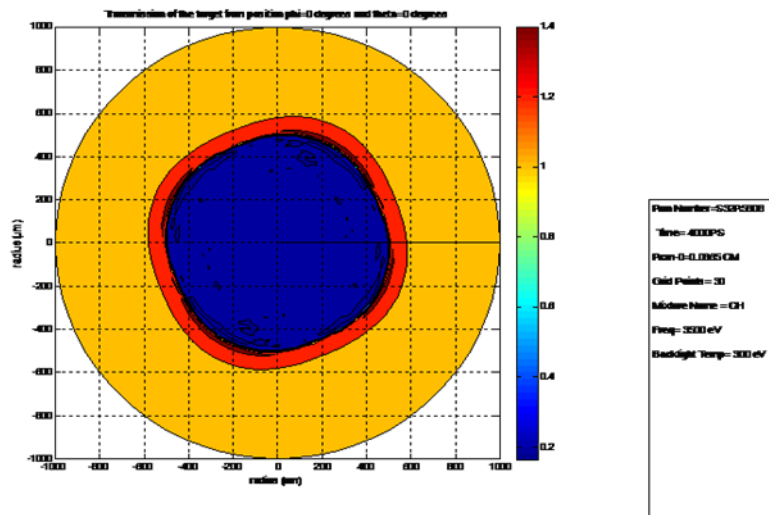


Figure 13: 2-D backlighting image of Tucker's original design from the polar view displaying contours of transmission. There is a four-fold pattern displaying structure around the edge and inside the target shell. The azimuthal uniformity is mediocre.

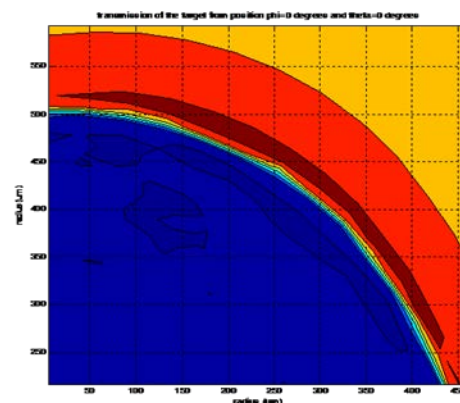


Figure 14: Zoomed in view of the upper right portion of the image shown in Fig. 13. It shows that in the black ring in Fig. 13, the transmission is rapidly transitioning from low to high.



outside the target's shell. The thin black ring shows the outer edge of the target's shell. Inside the black ring, the transmission rapidly transitions from the higher value outside the shell to the lower value inside (Fig. 14).

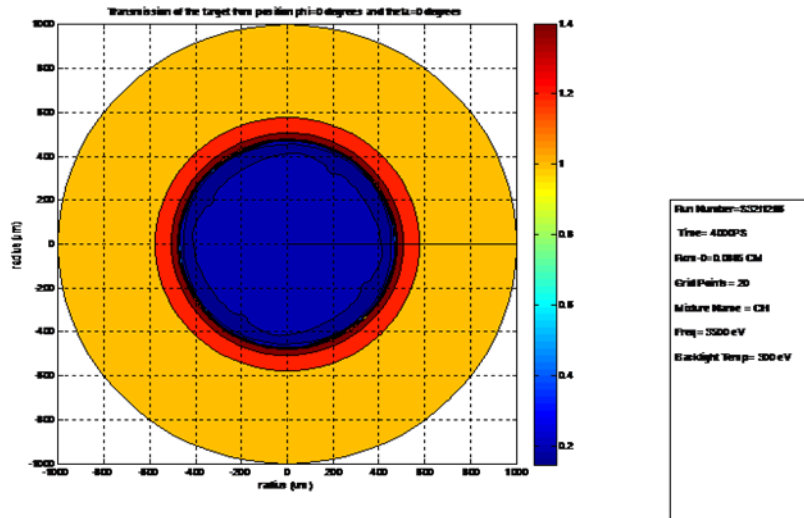


Figure 15: 2-D backlighting image of Tucker's final design from the polar view. The azimuthal uniformity has been greatly improved.

The image of Fig.13 shows a four-fold nonuniformity pattern around the outside ring of the target. The offset of the pattern from 0,90,180, and 270 degrees corresponds with the offset of the beams on the NIF equatorially (see Fig. 11). Slight nonuniformities can also be seen directly

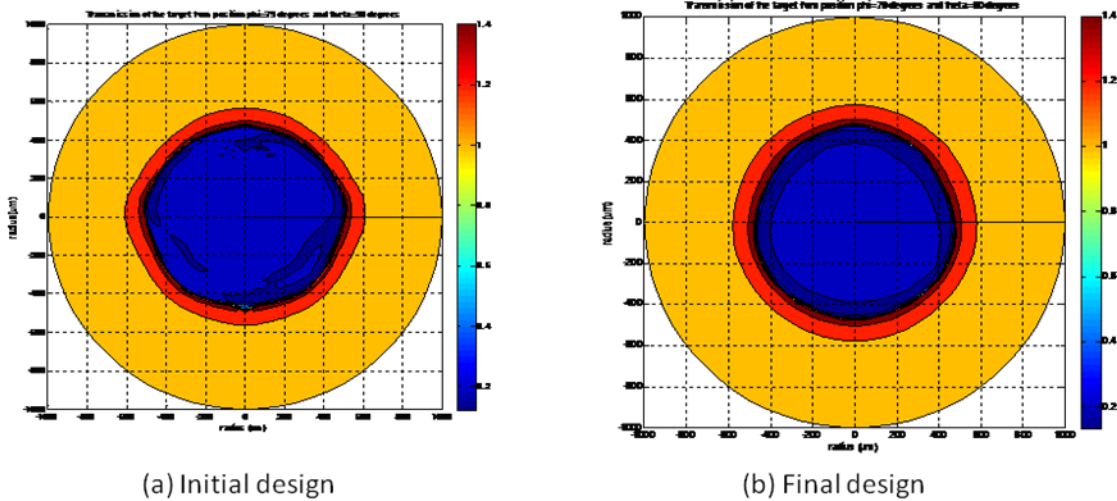


Figure 16: (a) 2-D backlighting image of Tucker's original design from the equatorial view. The equatorial positions are compressed less than the polar positions, and there is structure present inside the target shell. (b) 2-D backlighting image of Tucker's final design from the equatorial view. The equatorial positions are slightly less compressed than the polar regions. The structure has been reduced.

inside the ring, also in a four-fold pattern. When viewing Tucker's final design from the polar view (Fig. 15), the overall shape of the target is much more round. Most of the structure around the outside of the ring is eliminated. Some structure inside the ring, also in a four-fold pattern, can just be perceived.

In the equatorial view of Tucker's original design (Fig. 16a), it is clear that the equatorial positions are compressed much less than the polar positions. There is also a significant amount of structure directly inside the shell. In the equatorial view of Tucker's final design (Fig. 16b), the nonuniformity is much less, but the equatorial positions are still compressed slightly more. The inner structure has also been reduced.

## Conclusion

A shock-ignition experiment has been proposed for the National Ignition Facility. To model x-ray backlighting of targets for these experiments, a computer code *Blackthorn* has been written. *Blackthorn* combines a 1-D LILAC profile with 3-D SAGE predictions to create 1-D plots of x-ray intensity and 2-D backlighting images that can be used to diagnose the uniformity of target compression. *Blackthorn* can also help optimize the x-ray frequency, backlighter temperature  $T_{XR}$ , and times to take the backlighting images. The exact  $T_{XR}$  will depend on the number of beams used for backlighting and the material of the backlighting source. *Blackthorn* determined that 3500 eV is an optimal frequency to form backlighting images, which should be taken just after the laser pulse has been turned off to reduce the effects of self-emission. *Blackthorn* shows a clear distinction between optimum designs, like Tucker's design which produces very spherical images, and non-optimum designs, which produce clearly nonuniform images, enabling nonuniform implosions to be diagnosed. *Blackthorn* can thus be used in support of research on the NIF towards the possibility of obtaining fusion energy using shock-ignition.

### Acknowledgements:

I would like to thank Dr. Craxton for inviting me to the summer program, taking time to advise my project, and supporting me during and after the program. I would also like to thank Laura Tucker for aiding my research with a more optimized capsule design.

### References:

1. J.D. Lindl, "Development of the Indirect-Drive Approach to Inertial Confinement Fusion and the Target Physics Basis for Ignition and Gain," *Phys. Plasmas* **2**, 3933 (1995).
2. J Nuckolls et al., "Laser Compression of Matter to Super-High Densities: Thermonuclear (CTR) Applications," *Nature* **239**,139 (1972).
3. S. Skupsky et al., " Polar Direct Drive on the National Ignition Facility ", *Phys. Plas* **11**, 2763 (2004)
4. R.S. Craxton et al., "Polar Direct Drive : Proof-of-Principle Experiments on OMEGA and Prospects for Ignition of the National Ignition Facility," *Phys. Plas* **12**, 056305 (2005)
5. A.M. Cok, "Development of Polar Drive Designs for Initial NIF targets," LLE Summer High School Research Program (2006)
6. S. Atzeni and J. Meyer-ter-Vehn, "The Physics of Inertial Fusion," Clarendon (2004).
7. L.J. Perkins, et al., "Development of a Polar Drive Shock Ignition Platform on the National Ignition Facility," NIF Facility Time Proposal (2010).
8. R. Betti et al., "Shock Ignition of Thermonuclear Fuel with High Areal Density," *Phys. Rev. Lett.* **98**, 155001 (2007)
9. L.J. Perkins et al., "Shock Ignition : A New Approach to High Gain Inertial Confinement Fusion on the National Ignition Facility,"*Phys. Rev. Lett.* **103**, 045004 (2009)
10. L. Tucker, "A Design for a Shock Ignition Experiment on the NIF Including 3-D Effects," LLE Summer High School Research Program (2010)

11. R.S. Craxton and R.L. McCrory, "Hydrodynamics of Thermal Self-Focusing in Laser Plasmas," J. Appl. Phys. **56**, 108 (1984).
12. Ya. B. Zel'dovich, Yu. P. Raizer, "Physics of Shock Waves and High-Temperature Hydrodynamic Phenomena, " New York: Academic Press (1966-1967)
13. R. Epstein, Discussion about backlighting temperature, 11 October 2010
14. W.F. Huebner et al., " Astrophysical Opacity Library, " Los Alamos Scientific Laboratory Report LA-6769-M (1977)
15. G. Balonek, "How good is the Bright Ring Characterization for Uniformity of Deuterium Ice Layers Within Cryogenic Nuclear Fusion Targets?," LLE Summer Program (2004)

# **Using Surface Evolver to Model the Behavior of Liquid Deuterium**

Eric Pan

Webster Thomas High School

Advisor: Thomas B. Jones

University of Rochester

Laboratory for Laser Energetics

Summer High School Research Program 2010

February 2011

## **Abstract**

Successful exploitation of laser fusion as an energy source requires that laser targets be produced quickly on an assembly-line basis. The final step in fabricating a laser target is the fueling operation, where cryogenic liquid deuterium is loaded into thin polymer shells. This fueling must be done remotely because liquid deuterium must be maintained at around 20 Kelvin. It is required that precise volumes of liquid deuterium are dispensed, on the order of 90 microliters per target. This task is complicated because liquid deuterium has a contact angle of zero (perfectly wetting), behaving differently from other, more familiar liquids, such as water. To address this issue, this work used “Surface Evolver,” a software tool developed by K. Brakke that uses energy minimization to evolve fluid shapes into their final equilibrium forms subject to surface tension, gravity, and other forces. The behavior of liquid deuterium between parallel plates was modeled, including parallel vertical plates with varying widths and non-parallel horizontal plates. The parallel plate geometry is favored because electrodes can be attached to the plates for precise manipulation and dispensing.

## Introduction

At the Laboratory for Laser Energetics, the OMEGA-60 laser is used primarily to conduct fusion reactions. These fusion reactions involve using 60 laser beams to hit a small, cryogenic target inside the target chamber. These targets need to be fueled with cryogenic liquid deuterium into thin polymer shells. The current batch process for making these laser targets is rather slow, but it is still fast enough for the experiments. However, if laser fusion were to be used as an energy source, the targets would need to be produced on-site much quicker because the laser would need to be fired many times per minute.

Cryogenic liquid deuterium has a special property in that it has a zero contact angle, meaning that it is perfectly wetting. In order to better understand the behavior of cryogenic liquid deuterium, we can use a program called “Surface Evolver” to simulate its behavior. After giving it an initial input file that defines the initial shape of a body, the program will then output an evolved profile, which should be the one of minimum energy.

The simplest example is the evolution of a cube into a sphere, as shown in Fig. 1. “Surface Evolver” starts with an input file of a cube, which is representative of a cube of liquid in free space. In this simple example, the governing equation is  $E = \gamma A$ , where  $E$  is the energy that we want to minimize,  $\gamma$  is the surface tension (which is constant), and  $A$  is the contact area. To minimize the energy, we want to minimize the contact area since the surface tension is constant. A sphere of volume  $1 \text{ m}^3$  has a total surface area of  $4.83 \text{ m}^2$ , whereas a cube with the same volume has a total surface area of  $6 \text{ m}^2$ . Because the three-dimensional shape that has the smallest surface area is a sphere and not a cube, Surface Evolver will gradually evolve the cube into a sphere. This is why droplets in midair are more spherical and never cubes. In seeking the minimum energy state, “Surface Evolver” uses a series of commands including “refine,” which

increases the total number of vertices, and “go,” which processes the current body and tries to minimize the total energy using a gradient descent method. As the shape is further refined, the body approaches the shape of a perfect sphere.

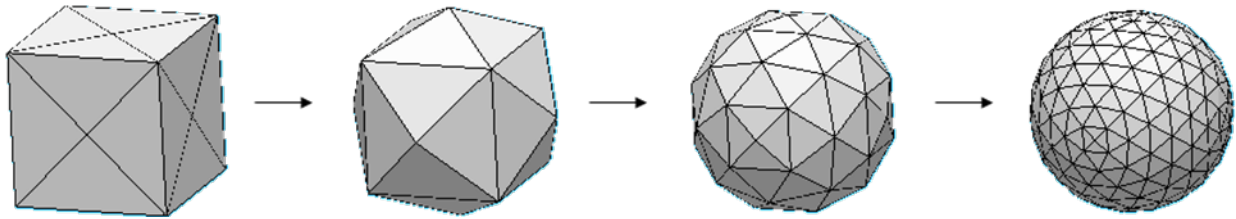


Figure 1: Process used by Surface Evolver to model the simple evolution of a cube into a sphere.

Similar to the above example, “Surface Evolver” can also model the behavior of liquid deuterium between two parallel plates. Given an initial shape, the program will evolve it and output a profile for the cryogenic liquid deuterium in between those two parallel plates, as shown in Fig. 2.

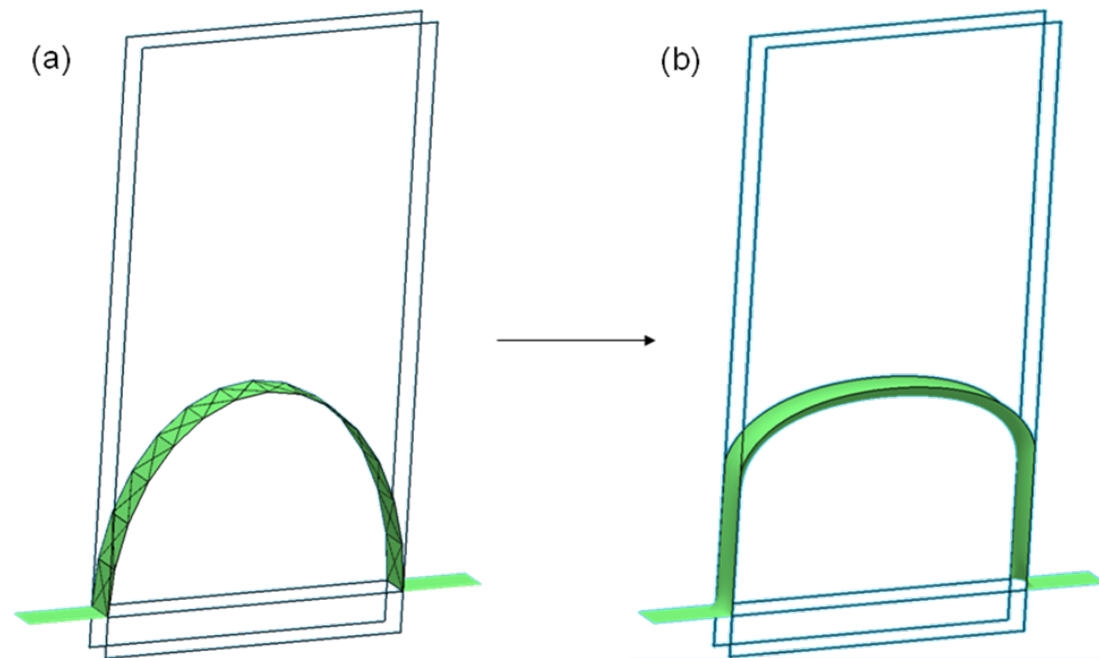


Figure 2: (a) Initial meniscus profile given to Surface Evolver and (b) meniscus calculated by Surface Evolver.



### Effect of Plate Width on Meniscus Height-of-Rise

The maximum height-of-rise of the meniscus, which occurs at the center of the plates, varies with the plate width. Some convenient measures of the height of the meniscus at the displacement from the center  $x$  are labeled in Fig. 3.

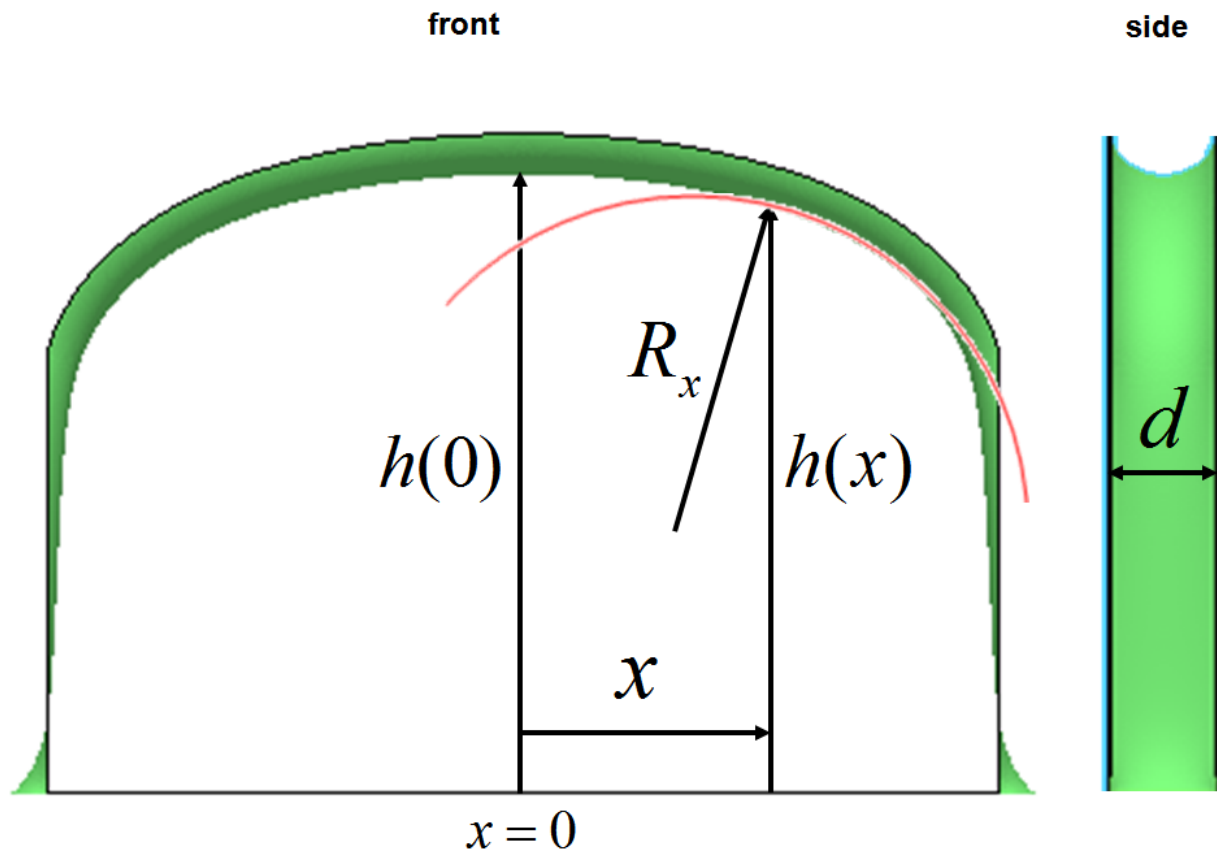


Figure 3: Properties of the meniscus used in Eqn. 1.

The following equation governs the height-of-rise as a function of  $x$ , the displacement from the center of the plates:

$$h(x) = \frac{\gamma \cos(\theta_c)}{\rho g} \left( \frac{2}{d} - \frac{1}{R_x} \right) \quad (1)$$

In Eqn. 1,  $h(x)$  is the height of the meniscus,  $\gamma$  is the surface tension,  $\theta_c$  is the contact angle,  $\rho$  is the density of the fluid,  $g$  is the acceleration due to gravity,  $d$  is distance separating the two parallel plates, and  $R_x$  is the radius of curvature at the position on the plate. In this experiment, the primary interest is in  $h(0)$ , the height-of-rise at the center of the plate.

For this “Surface Evolver” simulation experiment on the effect of the plate width on the maximum meniscus height-of-rise, the temperature was held at a constant 18.7 Kelvin. It is important to note that both the surface tension and the density of the liquid are dependent on the temperature. At this temperature, the surface tension is  $0.00382 \text{ J/m}^2$  and the density is  $174 \text{ kg/m}^3$ . Other constants included the gravitational acceleration, which was  $9.81 \text{ m/s}^2$ , and the plate separation, which was  $0.86 \text{ mm}$ . As the plates became wider, the radius of curvature at the center increased towards infinity. From Eqn. 1, that made the height-of-rise increase towards its maximum, which occurs when the meniscus is perfectly flat and the radius of curvature is infinity.

“Surface Evolver” does indeed give those results, as shown in Fig. 4. The wider plates have a higher height-of-rise at the center of the plates. The wider plates also have a much flatter region in the center where the radius of curvature approaches infinity.

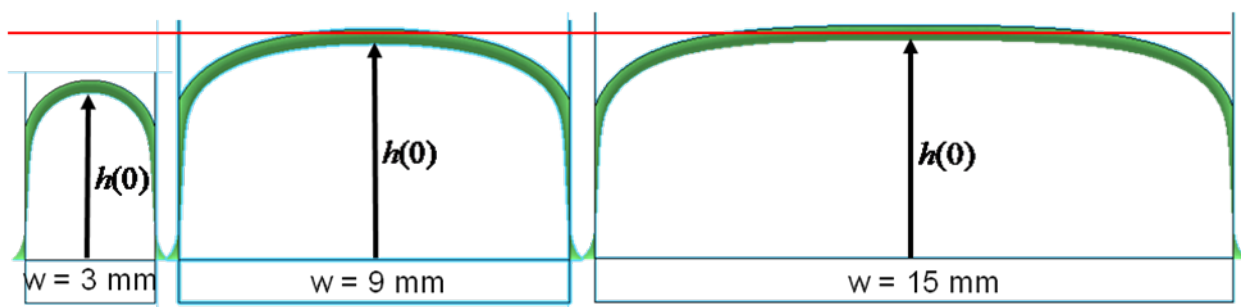


Figure 4: Calculated meniscuses for three different plate widths. The deuterium rises higher between wider plates, but levels off as the plates become wider. The red line marks the theoretical maximum height of rise.

## Comparison of measured profiles to theory

After “Surface Evolver” generated a meniscus profile, data was extracted to see whether the radius of curvature was consistent with the height as predicted by Eqn. 1. There were two ways to extract the data: using a dump-file from “Surface Evolver” containing all the three-dimensional coordinates and saving a bitmap from a screenshot of the profile. It was necessary to find the second derivative of the meniscus profile to calculate the radius of curvature. The following equation describes how to calculate the radius of curvature:

$$R_x = \frac{\left[ 1 + \left( \frac{dy}{dx} \right)^2 \right]^{3/2}}{\left| \frac{d^2y}{dx^2} \right|} \quad (2)$$

In Eqn. 2,  $R_x$  is the radius of curvature,  $dy/dx$  is the first derivative, and  $d^2y/dx^2$  is the second derivative of the function  $y(x)$ .

Because “Surface Evolver” uses a numerical method instead of an analytical method to solve for the configuration of lowest energy, the values for the points are not exact. Furthermore, the bitmap had additional numerical noise because the measurements were limited by the pixel resolution.

Since the bitmap method has pixels evenly spaced out along the  $x$ -axis, a first derivative could be numerically obtained at some point by taking the slope between the two points immediately to its left and right. The second derivative could be calculated using this same method on the points from the first derivative. However, this yielded extremely noisy and thus meaningless results. The unsmoothed second derivative had most of its values between  $\pm 50,000$  compared to the smoothed second derivative, which only ranged between  $-100$  and  $-350$ .

To address this matter, a MATLAB program was written to smooth out the curve. This smoothing algorithm can reduce the numerical noise enough so that the results from the data extracted from both the dump-file and the bitmap image are sufficiently smooth. The smoothing algorithm takes the first  $n$  points starting with the first point on the curve and fits a line to it. Thus, a value for the first derivative, or the slope of the best-fit line, can be obtained at the average of the  $x$ -values for the first  $n$  points. We can repeat this process for the next  $n$  points starting at the second point, then the third point, and so on.

To get the smoothed second derivative, this same algorithm was applied on the points obtained for the first derivative. Due to the nature of this smoothing algorithm, it takes off points on both the left and right ends of the curve it is smoothing. This loss of side points does not significantly affect our analysis because the primary focus is on the meniscus at the center of the plates. There are remarkable differences between the unsmoothed first and second derivatives, as shown in Fig. 5. Whereas the unsmoothed second derivative is so noisy that no real meaning can be gotten from it, the smoothed second derivative is very well-behaved.

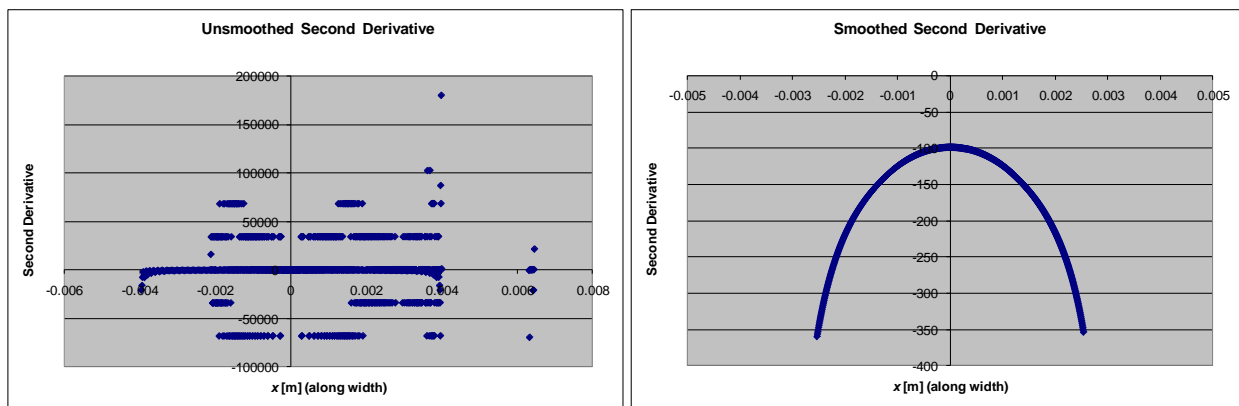


Figure 5: Comparison of the unsmoothed and smoothed second derivative. The unsmoothed curve has a huge range of values, and such a large distribution of the points makes it meaningless. On the other hand, the smoothed curve had a much smaller range and looks reasonable. Note that the smoothed curve does not extend as far as the unsmoothed one. The right-most point on the smoothed curve is at around 0.0025 m, whereas the right-most point on the unsmoothed curve reaches around 0.0040 m.

To get the points from “Surface Evolver,” the image method was preferred over the dump-file method because the picture had evenly spaced pixels whereas the dump-file contained points scattered at irregular intervals due to “Surface Evolver” using a numerical method. Having the points at set intervals apart made it much easier to numerically calculate the curvature, which is required for the predicted meniscus height-of-rise. Also, after many refinements, the dump-file would have many more points than were actually needed. Even though the precision of the bitmap method was limited to the resolution of the image, the smoothing algorithm made the smoothed-out bitmap calculation virtually the same as the smoothed-out dump-file calculation, as shown in Fig. 6.

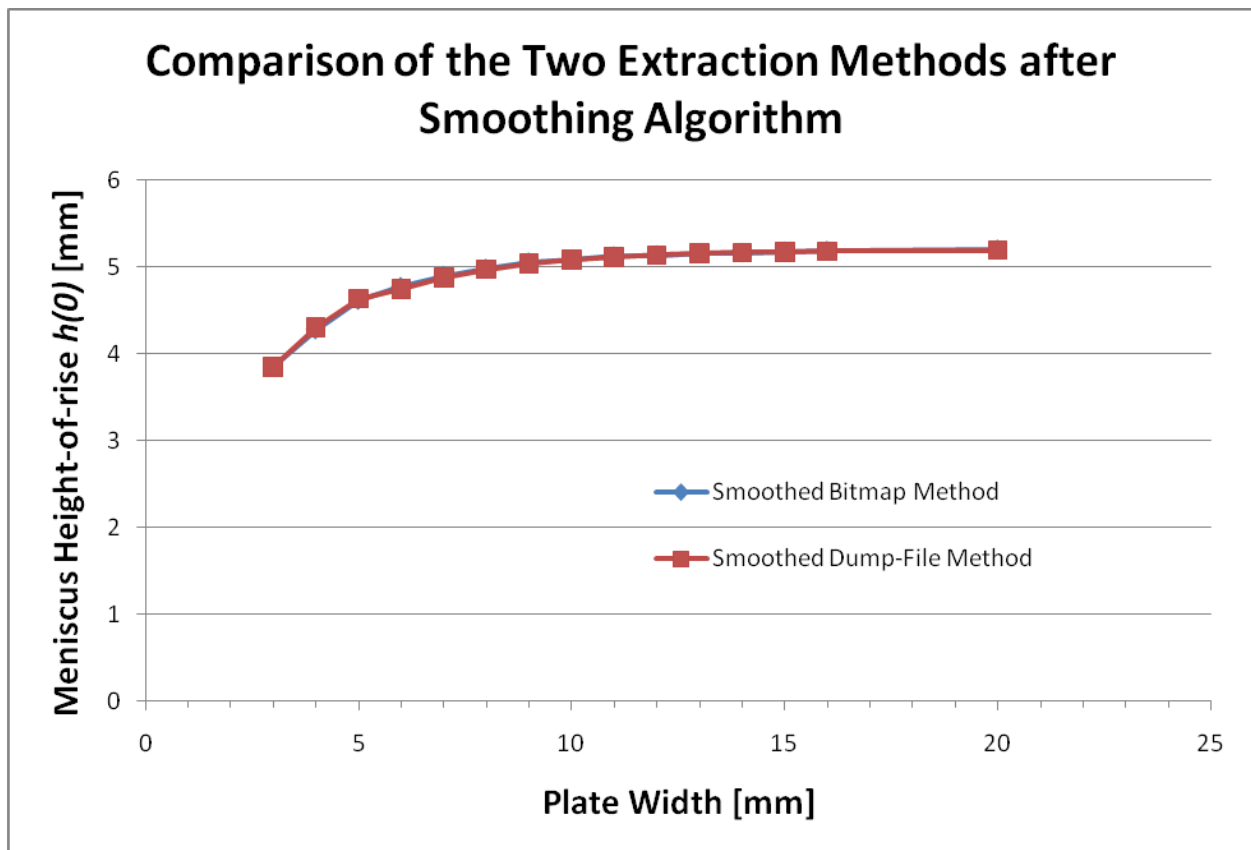


Figure 6: Calculated meniscus height as a function of plate width. The blue points, which are largely obscured because the blue line is virtually the same as the red line, are calculated heights from the smoothed bitmap using Eqn. 1. The red points have been obtained from calculating the same height-of-rise from the smoothed dump-file using Eqn. 1. Because the two line up so well, the two methods yield basically the same results, which is expected since the data itself is inherently the same, just extracted using different methods.

## Results

After applying the smoothing algorithm, the radius of curvature could be calculated by substituting the first and second derivatives into Eqn. 2. This enabled a predicted meniscus height to be calculated using Eqn. 1. Both this curve calculated using Eqn. 1 and the curve directly extracted from “Surface Evolver” are very similar, as shown in Fig. 7. For wider plates, the calculated and extracted curves line up almost exactly, but for smaller plates such as 3 millimeters, the calculated curves are slightly under the extracted ones, most likely due to the smoothing algorithm not being able to handle fewer points or “Surface Evolver” having trouble calculating the profile under the edge effect near the edges of the plates. For very wide plates, for example, 16 millimeters, the calculated results are slightly above the extracted results. Overall, the calculated and extracted curves are very close for all cases.

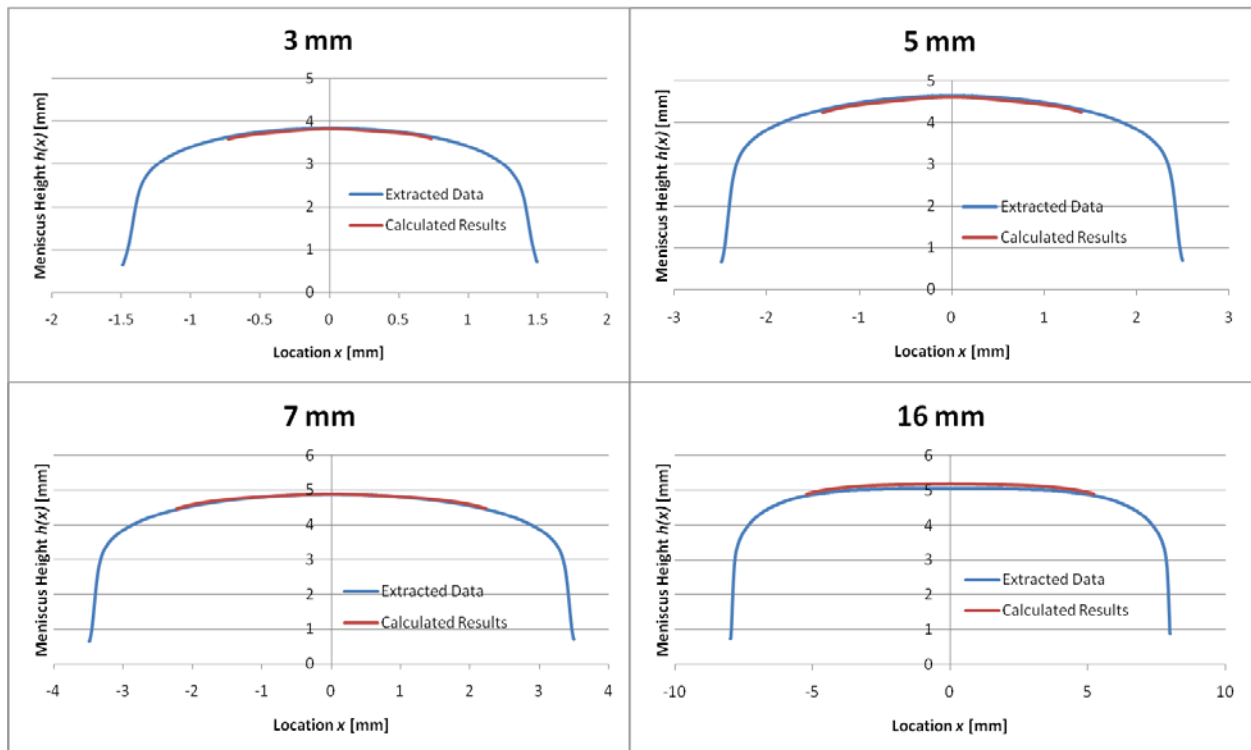


Figure 7: The comparison of the extracted data and calculated results for several different plate widths. As shown, they all line up very well, showing that “Surface Evolver” is consistent with the calculations based on Eqn. 1. The smaller plates have the extracted data slightly under the calculated result, whereas the larger plates have a slightly higher calculated result compared to the extracted data.

A comparison of the height of the meniscus at the center position ( $x = 0$  in Fig. 7) obtained by the two methods is given in Fig. 8, where the maximum height-of-rise is plotted against the plate width. The two line up very closely, indicating that “Surface Evolver” is indeed calculating the profile correctly, as shown in Fig. 8. It is possible to see the trend that the meniscus maximum height-of-rise for narrower plates is not as high as that of the wider plates. Also, it is noticeable that the meniscus height eventually levels out such that all of the maximum heights after around a plate width of 10 millimeters are approximately the same. Performing a logistic regression on the data, a best-fit curve was obtained for the meniscus height-of-rise at the center as a function of plate width for the given temperature and plate separation distance, where  $h_{max}$  is the height of the meniscus in meters and  $w$  is the width of the plate in meters:

$$h_{max} = \frac{0.005045}{1 + 1.767e^{-576.7w}} \quad (3)$$

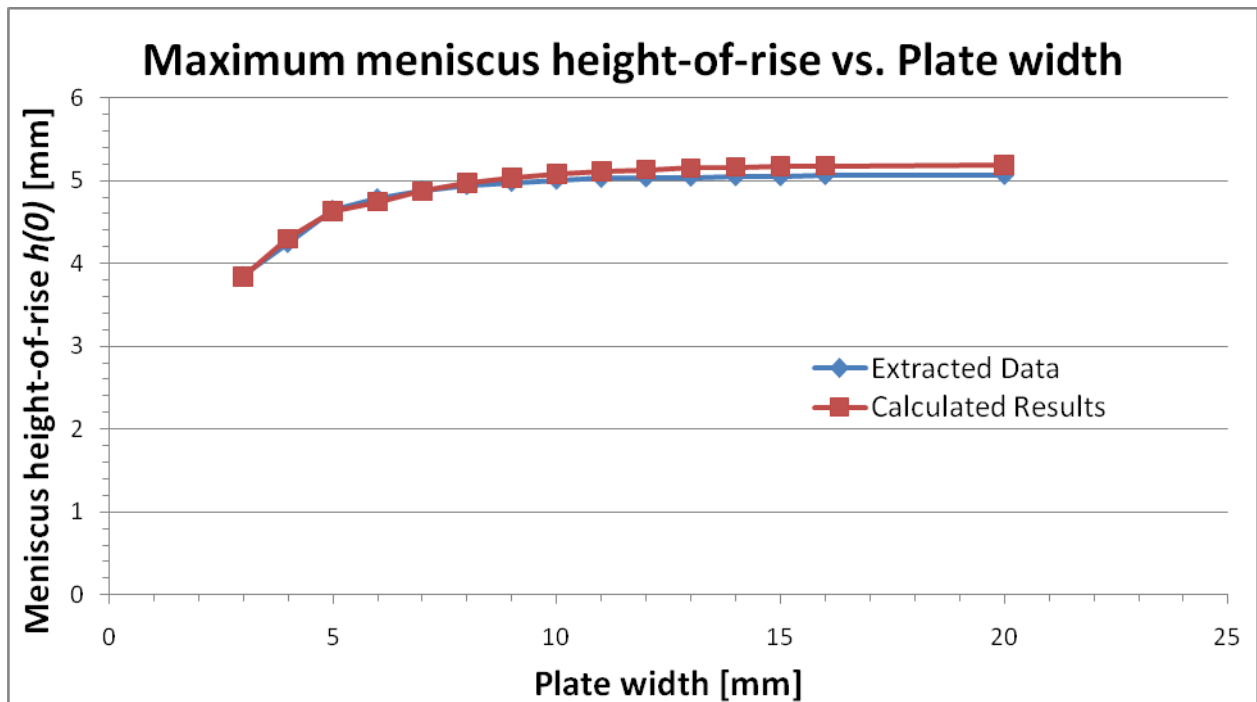


Figure 8: Meniscus height as a function of plate width. The blue points are heights measured directly from “Surface Evolver” results such as the ones in Fig. 4. The red points have been obtained by measuring the curvature of the “Surface Evolver” profile and substituting it into Eqn. 1. The close agreement shows that the “Surface Evolver” results are consistent with Eqn. 1.

Surface Evolver helps understand how cryogenic liquid deuterium behaves between two parallel plates. The parallel plate geometry is desirable because it is much easier to attach electrodes onto flat plates than to put them on other shapes, such as a cylindrical tube. An applied voltage will then be able to draw up the liquid further, which is called liquid dielectrophoresis.<sup>[1]</sup> Being able to use a voltage to control the movement of the liquid deuterium is a viable method of moving it remotely at cryogenic temperatures.

This voltage can increase or decrease the amounts of liquid deuterium by very small amounts. It is hoped that this can be used to manipulate the liquid deuterium and dispense very small amounts of it with good accuracy.

### **Movement of a Droplet between Horizontal Plates**

A droplet of liquid between two perfectly horizontal plates will stay put between the plates, but if the plates are not parallel to each other, then the droplet will tend to move. For hydrophobic droplets, which have contact angles greater than  $90^\circ$ , the droplet will begin to move towards the diverging area of the plates. For hydrophilic droplets, which have contact angles less than  $90^\circ$ , the droplet will begin to move towards the converging area of the plates, as shown in Fig. 9.

This setup is not as amenable to “Surface Evolver” because this seeks to actually move the droplet around whereas the previous experiment obtained an equilibrium position of the same deuterium between the plates. However, “Surface Evolver” will still move the droplets in the correct directions based on their contact angles. Although the droplet is moving in the correct direction, it is not doing so as a function of time because the evolutions are on a gradient descent method, not as an evolution with time.



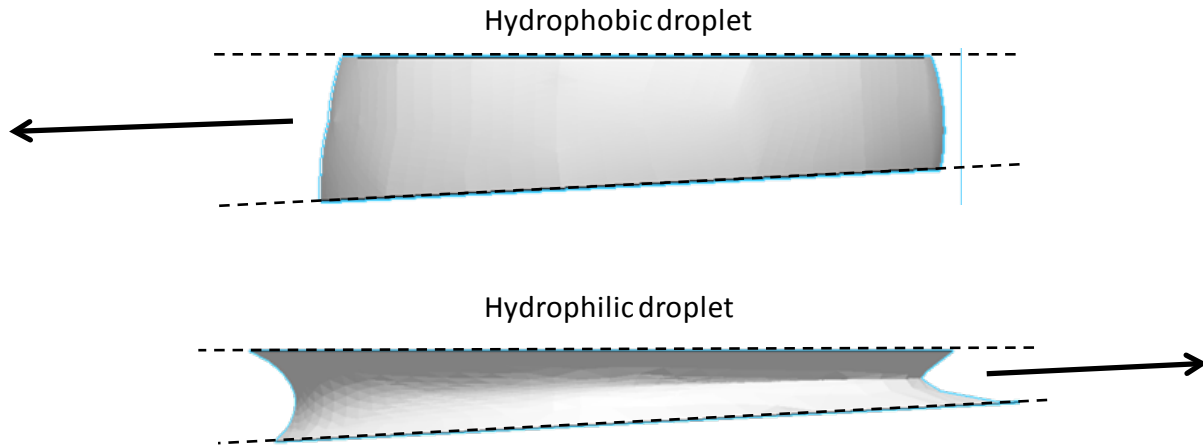


*Figure 9: The movement of a hydrophobic droplet and a hydrophilic droplet. The hydrophobic droplet is in a wider region of the plates and is moving towards the diverging area. The hydrophilic droplet is in a narrower region of the plates and is moving towards the converging area. Note that the textures on the two droplets do not look smooth because “Surface Evolver” is not good at physically moving droplets; instead it just seeks out an equilibrium shape.*

Liquid deuterium is an extremely hydrophilic droplet because it has a contact angle of  $0^\circ$ , so it will move towards the narrower area between the plates. Because of this behavior, it is possible to transport miniscule volumes of cryogenic liquid deuterium to meet the target shells using horizontal plates after a specific volume has been measured out and dispensed.

Also, a voltage can be applied by attaching electrodes onto the plates. As before, the voltage will change the behavior of the liquid deuterium, allowing greater control over its movement so that it can be ultimately dispensed and transported manually into target shells.

Due to the effect of electrowetting, the applied voltage will increase the contact angle of a hydrophilic droplet such as liquid deuterium,<sup>[2]</sup> so that it can still be moved around once it exits the horizontal parallel plates.

## **Conclusion**

“Surface Evolver” is very effective in modeling the behavior of cryogenic liquid deuterium in a vertical parallel plate geometry. MATLAB was used to process the data from “Surface Evolver,” which produced accurate results that are consistent with the theoretical predictions regarding the meniscus height-of-rise. By using this software tool, it is possible to see the effects of the plate width on the maximum meniscus height-of-rise, which occurs in the middle of the plate. Although “Surface Evolver” is not well-suited for showing the behavior of a droplet of liquid between two horizontal, non-parallel plates, the computer program is able to show both the general shape of the droplet and the direction it will move based on the plate misalignment angle and the contact angle between the plates and the droplet. Gaining a better understanding of the behavior of liquid deuterium can aid in the design of an effective assembly-line method to build and transport laser targets on-site to make laser fusion become a viable energy source in the future.

## **Acknowledgements**

I would like to thank Dr. Stephen Craxton for running the high-school summer program at the Laboratory Laser Energetics and giving me this research opportunity. I would also like to thank Prof. Thomas B. Jones for being my advisor and for instructing me and helping me through my research. Additionally, I would like to thank Weiqiang Wang for assisting me in learning how to use “Surface Evolver” to run various simulations. Lastly, I would like to thank Shirley Bei and Michael Richards for helping me with MATLAB.

## References

- [1] T. B. Jones, R. Gram, K. Kentch, D. R. Harding, "Capillarity and dielectrophoresis of liquid deuterium," *J. Appl. Phys.* **42**, 225505 (2009).
- [2] C. Roero, "Contact angle measurements of sessile drops deformed by a DC electric field," Proc. of 4th International Symposium on Contact Angle, Wettability and Adhesion, Philadelphia, USA, 2004.

# **Tritium Desorption from Stainless Steel Surfaces at Variable Temperatures**

**Ryan Shea**

**Fairport High School**

**LLE Advisor: Dr. Walter Shmayda**

**July-August 2010**

## **Abstract**

An experiment has been performed to measure the effect of temperature on the outgassing rate of tritium from stainless steel. The removal of water, and more importantly tritium, is an important issue when conducting D-T fusion experiments. Tritium can contaminate equipment and metal components of a nuclear fusion test chamber. The removal of tritium from these devices is important because it allows facility personnel to work with these devices safely. Using a helium gas stream and a glass exposure chamber insulated inside a ceramic oven, the effect of temperature on the rate of tritium desorption was measured to find the optimal temperature for the removal of tritium and water. The helium gas stream flowed through the exposure chamber at a rate of 100 ml/min to remove surface contamination from a stainless steel coupon inside the chamber. The tritium in the gas stream was transferred to a liquid solution, which was counted in a liquid scintillation counter to determine the amount of activity removed at the different temperatures. The data shows that the removal of tritium is affected by three variables: the rate of tritium diffusion to the surface from the bulk, the rate of tritium desorption from the surface, and the rate of tritium removal by the gas stream.

## **Introduction**

The increasing need to find an alternative fuel source has led to a similar increase in the amount of research performed to study and analyze nuclear fusion reactions. Deuterium

and tritium, (DT), are the primary source of fuel for nuclear fusion reactions. Tritium is a heavy isotope of hydrogen containing one proton and two neutrons. It is radioactive and can contaminate devices used to monitor the nuclear fusion reactions. This can lead to problems if the tritium migrates from the surface of the device into the bulk. If the bulk of an object is contaminated, simply removing tritium from the surface will fail to completely decontaminate the device because surface contamination will occur again as tritium migrates back out of the bulk. Similar problems are experienced with water contamination in industries requiring moisture-free plumbing or apparatus. Increasing purity requirements in the semiconductor industry have called for a removal of moisture from all pure gas streams. Water desorption from the inner surfaces of metal process lines can contaminate a pure gas passing through the plumbing with low levels of water vapor. This can lead to a loss of yield and lifetime in large-scale devices.

The removal of tritium and water from an object is affected by many factors. Humidity has been shown to increase the rate of removal of tritium from contaminated devices. To further understand the process by which tritium is removed from a device the effect of temperature on the rate of removal has been studied. The desorption process depends on the three main factors shown in *Figure 1*: the rate of tritium diffusion from the bulk into the surface oxide, the tritium diffusion rate through the oxide layer, and the rate of tritium removal from the surface of the air-oxide interface. Tritium diffuses from the metal bulk through the oxide layer to the surface where it desorbs into the gas stream. Each step has a distinct rate. For simplicity the three separate processes have been treated

as one process in this report. Modeling of the separate processes involved in tritium desorption from stainless steel has been performed by Karin Hsieh<sup>1</sup>. She considers the factors affecting tritium desorption from the surface and diffusion from the bulk and through the oxide layer in her models of the tritium desorption rate.

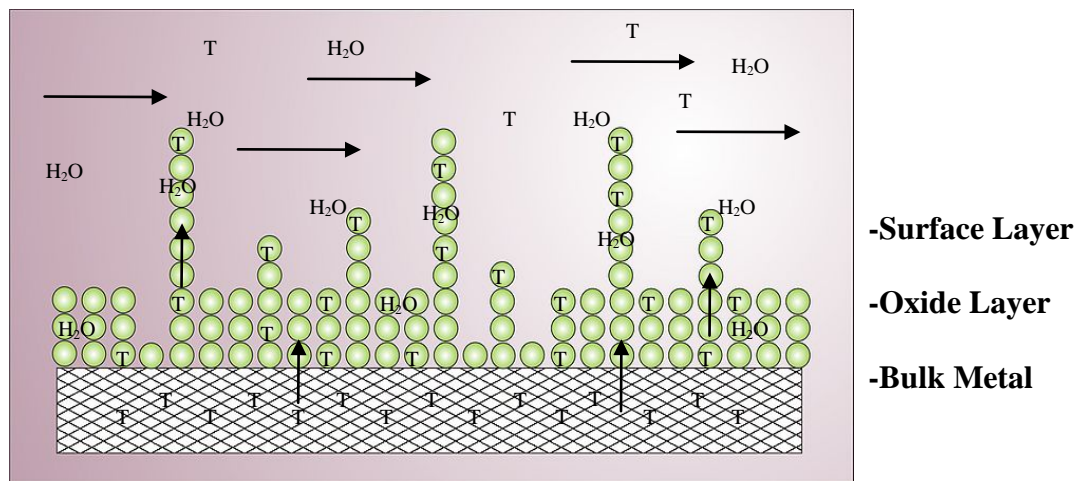


*Figure 1: Structure of a surface showing the bulk metal, the oxide layer, and the air-oxide interface. Tritium diffuses from the bulk metal through the oxide layer to the surface layer where it desorbs into the gas stream.*

### **Experimental Setup**

The experiment is illustrated in *Figure 2*. Helium flows from a high-pressure tank through a regulator where the helium pressure is reduced to about 20 psi and into a purifier to remove any traces of moisture and organic contamination in the helium. The helium flow rate is set at 100 ml/min with a mass flow meter. The water vapor content in the helium is measured with a dew point sensor, to ensure the stream is dry before it is introduced into

the exposure chamber. The exposure chamber is a 43.2 cm long quartz tube situated inside a ceramic oven that is used to control the temperature of the tube. A thermocouple located inside the tube sends information on the temperature back to a laptop computer where it is recorded by a data acquisition program. The quartz tube contains one of the small tritiated stainless steel samples, dubbed coupons due to their rectangular shape. The coupon is pushed about 23 cm into the oven, which is then closed up to prevent any leakage of radioactivity. The helium purge transfers tritium from the coupon surface to 100 ml of liquid scintillation cocktail. It takes approximately 47 seconds for a slug of helium to flow from the oven to the liquid scintillation cocktail (LSC). The collection efficiency of the LSC approaches 100%. The activity of the tritiated LSC is monitored continuously by sampling the LSC in a liquid scintillation counter. This device counts the number of photons emitted by the LSC when the tritium decays into helium-3 by releasing electrons into the cocktail. The electrons cause the LSC to fluoresce. This measurement technique provides a very accurate count of the total radioactivity in the LSC and consequently a good measure of how much tritium has been removed from the stainless steel coupon. The sample of solution is returned to the vessel containing the LSC and remixed. The activity of the LSC increases with time as the trial progresses. The LSC sample takes about 77 seconds to complete the circuit. A program that works with the liquid scintillation counter collects the raw data, provides a running average and converts the count per minute to activity in microcuries per unit volume.

The data collected from each run by the data acquisition program is transferred into



a Microsoft Excel file. To help to calibrate the software and the oven, three test trials were run on low activity coupons. After the initial test coupons, four stainless steel coupons were used and labeled stainless steel coupon # 1 through 4. All of these coupons were desorbed between 439 and 454 days after the tritium exposure.

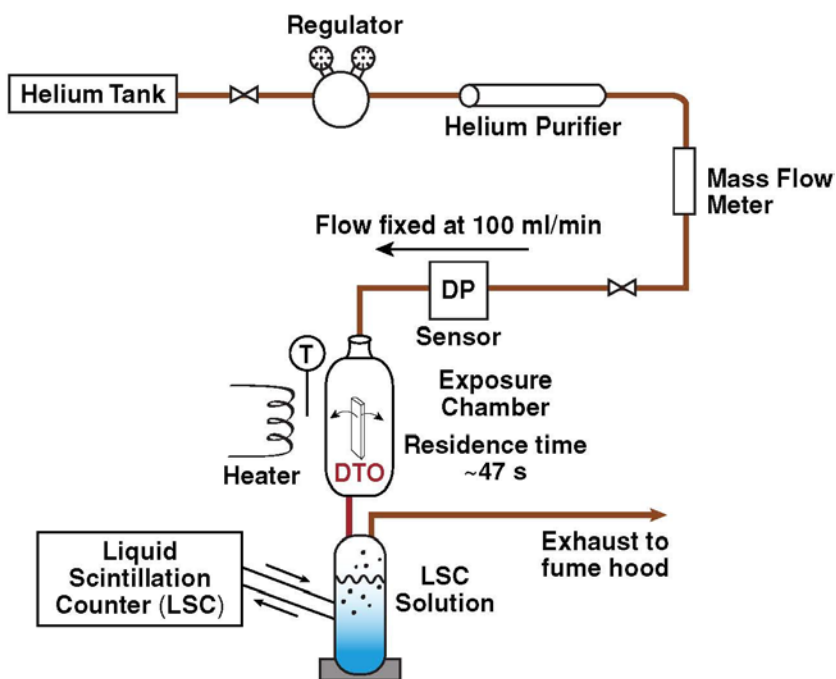
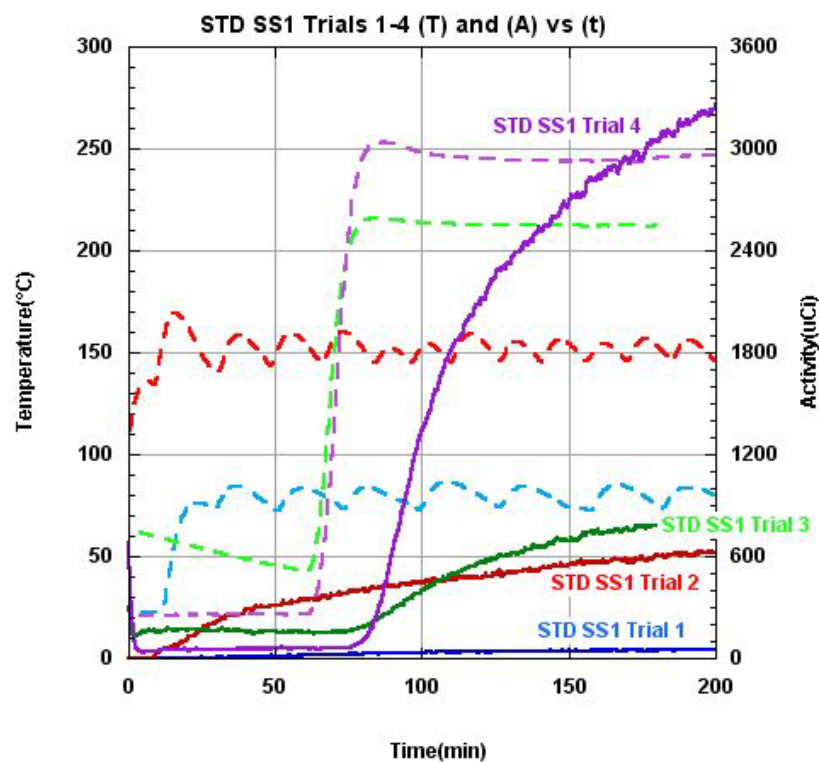


Figure 2: The experimental arrangement.

## **Results and Interpretation**

Twenty-three experiments were performed by exposing four coupons to different temperature combinations to determine the effect of temperature on the rate of tritium removal from stainless steel. The first stainless steel coupon was baked at four consecutive

temperatures: 75°C, 150°C, 200°C, and 250°C to determine if a progressive increase in temperature will cause a progressive release of activity from the contaminated sample. As show by *Figure 3* the amount of activity collected for each trial did increase with increasing temperature. Starting with the 250°C run and for every subsequent run, the oven was kept at room temperature for 1 hour at the start of the experiment before the temperature was ramped up to the final dwell temperature. This was done to ensure that any surface contamination from the previous experiment was removed before the effect of the new temperature was monitored.



*Figure 3: Evolution with time of temperature (the dashed lines) and activity (the solid lines) for the four runs of stainless steel coupon #1.*

This was done to clearly demarcate the starting point of the temperature ramp and to ensure that a stable reference activity for the LSC was established for each run. The temperature oscillations observed in *Figure 3* were caused primarily by limitations in the program controlling the oven's ramp rate and dwell temperature. A comparison of runs three and four shows clearly that an increase in temperature causes an increase in the amount of tritium desorbed from a contaminated sample; however, the data does not indicate between which temperatures the greatest increase in tritium removal will occur.

Curves such as those shown in *Figure 3* do not show fully how successful each trial was in increasing the rate of tritium removal by the helium gas stream. It is more useful to plot the outgassing rate in microcuries per unit surface area per unit time against time. The conversion from activity to outgassing rate is obtained by using the following equation.

$$Outgas\ rate = \frac{d(Activity)}{dt} * \frac{1000}{60 * 22.24} \frac{\mu Ci}{min * cm^2} \quad (1)$$

The 1000 converts millicuries to microcuries, the 60 is used to convert seconds to minutes, and 22.24 cm<sup>2</sup> is the surface area of the metal coupon. Plots of outgassing rate against time are shown in *Figure 4*. This figure gives a much better measurement of how effectively tritium was outgassed from the contaminated coupon at each temperature.

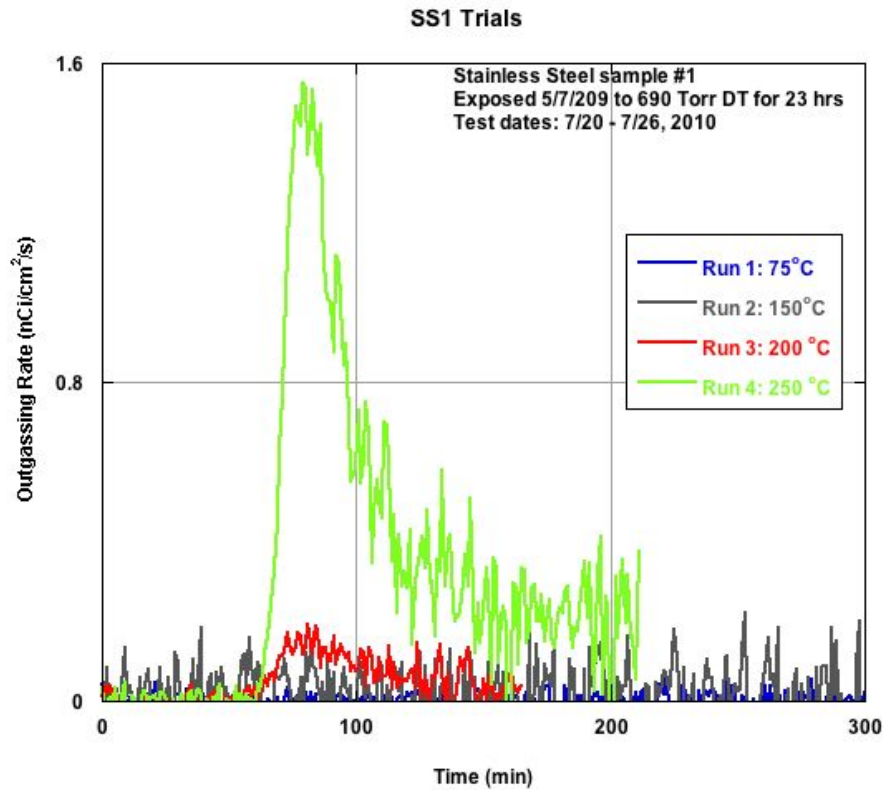
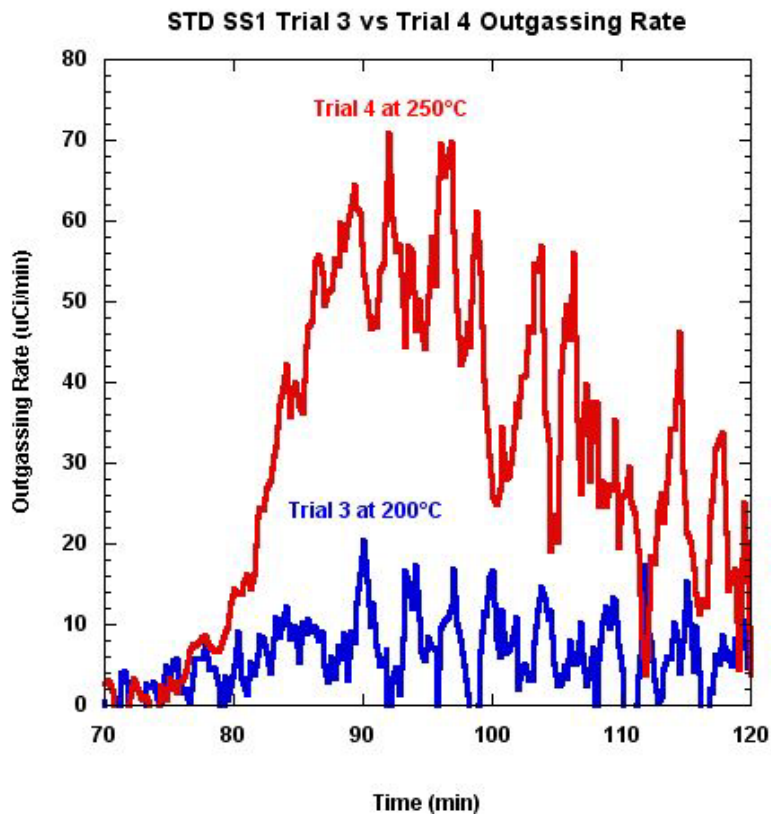


Figure 4: The outgassing rate against time for the four runs of stainless steel coupon #1.

In graphs such as *Figure 4*, a strong peak indicates that a large amount of tritium has been successfully removed from the coupon surface. Here the 75°C and 150°C runs both have very flat curves indicating much smaller outgassing rates compared to the higher temperature trials. The 200°C run has a small but noticeable peak around the 80 minute mark. This indicates that for this run outgassing of tritium was greatest at the 80<sup>th</sup> minute of the experiment. It also indicates us that using 200°C to desorb tritium was moderately successful in increasing the rate of outgassing from the contaminated coupon. A stronger peak is found for the 250°C run, approaching 1.6 nCi/cm<sup>2</sup>/s near the 80<sup>th</sup> minute of the

trial. The 250°C run increased the outgassing rate of tritium by a factor of about 3.5 relative to the 200°C run as shown in *Figure 5*. *Figure 5* provides the same data as *Figure 4* but on an expanded scale around the time of interest, 80 min. Also noticeable is the fact that the coupon continued to outgas tritium at relatively high rates during the 250°C run, confirming that a higher temperature is key when trying to remove tritium from a contaminated metal.



*Figure 5- Outgassing rate at the 200°C and 250°C runs for stainless steel coupon #1, around the time of peak outgassing.*

An important aspect of the experiment was to determine the total amount of radioactivity removed from each coupon. *Figure 6* shows the percentage of the total radioactivity that was removed during each run at each dwell temperature as well as the total amount of activity removed. It is clear from *Figure 6* that the 250°C run removed the largest amount of tritium by far from the coupon, with nearly 75% of the total tritium removed. It is also important to note that at 75°C, less than 1.5% of the total tritium is removed from the coupon.

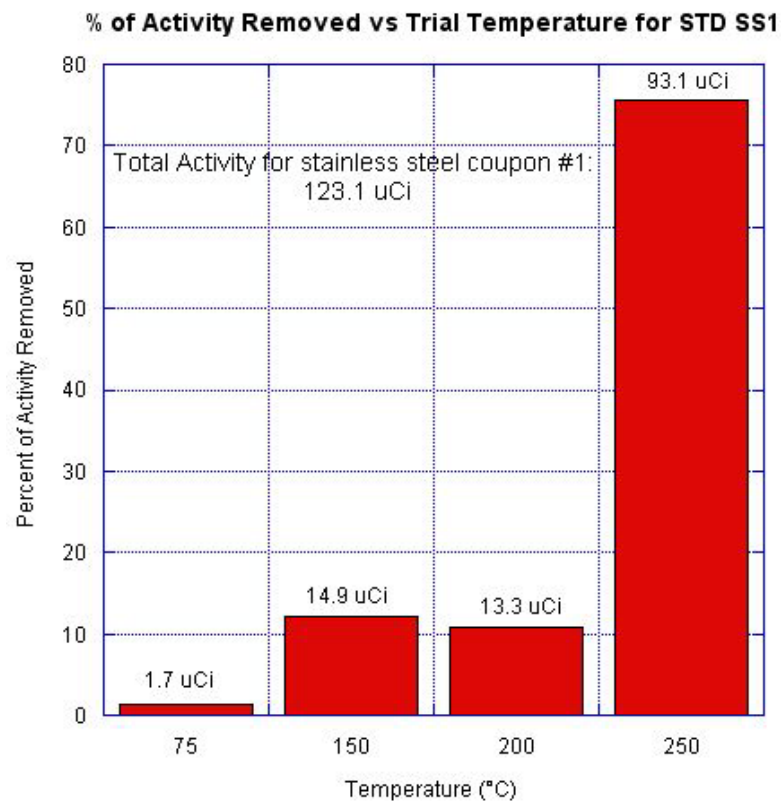


*Figure 6: Percent of the activity removed at different dwell temperatures for the four runs of stainless steel coupon #1.*

To further confirm the effect of temperature on the outgassing rate of tritium from a contaminated sample, a second stainless steel coupon was subjected to a sequence of 6 bake outs at progressively higher temperature. *Figure 7* plots the temperature (the dashed lines) and activity (the solid lines) against time for these runs. As before, each trial was held at room temperature for an hour before being ramped to the final dwell temperature. These experiments re-affirm that tritium desorption increases with increasing temperature.

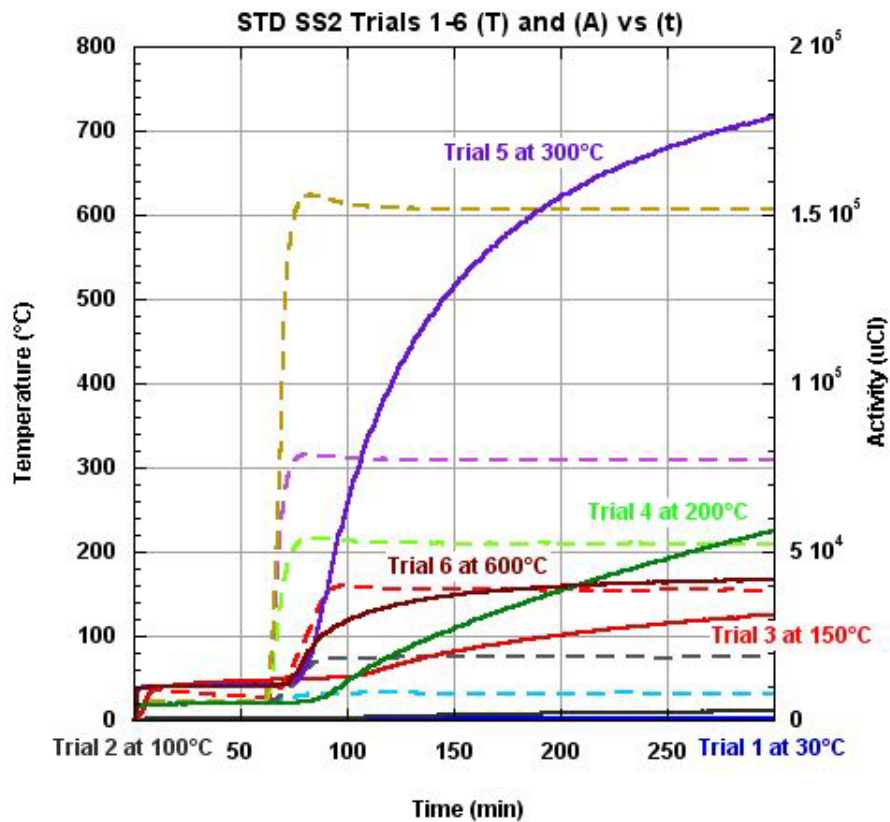


*Figure 7: Evolution with time of temperature (dashed) and activity (solid) for the six sequential bake outs of stainless steel coupon #2.*

*Figure 7* demonstrates that increasing the bake out temperature from 100°C to

150°C increases the total activity released by a factor greater than 10. However, increasing the bake out temperature by an additional 50°C, from 150°C to 200°C, increases the total activity collected only by a factor of about 1.8. This suggests that increasing the bake out temperature above 100°C is important in increasing the total amount of tritium released from a contaminated coupon.

*Figure 7* has two additional interesting aspects that should be noted. First, each trial started with a 60-minute dwell time at room temperature before ramping to the final dwell temperature within about 5 minutes. Yet on each run the activity didn't start to show this ramp until 20 minutes later, nearly 80 minutes into the run. Several modifications to the experiment were tried to reduce this response time; however, it proved impossible to reduce the response time below 75 minutes. The lag was attributed to the delayed in transferring heat from the oven to the coupon. Second, the activity collected during the 600°C bake out stagnated at 40 millicuries about 150 minutes into the run. Clearly the majority of the activity was removed from the bulk and oxide layer during the previous bake out at 300°C and suggests that it is not necessary to bake out metal at temperatures as high as 600°C. The evolution of the outgassing rates against time for these bake outs is plotted in *Figure 8*. It is noteworthy that the steady state outgassing (after the initial peak) also increases with increasing temperature, clearly demonstrated by the 200°C and 300°C runs, to suggest that the higher diffusivity of tritium leaving the metal is contributing to the outgassing rate.



The curves once again show an increase of over a factor of 10 between the outgassing rates at 100°C and 150°C. It is also important to note that the increase from 200°C to 300°C increases the outgassing rate by a factor of nearly 6.5 which can be seen clearly in *Figure 9*.

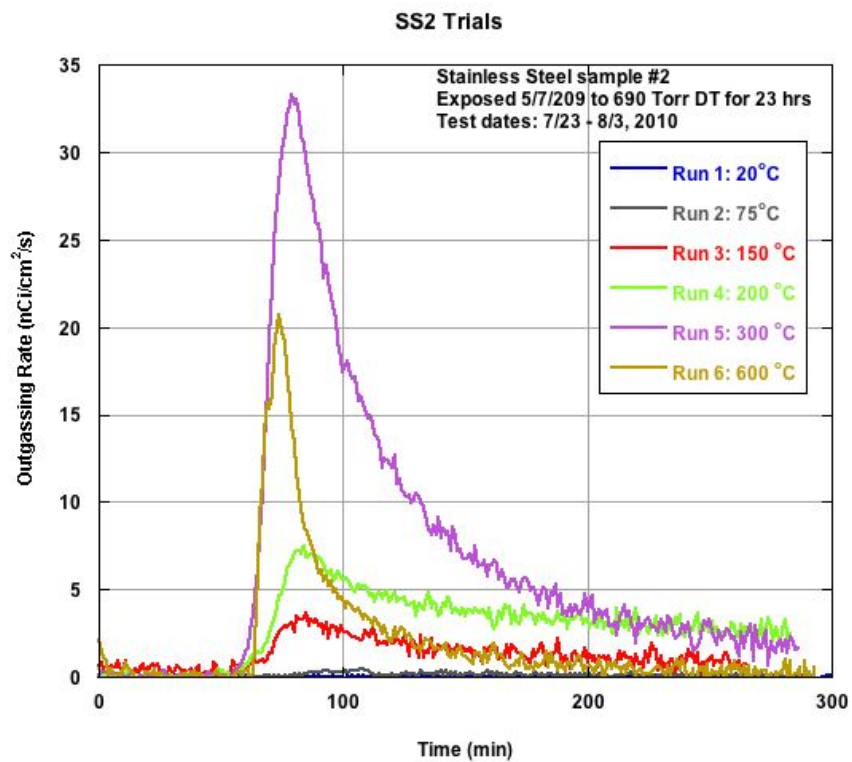


*Figure 8- Outgassing rate against time for the six runs of stainless steel coupon #2.*

*Figure 9* zooms in on some of the data given in *Figure 8* to show how increasing the bake out temperature shifts the peak outgassing rate towards earlier times. The 150°C curve peaks around 115 minutes, the 200°C curve peaks at about 95 minutes and the 300°C curve

peaks at about 80 minutes. The coupon temperature exceeds 100°C at earlier times as the bake out temperature increases from 150°C to 300°C and so surface desorption starts earlier.

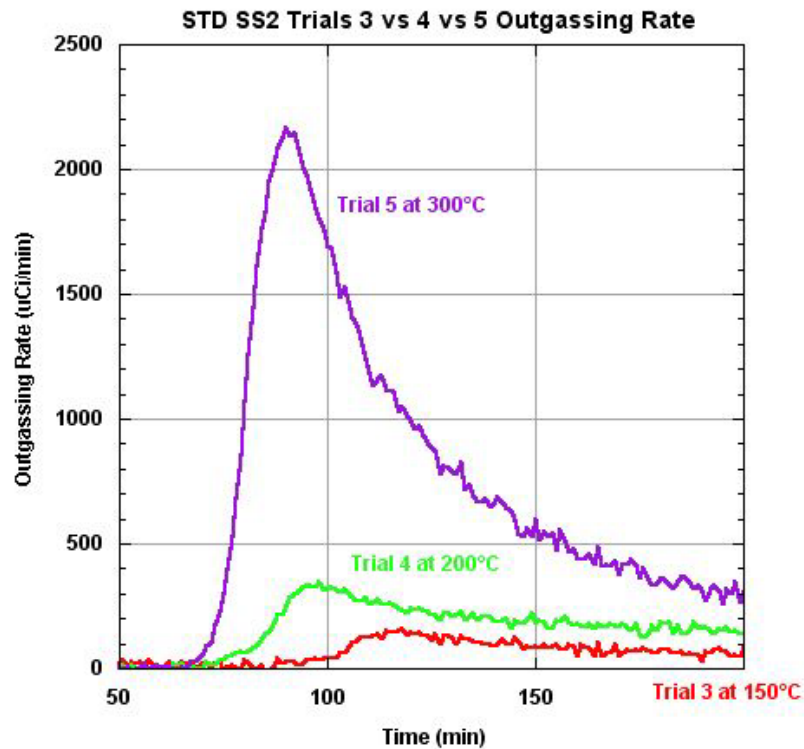


Figure 9- Peak outgassing rates for the 150°C, 200°C, and 300°C runs of stainless steel coupon #2, around the time of peak outgassing.

The percentage of the total activity removed in these runs was plotted for the different dwell temperatures in Figure 10. Tritium release increases noticeably once the bake out temperature exceeds 100°C. Furthermore, Figure 10 also shows that the 300°C

run removed about 49% of the total tritium inventory whereas the 200°C bake out only removed 18% of the inventory. By comparison, the 100°C bake out only reduced the tritium inventory by about 2%. Baking out at or around 300°C is an effective and rapid way of reducing the bulk of the tritium inventory from stainless steel.

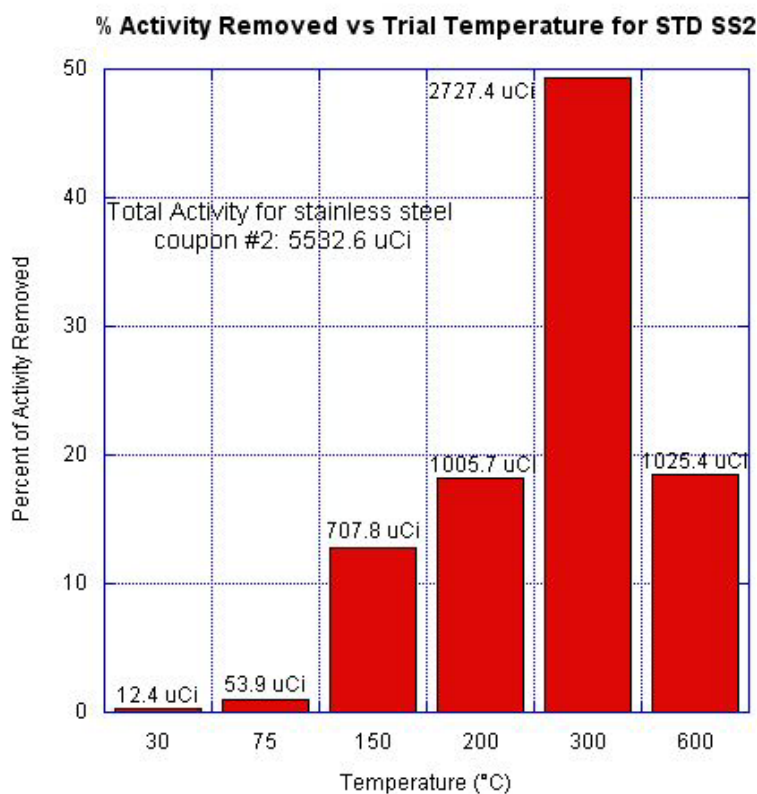
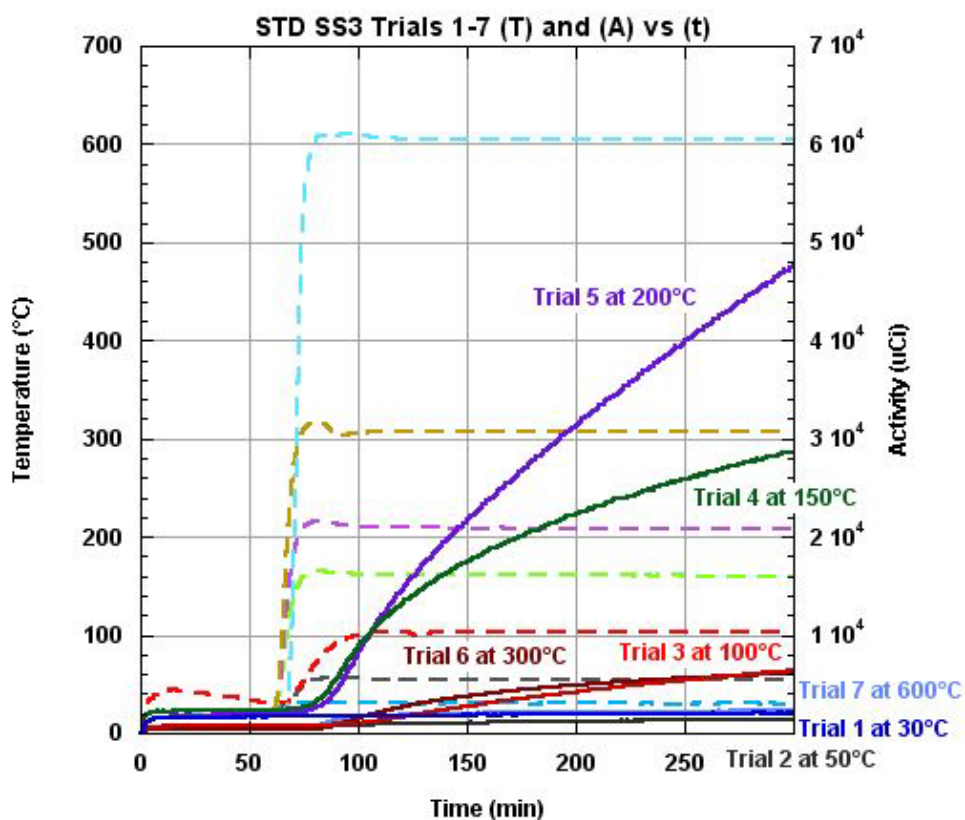


Figure 10: Percent of activity removed at different dwell temperatures for the six runs of stainless steel coupon #2.

A third stainless steel coupon was subjected to seven bake outs with a focus on

lower bake out temperatures. As shown in *Figure 11*, one trial was run at 30°C to get a base-line activity curve and outgassing rate. Subsequently, the bake out temperature was increased to 50°C and then incremented by 50°C in each successive run until the 200°C run. The sequence was completed with runs at 300°C and 600°C. As in the previous coupon most of the tritium inventory was depleted by the 300°C run. Residual tritium was released in both the 300°C and 600°C runs.



*Figure 11- Temperature and activity evolution with time for the seven experimental trials of stainless steel coupon #3.*

*Figure 11* shows a six-fold increase in the total activity removed when the bake out temperature is increased from 100°C to 150°C while an additional 50°C increase from 150°C to 200°C increases the total activity released by less than a factor of two. Tritium is bound to the surface and in the near surface as water. Bake out temperatures just above 100°C allow this tritium to boil off. However, the diffusion rate through the oxide and in the bulk metal is very low. Tritium in the lower oxide layers is not sufficiently mobile to reach the air-oxide interface. Consequently, increasing the temperature to 200°C has a less dramatic effect on the tritium release rate. Below 100°C tritium release is sluggish and only possible by the mostly weakly bound water molecules.

The plots of outgassing rate against time shown in *Figure 12* were obtained by differentiating the curves of *Figure 11* with respect to time. These curves highlight the difference in outgassing rate. When the bake out temperature is below 100°C, a discernable outgassing peak does not exist; when the temperature exceeds 100°C, the outgassing curve exhibits a peak approximately 20 to 40 min after the bake out begins. These curves are peaked because above 100°C there is a sudden and rapid release of surface-bound water followed by a slower, temperature-dependent diffusion-controlled transmission of tritium from the metal and the oxide to the surface where it is released to the purge gas. The diffusion of tritium from the metal bulk increases with increasing bake out temperature.

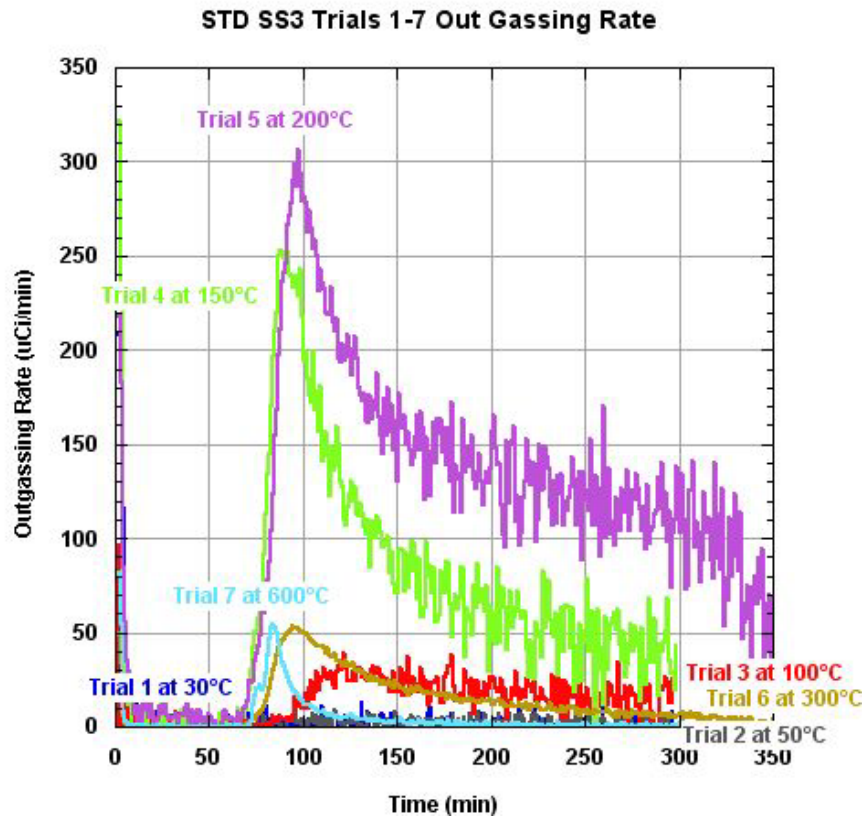


Figure 12- Outgassing rate against time for the seven experimental trials of stainless steel coupon #3.

Inspection of *Figure 12* supports the discussion in the previous paragraph. The outgassing rate at times long after the peak is sensitive to the bake out temperature. At 100°C and 150°C the outgassing rates at 250 min are small because the tritium that can participate in the outgassing must be close to the air-oxide. Tritium located at greater depths cannot reach the surface. At 150°C, the outgassing rate at 250 min is lower than for

the 200°C case for the same reason. However, at 600°C the diffusion rates are rapid compared to the rates at 300°C and the outgassing rate at long times decays towards zero much more rapidly. All the tritium is removed from the bulk more quickly at 600°C.

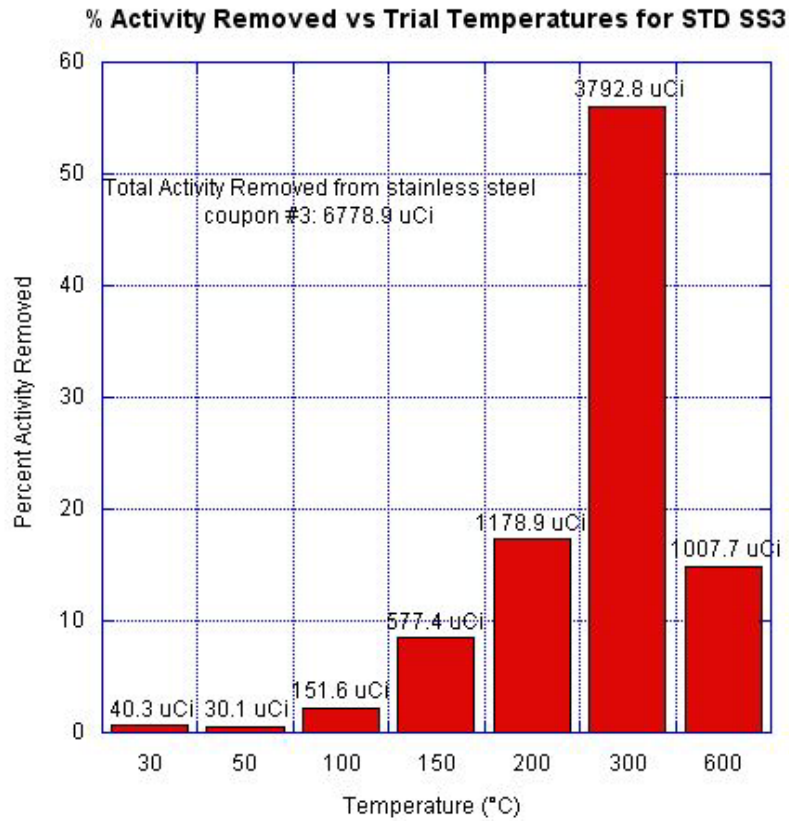


Figure 13- Percent activity removed at different dwell temperatures for the seven runs of stainless steel coupon #3.

The percentage of activity removed from the third stainless steel coupon for the seven runs was plotted against the bake out temperature in Figure 13. Almost 55% of the

total activity was removed in the 300°C run. This value seems high when compared to the activity curve in *Figure 11* and suggests there was an error in the data collection during the run or in the measurement of the total activity collected. The two measurements are based on independent measurement techniques. However, if the measurement of the total activity collected is erroneous, the error cannot exceed approximately 0.5 mCi because each sample is known to contain a total of 6.3 mCi. It is noteworthy that below 100°C the total amount of activity released is very small and consistent with the understanding that the tritium originates from the region close to the air-oxide interface.

To understand more clearly the effects of just exceeding 100°C and to ensure that lowering the temperature in a sequential run does not have an unexpected effect on the outgassing rate, a fourth stainless steel coupon was baked out six times at temperatures close to 100°C. The data is shown in *Figure 14*. The temperature for each run was ramped up to the final dwell temperature after one hour, similar to the previous two coupons. *Figure 14* shows that at temperatures below 100°C, the activity slopes are flat (not peaked) and low. The outgassing rates are small. At temperatures above 100°C, the activity curves have much larger slopes and exhibit an initial peak when they are differentiated. The 50°C run has high activity because the liquid scintillation cocktail was not changed after the baseline run. The starting activity in the 85°C run was much higher than in the 125 °C case because the surface tritium was replenished by tritium diffusing from the bulk metal into the oxide layer and up to the air-oxide interface during the 125°C run. The activity in *Figure 14* is given in counts per minute instead of disintegrations per minute due to a slight



glitch with the data acquisition program.

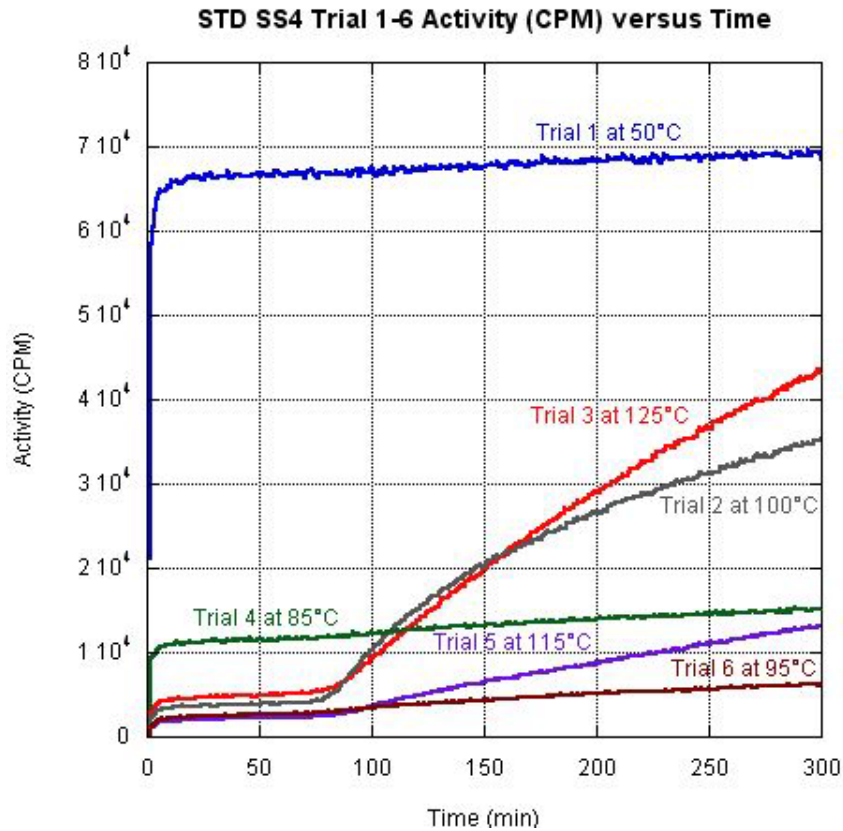


Figure 14- Activity in counts per minute against time for the six runs of stainless steel coupon #4.

Figure 15 provides the outgassing rates plotted against time for the activity curves shown in Figure 14. The outgassing rate decreases from run 2 to 3 even though the temperature increases. This suggests there are two processes at work: desorption from the surface and diffusion through the oxide layer. The latter process is slower and

consequently the tritium inventory in the oxide near the oxide air interface is depleted. The tritium contribution for the bulk metal is probably not a factor because the diffusion coefficient is small at these temperatures.

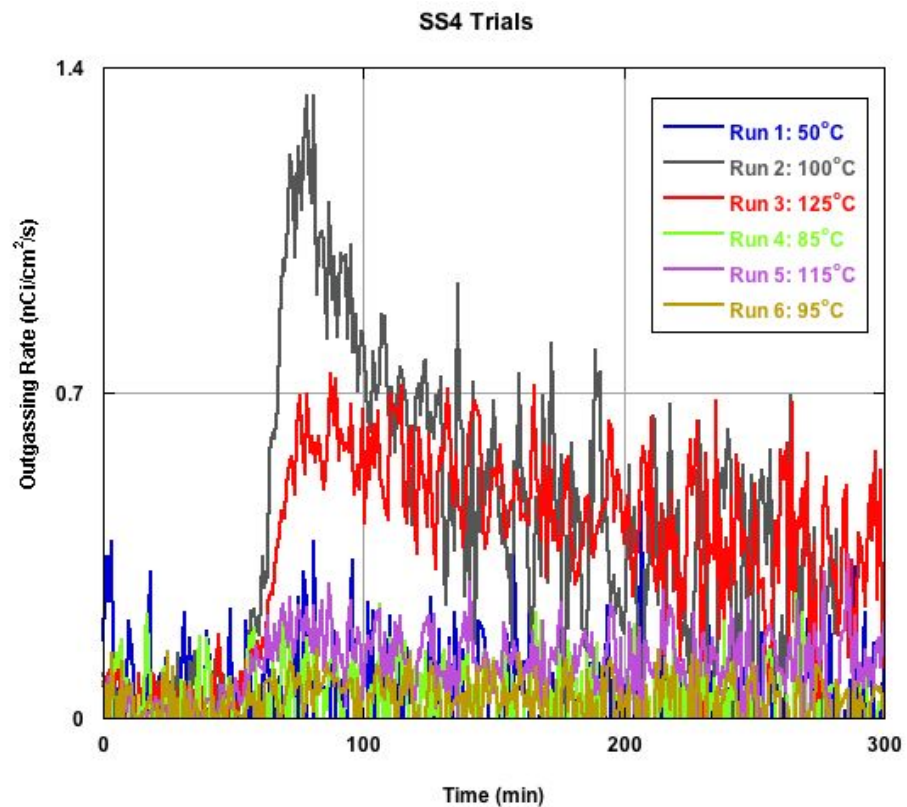
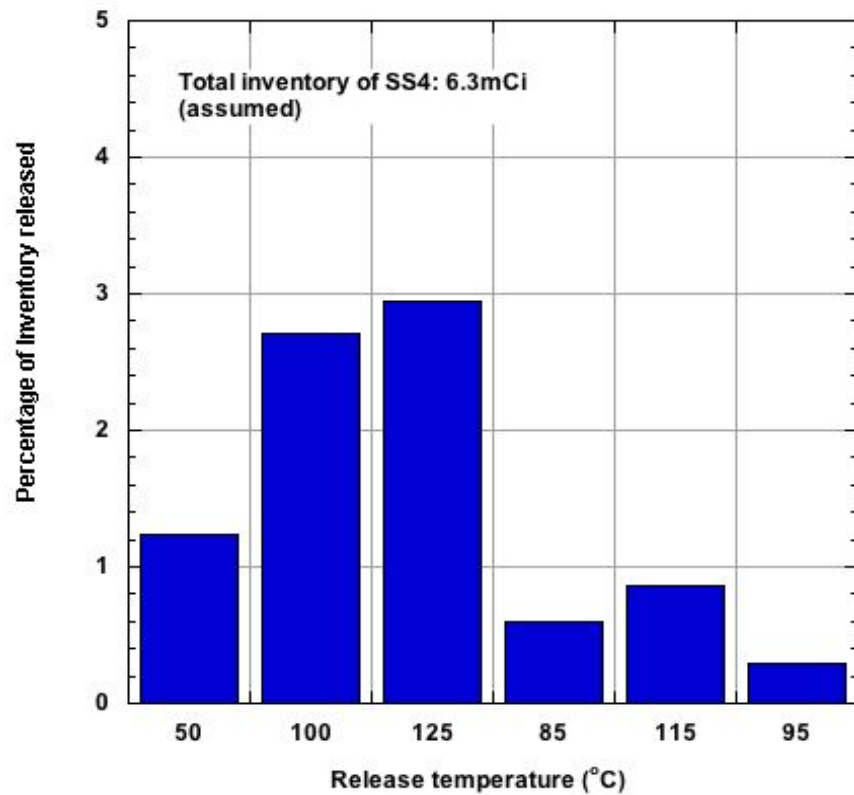


Figure 15 Outgassing rate against time for the six experimental trials of stainless steel coupon #4

Figure 15 also exhibits the expected peak in the outgassing rate when the bake out temperature exceeds 100°C and then decreases to a negligible value once the tritium is removed from the outermost layers. Note that the 115°C run also has a low outgassing rate

and further strengthens the suggestion that the 100°C and 125°C runs depleted the tritium inventory in the coupon's oxide layers close to the air-oxide interface.



*Figure 16: Percent activity removed at different dwell temperatures for the six runs of stainless steel coupon #4.*

The percentages of activity removed at the different bake out temperatures are provided in *Figure 16*. Only 8.5% of the total tritium inventory was removed during these runs. Since tritium from the bulk is unlikely to contribute to the amount removed, it can be concluded that the oxide layer contains about 10% of the total tritium inventory; the

remainder of the tritium resides in the metal bulk and in the oxide layers closest to the metal bulk. Increasing the desorption temperature slightly above 100°C is effective at reducing the oxide-bound tritium inventory but not at depleting the total tritium inventory. Even though there is an increase in the amount of tritium removed at 115°C relative to the 85°C run, the increase does not approach the levels of the 100°C and 125°C runs, further supporting the contention that a significant fraction of the oxide-bound tritium had been removed but that the innermost layers of tritium and tritium incorporated in the metal had not been able to diffuse through the oxide layer and desorb from the surface.

### **Conclusion**

An experiment has been performed to understand the effects of different dwell temperatures on the desorption rate of tritium from a contaminated stainless steel coupon. It has been shown that an increase in bake out temperature results in an increase in the desorption rate of tritium from the metal sample. Approximately 10% of the tritium resides near the surface under the present exposure conditions. The bake out temperature needs to exceed 100°C if the intention is to deplete the near-surface tritium inventory and to reduce outgassing from the metal once it is cooled to room temperature. The bake out temperature needs to exceed 300°C if the intention is to deplete the tritium inventory in the metal bulk. Bake out temperatures above 300°C accelerate the depletion of the tritium inventory in the bulk.

## **References**

1. K. Hsieh, LLE Summer High School Research Program, 2010

## **Acknowledgements**

I'd like to thank Dr. Craxton for giving me the opportunity to be part of this amazing program. I'd like to thank my advisor Dr. Shmayda for his help and support throughout the entire project. I'd like to thank Karin Hsieh, Ben Petroski, Ed Schroeder, and Matt Sharpe for their helpful support and critiques throughout the entire program. Last I'd like to thank Jean Steve for helping with all the paperwork and all the support she gave me throughout the program. Thank you all so much.

*A Design for a Shock Ignition Experiment on the NIF Including 3-D Effects*

**Laura Tucker**

Brighton High School

Rochester, New York

Advisor: Dr. R. S. Craxton

**Laboratory for Laser Energetics**

University of Rochester

Rochester, New York

January 2011

## 1. Abstract

A design for a plastic shell target has been developed for a proposed experiment for the National Ignition Facility (NIF) to investigate a two-stage shock-ignition concept in which 96 beams are used in each step (compression and ignition). To compensate for the NIF's beam configuration, the polar drive method was used, which involves pointing the beams toward the target equator. The beam pointings were also adjusted in the azimuthal direction. Two-dimensional hydrodynamic simulations using the code *SAGE* were combined with 3-D predictions of energy deposition to produce 3-D density profiles. Numerous simulations varying the selection of the 96 beams and the beam pointing, focusing, and energy ratios were used to identify an optimum design for the compression stage. Including variations in both  $\theta$  and  $\phi$ , the center of mass of the imploded shell has an rms deviation of just 8  $\mu\text{m}$  after implosion through 400  $\mu\text{m}$ .

## 2. Introduction

Nuclear fusion is a relatively recent approach to providing clean, renewable energy. One method used to achieve nuclear fusion is using laser beams to irradiate a target. The spherical target contains two hydrogen isotopes, deuterium and tritium, inside a shell of glass or plastic. When irradiated with the heat of the laser beams, the shell ablates outward and this force compresses the fuel inside the target thus creating a very high temperature and pressure environment. These extreme conditions compress the hydrogen isotopes, causing the nuclei to fuse and the fuel to explode. The deuterium and tritium fuse to form a helium nucleus and one energetic neutron. The remaining energy (that not collected from the released neutrons) is redeposited in a process known as ignition.

There are currently two different approaches to laser-driven nuclear fusion: direct drive and indirect drive. In direct drive fusion, laser beams hit the target at normal incidence from all directions [Figure 1(a)]. This is the type of fusion for which the beams of the University of Rochester’s Laboratory for Laser Energetics’ OMEGA laser system are configured. In indirect drive, the target sits inside a metal cylinder, usually made of gold, called a “hohlraum.” Laser beams enter the hohlraum through openings in the top and bottom and penetrate the insides [Figure 1(b)]. Once hit by the beams, the walls of the hohlraum emit x rays which then irradiate the target and provide the energy needed for compression. Indirect drive implosions have the disadvantage of having much lower energy efficiency due to the fact that much of the laser energy is absorbed by the hohlraum or lost through the openings. Overall, only about 20% of the laser energy is actually absorbed by the target, but this lower efficiency is made up for by the greater uniformity of the x-ray radiation.

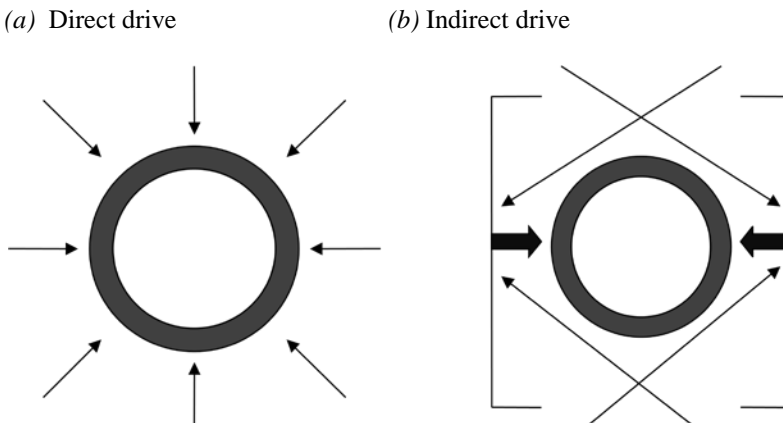


*Figure 1. The two main approaches to inertial confinement fusion. (a) In direct drive, the laser beams directly irradiate the target. The thin lines represent these laser beams. (b) In indirect drive, the target is contained in a cylindrical hohlraum, which is hit on the insides by laser beams that enter through holes in the top and bottom. The hohlraum then produces x rays (represented by the thick lines) which irradiate the target.*

The National Ignition Facility (NIF) at Lawrence Livermore National Laboratory is currently the world’s largest and most powerful laser. Completed in 2009, the NIF beams are configured for indirect drive fusion experiments. The laser beam ports are arranged in four rings at angles  $\theta$  of  $23.5^\circ$ ,  $30.0^\circ$ ,  $44.5^\circ$ , and  $50.0^\circ$  from the vertical in the upper hemisphere with four corresponding rings in the lower hemisphere. There are a total of 48 ports; laser beams are



arranged in groups of four called quads, so there is one quad per port. The fact that the beams are clustered near the poles is disadvantageous for direct drive fusion experiments. If the quads are simply pointed towards the center of the target, the equator will not be given as much drive as the poles and will therefore bulge as the target is compressed [Figure 2(a)]. This nonuniformity of implosion causes a severe loss of neutron production, which is not made up for even by the much greater energy of the NIF laser. Therefore, the beams of the laser must be repositioned away from the center of the target and towards the equator in a method called polar drive [Figure 2(b)].<sup>1,2</sup>

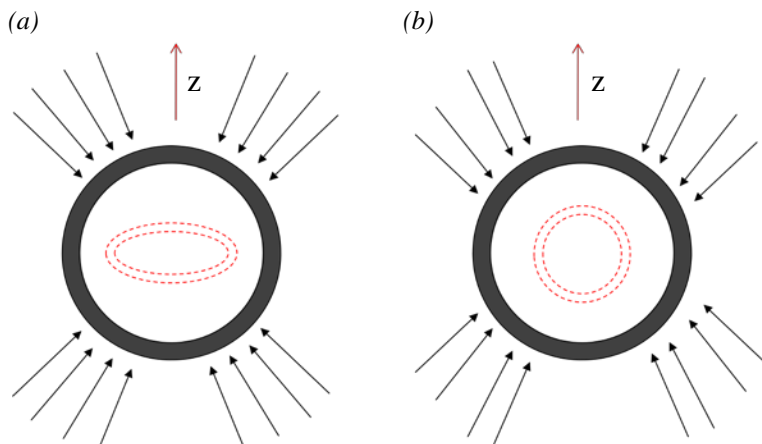


Figure 2. The possible NIF direct drive beam pointings and the resulting compression pattern of the target shell. (a) When the laser beams are pointed directly at the center of the target, the shell implodes nonuniformly. (b) By shifting the beams away from the target center and towards the equator, maximum implosion uniformity can be achieved.

### 3. Shock Ignition

Shock ignition<sup>4</sup> is a new concept for creating maximum-energy-gain fusion. Standard direct drive fusion experiments currently use a single long, high-intensity laser pulse which both compresses and ignites the target fuel in one step. A new proposal has recently been made to divide these laser pulses into two steps.<sup>5</sup> The first consists of a lower-intensity, longer laser pulse which is used to compress the target and bring the fuel as close together as possible without igniting it. The second pulse is called the shock pulse. It is extremely short and intense and its purpose is to create ignition. Due to design limitations, each NIF quad can only carry one type of pulse, and so the quads must be split between those used for the compression pulse and those

used for the shock pulse. For these designs, half of the quads were chosen to carry the compression pulse in a process that will be described in detail in this report, and the remaining quads were reserved for use in future experiments including the shock pulse [See Figure 3(a)]. The energy and duration of the initial and shock pulses compared to those of a conventional direct drive pulse can be seen in Figure 3(b).

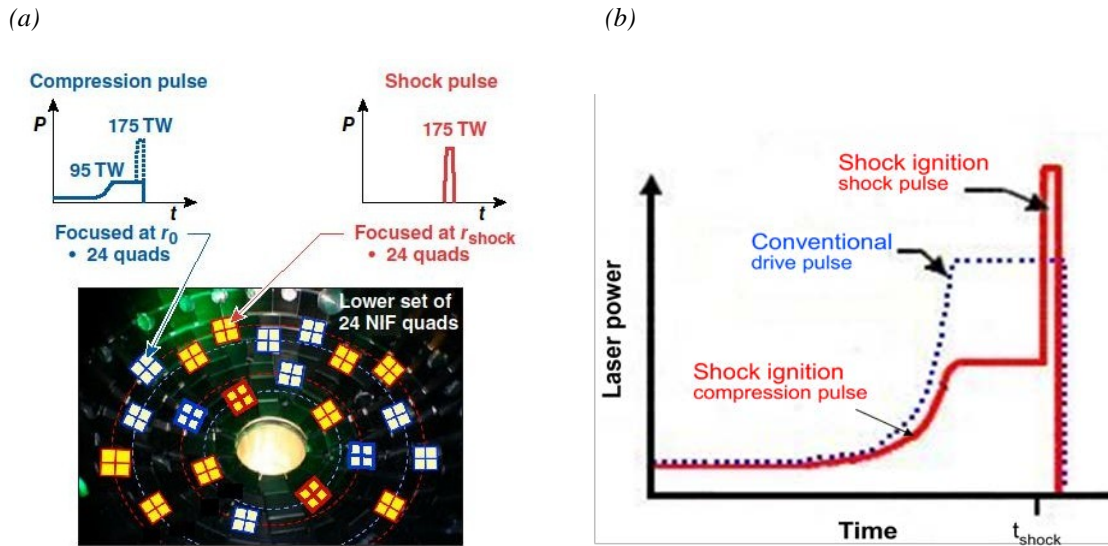


Figure 3. Graphical representations of conventional and shock ignition direct drive laser pulses. (a) Half of the NIF quads on both the top and bottom of the target chamber were chosen to be used in the compression pulse, therefore reserving the remaining quads for the shock pulse.[From Ref. 6] (b) The blue dotted line represents the conventional direct drive pulse, while the thick red line illustrates the initial compression pulse and the final, high-intensity shock pulse of shock ignition.

#### 4. Shifting and Defocusing

The proposed shock ignition designs<sup>6</sup> use the method described in Refs. 7 and 8 to implement polar drive using existing NIF hardware. The key parameters available for creating these designs are the specifications for shifting the beam pointings in the vertical and horizontal directions, defocusing the beams, and choosing which quads to use in the compression pulse. Located near the end of the NIF laser system are mirrors (see Figure 4) which can be moved in order to shift the pointing of the individual beams (to an accuracy of about 50 microns in theory) and cause the center of the beam to hit the target at a different point on the surface. By

repositioning these beams, greater or less energy may be distributed to certain points on the target surface, and the shape of the imploding target may therefore be manipulated.

The defocus of the beams can be adjusted by repositioning the focus lens towards or away from the target. This causes the focal point of the laser beam to change and therefore the size and intensity of the beam spot to increase or decrease [see Figures 4(a) and (b)].

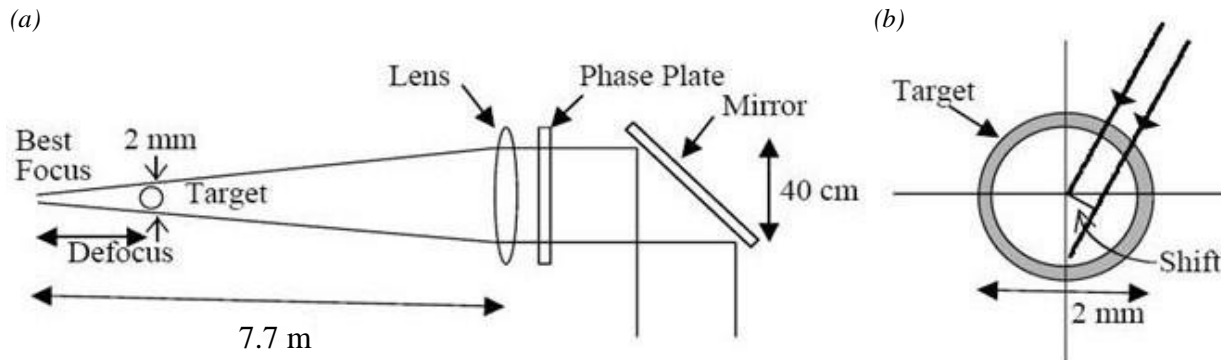


Figure 4. (a) Diagram (not to scale) showing the parts of the laser that control the parameters used in this work. Moving the lens along the beam axis controls the size of the beam at the target and tipping the mirror controls beam pointing. (b) Diagram showing how beam ring shifts are measured perpendicular to the beam direction. The angle of the beam from the vertical remains virtually constant. [From Ref. 7]

## 5. Optimization Process and the Optimized Designs

The goal of the optimization process was to develop a design, using only 24 of the NIF's 48 quads, that would cause the target shell to implode with maximum uniformity in both the azimuthal ( $\Phi$ ) and vertical ( $\theta$ ) directions. Several hundred 2-D hydrodynamic simulations including 3-D ray tracing were run using the code *SAGE* and analyzed, each with different variations of pointings, defocuses, and beam choices. The effects of certain variations were measured by isolating a single variable to be changed in increments and analyzing the outcomes of the changes. Initial analyses were based upon raytrace plots of target implosion and corresponding 1-D lineouts of average center-of-mass radius versus angle from the  $z$  axis ( $\theta$ ). Figure 5 shows two examples of the raytrace plots. Figure 5(a) depicts the target soon after the

laser pulse has been initiated and Figure 5(b) shows the target after it has imploded for 4 ns to a size of about half its original radius.

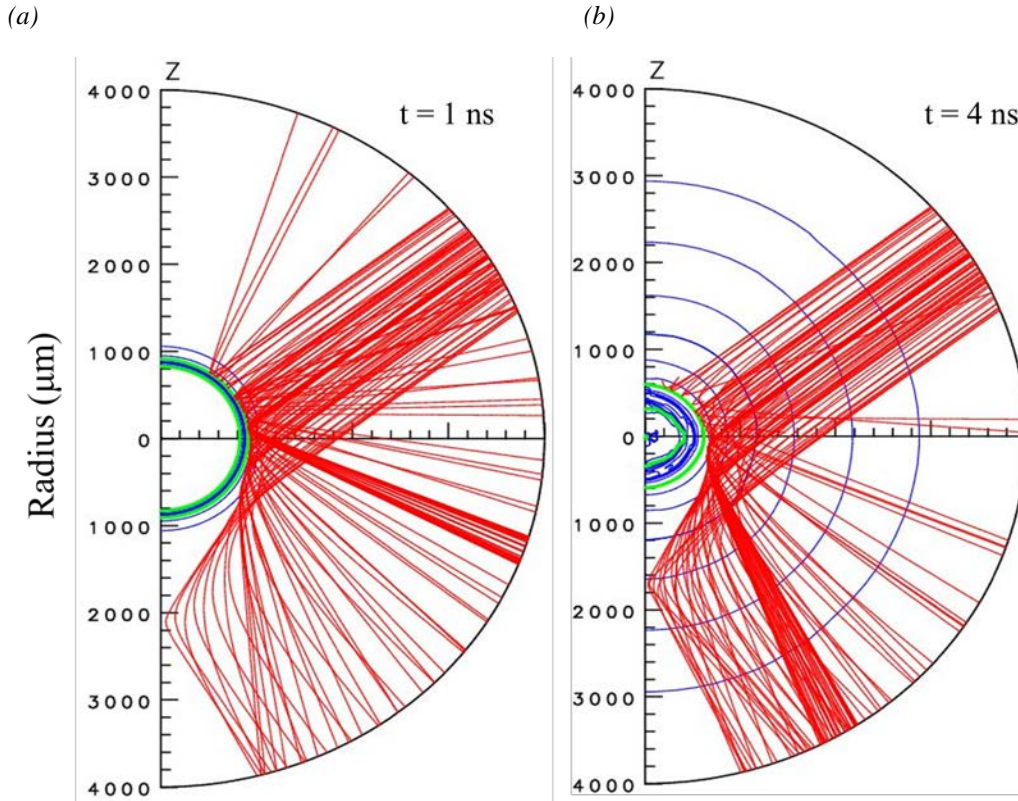


Figure 5. A comparison of two raytrace plots depicting the implosion of a target through time. (a) The relative position of the target shell is designated by the bright green lines. After only 1 ns of the laser being turned on, the shell has compressed inward very little from its original radius of 898  $\mu\text{m}$ . (b) After 4 ns, which is the length of the entire compression pulse, the target shell has imploded to about half of its original radius. The red lines in each case represent the paths of the laser beams originating from the fourth ring of quads on the NIF- the row closest to the equator of the target chamber.

The importance of optimizing the design is shown in the differences between Figures 6(a) and 6(b). Figure 6(a) depicts the results of using an initial design reported in Ref. 9. The initial design shows the characteristic bulging at the equator (depicted by the bright green lines outlining the position of the target shell) that is common in polar drive designs for the NIF<sup>10</sup> due to the lack of drive at the equator. In the design with the optimized parameters, the bulge has been smoothed considerably. The beams pointed at the equator (the 50<sup>o</sup> ring 4 of the NIF target

chamber) have also been given a tighter focus and 20% greater energy than the other beams in order to create greater intensity and therefore more equatorial drive.

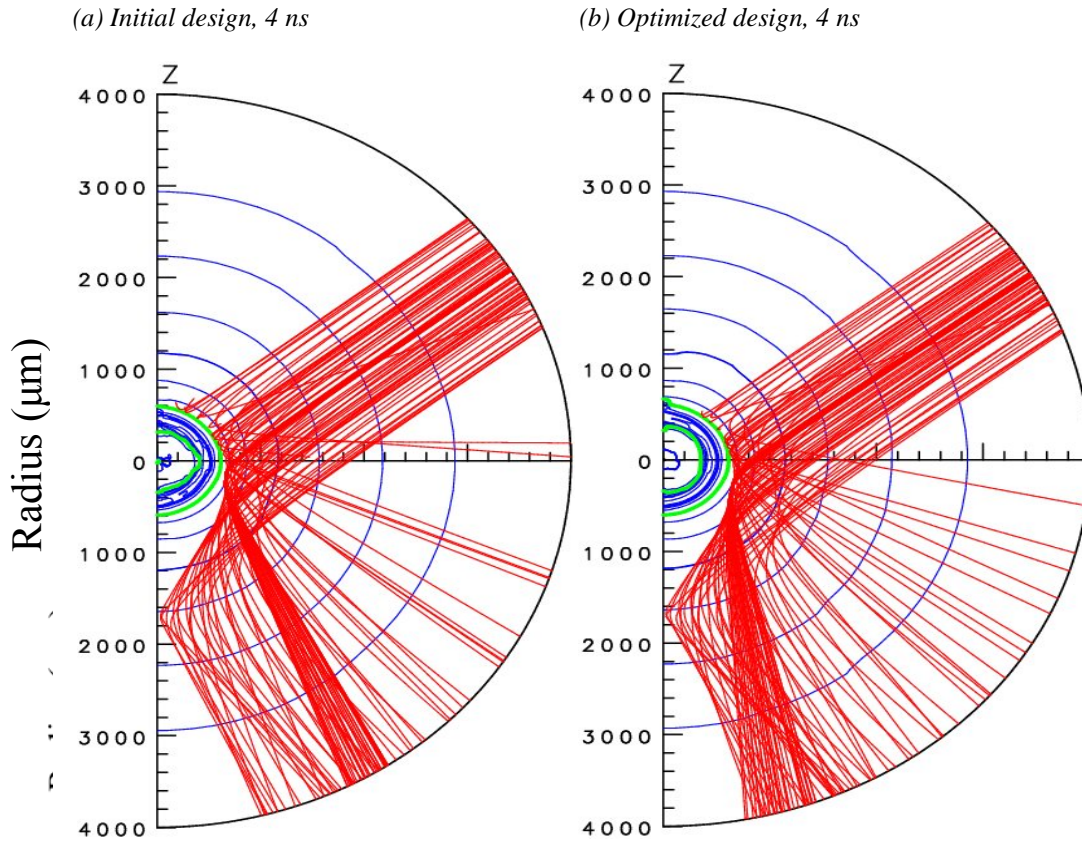


Figure 6. A comparison of two raytrace plots portraying the differences in the uniformity of the target compression after the laser beams have been on for 4 ns. (a) The initial design shows the protrusion at the equator that is common for targets compressed with polar drive on the NIF. (b) The optimized design limits the protrusion at the equator and greatly increases the circularity of the target.

These 2-D raytrace plots were converted into 1-D center-of-mass radius lineouts in order to better quantify the degree of nonuniformity in each of the target implosions. The radius of the target shell was plotted versus the vertical angle from the  $z$  axis for each case, and the root-mean-square deviation (rms) of the center-of-mass radius was calculated to determine the nonuniformity of the compression. The blue curve in Figure 7 depicts the target shell compression for the initial design, and can be compared with the red curve that depicts the

compression of the final, optimized design. As evidenced by the graph, the initial design has a much greater center-of-mass radius at the equator than elsewhere on the sphere, which means that the target shell is protruding in this region. The target shell in the optimized design has a much more even center-of-mass radius versus angle plot, meaning that the radius is similar throughout the shell and it is therefore a more spherical and uniform implosion.

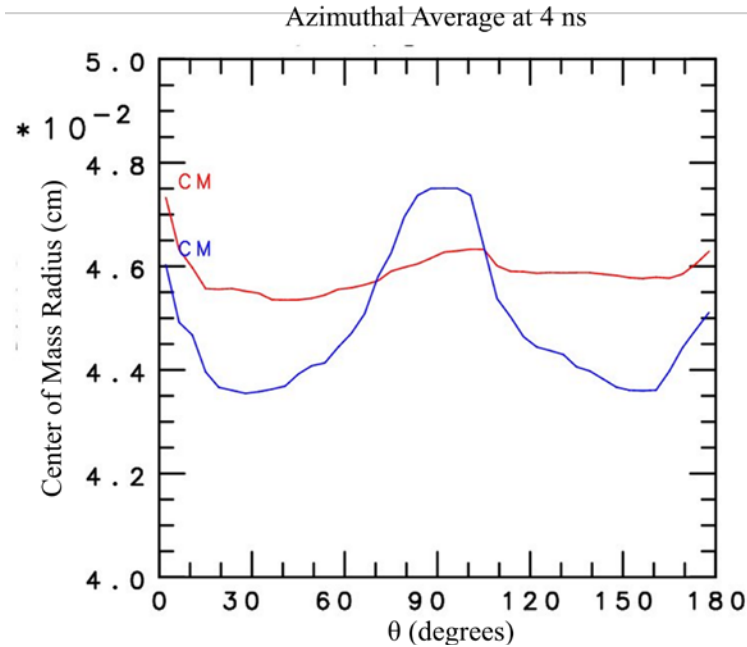


Figure 7. The center-of-mass radius plotted versus angle  $\theta$  from the z axis for the initial and optimized designs. The lineout of the azimuthal average of the initial center-of-mass radius (blue) shows that the equator has not imploded as far as the poles and therefore needs extra drive to achieve even compression (rms = 3.10%). The lineout of the target shell in the optimized design (red) shows greatly improved implosion uniformity (rms = 0.64%).

The nonuniformity, measured by the rms of the center-of-mass radius, has been greatly reduced. At 4 ns, after the target shell has moved in approximately 450  $\mu\text{m}$  from its original radius of 898  $\mu\text{m}$ , the rms has changed from 3.10% (14.0  $\mu\text{m}$ ) in the original design to 0.64% (2.9  $\mu\text{m}$ ) in the optimized design. However, there are still some slight irregularities. A small protrusion still exists at the equator of the shell, as evidenced by the greater radius there. There are also peaks present at 0 and 180°, the poles of the target, which are caused by noise in the hydrodynamic simulation, as is the lack of symmetry in the graph. Without this noise, the target

nonuniformity would be even lower than 0.64%. The overall results of the optimized design are much smoother and have a much lower degree of nonuniformity than the initial design.

The next step of the optimization process was to maximize the azimuthal uniformity. Because only half of the NIF beams are used in the compression pulse, it cannot be assumed that the target will compress uniformly in the azimuthal direction. To estimate the three-dimensional uniformity, simulations were run that calculated the 3-D distribution of deposited energy on the surface of the target. To relate this quantity to the distance that the shell imploded, several hydrodynamic simulations were run, each with a differing amount of energy in the laser beams. By plotting the distance the shell imploded after 4 ns in each simulation versus the relative energy of the beams in that case, it was found that the increase in deposited energy is related to the increase in the distance moved inward by a factor of 0.72 (see Figure 8). This information was then used to create 3-D plots of the predicted center-of-mass radius.

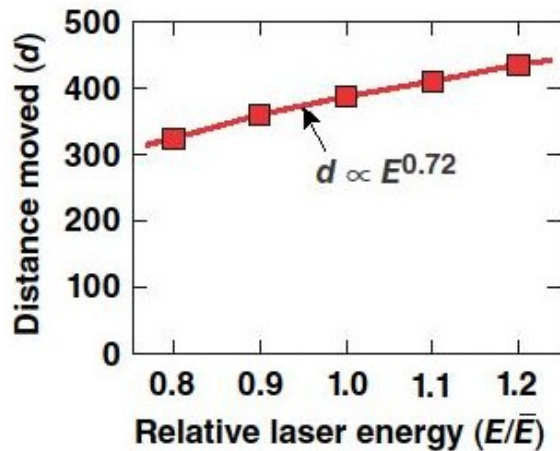


Figure 8. A graph plotting the distance the shell has imploded against the amount of energy in the laser beams. By observing the change in implosion distance versus the change in beam energy, it was found that the two were related by a factor of 0.72.

Figure 9 shows one such center-of-mass profile based on the initial design. The great variation in the radius can be seen from the large amplitudes of the peaks and valleys on the surface of the profile. The shaded-in quads represent those that are used for the laser pulse. The areas where the target is overcompressed (red) match these quads. In particular, the use of every

other quad in the first two rings results in a strong two-fold nonuniformity pattern around the azimuth near the poles.

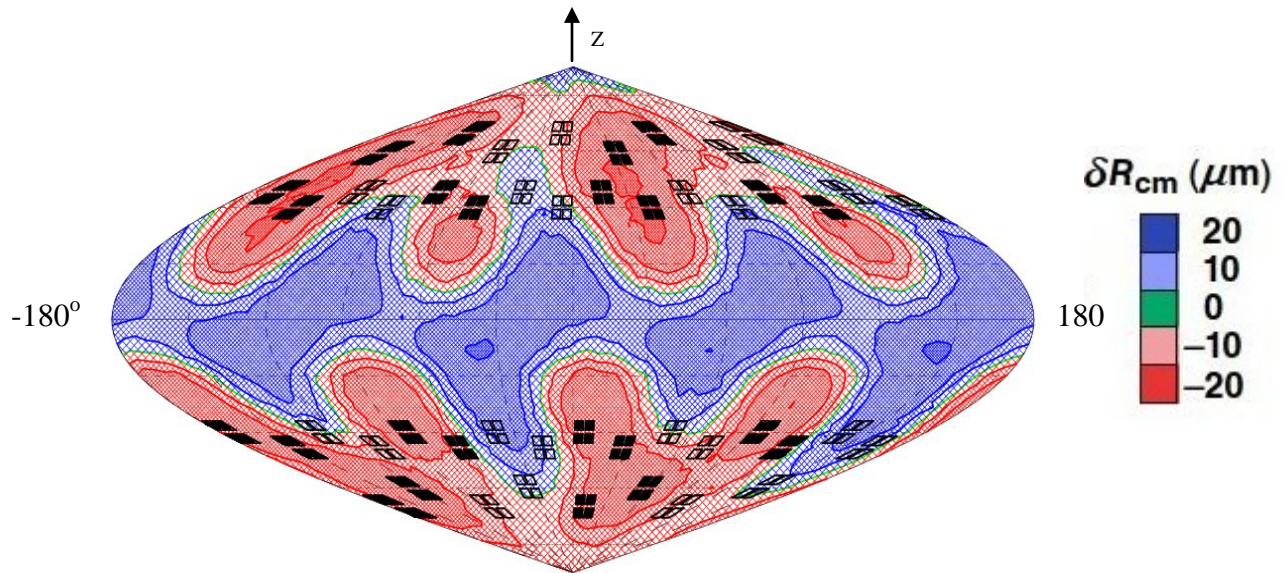


Figure 9. 3-D center-of-mass profile showing the azimuthal nonuniformity over the target surface at 4 ns in the initial design. The red represents the areas on the target shell that have a lower-than-average center-of-mass radius, and the blue illustrates the higher-than-average center-of-mass radii. The shaded-in quads represent the 24 which are used for the laser pulse. The target surface is not very evenly compressed, with a radius rms of 4.76% ( $21.7\mu\text{m}$ ). This high degree of nonuniformity and the patterns in the center-of-mass radii are undesirable.

Variations in beam positioning, defocuses, and choices of beams used were tested until the optimal azimuthal uniformity was reached. For example, the bottom two beams in each quad in Ring 3 (known as Ring 3B) were given varying horizontal displacements in multiple simulations. These simulations were then analyzed in order to determine which displacement value would create the most uniform deposited energy profiles and therefore the most uniform target implosion (see Figure 10). In this case, we can see the distinct pattern of areas of high and low deposited energy when the beams were given very little horizontal displacement. As the beams moved more to the side, the pattern began to smooth out, providing a more even amount of energy to the target surface. Lastly, as the beams continued moving to the side, an inverted pattern appears from the beams overlapping again in different positions on the target shell.



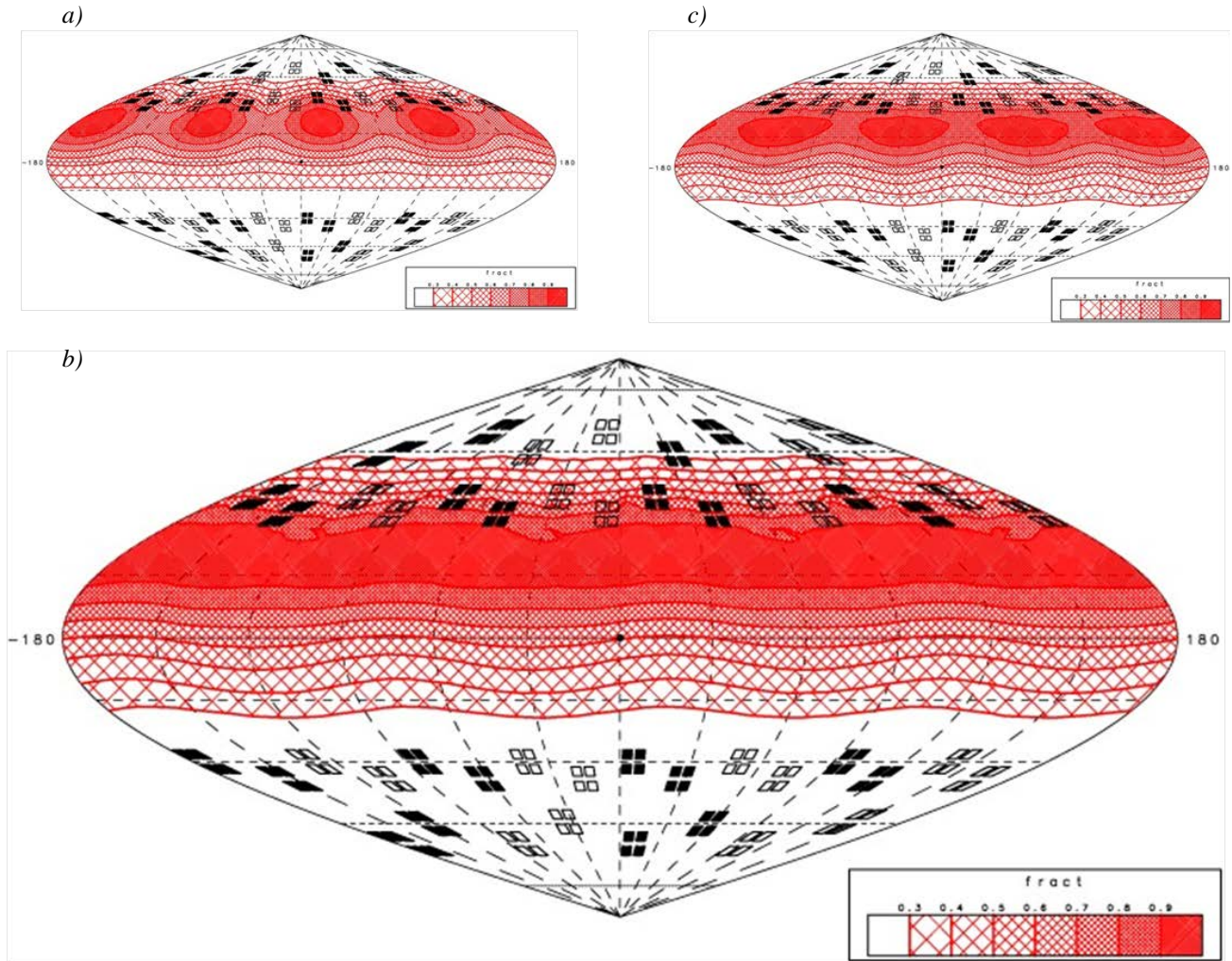


Figure 10. 3D cumulative deposited energy profiles at 4 ns for Ring 3B beams at various horizontal pointings  $\Delta y$ . The contours represent fractions of the maximum deposited energy, ranging from 0.3 to 0.9 with intervals of 0.1. (a) The horizontal pointings of the initial design ( $\Delta y=210 \mu\text{m}$ ) caused very prominent patterns in the surface nonuniformity. (b) By adjusting the horizontal pointings, the deposited energy uniformity and therefore the center-of-mass radius uniformity were optimized ( $\Delta y=410 \mu\text{m}$ ). (c) Shifting the beams too far in the horizontal direction caused an inversion in the cumulative deposited energy pattern ( $\Delta y=490 \mu\text{m}$ ).

In attempts to achieve maximum azimuthal uniformity, the choice of quads used in the compression pulse was also altered from that of the original design. Since half of the beams were to be used in the compression stage, an alternating pattern of quads was chosen from each ring for the initial design, as shown in Figure 11(a). It was discovered during the optimization process that certain patterns in quad choice were more successful in providing uniform energy deposition

to the surface of the target shell. The final design continued to use alternating quads in Rings 3 and 4 but used all four quads in Ring 2 while using none of the quads in Ring 1 [Figure 11(b)].

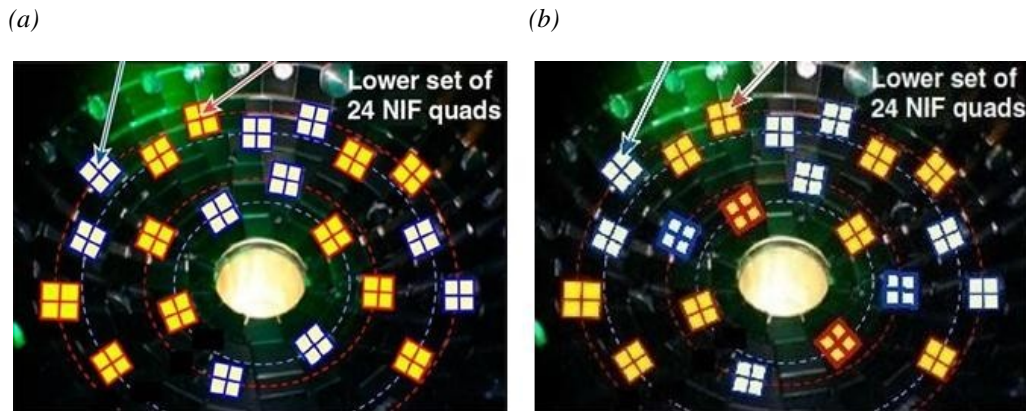


Figure 11. Images of the lower set of NIF quads depicting the quads used in each type of pulse in both the initial and optimized designs. (a) The initial design uses alternating quads from each ring to compress the target. The quads outlined in blue represent those used in the compression pulse stage. [From Ref. 5] (b) The optimized design uses all quads in Ring 2 and none of the quads in Ring 1 in the compression pulse in order to achieve optimal azimuthal implosion uniformity. [From Ref. 6]

The 3-D center-of-mass profile of the final design shows much greater uniformity of implosion (See Figure 12). The rms of the final design has been lowered by almost a factor of three to 1.76% (8.1  $\mu\text{m}$ ) after the target has moved in from 898  $\mu\text{m}$  to 458  $\mu\text{m}$ . The parameters of the final design are detailed in Table 1.

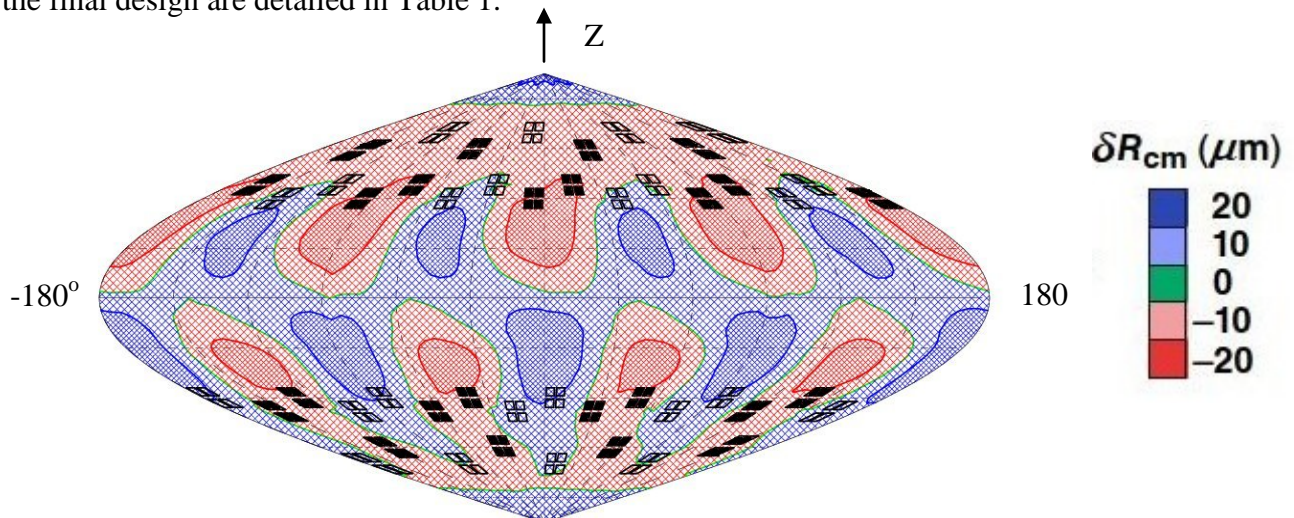


Figure 12. 3-D center-of-mass profile depicting azimuthal nonuniformity over the target surface at 4 ns in the final design. The nonuniformity of the center-of-mass radius has been greatly reduced over the azimuth, with an rms of 1.76% (8.1  $\mu\text{m}$ ) after moving inwards 440  $\mu\text{m}$ .

*Table 1. Beam parameter specifications (defocus and horizontal and vertical repointings) for the optimum design. The values of  $a$  and  $b$  indicate the half-intensity focal-spot radii of the phase plates currently installed on the NIF*

Ring	$\theta$	$a, b$ ( $\mu\text{m}$ )	Defocus cm	Vert. PT ( $\mu\text{m}$ )	Horiz. PT ( $\mu\text{m}$ )
1A	21.24	882, 631	–	–	–
1B	25.93	882, 631	–	–	–
2A	28.01	824, 590	2.2	–70	0
2B	32.70	824, 590	2.2	–70	0
3A	42.19	635, 367	2.0	160	$\pm 250$
3B	46.89	635, 367	1.7	–340	$\pm 380$
4A	47.68	593, 343	1.2	–520	$\pm 420$
4B	52.38	593, 343	1.0	–500	$\pm 450$

## 6. Conclusion

An experimental design, taking into account beam defocus, beam choice, and pointing parameters, has been developed using 2-D hydrodynamic simulations with 3-D ray tracing to provide optimal implosion uniformity for proposed direct-drive shock ignition experiments on the NIF. Using the optimized design, it is possible to carry out shock ignition experiments on the NIF in the near future, using only 96 of the 192 total beams to compress the target shell. Specific beam pointings and defocuses have been chosen to provide optimal implosion uniformity.

## 7. Acknowledgments

I would like to sincerely thank Mr. Bradley Allen for encouraging me to participate in this program and my parents for furthering this encouragement. I would also like to thank my advisor Dr. R. Stephen Craxton for not only offering myself and many other students this incredible opportunity but also giving me invaluable guidance and support. Lastly, I am very grateful to the Laboratory for Laser Energetics for providing this program.

## References

1. S. Skupsky, J. A. Marozas, R. S. Craxton, R. Betti, T. J. B. Collins, J. A. Delettrez, V. N. Goncharov, P. W. McKenty, P. B. Radha, T. R. Boehly, J. P. Knauer, F. J. Marshall, D. R. Harding, J. D. Kilkenny, D. D. Meyerhofer, T. C. Sangster, and R. L. McCrory, "Polar Direct Drive on the National Ignition Facility," *Phys. Plasmas* **11**, 2763 (2004).
2. R. S. Craxton, F. J. Marshall, M. J. Bonino, R. Epstein, P. W. McKenty, S. Skupsky, J. A. Delettrez, I. V. Igumenshchev, D. W. Jacobs-Perkins, J. P. Knauer, J. A. Marozas, P. B. Radha, and W. Seka, "Polar Direct Drive: Proof-of-Principle Experiments on OMEGA and Prospects for Ignition on the National Ignition Facility," *Phys. Plasmas* **12**, 056304 (2005).
3. R. Betti, C. D. Zhou, K. S. Anderson, L. J. Perkins, W. Theobald, and A. A. Solodov, "Shock Ignition of Thermonuclear Fuel with High Areal Density," *Phys. Rev. Lett.* **98**, 155001 (2007).
4. L. J. Perkins, R. Betti, K. N. LaFortune, and W. H. Williams, "Shock Ignition: A New Approach to High Gain Inertial Confinement Fusion on the National Ignition Facility," *Phys. Rev. Lett.* **103**, 045004 (2009).
5. L. J. Perkins *et al.*, "Development of a Polar Drive Shock Ignition Platform on the National Ignition Facility," NIF Facility Time Proposal (2010).
6. R. S. Craxton, L. Tucker, T. Mo, K. S. Anderson, R. Betti, L. J. Perkins, G. P. Shurtz, X. Ribeyre, and A. Casner, "A 96/96-Beam Polar-Drive Configuration for Shock Ignition on the NIF," 52<sup>nd</sup> Annual Meeting of the American Physical Society, Division of Plasma Physics (2010).

7. Alexandra M. Cok, “Development of Polar Direct Drive Designs for Initial NIF Targets,” Laboratory for Laser Energetics High School Summer Research Program (2006).
8. A. M. Cok, R. S. Craxton, and P. W. McKenty, “Polar-drive designs for optimizing neutron yields on the National Ignition Facility,” *Phys. Plasmas* **15**, 082705 (2008).
9. R. S. Craxton, “2-D Polar-Drive Design for Shock Ignition on the NIF,” Laboratory for Laser Energetics (April 2010), unpublished.
10. R. S. Craxton and D. W. Jacob-Perkins, “The Saturn Target for Polar Direct Drive on the National Ignition Facility,” *Phys. Rev. Lett.* **94**, 095002 (2005).

# Liquid Crystal Beam Shaping Devices Incorporating Coumarin-Based Photoalignment Layers

Katherine M. Wegman  
Pittsford Mendon High School

Advisor: Kenneth L. Marshall

University of Rochester  
Laboratory for Laser Energetics  
Summer High School Research Program 2010

## 1. Abstract

Liquid crystal (LC) devices incorporating photosensitive polymers based on coumarin were investigated for laser beam shaping applications. Presently, the OMEGA EP laser system uses pixelated metal beam shaping devices, though their relatively low damage threshold (approximately  $0.2 \text{ J/cm}^2$ ) makes them poor options for long-term usage. LC devices have the major advantages of a much higher damage threshold (9-18  $\text{J/cm}^2$ ). Previously,  $10 \text{ }\mu\text{m}$  pixelated LC beam shapers were fabricated by patterning a commercially available cinnamate-based photopolymerizable LC alignment material (ROLIC) through a mask using polarized UV light to control the LCs' orientation. This project investigated fabrication and characterization of LC beam shaping devices employing a coumarin-based linearly photopolymerizable polymer (LPP) as an alternative to the cinnamate-based LPP. After developing an experimental procedure for creating coumarin-based LPP liquid crystal cells, analyzing cell transmission data, and evaluating LPP coating uniformity, it was determined that the coumarin-based LPP could be photolithographically patterned. However, more research is needed to improve coating uniformity and determine the UV irradiation conditions necessary to improve pixel resolution.

## 2. Introduction

Beam shaping devices are important to the design of high-energy laser systems. In order for the beam to reach the intensity of its final output, it must first pass through amplifiers. Laser beam amplifiers cause spatially varying gain in the beam, meaning that the resulting amplified beam is non-uniform. Beam shaping mechanisms precompensate for this spatially varying gain, thus producing uniform amplified beams and facilitating optimal energy extraction. Figure 1 portrays, in theory, the effectiveness of precompensating for spatially varying gain using beam shaping devices. The resulting output beam from the amplifier is of the desired uniform intensity.

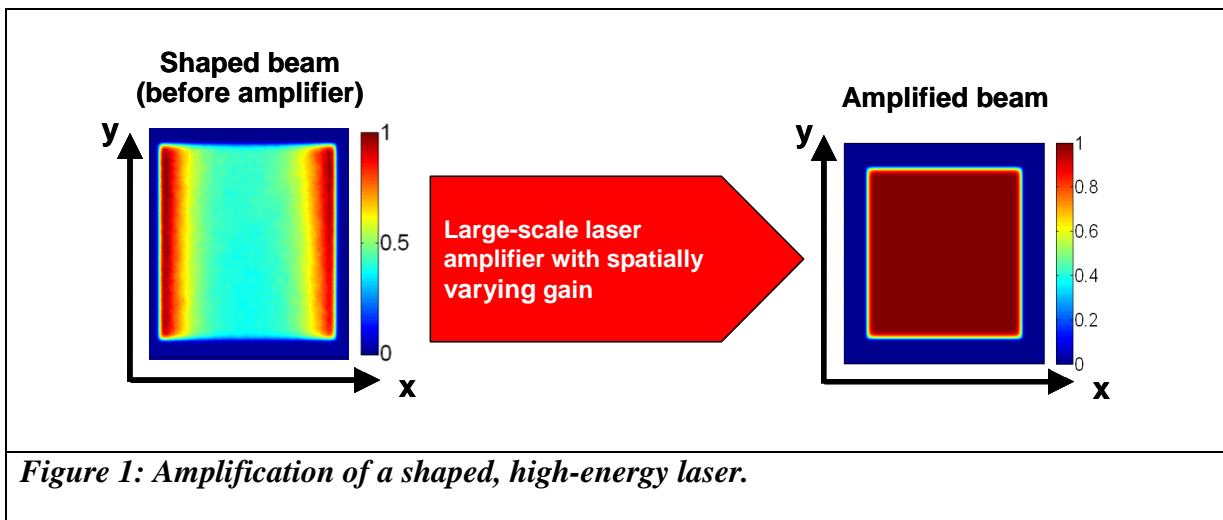


*Figure 1: Amplification of a shaped, high-energy laser.*

The OMEGA EP laser system, which was developed to provide ultrahigh intensities for advanced x-ray and proton-beam radiography of compressed targets, currently incorporates metal-mask fused-silica beam shapers. These masks have microscopic pixels allowing for either full transmission or no transmission of laser beam light. Despite these two transmission extremes, metal masks can produce a range of transmissions over the device dependent on the concentrations of the pixels. Using a

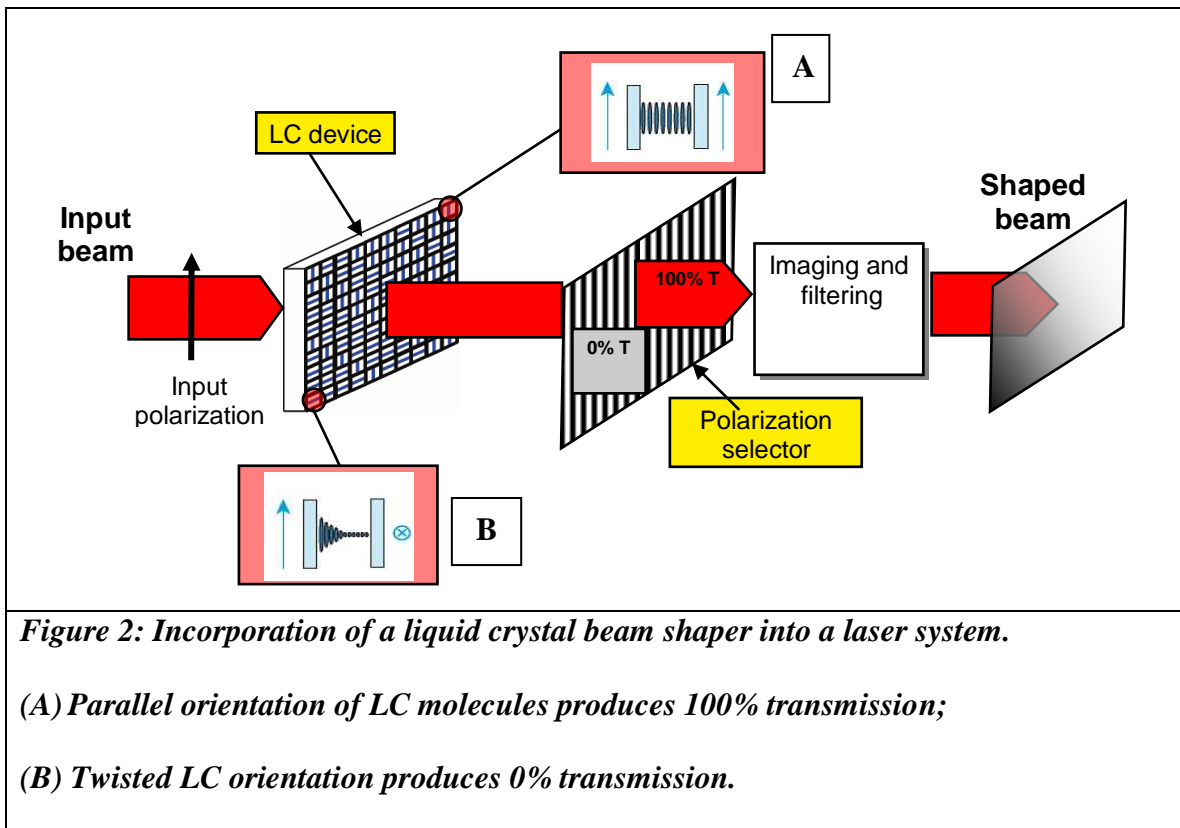
metal mask with a high concentration of full-transmission pixels (i.e., metal has been removed to expose the transmissive fused silica glass underneath) in one area, for example, will allow for high percentages of locally transmitted light.<sup>1</sup>

While the metal masks are effective in shaping the beam, they decrease the optimal energy extraction of the system because of their low damage threshold (approximately 0.2 J/cm<sup>2</sup> at 1054 nm, 1 ns). That is, the beam's intensity is limited by the damage threshold of the beam shaping mechanism. Liquid crystal beam shaping devices have been investigated for use in high-energy laser beam shaping because their components—the LCs and LPP on which they align—have much higher damage thresholds (9-18 J/cm<sup>2</sup> at 1054 nm, 1 ns and up to 60 J/cm<sup>2</sup> at 1054 nm, 1 ns, respectively).<sup>2</sup>

An additional advantage to LC beam shapers is that, when they are paired with a polarizer, the LC molecules' orientations can allow for full transmission of polarized light, no transmission of polarized light, or a percentage of polarized light transmission. Full transmission of polarized light can be achieved by assembling the LC devices such that the LC molecules align parallel to each other throughout the device, and in the same direction of the polarized light. No transmission of polarized light can be achieved by assembling the LC devices such that the molecules' alignment "twists" 90°. Since the polarized light can only pass through LC molecules oriented in the same direction as the light's polarization, the 90° change in LC molecule orientation effectively blocks the transmission of light. Partial transmission of light is achieved with LC devices that have been assembled such that the molecules are arranged at any degree of orientation between parallel and perpendicular assembly.<sup>1</sup>

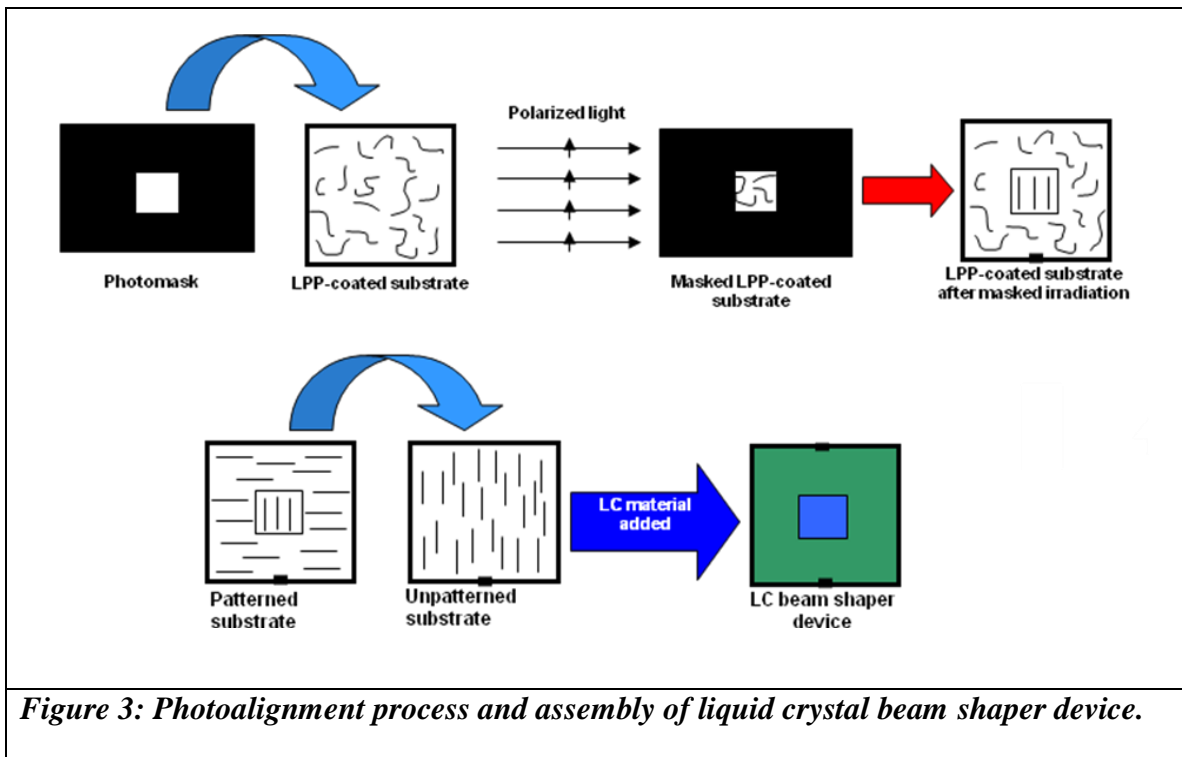


Figure 2 is a schematic of the LC beam shaper's incorporation into a laser system. The beam shaping mechanism consists of pixels that allow either full transmission or no transmission of the light. The magnified diagrams of the pixels show the orientation of the LC molecules within the cell.



The two current methods of liquid crystal alignment are mechanical buffing and the cleaner, non-contact, preferred process of “photoalignment”.<sup>4</sup> Photoalignment was the method used in this experiment. Photoalignment facilitates LC alignment by using polarized UV light, rather than physical contact, to align a linearly photopolymerizable polymer (LPP) that has been deposited on the surface of a substrate. In the process, irradiation by polarized UV light causes the polymer chains of the coumarin-based LPP to align on the surface of the substrate in the same direction as the polarization of the UV

light. UV irradiation causes the partially polymerized LPP to become cross-linked, enabling the alignment of liquid crystal molecules along it.<sup>2</sup> Patterning of the LPP is possible when irradiation first occurs through a photomask substrate, before the mask is removed and the substrate rotated 90° and re-irradiated. Van der Waals forces enable the LCs to align along the patterned LPP when the device is assembled.<sup>4,5</sup> The photoalignment and LC cell assembly process is depicted in Figure 3.



**Figure 3: Photoalignment process and assembly of liquid crystal beam shaper device.**

The center of the assembled device shown in Figure 3 would allow for full transmission of light, as did the LC molecule orientation in case A of Figure 2. The rest of the LC beam shaper device, colored green in Figure 3, would allow for 0% transmission of light, as in case B of Figure 2.

Previous research on LC devices has incorporated the cinnamate-based LPP ROP-103/2CP, produced by the company ROLIC. Using this LPP, LC devices have been

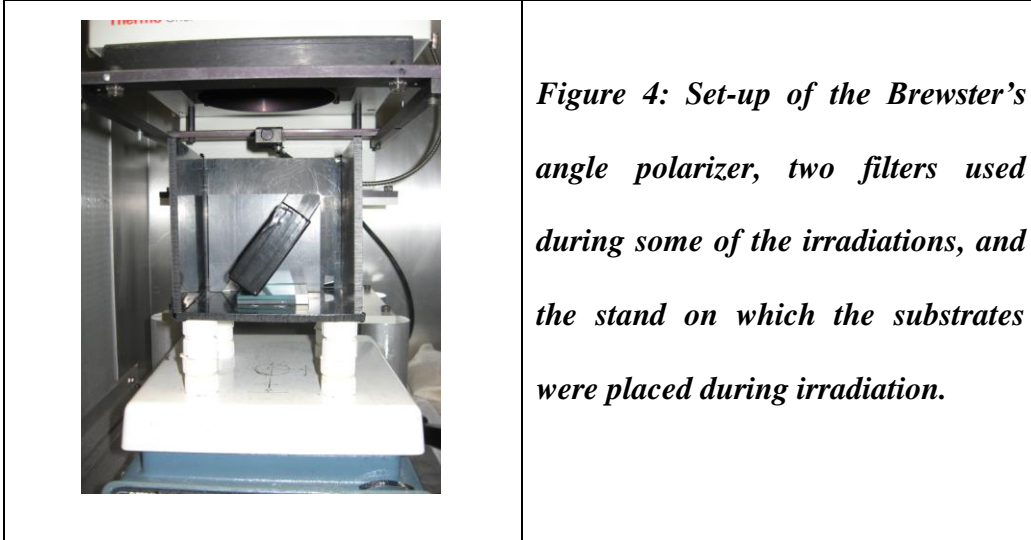
patterned with high resolution 10  $\mu\text{m}$  pixels.<sup>1</sup> However, ROP-103/2CP is no longer available commercially, leading to the investigation of a new coumarin-based LPP invented and synthesized at the Laboratory for Laser Energetics. In addition to its greater availability, coumarin presents the advantage of a higher damage threshold than that of ROP-103/2CP. This project involved the development of a photoalignment and LC cell preparation procedure for beam shaper devices incorporating the novel coumarin photoalignment material rather than the formerly used ROP-103/2CP.

### **3. Experiment**

Pre-cut fused-silica glass substrates were used for the assembly of the liquid crystal devices. The substrates were wetted with water, scrubbed with 0.05  $\mu\text{m}$  deagglomerated alumina micropolish, and rinsed with filtered deionized water before being subjected to the seven-second water break test. This test served to reveal any organic surface contaminants that were not removed by the scrubbing. Each substrate was flooded with water and observed for seven seconds to see if the surface tension of the water on the substrate was broken, which would indicate a need for additional manual cleaning prior to the substrate's placement in an ultrasonic bath. After the water break test, the substrates were cleaned with approximately 8 ml of Extran detergent in the ultrasonic bath at 69°C for 60 minutes. After removal from the ultrasonic bath, the substrates were rinsed with tap water for 3-5 minutes followed by filtered deionized water for 3-5 minutes. The substrates were then dried with a nitrogen air gun and put on a hotplate to dry at 130°C for 15 minutes. The dry substrates were allowed to cool to room temperature before spin-coating.

The cleaned substrates were placed on a spin-coater, covered with a glass dish to prevent evaporation of the chlorobenzene base coat and allow it to equilibrate with the glass substrate and produce a saturated vapor atmosphere. The glass cover dish had multiple holes around its circumference that were taped over to create a closed atmosphere in which any chlorobenzene vapors would remain during spin-coating. The substrates were flooded with pure chlorobenzene using a 0.2  $\mu\text{m}$  PTFE 13 mm hydrophobic syringe filter, clean needle, and glass syringe inserted through one of the taped-over holes. The chlorobenzene-flooded substrate was spun at 3000 rpm for 60 seconds to evenly coat the surface of the substrate before the LPP was applied. The chlorobenzene-coated substrate was then flooded with 0.3wt% diluted coumarin (LPP) in chlorobenzene, which was deposited on the substrate through a 0.2  $\mu\text{m}$  PTFE 13 mm hydrophobic syringe filter using a second clean needle and glass syringe. The substrate was immediately spun at 3000 rpm for 120 seconds. The coated substrates were allowed to air-dry for 10 minutes.

After they had air-dried, the substrates were pre-baked at 50°C for 15 minutes. The pre-bake was developed after a comparison of pre-baked photoaligned coatings and non-pre-baked photoaligned coatings concluded that pre-baking the coated substrates prior to photoalignment resulted in a more uniform coating. After the pre-bake, the substrates were vacuum dried for one hour at room temperature and a pressure of approximately 0.1 torr to drive out the residual chlorobenzene. Photoalignment was accomplished by placing the substrates beneath a 500-watt mercury xenon UV lamp at 325 nm. They were placed beneath a “pile of plates” polarizer made of fused-silica microscope slides arranged at Brewster’s angle of 56.1° (Figure 4).



Photopatterning of the alignment layer was accomplished by irradiating one substrate at  $0^\circ$  rotation with no mask. The second substrate was irradiated twice: first using a patterned mask, and second with the mask removed and the substrate rotated  $90^\circ$ . Irradiation times varied based on photomask substrate composition and the transmission of filters used.

Substrates were assembled into cells using Epo-Tek 5-minute epoxy. The gap between each cell's constituent substrates was controlled by dispersing  $8\ \mu\text{m}$  glass microspheres into the epoxy. A small amount of this spacer-containing adhesive was placed on each of the four corners of the first substrate. The second substrate was placed on the first one in such a way that the initial direction of  $0^\circ$  of rotation in the first substrate matched that of the second substrate (parallel assembly). The assembled cells were placed on a hotplate at  $72^\circ\text{C}$  and filled with a mixture of nematic E7 and 0.07wt% CB15 (an anti-reverse twist agent used to prevent random incorrect orientations of LC molecules) using a third clean needle, glass syringe, and  $0.2\ \mu\text{m}$  PTFE 13 mm

hydrophobic syringe filter. The completed cells were allowed to cool to room temperature on a hotplate at a rate of 10°C per hour. All operations except substrate cleaning and photoalignment took place in class 100 hoods.

#### **4. Discussion**

Coumarin-based photoalignment materials have been photolithographically patterned with high-resolution masks for the first time, though further research is needed to achieve sharp, high-contrast, and well-resolved pixels of 10  $\mu\text{m}$  or less. Much of this project was focused on determining the proper irradiation conditions for the coumarin polymer.

As prior research with the ROP-103/2CP LPP had shown, there is a correlation between photoalignment resolution and irradiation time.<sup>1</sup> The coumarin polymer was found to be highly sensitive to both the wavelength and intensity of the UV irradiation. LC cells prepared with masked LPP-coated substrates that had been irradiated with the highly transmissive fused-silica photomask for five seconds or more were found to be overexposed; that is, the pixels in the devices were larger and darker than desired (Figure 5). In contrast, the LPP was found to be underexposed after a one second irradiation time. This was concluded after the completed cell failed to reach full extinction, blocking all light transmission, when viewed under crossed polarizers.

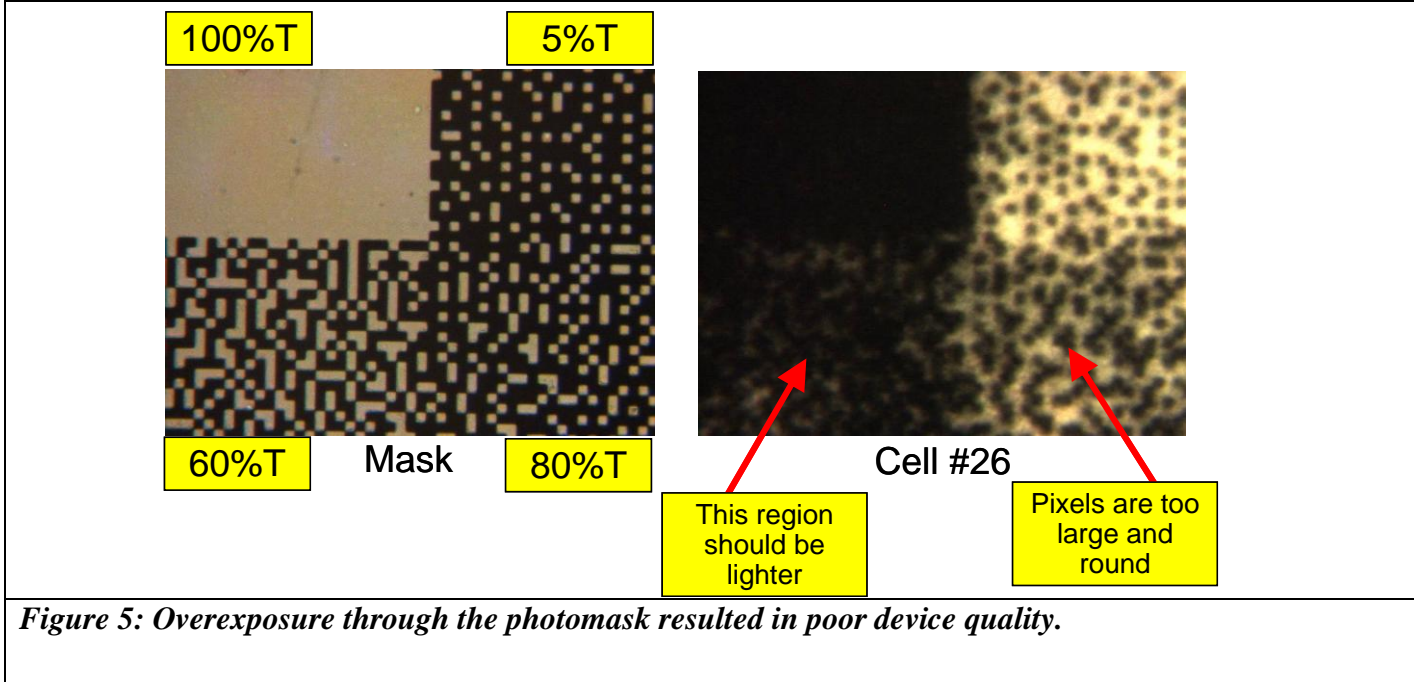
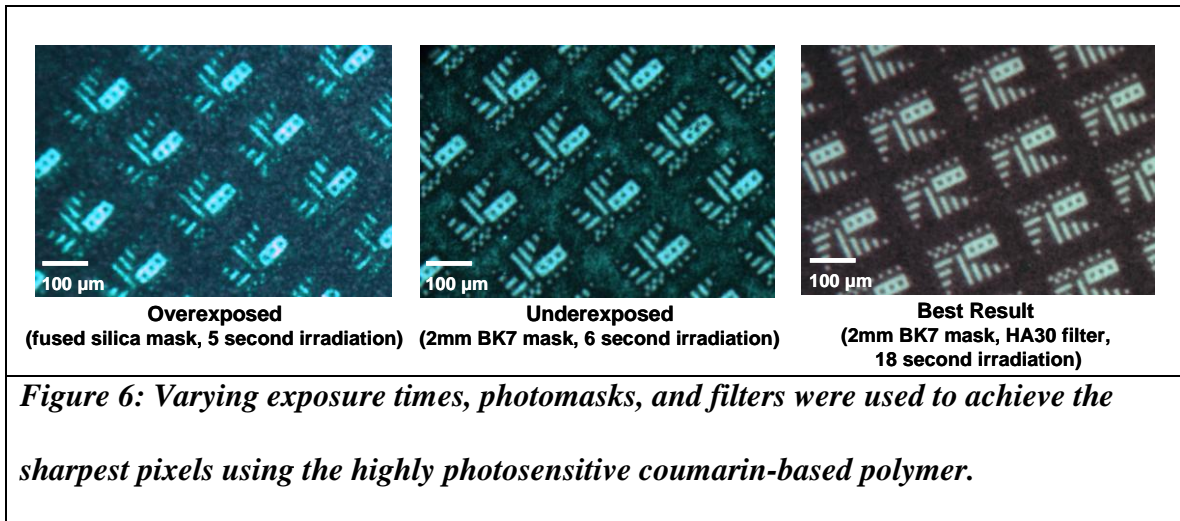


**Figure 5: Overexposure through the photomask resulted in poor device quality.**

In order to lengthen the LPP irradiation time and increase the range from underexposed to the ideal exposure time, various filters and a lower-transmission BK7 photomask were used to reduce the intensity of the UV light irradiating the coumarin polymer. Irradiation times using the filters were determined by analyzing a series of cells at different exposure levels, each of which had been irradiated through the BK7 mask. By multiplying the known value of the UV lamp’s energy flux, or the rate of transfer of energy per unit area, by the exposure time each cell had been irradiated, the upper and lower irradiation fluence limits were determined. Using this data, the proper irradiation times for multiple filters were determined. The clearest pixels and most successful coumarin LPP patterning was achieved using the BK7 photomask and HA30 filter. Figure 6 shows the varying quality and irradiation conditions for an overexposed cell, an underexposed cell, and the best result.



## 5. Conclusion

The purpose of this project was to investigate the feasibility of using coumarin-based photoalignment layers in liquid crystal beam-shaping devices. While coumarin-based LPPs have been patterned for the first time, further research is needed to achieve higher-quality pixels.

In even the highest quality devices that have been made, the dark areas appeared to have a grainy texture; the device does not achieve zero transmission of light in the intended areas. Coating smoothness was confirmed using atomic force microscopy and a Nomarski microscope, but the source of the graininess is yet unknown. Further research is needed to investigate and correct the issue of graininess in the LC cells incorporating coumarin-based LPPs.

With further research, coumarin-based LPPs could be used in beam shaping devices of large-scale laser systems, eventually replacing the metal beam shapers. Achievement of this long-term goal would greatly increase the damage threshold of the



laser system, as the beam will be adequately shaped using optical materials capable of withstanding highly damaging beams.

## **6. Acknowledgements**

I thank Dr. R. Stephen Craxton for directing the Laboratory for Laser Energetics' High School Summer Program and selecting me for participation in the program. I thank my advisor, Kenneth L. Marshall, for his guidance, instruction, and supervision for the duration of my summer research. I also acknowledge Simon K. H. Wei, who synthesized the coumarin polymer used in this research, and Marisa Vargas, whose assistance and support were crucial to the progress of this research. Lastly, I thank Christophe Dorrer and Materials Lab students John R. Boulé III and Paul Leung for their additional support throughout the program.

## References:

- [1] Vargas, Marisa C., "Laser Beam Shaping With Optically Patterned Liquid Crystals"; LLE Summer High School Research Program, 2010.
- [2] K. L. Marshall, J. Gan, G. Mitchell, S. Papernov, A. L. Rigatti, A. W. Schmid, and S. D. Jacobs, "Laser-Damage-Resistant Photoalignment Layers for High-Peak-Power Liquid Crystal Device Applications," in *Liquid Crystals XII*, edited by I. C. Khoo (SPIE, Bellingham, WA, 2008), Vol. 7050, Paper 70500L.
- [3] M. Schadt and H. Seiberle. *Journal of the SID* **5**, 367-370 (1997).
- [4] M. Schadt, K. Schmitt, V. Kozinkov, and V. Chigrinov, *Jap. J. Appl. Phys.* **31**, 2155-2164 (1992).
- [5] M. Schadt, H. Seiberle, A. Schuster, and S.M. Kelly, *Jap. J. Appl. Phys.* **34**, 3240-3249 (1995).

# **Determination and Correction of Optical Distortion in Cryogenic Target Characterization**

Francis White

McQuaid Jesuit High School  
Rochester, NY

Advisors: Dana Edgell, Mark Wittman

Laboratory for Laser Energetics  
University of Rochester  
Rochester, NY  
January 2011

## **Abstract**

The DT ice layer in cryogenic targets used for direct-drive inertial fusion experiments must have an rms surface roughness less than 1  $\mu\text{m}$  for successful implosion. The solid fuel layer is characterized by both shadowgraphy and x-ray phase-contrast imaging in layering experiments being performed at LLE. Optical distortion present in these characterization methods must be determined and corrected for accurate measurement of the fuel layer's uniformity. It was determined that x-ray images inherently possess distortion less than 0.1  $\mu\text{m}$ . To eliminate ellipticity of a circular object imaged with x rays, a precisely spherical steel ball was examined at various angles of camera tilt with respect to the x-ray beam axis, and the optimum tilt angle was determined. To calibrate the shadowgraphic imaging system, a zoom scan was performed using a regularly spaced dot array to center its optical axis on the center of the capsule and determine the imaging system's distortion. It was found that distortion varies with magnification and must be calibrated for each field of view. The imaging system's focus was registered and scanned to produce the highest contrast image of the steel ball. It was determined that the best focus varies slightly with magnification and must be corrected when changing the field of view. Finally, the known  $l$ -modes of a surrogate "bright-ring" target were reproduced by correcting for distortion using the information obtained from these calibration experiments.

## 1. Introduction

In laser-driven direct-drive inertial confinement fusion (ICF) experiments, energy is delivered to a target from multiple high-power lasers causing an implosion. The 60-beam, 30-kJ OMEGA Laser System<sup>1</sup> at the University of Rochester Laboratory for Energetics (LLE) conducts direct-drive ignition (DDI) experiments, in which laser energy is directly transferred to a target. In indirect-drive ignition (IDI) experiments, which are to be carried out at the National Ignition Facility (NIF),<sup>2</sup> laser energy is transferred to a metal container surrounding the target, and generated x rays energize the target. The design for direct drive ignition (DDI) calls for a layer of condensed hydrogen fuel adhered to the inner surface of a spherical shell ablator. The hydrogen fuel is delivered to the capsule via a fill tube. When photon energy is deposited on the target, the outer surface ablates causing an implosion that compresses the hydrogen fuel layer and gaseous fuel at the center of the target. Perturbations on the inner ice surface of the target can cause asymmetric implosion which may result in a failed ICF experiment. Specifications for DDI experiments on the NIF require the inner ice layer to have a total root-mean-square (rms) deviation of less than 1  $\mu\text{m}$ . Therefore, it is imperative that the cryogenic targets be characterized with a resolution of  $\sim 0.1 \mu\text{m}$  to determine whether or not this uniformity requirement is met.

Two optical imaging systems are currently being used to characterize cryogenic targets: x-ray phase contrast imaging<sup>3-5</sup> and backlit optical shadowgraphy.<sup>6</sup> In x-ray imaging, the fuel layer is diagnosed by measuring rings due to x rays refracting at the inner ice surface. These rings appear in the image within a few microns of the actual ice surface. In optical shadowgraphy, the fuel layer is diagnosed by measuring the “bright

ring” due to light reflecting off the inner ice surface. OMEGA uses optical shadowgraphy, while the NIF uses x-ray phase contrast imaging.

The purpose of this project was to determine and correct optical distortion in both of these characterization methods. The distortion was measured for each of these techniques to enable correction in the final uniformity analysis. It was found that x-ray imaging is inherently distortion free, but that the camera’s angle must be adjusted to remove ellipticity in the image. The shadowgraphy imaging system was calibrated and reproduced the known modes fabricated on a surrogate target with known imposed perturbations.

## **2. X-ray Phase Contrast Imaging and Backlit Optical Shadowgraphy**

Cryogenic fill-tube targets are characterized using x-ray and visible-light imaging systems. The cryogenic fill-tube-target test facility (CFTF) shown in Figure 2 uses both characterization methods to test cryogenic targets for imperfections. The x-ray and shadowgraphy imaging systems are oriented orthogonally to each other. A right-handed coordinate system has been imposed on this setup. By definition, the x-axis is oriented horizontally along the x-ray imaging system with the positive direction pointing towards the x-ray camera. Likewise, the y-axis is oriented vertically along the shadowgraphy imaging system with the positive direction pointing away from the shadowgraphy imaging optics. The z-axis is orthogonal to both the x and y axes with the positive direction pointing down the fill tube toward the capsule. The coordinate system is important because the two imaging techniques must both be optimized at once when the center of the capsule coincides with the origin, i.e., the intersection of the optical axes of

both systems. This can be accomplished by manipulating the target's position with the xyz-positioner.

## **2.1 X-ray Phase Contrast Imaging**

X-ray phase contrast imaging is to be the primary diagnostic of cryogenic targets used on the NIF. This technique uses refracted x rays to determine information about a cryogenic target's inner condensed deuterium-tritium (DT) layer. A tungsten anode generates x rays which pass through a target suspended in the target chamber. The x rays pass through the target and are collected by a 1340x1300 pixel, 16 bit x-ray camera. The largest refraction occurs at grazing-incidence angles, i.e., x rays that pass through the target tangential to the DT ice surface have the greatest deflection. This is illustrated in Figure 3. In general, however, the x-ray deflection is very small. Since the imaging system relies on the x-ray deflection to create an accurate intensity map of the target, the x rays must propagate for approximately 1 m after passing through the target to create sufficient deflection before being collected by the x-ray camera.

The deflection of the x rays causes a variation of x-ray intensity. Deflection of x rays off the inner ice surface creates a bright ring in the resulting phase-contrast image. Figure 4 is an example of an x-ray phase contrast image of a thick-walled plastic calibration target. The inner blue ring is the result of x rays refracting off the inner ice surface. These high intensity rings appear within a few microns of the actual ice surface.<sup>5</sup>

## **2.2 Backlit Optical Shadowgraphy**

Optical backlit shadowgraphy is one of the most widely used diagnostics of cryogenic targets used in ICF experiments. Red light with a wavelength of 627 nm passes through the target and is collected by a 2048x2048 pixel, 12 bit CCD camera. Rays are both reflected and refracted at the shell wall and inner ice layer interface. Some of these rays form characteristic rings on the resulting intensity map (Figure 5). The brightest (most intense) ring is caused by rays that totally internally reflect off the inner ice surface. This is illustrated in Figure 6, in which the yellow lines indicate rays passing through the target and the red lines indicate the apparent paths of the rays viewed by the camera. Figure 6 shows that when these rays are traced back they form a caustic, which appears as the bright ring. Ray tracing programs correlate the position of the bright ring in the shadowgraph to the position of the inner surface of the ice layer allowing characterization of the nonuniformity of the inner surface.<sup>6</sup>

## **3. Experimental Correction of Optical Distortion**

### **3.1 X-ray Phase Contrast Imaging: Optimal Camera Tilt Angle**

It was discovered that x-ray images do not need to be calibrated for distortion, but that incident camera angle is important. Ellipticity in the image of a circular object is produced when the camera is tilted with respect to the axis of symmetry of the incident radiation. To find the optimum tilt angle, ellipticity (measured by Fourier mode 2 in the radius of the circular image of a precisely spherical steel ball as a function of angle) was examined as the angle of the camera relative to the y and z axes were varied. The



optimum tilt angle occurs when the mode 2 is minimized. This occurred when  $\theta_y = -2^\circ$  and  $\theta_z = -1^\circ$ . (see Fig. 7 and 8).

## **3.2 Backlit Optical Shadowgraphy**

### **3.2.1 Determining the Best Focus**

A focus scan of a precisely spherical steel ball was used to find the focus that produced the highest contrast edge. It was discovered that the best focus varies with magnification and must be calibrated for each field of view. The results of experiments involving a 1.0-mm field of view and a 3.4-mm field of view are summarized below in Figures 9 and 10. The focus was varied through rotations of a focusing ring integral to the imaging system (measured in arbitrary units). The optimal focus occurs when the contrast at the edge of the steel ball is the greatest. This is measured by the steepness of a lineout of intensity (i.e. slope) at the perimeter of the steel ball. As a precaution, in the 1-mm field of view experiment, the dial was rotated from 1.18 back to 1.02 after gathering the original data in order to check for hysteresis. Since both sets of data peak at a dial indicator position of 1.1, hysteresis was not present.

### **3.2.2 Measurement of Distortion**

There is distortion in any optical system. In order to adequately characterize cryogenic targets with backlit shadowgraphy, distortion needs to be corrected. There are two kinds of optical distortion: pincushion and barrel. In “pincushion distortion,” image magnification increases with distance from the optical axis, while in “barrel distortion” image magnification decreases with distance from the optical axis.<sup>7</sup> To correct optical

distortion, one has to know how far the distance between points in the image varies as a function of distance from the optical axis. Thus, a zoom scan of a dot array (Figure 11) was used to adjust the shadowgraphic imaging system's optical axis and measure its distortion ( $D$ ), which varies directly with the cube of the distance ( $r$ ) from the optical axis ( $D \sim r^3$ ). It was experimentally determined that  $D$  varies with magnification and that the imaging system must be calibrated for each field of view.

### 3.2.3 Distortion Correction

In order to show that the distortion correction is accurate, the known modes of a surrogate "ring" target were reproduced. The outer perimeter of the ring is circular with a diameter of  $900 \mu\text{m}$ , while the inner ring has a known mode structure that meets NIF specifications. Figure 12 is a shadowgraphic image of the surrogate target before the distortion correction. Figure 13 is an "unwrapping" of Figure 12 showing the radial variation in intensity near the target edge. Each vertical line in Figure 13 is a radial lineout of the intensity in the bright ring to outer edge region of Figure 12. The angle in the unwrapping has zero at the far right side of Figure 12 and increases in the counterclockwise direction. Figure 14 is a graph of the power spectra of the surrogate target's outer and inner rings. The large variation in the magnitude of mode 2 with respect to the calibration target's NIF design spec (dotted line) is indicative of the optical distortion discussed above. Following the distortion correction, the power spectrum of the outer edge became relatively constant, and the power spectrum of the inner ring more closely matched the NIF specification of  $1.00 \mu\text{m ms}$ . These new power spectra are plotted in Figure 15.

#### **4. Conclusion**

Both the x-ray phase contrast imaging and backlit optical shadowgraphy characterization systems were calibrated and corrected for distortion. The distortion was measured for each of these techniques to enable correction in the final uniformity analysis. It was found that x-ray imaging is inherently distortion free, but that the angle of the camera is important in removing ellipticity from the image. For the shadowgraphic imaging system, it was found that the optimal focus depends on the field of view. Moreover, the pincushion distortion present in this imaging system was discovered to vary with magnification and must be calibrated for each field of view. Corrections to this distortion were found to be accurate by reproducing the known *l*-modes fabricated on a surrogate target.

#### **5. Acknowledgements**

I would like to thank Dana Edgell and Mark Wittman for their incredible support helping me complete this project. It is truly kind that they would take in a high school student (with absolutely no prior knowledge of laser fusion) and support me in this scientific endeavor. Work on this project wasn't always easy, but I've come away knowing what it means to work for the benefit of mankind. I would also like to thank Dr. Craxton for his tireless efforts in directing the LLE Summer Research Program for High School Students. He has given me and so many other high school students the opportunity to experience science as professional scientists do it. I am in his debt. Lastly, I would like to thank my fellow high school internees. Because of their support and camaraderie, I had one of the most enjoyable summers ever.

## 6. References

1. T. R. Boehly et al., "Initial Performance Results of the OMEGA Laser System," *Opt. Commun.*, **133**, 495 (1997).
2. W. J. Hogan et al., "The National Ignition Facility," *Nucl. Fusion*, **41**, 567 (2001).
3. D.S. Montgomery, A. Nobile, and P.J. Walsh, "Characterization of National Ignition Facility cryogenic beryllium capsules using x-ray phase contrast imaging," *Rev. Sci. Instrum.* **75**, 3986 (2004).
4. B.J. Kozioziemski et al., "Quantitative characterization of inertial confinement fusion capsules using phase contrast enhanced x-ray imaging."
5. T. Lu., "X-Ray Phase-Contrast Characterization of Cryogenic Targets," *2009 Summer Research Program for High School Juniors at the University of Rochester's Laboratory for Laser Energetics*
6. D. H. Edgell et al., "Three-Dimensional Characterization of Cryogenic Target Ice Layers Using Multiple Shadowgraph Views," *Fusion Science and Technology*, **49**, 617 (2006).
7. "Distortion," <http://toothwalker.org/optics/distortion.html>.



*Figure 1. Photograph of a cryogenic fill-tube target with a 3 mm diameter. The fill tube enters the target with a 30  $\mu\text{m}$  diameter.*

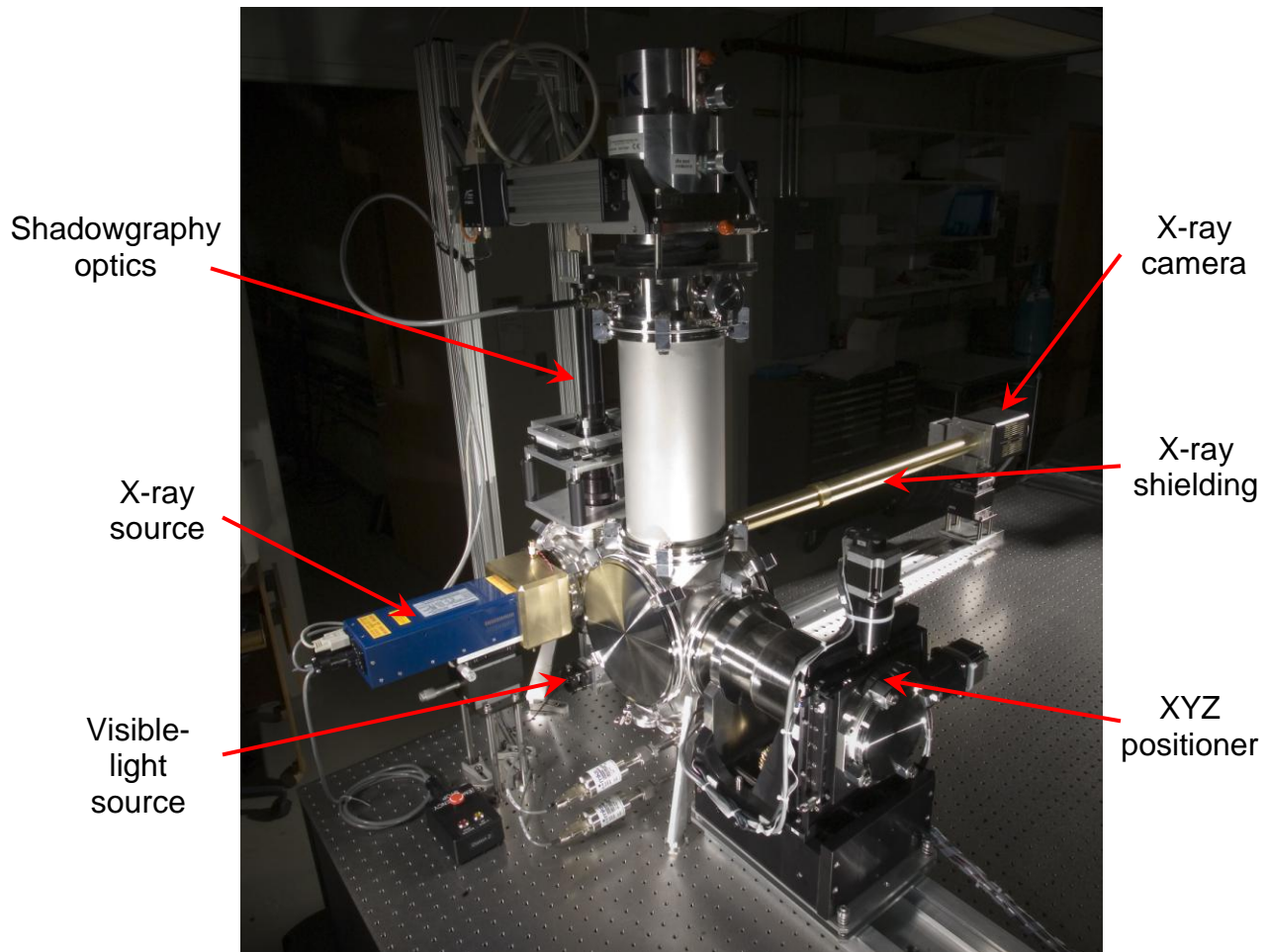


*Figure 2. Photograph of the x-ray and optical characterization systems in the experimental setup.*

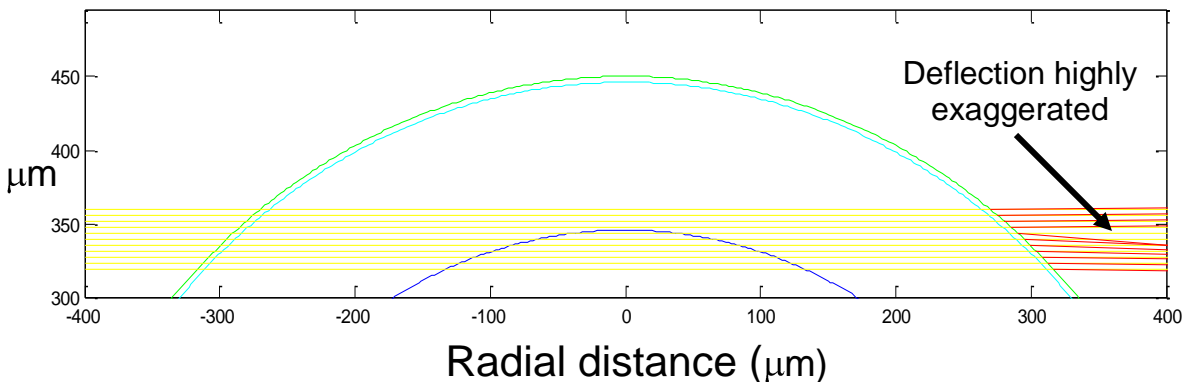


*Figure 3. Ray trace of x rays (depicted as horizontal yellow lines) as they are deflected upon passing through the cryogenic target. The largest refraction occurs at grazing incident angles*

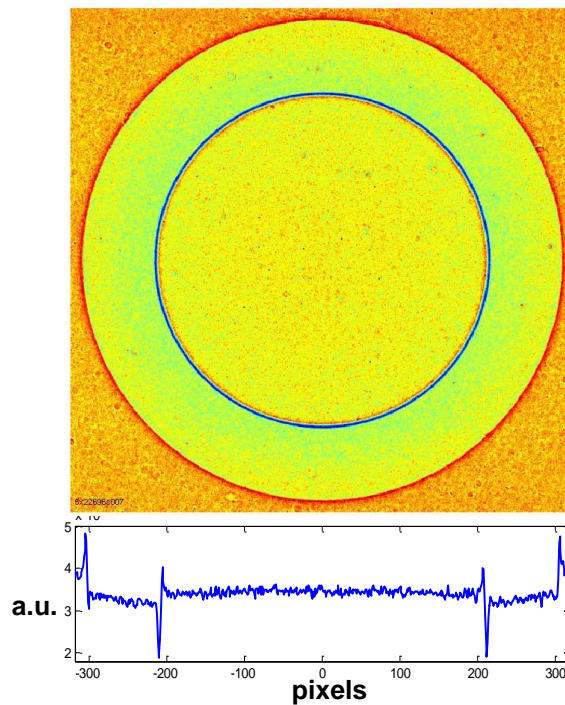


*Figure 4. X-ray phase contrast image of a thick-walled plastic shell used for calibration purposes (from Ref. 5). A lineout of intensity is added. (False-color enhancement of an original black-and-white image.)*

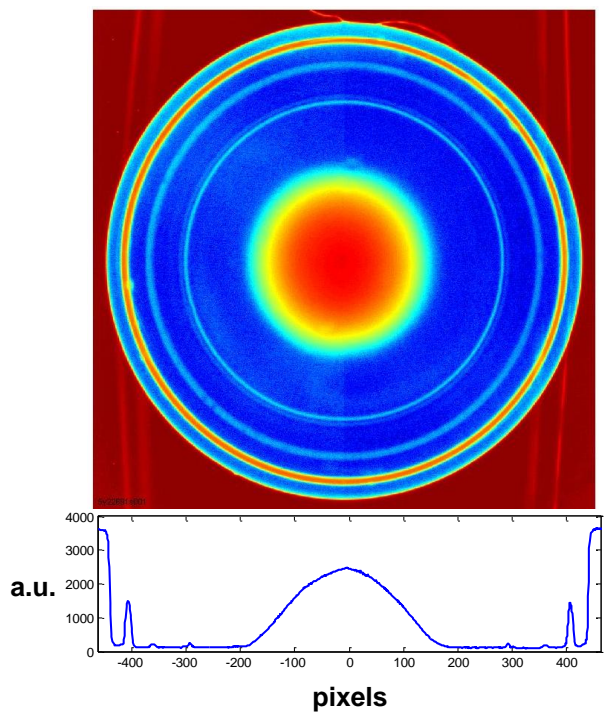


Figure 5. Shadowgraphic image of a thick-walled plastic calibration target. (False-color enhancement of an original black-and-white image)

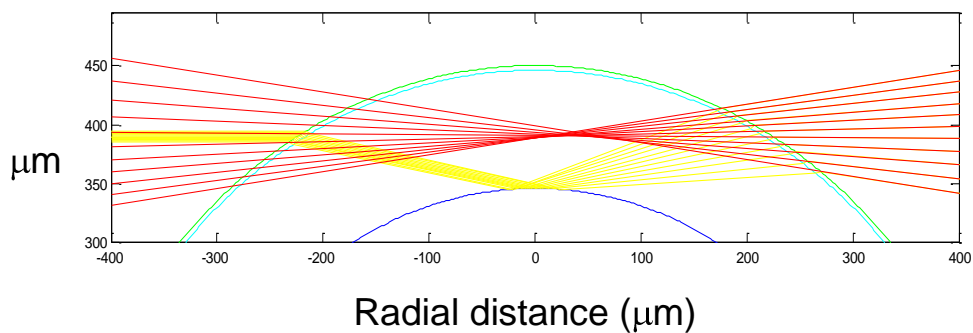


Figure 6. Ray trace of visible light as it passes through the target. The yellow lines represent light that enters the target (from the left) and totally internally reflects off the inner ice layer. The intersection of the red lines (the apparent paths of the rays that form the image) form a caustic which indicates the location of the bright ring.



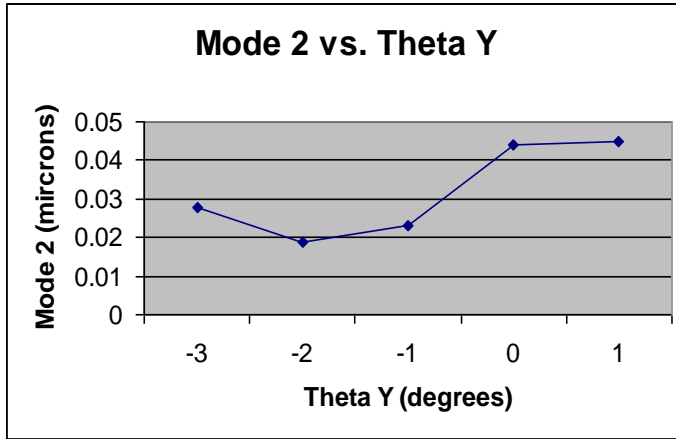


Figure 7. Plot of the mode 2 amplitude versus tilt angle about the y-axis. The minimum mode 2 occurs at

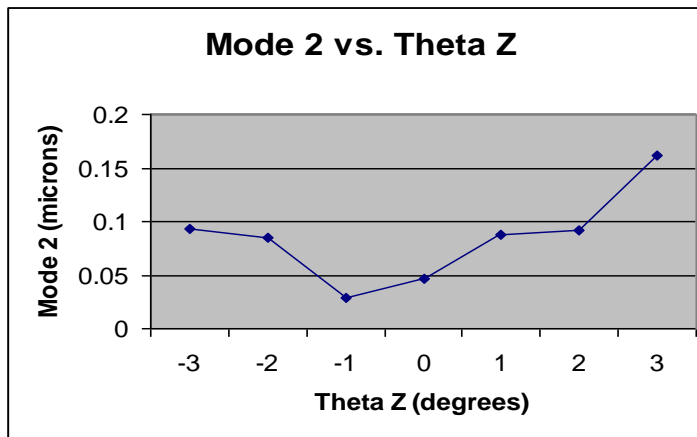


Figure 8. Plot of the mode 2 amplitude versus tilt angle about the z-axis. The minimum mode 2 occurs at

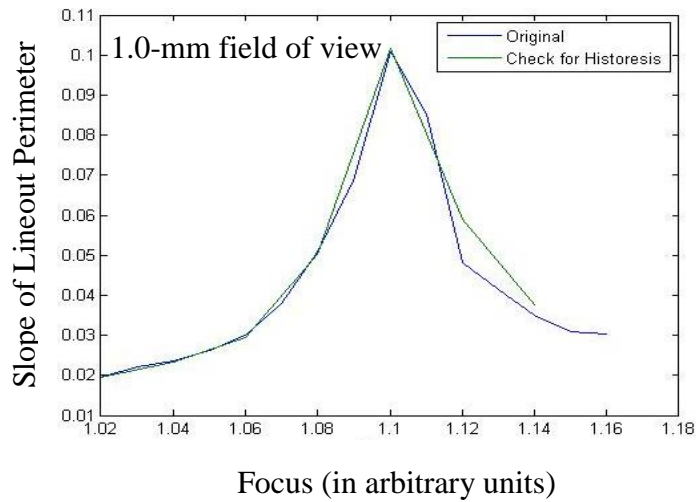


Figure 9. Plot of focus versus slope at a 1-mm field of view. Points along the blue curve were taken as the focus dial was turned to the right. Points along the green curve were taken as the focus dial was turned to the left from 1.14 in order to check for hysteresis. The optimal focus occurs at 1.1 where both lines achieve a maximum. Because both curves peak at 1.1, there was no hysteresis in the bearings.

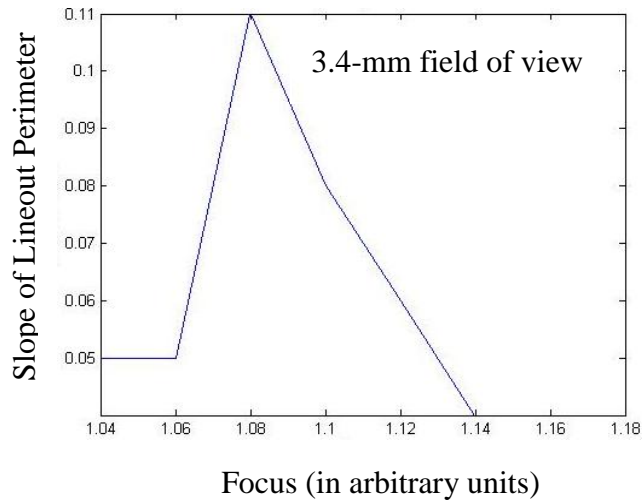
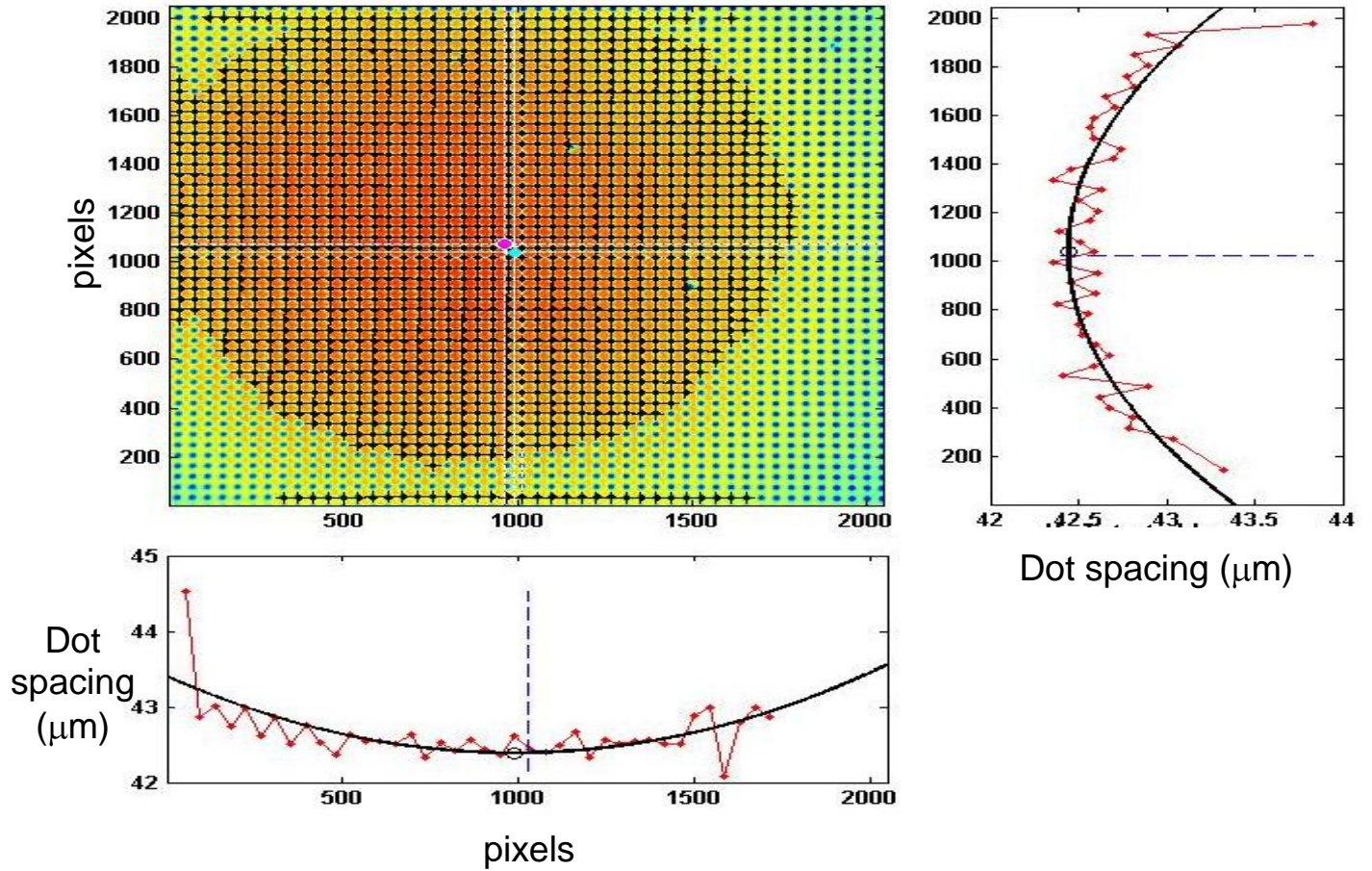
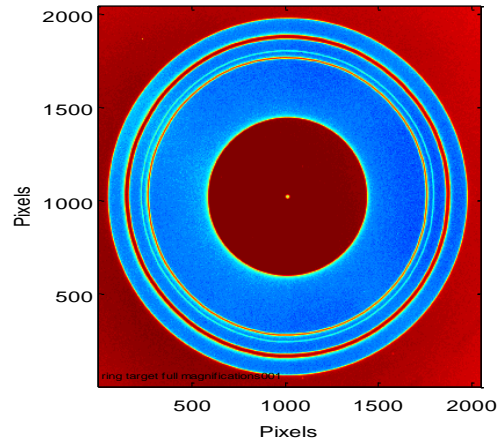


Figure 10. Plot of focus versus slope at perimeter at a 3.4-mm field of view. This curve achieves a maximum at a focus of 1.08, which indicates that best focus varies with magnification.



*Figure 11. Shadowgraphic image of a dot array showing pincushion distortion. Distortion causes the black dots to spread out radially from the optical axis and must be corrected for. The two graphs show the distance between successive points in the image in the x and y directions.*



*Figure 12. Shadowgraphic image of a surrogate ring target. The perimeter of the target is circular. The inner red ring has a known mode structure that meets NIF specifications*

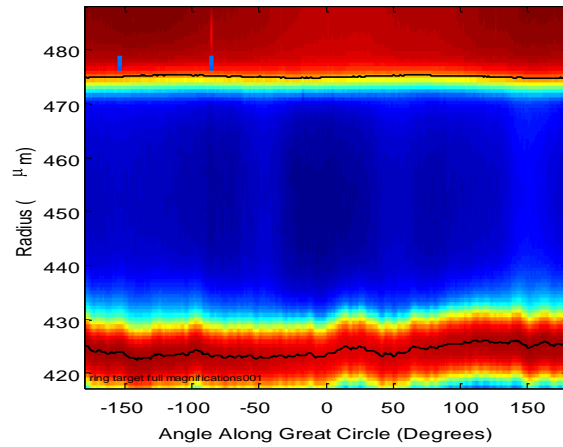


*Figure 13. Line out of Figure 12 without distortion correction.*

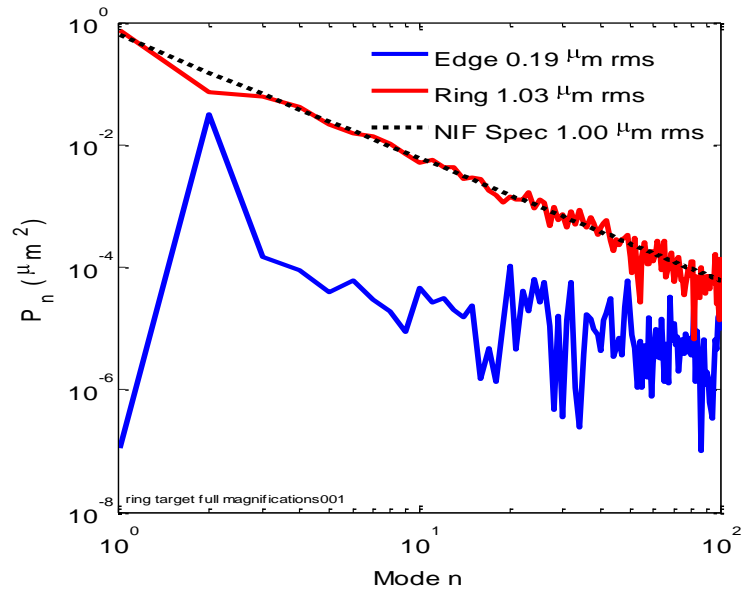


Figure 14. Power spectrum of the surrogate target's outer edge (blue) and first inner ring (red) before distortion correction.

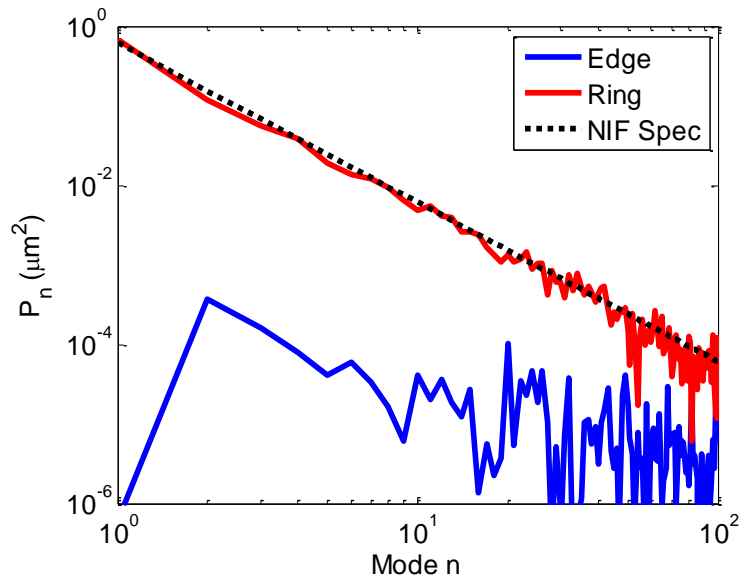


Figure 15. Power spectra of the inner ring and outer edge following the distortion correction. The outer edge (blue) is relatively constant and the inner ring (red) meets NIF specifications (dotted line).

**Electron-Ion Temperature Relaxation Models for Inertial Confinement Fusion**

Barry Xu

Brighton High School  
Rochester, NY

Advisor: S.X. Hu

Laboratory for Laser Energetics  
University of Rochester  
Rochester, NY  
November 2010

## 1 Introduction

At the Laboratory for Laser Energetics (LLE) at the University of Rochester and the National Ignition Facility (NIF) in Livermore, California, research is being focused on the process and application of laser fusion. While there are two main methods of laser fusion, direct and indirect drive, the Laboratory for Laser Energetics mainly deals with direct drive fusion, a process that directly irradiates a target, using the 60-beam OMEGA laser system.

During direct drive, inertial confinement fusion (ICF) is a process in which a cryogenic target is irradiated by high intensity pulses from a laser. The target is a spherical plastic (CH) capsule, approximately 10  $\mu\text{m}$  thick with a diameter of  $\sim 860 \mu\text{m}$ , coated with approximately 65  $\mu\text{m}$  of deuterium-tritium (DT) ice, and filled with three atmospheres of DT. During ICF, the laser pulses partially ablate the CH and deliver the energy necessary to implode the target shell, through the “rocket” effect. This effect compresses the target through laser-driven shocks and spherical convergence [1, 2].

The result is the creation of three distinct regions of particles. Plasma is formed and ejected by the target, creating a high temperature, low density corona around the target. The next region is the (relatively) low temperature and high density shell, which is followed by the hotspot center, which is high temperature and medium density. All three parts are created in about four nanoseconds on the OMEGA laser system and about twelve nanoseconds for the NIF designs.

When the laser irradiates the target, most of the energy is absorbed by the inverse bremsstrahlung process, in which electrons oscillating in the laser electric field undergo momentum transfer collisions with the ions that convert their oscillating energy to

thermal energy. The inverse bremsstrahlung absorption rate is proportional to this collision rate, which is directly proportional to the Coulomb logarithm.

The Coulomb logarithm is a coefficient that helps to model the electron-ion relaxation rate. However, four different models have been proposed for calculating the Coulomb logarithm, the Spitzer model, the Lee-More Model, the Molecular Dynamic (MD) model, and the Brown-Preston-Singleton (BPS) model. Each model calculates the Coulomb logarithm using a different method, such as considering quantum degeneracy effects and using classical molecular dynamics.

These simulations were focused mainly on determining which model most accurately predicted fusion results and the best gain. A program was written to be used with hydrodynamic simulations using triple-picket pulse designs for both the LLE and NIF designs. Also, each model was used to calculate the neutron yield, the laser absorption, the compression areal density  $\rho R$ , and the neutron production rate.

## 2 Simulation Models

### 2.1 *Electron-Ion Relaxation Rate*

When the electrons first absorb the laser energy, they must then transfer that energy to the ions in order for fusion to occur. This electron-ion temperature relaxation rate is defined as:

$$\frac{dT_{e/i}}{dt} = \nu \cdot (T_i - T_e) \Rightarrow \nu = \nu_o \cdot \ln \Lambda \quad (1)$$

where  $\ln \Lambda$  is the Coulomb logarithm and the prefactor,  $\nu_o$ , is a function of density, charge and mass given by



$$v_o = \frac{8}{3} \cdot n_i e^4 Z^2 \frac{\sqrt{2\pi m M}}{(m k_B T_i + M k_B T_e)^{3/2}} \quad (2)$$

where M and m are the ion and electron masses, respectively,  $T_i$  and  $T_e$  are the ion and electron temperatures, Z and e are the ion and electron charges,  $n_i$  is the ion density, and  $k_B$  is the Boltzman Constant [2, 4].

The Coulomb logarithm in the above equation is a unit-less coefficient. This helps to characterize the long range and short range electron-ion collisions in plasmas. The main issue is that the Coulomb logarithm has been approximated in four distinct ways, using various expressions. This leads to debate over which model is most accurate. In the next section, each model is given and analyzed.

## 2.2 Coulomb Logarithm expressions

Four different equations for the Coulomb logarithm have been examined in these calculations. The first one is the Spitzer equation, proposed in 1953, given by:

$$\ln \Lambda = \ln \left( \frac{3}{2 Z_e Z_i e^3} \sqrt{\frac{k_B^3 T_e^3}{\pi m_e}} \right) \quad (3)$$

where  $Z_e$  and  $Z_i$  are the electron and ion charge, with  $Z_e$  equal to one [3]. This equation was created to mitigate the problem of integral divergence in binary collisions. Also, a cut-off was introduced to some of the impact parameters.

The second model that was analyzed is the Lee-More model, proposed in 1984 [5]. Their model includes electron degeneracy effects for low temperature plasmas and is given by:

$$\ln \Lambda = \frac{1}{2} \ln \left[ 1 + (b_{\max}^2 / b_{\min}^2) \right] \quad (4)$$

The distance  $b_{\max}$  is defined as the Debye-Hückel screening length,  $\lambda_{DH}$ , with degeneracy modification, defined as:

$$\frac{1}{\lambda_{DH}} = \sqrt{\frac{4\pi n_e e^2}{k_B \sqrt{T_e^2 + T_F^2}} + \frac{4\pi n_i Z^2 e^2}{k_B T_i}} \quad (5)$$

where  $T_F$  is the Fermi degeneracy temperature. This gives the largest impact parameter for classical collisions. The smallest impact parameter,  $b_{\min}$ , on the other hand, is the larger of the classical collision distance and the de-Broglie wavelength of thermal electrons:

$$b_{\min} = \max\left(\frac{Ze^2}{3k_B T_e}, \frac{\hbar}{2\sqrt{3mk_B T_e}}\right) \quad (6)$$

The Lee-More model for the Coulomb logarithm is implemented into the hydrocodes LILAC [7] and DRACO [8] that are being used at LLE for implosion simulations.

In 2008, the relaxation rate problem was revisited for ICF plasma conditions by Dimonte and Daligault [4]. Their calculations incorporated classical<sup>1</sup> molecular dynamic simulations for electron-ion plasmas with like charges. They came up with a coupling parameter,  $g$ , for their expression of the Coulomb Logarithm:

$$\ln \Lambda = \ln\left(1 + \frac{0.7}{g}\right) \quad (7)$$

The parameter “ $g$ ” is the ratio between the smallest and the largest impact parameter, defined as:

$$g = \frac{R_c}{\lambda_D} = \frac{Ze^2}{\lambda_D k_B T_e} \quad (8)$$

---

<sup>1</sup> The classical model is derived from Newton’s laws and equations.

where  $R_c$ , the Landau length, characterizes large angle scatterings, representing the smallest impact parameter. The electron Debye length,  $\lambda_D$ , is the largest impact parameter, with the fields at larger distances being screened out [4].

The fourth and final model examined was the model proposed by Brown, Preston, and Singleton (BPS) in 2009. In contrast to numerical simulations, analytical studies using dimensional continuation resulted in a BPS model for a wide range of plasma conditions, including quantum and coupling effects. The BPS formula is comprised of three terms [6], a main term and two correction factors, shown here:

$$\ln \Lambda_{BPS} = \ln \Lambda_{BPS}^{QM} + \ln \Lambda_{BPS}^{\Delta C} + \ln \Lambda_{BPS}^{FD} \quad (9)$$

The leading term is based on quantum mechanics and accounts for quantum effects. The second term is a correction for when the plasma parameters are not near the quantum limit; and the third term takes into account the many-body electron degeneracy effects when Fermi-Dirac statistics become important. Each term, ignoring small electron-ion mass ratio effects, can be given as:

$$\ln \Lambda_{BPS}^{QM} = \frac{1}{2} \left[ \ln \left( \frac{8k_B^2 T_e^2}{\hbar \omega_e^2} \right) - \gamma - 1 \right], \quad (10)$$

$$\ln \Lambda_{BPS}^{\Delta C} = -\frac{\varepsilon_H}{k_B T_e} \sum_i \frac{Z_i^2 \omega_i^2}{\omega_i^2} [1.20205 \times \left[ \ln \left( \frac{k_B T_e}{Z_i^2 \varepsilon_H} \right) - \gamma \right] + 0.39624] \quad (11)$$

$$\ln \Lambda_{BPS}^{FD} = \frac{n_e \lambda_e^3}{2} \left[ \frac{-1}{2} \left( 1 - \frac{1}{2^{3/2}} \right) \times \left\{ \ln \left( \frac{8k_B^2 T_e^2}{\hbar^2 \omega_e^2} \right) - \gamma - 1 \right\} + \left( \frac{\ln 2}{2} + \frac{1}{2^{5/2}} \right) \right] \quad (12)$$

where  $\varepsilon_H$  is the binding energy of hydrogen,  $\hbar$  is the Planck constant, and  $\gamma$  is the Euler constant<sup>2</sup>. The electron and ion plasma frequencies are given by  $\omega_e$  and  $\omega_i$ , respectively;

---

<sup>2</sup> The Euler constant  $\approx 0.57721$ .

and  $\omega_i$  is the average ion frequency. BPS also included an electron thermal wavelength,  $\lambda_e$ , which is a derivative of the thermal de-Broglie wavelength [6].

Each model was then run through simulations using the hydro-code LILAC, as described in the next section. Then based on the results, a model was proposed to most accurately model the Coulomb logarithm.

### 2.3 *Implementation into the LILAC Code*

Each of the above mentioned models was implemented into the 1-D hydro-code, LILAC. A subroutine was written using the FORTRAN programming language. The program differentiated between the various regions of the reaction area, the hotspot, the shell, and the coronal plasma.

Each model was run through simulations with varying electron and ion temperatures, modeling the approximate temperatures for the three regions. After the Coulomb logarithm was calculated for each region, the program was run and calculated the various output data using the information from an OMEGA cryogenic shot and the NIF designs for the triple-picket pulse shape.

## 3 **Results and Analysis**

### 3.1 *Predicted Coulomb Logarithm*

The program was run for the following conditions: a)  $T_e = 5$  keV and  $T_i = 10$  keV, which models the “hotspot” center during shock convergence for the NIF designs; b)  $T_e = 2.5$  keV and  $T_i = 5$  keV, which models the “hotspot” center during the shock convergence for the OMEGA designs; c)  $T_e = 2$  keV and  $T_i = 1$  keV, which models the typical corona temperatures for an OMEGA shot; and d)  $T_e = 50$  eV and  $T_i = 100$  eV, which models the imploding shell conditions for an OMEGA target.

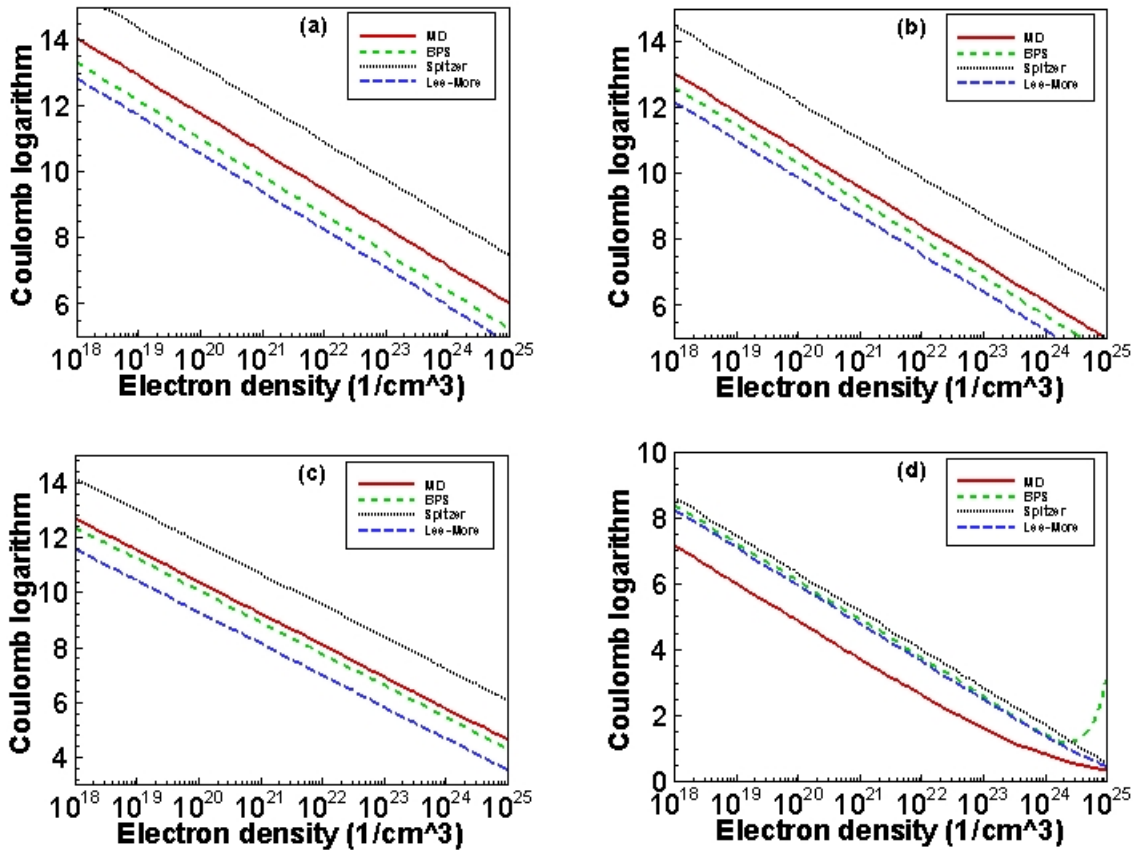


**Figure 1: The Coulomb Logarithm calculated for various conditions**  
 The Coulomb logarithm as a function of electron density for the four different electron-ion temperature relaxation rates at different plasma temperatures. a)  $T_e=5$  keV and  $T_i=10$  keV, b)  $T_e=2.5$  keV and  $T_i=5$  keV, c)  $T_e=2.0$  keV and  $T_i=1.0$  keV, and d)  $T_e=50$  eV and  $T_i=100$  eV

From this data, the Spitzer model predicted the highest Coulomb logarithm for almost all temperatures and densities. Also, in Fig 1(a) and 1(b), the difference between the two newer models and the Lee-More model was consistently  $\sim 10\%$ . For temperatures above 1 keV, the BPS and MD models were generally within 5-7% of each other. In Fig. 1(c), which shows the typical coronal temperatures, the MD and BPS models produced very similar results, which are  $\sim 15\%$  higher than the standard Lee-More model prediction near the critical density regime ( $n_e \sim 9.1 \times 10^{21}$  electrons/cm<sup>3</sup>) of OMEGA’s UV laser ( $\lambda = 0.351 \mu\text{m}$ ). This difference in  $\ln\Lambda$  affects the amount of laser absorption in the corona, subsequently affecting target performance.

Inside the target shell, the temperature is  $\sim 100$  eV during the implosion, where the DT plasma is moderately coupled and partially degenerate [9]. At this point, it is expected that quantum and many-body effects start becoming important; for such conditions, Fig. 1(d) shows that the BPS and the Lee-More models are very similar, but the classical MD model deviates from this, making it no longer valid. The BPS calculation, in Fig. 1(d), shows an increase for very high densities, which clearly shows the degeneracy effects because the plasma temperature is well below the Fermi temperature.

### 3.2 Hydro-Simulation Result: OMEGA

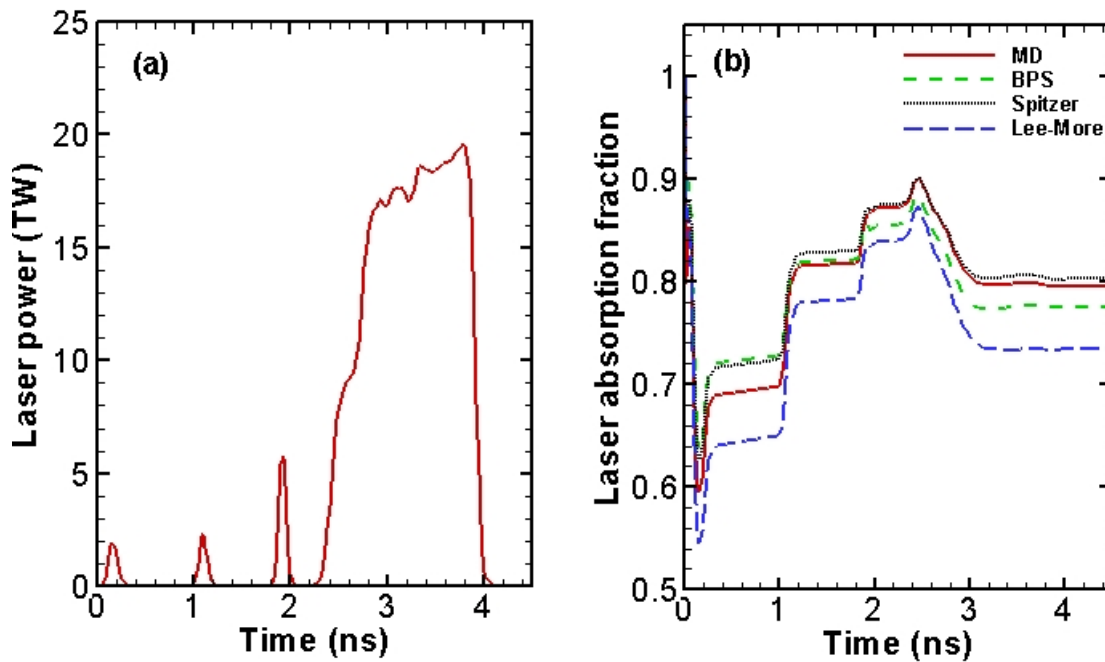


**Figure 2: Pulse Shape and Laser Absorption for the OMEGA system**

These graphs show a) the laser pulse shape for cryogenic DT implosions on OMEGA using three initial shocks to induce a compression shockwave and a fourth to implode the shell; b) the time-dependent laser absorption predicted by the four models.

These models were implemented and then simulated using a triple picket plus a main step pulse shape, for both the OMEGA facility and the direct drive NIF designs, to implode the cryogenic target [10]. Fig. 2(a) shows the exact pulse shape for the OMEGA shot. The first three pickets shot at the target start shock waves that propagate through the shell and coalesce causing it to compress inward. This places the target into the appropriate adiabat ( $\alpha \sim 2$ ) and gives the target a high compression areal density  $\rho R \sim 300$  mg/cm<sup>2</sup> [10]. The OMEGA simulation results are plotted in Figs. 2 and 3. Laser absorptions predicted by the different models are displayed in Fig. 2(b), with the Lee-More model predicting the least amount of absorption. This is expected because Fig. 1(c) predicts the Lee-More model calculating the smallest Coulomb logarithm for the coronal plasma.

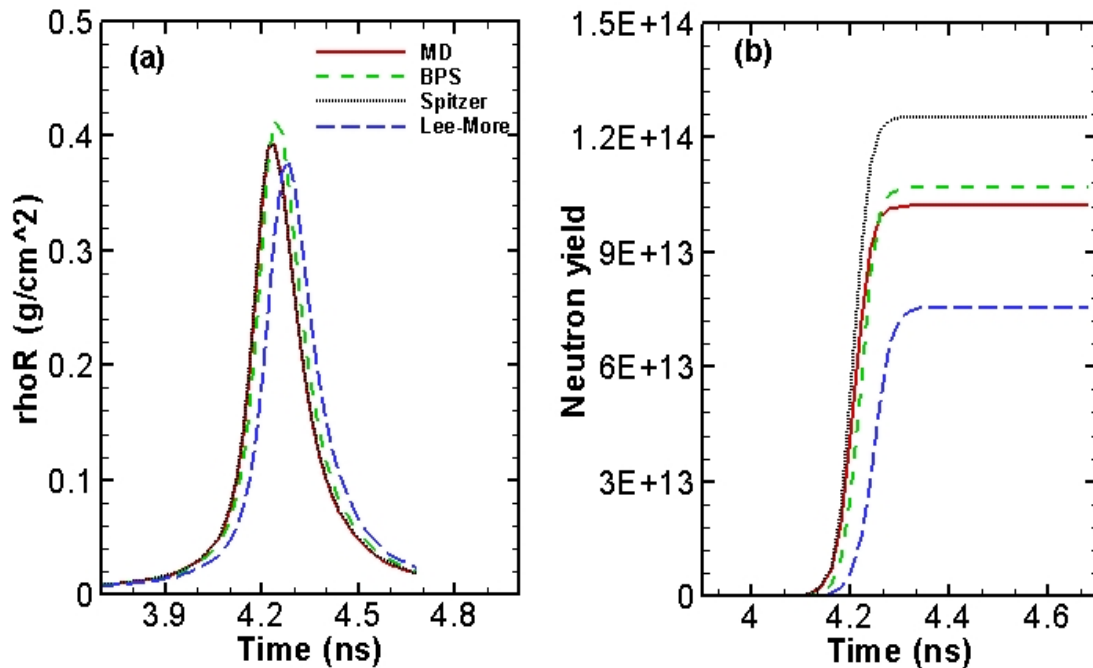


**Figure 3: Graphs of  $\rho R$  and neutron yield**

Each of these graphs show the predicted value for  $\rho R$  and neutron yield as functions of time. a)  $\rho R$  is the density times the radius and is a measure of the compression; b) this is the predicted neutron yield for each model, with the Spitzer model predicting the most.

A point of interest is that the inverse bremsstrahlung absorption is linearly proportional to the Coulomb logarithm. At the end of the main pulse, in Fig. 2(b), the classical MD result is the closest to the Spitzer result. This is expected since both the Spitzer and MD equations are based on the Newtonian model of particle interactions. The BPS model appears between the Lee-More and the MD models. The difference in absorption can be as high as 7%, which is a measurable difference in experiments.

The corresponding compression areal density  $\rho R$  and the neutron yield are shown in Fig. 3(a) and Fig. 3(b), respectively. Compared to the Lee-More model, all of the models have a higher peak  $\rho R$ , and the peak occurs earlier for all of them than the Lee-More model. This is consistent with the higher absorption, as seen in Fig. 2(b). For neutron yield, both the BPS and MD models predict similar outputs, but both differ from the Lee-More model by  $\sim 30\%$ . Again, this difference in neutron yield constitutes a measurable difference in experiments.

Based on the results from the OMEGA data, the Spitzer model appears to predict a value of the Coulomb logarithm that is too high. Also, the Lee-More model seems to predict too low a value. This can be attributed to the fact that these models do not take into account all of the same effects as the BPS and MD models, both of which predict moderate values for the Coulomb logarithm and, in turn, moderate values for the neutron yield.

### 3.3 *Hydro-Simulation Results: NIF*

The results from the LILAC simulations using the direct-drive NIF designs suggested a similar outcome. However, it is worth noting that the targets used by the NIF differ from the targets used by the OMEGA facility. Mainly, the target is bigger; the deuterated plastic shell is  $\sim 37 \mu\text{m}$  with  $\sim 150 \mu\text{m}$  DT ice. This is because the NIF can



deliver more energy to the target, as evidenced by the pulse shape shown in Fig. 4(a), which lasts 2.5 times longer than the OMEGA system and has a much higher peak power.

Fig. 4(b) shows that the total amount of laser absorption is  $\sim 95\%$  for all four models. This can be attributed to the fact that, on the NIF, the plasma density scale length is longer than on OMEGA, resulting in more laser absorption. Fig 4(b) shows that the Lee-More model predicts a lower amount of absorption, especially during the first picket. This would affect the neutron production because the amount of compression the target undergoes is proportional to the amount of energy absorbed.

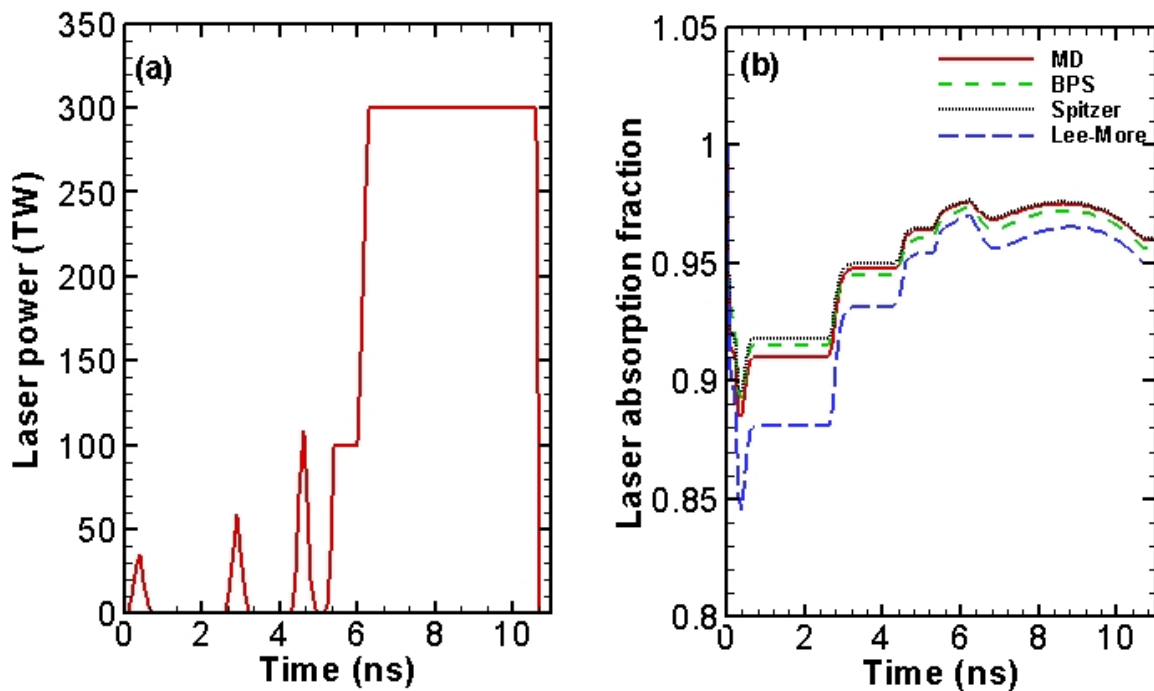


**Figure 4 Pulse Shape and Laser Absorption on the NIF designs**

These graphs show a) the laser pulse shape for the NIF designs is time dependent; b) the laser absorption predicted by each model for the NIF designs.

Compression  $\rho R$  is shown in Fig. 5(a). The variations in peak  $\rho R$  can be accounted for by the differences in shock dynamics. Fig 5(b) shows the neutron yield for the NIF simulations. Again, because all of the predicted laser absorption percentages are

so close together [see Fig. 4(b)], the variations between the predicted neutron yields are relatively small. Based on the neutron yield, the gain (the ratio between the total energy output and the total input energy) predicted by each of the models can be seen in Table 1. There is a variation of ~9% between all of the models.

**Table 1** Calculated gains for each of the proposed models.

Model	Spitzer	Lee-More	MD	BPS
Gain	48.2	45.5	49.5	49.3

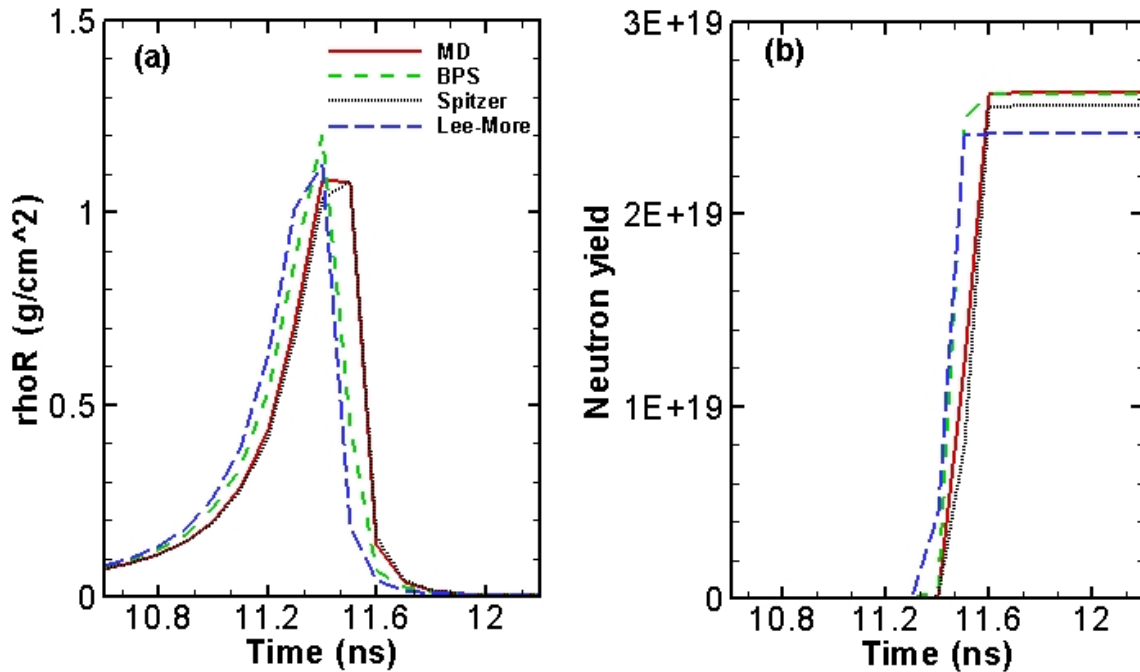


**Figure 5** The areal density and the neutron yield for the NIF designs  
 These graphs display a) the areal density,  $\rho R$  in  $\text{g/cm}^2$  and b) the neutron yield predicted.

### 3.4 Proposed Model

From the results obtained and the analysis of the models, a “best-fit” model was determined for calculating the Coulomb logarithm. As the coronal hotspot temperatures increase above 2 keV for ICF implosions, the MD simulations, which were performed in an ab initio fashion, should better characterize the processes at lower densities. This is due to the fact that these lower density regions behave more according to classical

thermal equilibrium processes, which the MD model accurately accounts for. On the other hand, the BPS formula accounts for the moderately coupled and partially degenerate plasmas in the low-adiabat shell, making it more applicable for those conditions.

Therefore, a combined model for the Coulomb logarithm would be the most accurate. The classical MD model would be used for plasma electron densities less than the critical density,  $n_c$ , the maximum density that can be achieved by a 351-nm laser,  $\sim 1 \times 10^{22} \text{ e/cm}^3$ , and the BPS formula for the dense shell.

$$\ln \Lambda = \begin{cases} \ln \Lambda_{BPS} & (n_e > n_c) \\ \ln \Lambda_{MD} & (n_e < n_c) \end{cases} \quad (13)$$

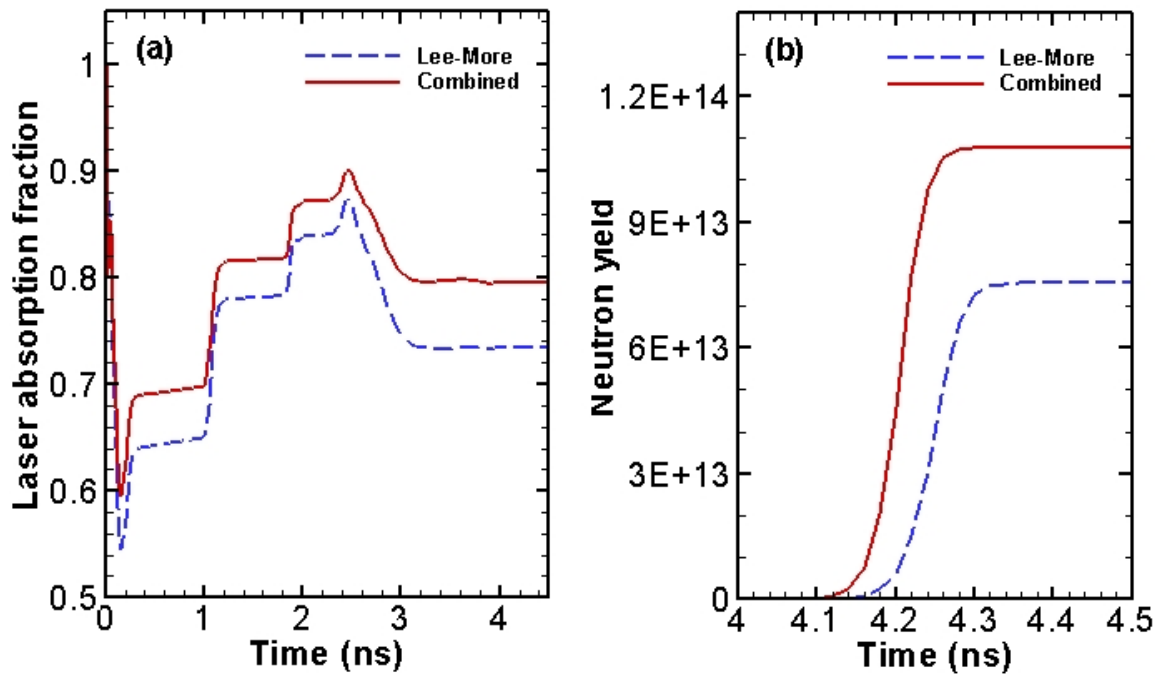


**Figure 6 The proposed model compared with the Lee-More model for OMEGA**  
 These graphs show a) the laser absorption fraction and b) the predicted neutron yield, for both the proposed model and the Lee-More model.

Using this combined model, OMEGA implosions, discussed in Figs. 2 & 3, and NIF implosions, discussed in Figs. 4 & 5, have been simulated. The simulation results are shown in Figs. 6-9 and are shown with the Lee-More model for comparison. The laser absorption, which is plotted in Fig 6(a), shows that the combined model predicts ~6% higher absorption than the Lee-More model. Consequently, the Combined model predicts ~30% larger neutron yield than the Lee-More model, which is a significant increase.

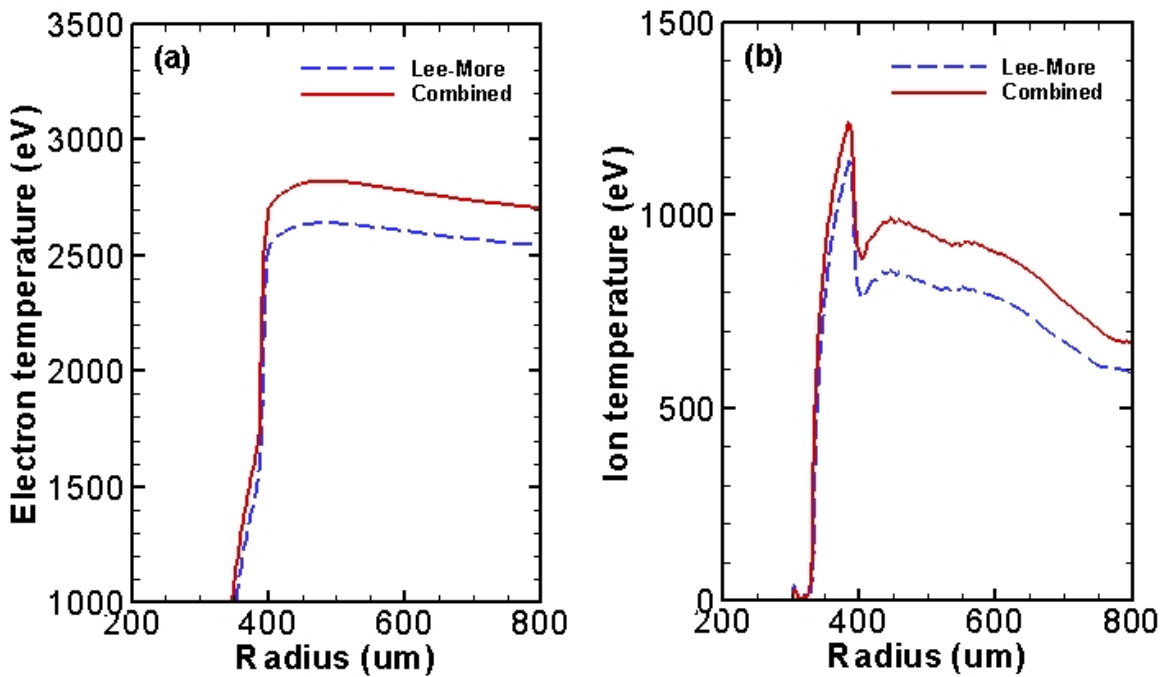


**Figure 7 Predicted temperatures by the proposed model and the Lee-More model for OMEGA**  
 These two graphs show a) the electron temperature and b) the ion temperatures predicted by the models as a function of radius. This is important because it affects the overall performance of the shot.

Also, it is worth noting that the coronal electron and ion temperatures are quite different for the two models. Fig. 7 shows that at  $t = 3.0$  ns, which is just after the main pulse has started to irradiate the target, there is a difference of ~10% between the electron temperatures, and a ~20% difference in the ion temperatures. Such large temperature

differences should be measurable with Thomson scattering [11], which would differentiate the electron-ion temperature equilibration models discussed in this paper.

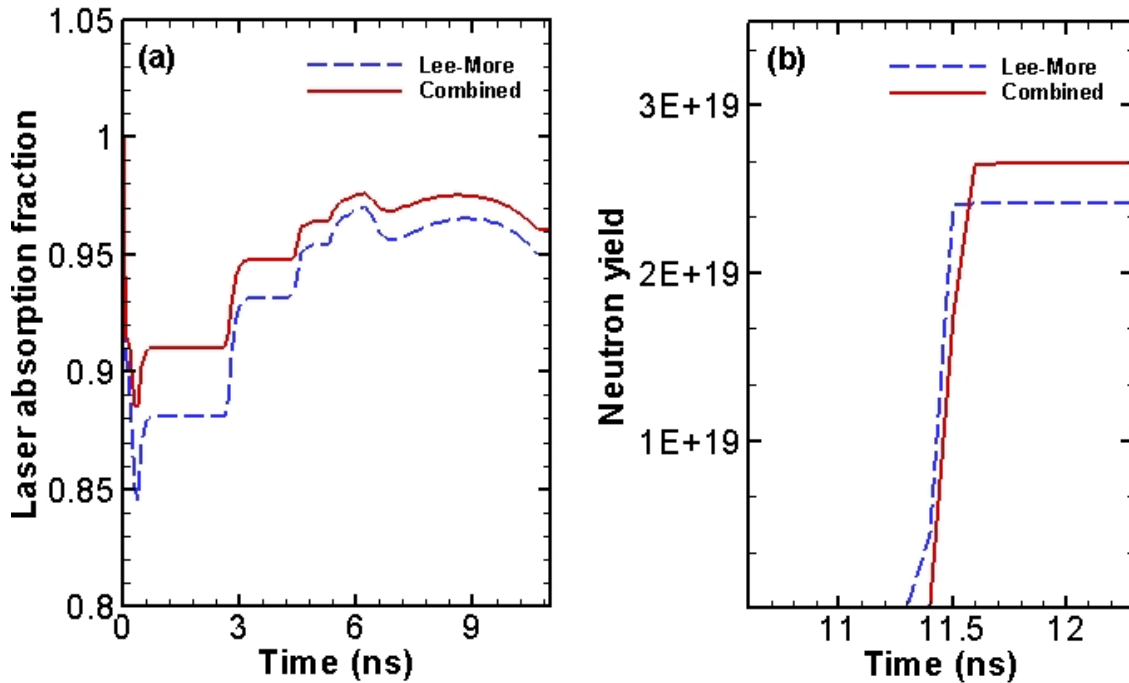


**Figure 8 The proposed model compared with the Lee-More model for NIF designs**

These graphs show a) the laser absorption and b) the neutron yield for the NIF designs. Based on how close the laser absorptions are, it is understandable that the neutron yields are relatively close together.

Similar simulations have also been performed for the NIF design, using the pulse shape in Fig. 4(a). The combined model predicts ~2% higher laser absorption; this small increase is expected because of the high absorption achieved on the NIF. This leads to the Combined model predicting only ~10% more neutron yield than the Lee-More model, seen in Fig. 8. A higher neutron yield is predicted because the Combined model takes into account the many-bodied effects of the shell better than the Lee-More model.

For the NIF designs, the Combined model predicts higher electron and ion temperatures, Fig. 9, than the Lee-More model. The final target gain predicted by the Combined model is 49.8, which is ~10% higher than the 45.5 gain predicted by the Lee-More model.

Based on the results, the Combined model appears to be more effective at predicting the conditions during ICF fusion. This is based on the fact that it incorporates both classical and quantum mechanics effects.

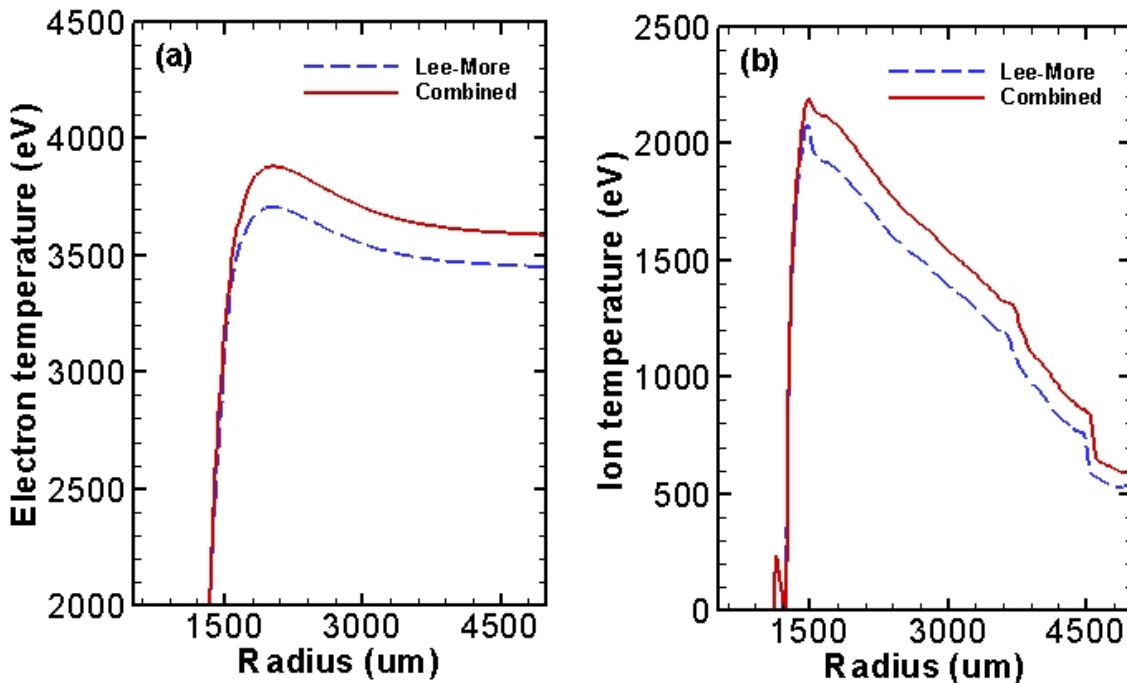


**Figure 9** The electron and ion temperature compared for both models for the NIF  
 These graphs show a) the electron temperatures and b) the ion temperatures as functions of radius.

#### 4 Conclusion

Electron-ion temperature equilibration effects on cryogenic DT implosions on the OMEGA system and the NIF designs have been investigated. Different electron-ion relaxation models have been examined. A subroutine for the hydro-code, LILAC, was written to implement each of the four models.

The hydro-simulations have shown that there are distinct variations between the four models that are readily noticeable in experiments. The implosion performance is sensitive to the electron-ion temperature equilibration models because the inverse bremsstrahlung laser absorption is closely related to the electron-ion Coulomb logarithm and the coronal temperatures.

These calculations have shown that the Spitzer and Lee-More models predict too high and too low Coulomb logarithms, respectively. The MD model is best for modeling regions with densities less than the critical density, due to the use of the classical Newtonian model, while the BPS model is better suited for higher densities due to the incorporation of quantum mechanics effects.

As a result of these calculations, a piece-wise model was proposed to model the Coulomb logarithm most effectively. The piece-wise model comprised the classical MD model for the coronal plasma and the “hotspot”, and the BPS model for the shell conditions using quantum effects. This ensures that the most accurate results are calculated.

Moving forward, the accuracy of this model can be confirmed using Thomson scattering, which would differentiate between the models based on the electron and ion temperatures calculated. Finally, to ensure that this model remains as accurate as possible, it should be revisited and re-analyzed with every new model of the Coulomb logarithm that is constructed and proposed.

**Acknowledgements:**

I would like to thank Dr. S.X. Hu for being my research advisor for this project, Dr. R.S. Craxton for reviewing my figures and suggesting improvements, and the University of Rochester Laboratory for Laser Energetics for allowing me to use their facilities.



**Bibliography**

- [1] S. Atzeni and J. Meyer-ter-Vehn, *The Physics of Inertial Fusion*. Oxford. Clarendon Press. 2004.
- [2] J.D. Lindl, *Inertial Confinement Fusion: The Quest for Ignition and Energy Gain Using Indirect Drive*. New York. Springer-Verlag. 1998.
- [3] L. Spitzer, *Physics of Fully Ionized Gases*. New York. John Wiley & Sons, Inc. 1962.
- [4] G. Dimonte and J. Daligault, “Molecular-Dynamics Simulations of Electron-Ion Temperature Relaxation in a Classical Coulomb Plasma” *Physics Review Letters*, vol. 101, 135001. September, 2008.
- [5] Y.T. Lee and R.M. More. “An electron conductivity model for dense plasmas” *Physics of Fluids*, vol 27, 1273. December, 1983
- [6] L.S. Brown and R.L. Singleton, Jr. “Temperature equilibration in a fully ionized plasma: Electron-ion mass ratio effects” *Physics Review E*, vol. 79, 066407. June 2009.
- [7] J. Delettrez *et al.*, “Effect of laser illumination nonuniformity on the analysis of time-resolved x-ray measurements in uv spherical transport experiments” *Physics Review A*, vol. 36, 3926. October, 1987.
- [8] P.B. Radha *et al.* “Multidimensional analysis of direct-drive, plastic-shell implosions on OMEGA”. *Physics of Plasmas*, vol. 12, 056307. April, 2005.
- [9] S.X. Hu, B. Militzer, V.N. Goncharov, and S. Skupsky “Strong Coupling Effects and Degeneracy Effects in Inertial Confinement Fusion Implosions”. *Physics Review Letters*, vol. 104, 235003. June, 2010.
- [10] V.N. Goncharov, et al. “Demonstration of the Highest Deuterium-Tritium Areal Density Using Multiple-Picket Cryogenic Designs on OMEGA” *Physics Review Letters*, vol. 104, 165001. April, 2010.
- [11] D.H. Froula et al., “Quenching of the Nonlocal Electron Heat Transport by Large External Magnetic Fields in a Laser-Produced Plasma Measured with Imaging Thomson Scattering” *Physics Review Letters*, vol. 98, 135001. March, 2007.

**Modeling Absorption Spectra of Optically Switchable Azobenzenes**

Andrew Yu

**Pittsford Sutherland High School**  
Pittsford, NY

Advisor: Kenneth L. Marshall

**Laboratory for Laser Energetics**  
University of Rochester  
Rochester, NY

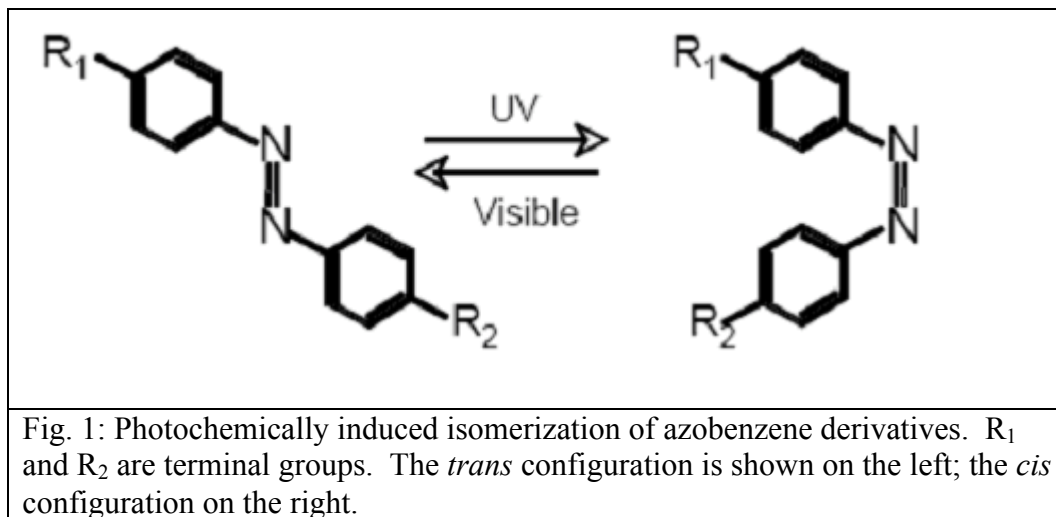
October 2010

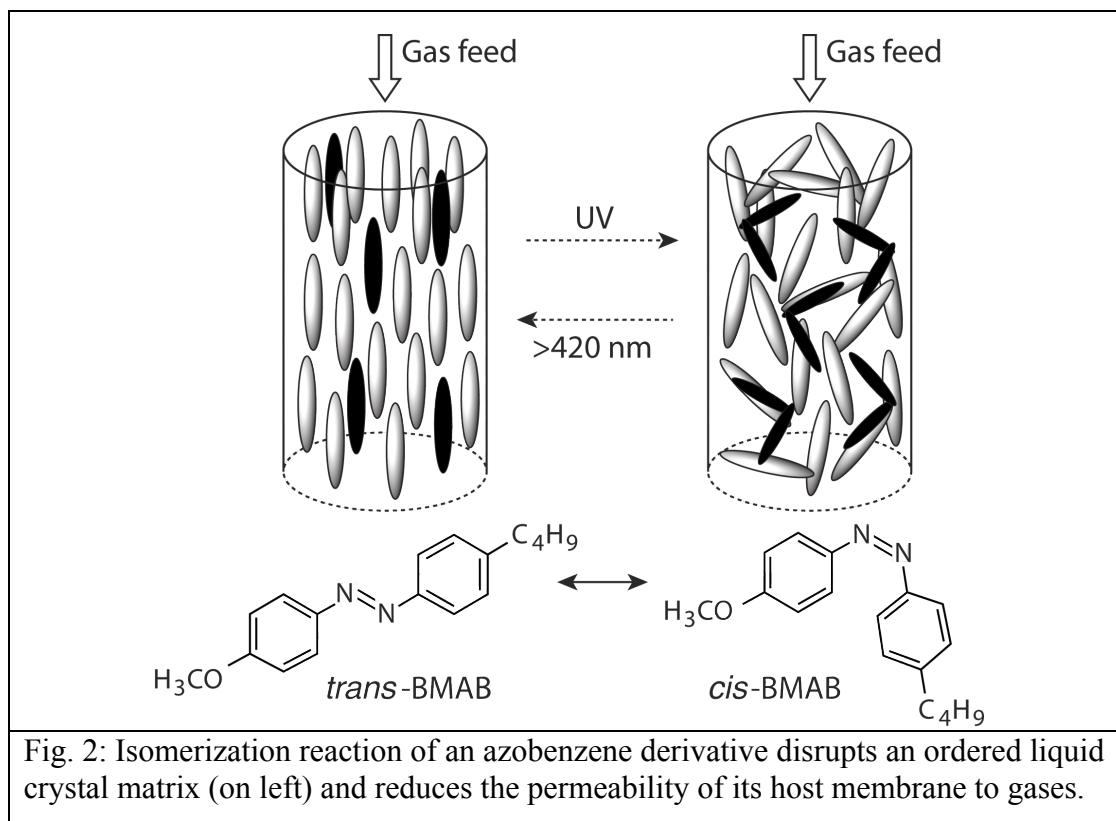
## **Abstract**

Azobenzenes have the unique ability to undergo reversible isomerization between two geometrical isomers (the straight *trans* form and the bent *cis*) when exposed to certain wavelengths of light, which provide energy for the change. Thus, when embedded in liquid crystal matrices, azobenzene derivatives can function as optically triggered switches regulating, for example, membrane permeability to gases. An optimal azobenzene for this application would have an energy barrier low enough to facilitate changes from *trans* to *cis* and back again, but high enough so that such changes would remain stable. In order to identify such suitable azobenzenes, a series of azobenzene derivatives were modeled using computer software. The resulting data were compared, and it was found that nitro groups lowered both thermal and photochemical barriers, while aminoester groups increased the thermal relaxation barriers. Thus, it seems feasible to engineer azobenzene derivatives specifically for use as optical switches in these doped membranes.

## Introduction

Azobenzene and its derivatives exhibit a unique ability to undergo isomerization when exposed to energy in the form of light. When subjected to irradiation with the correct wavelength of UV light, the straight *trans* configuration will transmute into the bent *cis* configuration; the reverse is true upon exposure to visible light (Fig. 1). This property, along with the concurrent rapid, easily reversible changes it comes with, allows azobenzenes to change the optical properties of liquid crystal systems to which they are added as dopants, or “guests”.<sup>1</sup> Azobenzene isomerization can change physical properties as well: the *trans* isomer’s para terminal groups are separated by 9.0 Å, while the same atoms in the *cis* isomer are only 5.5 Å apart.<sup>2</sup> Thus, azobenzene and its derivatives have many applications in regards to both liquid crystal systems and digital data storage.





Currently, much research at the Laboratory for Laser Energetics has been directed towards the use of these azobenzenes as optical switching devices in conjunction with liquid crystal membranes. Such membranes are constructed with pores filled with azobenzene-doped liquid crystal matrices. Such matrices can act as photochemical switches that moderate the permeability of their host membrane to gases (Fig. 2). In the *trans* configuration, the matrix is well ordered, and thus, gases can easily pass through the membrane. Under UV light, however, the transition from the *trans* isomer to the *cis* isomer disrupts the matrix, and membrane permeability drops dramatically<sup>3</sup>.

These optically switchable membranes have a variety of applications in optics and photonics, but require azobenzene molecules with specific properties. The desired azobenzenes must have energy barriers low enough to facilitate change from the *trans* to the *cis* configuration (C to A, Fig. 3), but high enough to minimize spontaneous relaxation

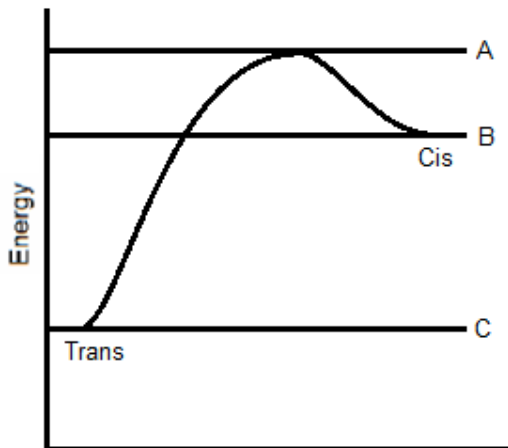


Fig. 3: Energy barriers in azobenzenes. To switch from the *trans* state to the *cis*, the isomerization barrier (C to A) must be overcome; as this requires UV light, this is called the photochemical barrier. Because the *cis* state is at a higher energy level than the *trans*, the reverse energy barrier (B to A) is lower, and can be overcome by visible light or thermal motion – hence, the name thermal barrier.

from the *cis* isomer to the *trans* due to thermal excitation (B to A, Fig. 3; this is more important for applications at higher temperatures). This project used computational chemistry to model a series of azobenzenes in an attempt to determine whether certain functional groups reliably alter energy barriers, and if so, what their effects are.

To do this computational modeling, the programs Spartan (Wavefunction, Inc) and Gaussian03 (Gaussian, Inc) were used. Spartan was used both as a molecular mechanical modeling tool and to calculate thermal relaxation barriers from the *cis* state to the *trans* state. Gaussian03 used molecular mechanical output from Spartan, along with its DFT (density-functional theory) capability, to calculate the photochemical barriers from the *trans* state to the *cis* state. The results indicated that nitro and dimethyl amino groups lowered both thermal and photochemical energy barriers, while aminoester groups raised thermal energy barriers (no significant effects on photochemical barriers).

### Previous Research

Computational chemistry is a well-established method of predicting the properties of molecules, without the need to synthesize and evaluate them in order to determine their suitability for applications. There are three main categories of excited state

computations: *ab initio* methods, such as Hartree-Fock and single-configuration interaction (CIS), semi-empirical methods, such as ZINDO, and DFT (Density-Functional Theory) and TDDFT (Time-Dependent DFT). Density-functional theory and its derivatives are recent developments that use 3-D electron density functions in their calculations rather than a many-electron wave function (Fig. 4).<sup>6</sup> The TDDFT modification to this method uses density functions to map the development of a perturbed system over time. The molecular system is perturbed with a light impulse containing all frequencies, and the maximum absorption wavelengths can subsequently be computed.

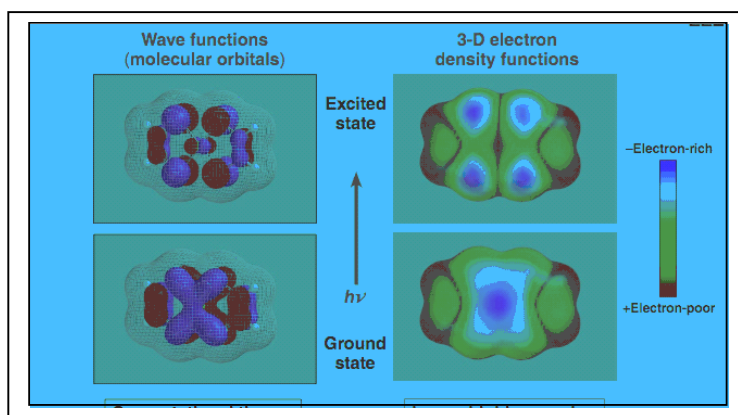


Fig. 4: Wave functions vs. density functions. Density functions require a significantly lower computational cost.

Several previous studies have been done through the high school summer research program at the Laboratory for Laser Energetics, focusing on optimal methods of excited state computations. One previous study showed that TDDFT was a relatively accurate tool for measuring absorption spectra of azobenzenes, reporting a mean absolute error of 47.1 nm.<sup>7</sup> A later study showed that TDDFT was more accurate than ZINDO when modeling azobenzene derivatives.<sup>8</sup>

## Methodology

TDDFT and ground state energy calculations for the *trans* state were performed using Gaussian03<sup>9</sup>, and ground state calculations for the *cis* state were performed using Spartan (Wavefunction, Inc). The process used in these calculations is detailed in Fig. 5.

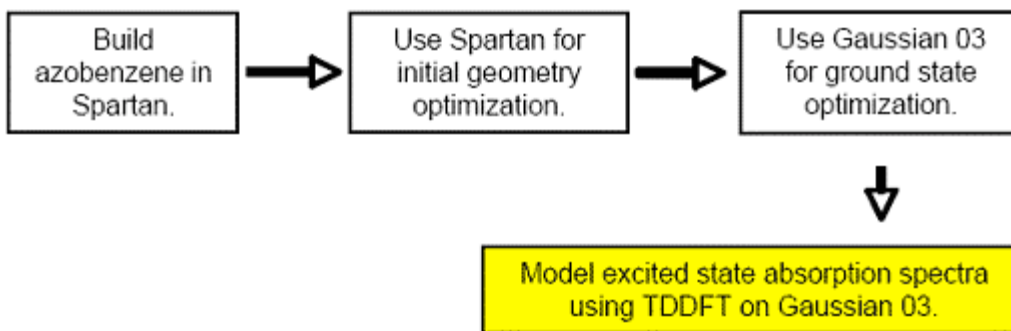


Fig. 5: Methodology used to predict excited state absorption spectra.

Spartan is a computational chemistry software package that includes tools for the visualization of molecules, as well as initial geometry optimizations. This program generates approximate Cartesian coordinates that can be subsequently fed into Gaussian03 for a more accurate geometry optimization through the use of DFT. These coordinates are then used as Gaussian03 input files themselves; the program uses the coordinates to calculate the excited state absorption spectra using TDDFT.

Previous studies were referenced in order to choose a basis set. A previous study by Marshall *et al.* determined that the 6-311G(3d, 2p) basis set was most appropriate for ground state geometry optimizations of azobenzene derivatives; therefore, this basis set was used for ground state optimization during this study.<sup>4</sup> Several other studies used a different basis set [6-311G+(3d, 2p), the “+” meaning that single diffuse functions have been added in order to increase accuracy] to model excited-state absorption spectra; thus, for purposes of comparison, this basis set was used in this study as well.



There are three broad categories of DFT methods, which use combinations of exchange and correlation functionals: exchange-only, pure, and hybrid functionals. Exchange-only and pure functionals use solely Hartree-Fock and DFT exchange-correlation, respectively; meanwhile, hybrid functionals are mixtures of Hartree-Fock and DFT exchange-correlation. The hybrid method B3LYP, which uses the LYP (Lee, Yang, Parr) expression for non-local correlation and VWN (Vosko, Wilk, Nusair) functional III for local correlation, was determined by a previous study to be the best method for modeling azobenzene derivatives, and as such, this method was used here.<sup>8,9</sup>

The series of azobenzenes examined was based upon previous research done by Wang<sup>8</sup> and Marshall *et al.*<sup>3</sup> The series consisted of nine azobenzenes studied by Wang, and two studied by Marshall *et al.* The full series can be seen in Table 1.<sup>3,8</sup> A full list of thermal and photochemical barriers is given in Table 2.

<b>1</b>		<b>6</b>	
<b>2</b>		<b>7</b>	
<b>3</b>		<b>8</b>	
<b>4</b>		<b>9</b>	
<b>5</b>		<b>10</b>	
<p>Table 1. Azobenzenes 1-9 were previously examined by Wang, and azobenzenes 10 and 11 were previously used by Marshall <i>et al.</i></p>		<b>11</b>	

Functional Group 1	Functional Group 2	<i>Cis-trans</i> thermal barrier (kcal/mol)	<i>Trans-cis</i> photochemical barrier (eV)
None	None	14.276	4.862
None	-DA	14.213	2.923
-CN	-DA	13.959	2.715
-NO <sub>2</sub>	-DA	12.944	2.144
-NO <sub>2</sub>	-AE	17.284	2.831
-CN	-AE	21.221	3.403
-CF <sub>3</sub>	-AE	21.142	3.318
-Cl	-AE	21.169	3.333
-Cl	-C <sub>6</sub> H <sub>4</sub> -AE	21.012	3.093
-COCH <sub>3</sub>	-C <sub>4</sub> H <sub>9</sub>	13.986	3.361
-OCH <sub>3</sub>	-C <sub>4</sub> H <sub>9</sub>	14.105	3.527
-OC <sub>2</sub> H <sub>5</sub>	-OCOC <sub>5</sub> H <sub>11</sub>	14.138	3.475

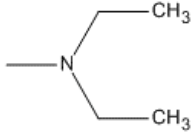
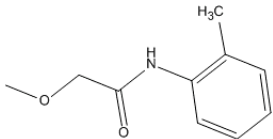
Functional group	Assigned code
Dimethyl amino 	DA
Aminoester 	AE

Table 2: *Cis-trans* thermal barriers and *trans-cis* photochemical barriers for the tested series of azobenzenes. The first row denotes an unmodified azobenzene (no functional groups); the ordering of functional groups is arbitrary.

## Results

It was found that nitro groups lowered both thermal and photochemical energy barriers, while aminoester groups raised thermal energy barriers. A combination of nitro and aminoester groups produced an optimal result, raising the thermal barrier while simultaneously lowering the photochemical barrier. For comparison purposes, Table 2 also shows the base values for an unmodified azobenzene.

From the data collected, it can be seen that aminoester groups, dimethyl amino groups, and nitro groups had significant, systematic effects on energy barriers between states. Of these, aminoester groups had the greatest effect on thermal barriers, raising them on average by 6.445 kcal/mol. Nitro groups had the greatest effect on photochemical barriers, lowering them on average by 0.751 eV. These results are summarized in Table 3.

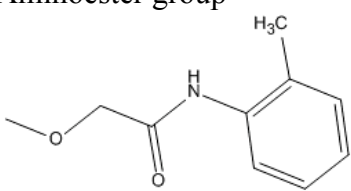
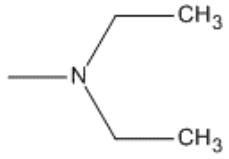
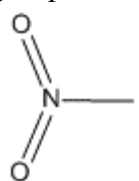
Functional group	<i>Cis-trans</i> thermal barrier difference (avg. with – avg. without)	<i>Trans-cis</i> photochemical barrier difference (avg. with – avg. without)
Aminoester group 	6.445 kcal/mol, $\sigma=1.71$	0.172 eV, $\sigma=0.53$
Dimethyl amino group 	-4.235 kcal/mol, $\sigma=3.30$	-0.699 eV, $\sigma=0.39$
Nitro group 	-2.092 kcal/mol, $\sigma=4.11$	-0.751 eV, $\sigma=0.43$

Table 3: Average thermal and photochemical barrier differences for different functional groups.

For membrane doping, azobenzenes with low photochemical barriers but high thermal barriers are optimal. Nitro groups satisfy the first requirement, as azobenzenes containing them were shown to have greatly lower photochemical barriers, but as they also lowered thermal barriers, they are alone insufficient for the creation of azobenzenes for membrane doping. Aminoester groups show the same weakness: they raise thermal barriers significantly, but also slightly raise photochemical barriers. However, one azobenzene tested included both functional groups, and showed itself to be the best azobenzene of the series: not only did it raise the thermal barrier (from a base of 14.276 kcal/mol to 17.284 kcal/mol), but it also lowered photochemical barriers (from 4.862 eV to 2.831 eV) as compared to unmodified azobenzene.

### **Discussion/Conclusion**

This study indicates that various functional groups can influence energy barriers in predictable ways. Specifically, azobenzenes modified with aminoester groups exhibit higher thermal barriers, while those modified with dimethyl amino and nitro groups had lower photochemical barriers (these two functional groups also lowered thermal barriers). An optimal azobenzene was seen to possess both an aminoester and a nitro group. This suggests that azobenzene dopants may in future be predictably developed and synthesized to fit certain needs. However, this is only a very preliminary study of feasibility. Future research would entail both selecting azobenzene series specifically by functional group, and detailed analysis using more computational chemistry packages. Also, Spartan and Gaussian03 often provided conflicting geometry optimizations when calculating values for *cis*-phase azobenzene derivatives. Because of this, future work may also focus on these inaccuracies, along with their resolution.

## **Acknowledgements**

I was sustained and supported in this project by many individuals. First of all, I owe Mr. Kenneth L. Marshall a great deal, both for serving me as my advisor and for providing resources and references. Next, I thank the University of Rochester and the Laboratory for Laser Energetics in particular for supporting the high school research program, and Dr. Stephen Craxton for selecting me to take advantage of this great opportunity. Tony Brancato and Victor Wang provided a great deal of technical and conceptual aid, respectively. Finally, I of course must thank the members of the Materials Lab at the Laboratory for Laser Energetics, and my fellow interns, for supporting me throughout the duration of this project.

## References

1. Delaire, Jacques; Nakatani, Keitaro. *Chem. Rev.* 2000, 100, 1817-1845.
2. G.J. Ashwell, *Nature* 347 (1990) 617.
3. K. Marshall et. al., “Photoswitchable Gas Permeation Membranes Based on Azobenzene-Doped Liquid Crystals”, SPIE 2010.
4. Marshall, K. L. *et al.*; “Using Time-Dependent Density Functional Theory (TDDFT) in the Design and Development of Near-IR Dopants for Liquid Crystal Device Applications”; *Proc. of SPIE* 2007 Vol. 6554, pp 65540F1-65540F13.
5. Levine, Ira N. (1991). *Quantum Chemistry*. Englewood Cliffs, New Jersey: Prentice Hall. pp. 455-544.
6. Hehre, W. J. *Ab Initio Molecular Orbital Theory*. 1986 (Wiley, New York).
7. Wang, Ernest, “Computational Modeling of Spectral Properties of Azobenzene Derivatives”; LLE Summer High School Research Program, 2007.
8. Wang, Victor, “Computational Modeling of Optically Switchable Azobenzenes”; LLE Summer High School Research Program, 2009.
9. Frisch, M.J. *et al.*, *Gaussian 03*, Gaussian, Inc., Pittsburgh, PA, 2004.